Doctral Dissertation
博士論文

Search for $\mu \to e\gamma$ with the first year data of the MEG II experiment

(MEG II実験初年データを用いた$\mu \to e\gamma$探索)

A Dissertation Submitted for the Degree of Doctor Of Philosophy

December 2023

令和 5年 12月博士 (理学) 申請

Department of Physics, Graduate School of Science,
The University of Tokyo

東京大学大学院理学系研究科物理学専攻

Atsushi Oya
大矢 淳史

Abstract

A search for $\mu \to e\gamma$ was performed at a sensitivity of 8.8×10^{-13} by observing 2.64×10^{12} muon decays with the first MEG II data taken for effectively four weeks. No signal excess was observed in this analysis and we set an upper limit of

$$\mathcal{B}(\mu \to e\gamma) < 7.5 \times 10^{-13}$$

at $90\,\%$ confidence level. This result indicates that the MEG II experiment, even with the very limited data statistics, approached the previous search, which gave $\mathcal{B}(\mu \to e\gamma) < 4.2 \times 10^{-13}$ as a result of a search with the sensitivity of 5.3×10^{-13}. This is a firm demonstration that a few years of MEG II experiment will reach its initial goal of searching for $\mu \to e\gamma$ with an order of magnitude better sensitivity.

In addition, a combined analysis was performed using the previous experiment and the MEG II 2021 data. The combined sensitivity was 4.3×10^{-13} , and we set an upper limit of

$$\mathcal{B}(\mu \to e\gamma) < 3.1 \times 10^{-13}$$

at $90\,\%$ confidence level. This is the most stringent limit ever for the $\mu \to e\gamma$ branching ratio.

Contents

Preface

Background of this thesis

The standard model (SM) of particle physics describes the fundamental elements of matter and the laws behind them. Its validity has experimentally been confirmed up to the electroweak scale around $\mathcal{O}(100\,\mathrm{GeV})$. However, several fundamental problems are addressed on the SM, and thus, the particle physics research is further continued to better understand them.

As candidate solutions for the problems of the SM, theorists have proposed various new physics models. In response to them, several experiments have been conducted in pursuit of their signature. An important branch among such efforts is *charged Lepton Flavor Voilation* (cLFV), mixing phenomena between charged leptons from three different generations, electron, muon, and tau. Searches for cLFV are intriguing because of the experimental cleanness; the SM strictly forbids cLFV, and thus, a discovery of such phenomena is clear evidence of new physics. The search is valuable also because cLFV-based tests of new physics models can likely be experimentally reachable, according to several predictions in theories beyond the SM.

The forerunner among the cLFV searches is $\mu \to e\gamma$, on which, the branching ratio is currently limited as $\mathcal{B}(\mu \to e\gamma) < 4.2 \times 10^{-13}$ $(90\,\%$ C.L.) by the MEG experiment [1]. This limit has already started to exclude some models beyond the SM. In some predictions, however, $\mathcal{B}(\mu \to e\gamma)$ still lies just below the current upper limit, being 10^{-14} – 10^{-12}. Accordingly, a new experiment — the MEG II experiment — is in progress to search for the $\mu \to e\gamma$ decay with an order of magnitude higher sensitivity.

Theme of this thesis

The main theme of this thesis is a search for $\mu \to e\gamma$ decay with the MEG II 2021 data as a pioneering work for the MEG II experiment. As well as building the analysis framework, the author also established the detector calibration and event reconstruction, which is also a subject of this thesis. The details of the analysis procedure, reconstruction, and calibration methods, and the result of the 2021 data analysis are described in this thesis.

The background suppression is the key ingredient to finally achieve an order of magnitude sensitivity improvement in the MEG II experiment, as is evident from the experience in the previous experiment. This requires improvements in the detector's resolution, which is demonstrated in this thesis. This thesis also presents that the detector's efficiency is improved by a factor of ~ 2. Consequently, this thesis confirms that an order of magnitude improvement can be realized in a few years by a continuous data taking of the MEG II experiment.

Outline of this thesis

This thesis is organized as follows. Chap.1 gives up-to-date knowledge about the $\mu \to e\gamma$ search with reviews of the theoretical motivations, experimental principles, and results of the previous experiment. The situation of the MEG II experiment before this thesis is then summarized, which is to clarify the original studies of this thesis that are briefly listed at the end of this chapter. Chap.2 describes the MEG II apparatus in detail, and then, Chap.3 summarizes the data-taking condition in 2021. Chap.4 explains the first step of the data analysis; the event reconstruction and selection. Chap.5 then describes the calibration of the detectors and evaluates their performances. Chap.6 gives the full methodologies of the analysis searching for $\mu \to e\gamma$ and discusses all the properties of the analysis. Chap.7 presents the result of the analysis with its interpretation and discusses the outlook of the MEG II experiment. Finally, this thesis is concluded in Chap.8.

Chapter 1

Introduction to $\mu \to e\gamma$

1.1 $\mu \to e\gamma$ search as a probe of new physics

Despite its success up to $\mathcal{O}(100\,\mathrm{GeV})$, the Standard Model (SM) is not considered as an ultimate theory, but a low energy approximation of a more fundamental physics. This is because the SM faces several problems, among which the following three are especially important as the background of $\mu \to e\gamma$ search. Firstly, the SM does not provide candidate particles for the dark matter and dark energy, which are observationally evaluated to account for $26\,\%$ and $69\,\%$ of the universe [2, 3]. Secondly, the observed neutrino oscillation [4, 5] is not viable with the massless description of neutrinos in the SM. The final one is called the hierarchy problem; no natural explanation is given as to why the measured Higgs mass of $125\,\mathrm{GeV}$ lies in the electroweak scale, which is several orders of magnitude smaller than the Plank scale of $\mathcal{O}(10^{19}\,\mathrm{GeV})$ [6, 7, 8].

These problems can be solved by introducing new physics beyond the SM, such as supersymmetry (SUSY) [9], grand unified theory (GUT), and see-saw mechanism [10, 11, 12]. The SUSY introduces new partner particles for those in the SM, which can provide a candidate for the dark matter and solve the hierarchy problem. The see-saw mechanism, on the other hand, grows our attention with its ability to explain the tiny neutrino mass ($< 0.151\,\mathrm{eV}$ [13]) and their mixing. This model introduces right-handed neutrinos with large Majorana mass terms, and the mass of the left-handed neutrino becomes M_D^2/M_R, where M_D is the Dirac mass and M_R is the Majorana mass. The GUT, which unifies interactions and matter particles, also motivates us because the gauge coupling constants get close to each other around $\mathcal{O}(10^{16}\,\mathrm{GeV})$ [9].

These new models can be probed by a $\mu \to e\gamma$ search, and this section aims to explain why. In the following sections, it is firstly clarified that $\mu \to e\gamma$ decay is strictly prohibited in the SM (Sec.1.1.1). Then, we review the predictions of $\mu \to e\gamma$ in the above models, which suggest the possibility of an experimental detection (Sec.1.1.3). In short, model probing power is given to $\mu \to e\gamma$ search by the cleanness in the SM and an enhanced rate in new physics predictions.

1.1.1 Charged leptons in the Standard Model

In the SM, the charged leptons have gauge coupling to the electromagnetic and the weak interactions, and the Higgs coupling for the mass generation. They are written as

$$\begin{aligned}\mathcal{L} = \ & e\bar{\ell}\gamma^\mu \ell A_\mu \\ & - \frac{g}{\sqrt{2}}(\bar{\nu}_{\ell_L}\gamma^\mu \ell_L W_\mu^+ + \bar{\ell}_L\gamma^\mu \nu_{\ell_L} W_\mu^-) \\ & - \sqrt{g^2+g'^2}\left\{\bar{\ell}_L\gamma^\mu\left(-\frac{1}{2}+\sin^2\theta_W\right)\ell_L + \bar{\ell}_R\gamma^\mu\sin^2\theta_W\ell_R\right\}Z_\mu \\ & - \frac{m_\ell}{v}\bar{\ell}\ell H.\end{aligned} \tag{1.1}$$

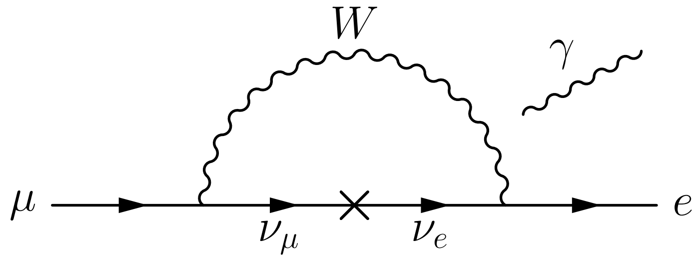

Figure 1.1: $\mu \to e\gamma$ decay mediated directly by the neutrino mixing

Here, any reactions of charged leptons preserve the lepton flavor, which is one of the most important properties of the SM. Therefore, $\mu \to e\gamma$ decay, which violates the lepton flavor, is strictly prohibited in the SM. However, this conservation law is not considered as a fundamental one that comes from a guiding principle. Rather, it has been thought to be an accidental conservation.

The observation of the neutrino oscillation revealed that the accidental conservation no longer holds. This phenomenon itself, however, cannot produce an observable $\mu \to e\gamma$ branching ratio. In fact, its contribution to the $\mu \to e\gamma$ branching ratio is given as [14, 15, 16]

$$\mathcal{B}(\mu \to e\gamma) = \frac{3\alpha}{32\pi} \sum_i \left| U_{\mu i} U_{ei} \frac{\Delta m_i^2}{M_W^2} \right|^2 \sim 10^{-54}, \tag{1.2}$$

where i runs over the neutrino generations. The non-zero branching ratio arises from the process shown in Fig.1.1. Hence, $\mu \to e\gamma$ decay search remains to be a clean channel to probe a new physics that goes even beyond the neutrino oscillation.

1.1.2 Model independent framework of $\mu \to e\gamma$ phenomenology

It is convenient to introduce a model-independent notation that characterizes $\mu \to e\gamma$ decay, which will be used hereafter in this thesis. The model-independent effective Lagrangian for $\mu \to e\gamma$ decay can be expressed by dipole operators,

$$\mathcal{L}_{\mu \to e\gamma} = -\frac{4G_F}{\sqrt{2}} \left[m_\mu A_R \bar{\mu}_R \sigma^{\mu\nu} e_L F_{\mu\nu} + m_\mu A_L \bar{\mu}_L \sigma^{\mu\nu} e_R F_{\mu\nu} + h.c \right], \tag{1.3}$$

where G_F is the Fermi coupling constant, and the $A_{R(L)}$ is the polarization-dependent coupling that induces $\mu \to e_{R(L)}\gamma$. When $\mu \to e\gamma$ decay is observed from a polarized muon at rest, the angular distribution of $\mathcal{B}(\mu \to e\gamma)$ is given as

$$\frac{\mathrm{d}\mathcal{B}(\mu \to e\gamma)}{\mathrm{d}\cos\theta_e} = 192\pi^2 \Big(|A_R|^2 (1 - P_\mu \cos\theta_e) + |A_L|^2 (1 + P_\mu \cos\theta_e) \Big), \tag{1.4}$$

where θ_e is the angle between the muon polarization vector and the positron emission angle, and P_μ corresponds to the magnitude of the polarization.

The total branching ratio of $\mu \to e\gamma$ behaves proportionally to $|A_R|^2 + |A_L|^2$. On the other hand, the above relation means that the angular distribution is sensitive to their ratio A_R/A_L. This ratio depends on the detail of assumed new physics models as will be discussed later in Sec.1.1.3. Therefore, experimental searches must be carefully designed with considerations about their sensitivity to each polarization. We will get back to this discussion later in Sec.6.1.5, where the main analysis for $\mu \to e\gamma$ search is described.

1.1.3 Predictions of $\mu \to e\gamma$ in theories beyond the Standard Model

This section focuses on the prediction of $\mu \to e\gamma$ decay in supersymmetric GUT [17, 18, 19] or supersymmetric see-saw models [20, 21, 22]. When the SUSY is exact, the particle masses must

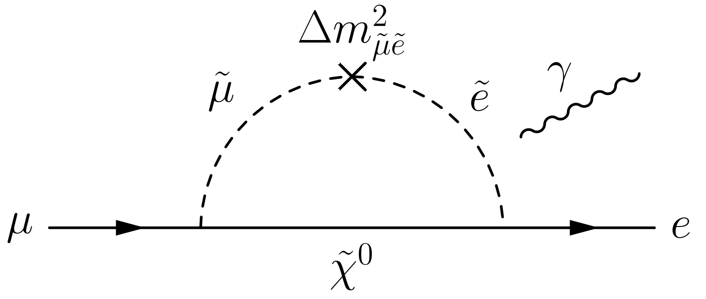

Figure 1.2: Diagram for $\mu \to e\gamma$ decay induced by slepton mass mixing [28].

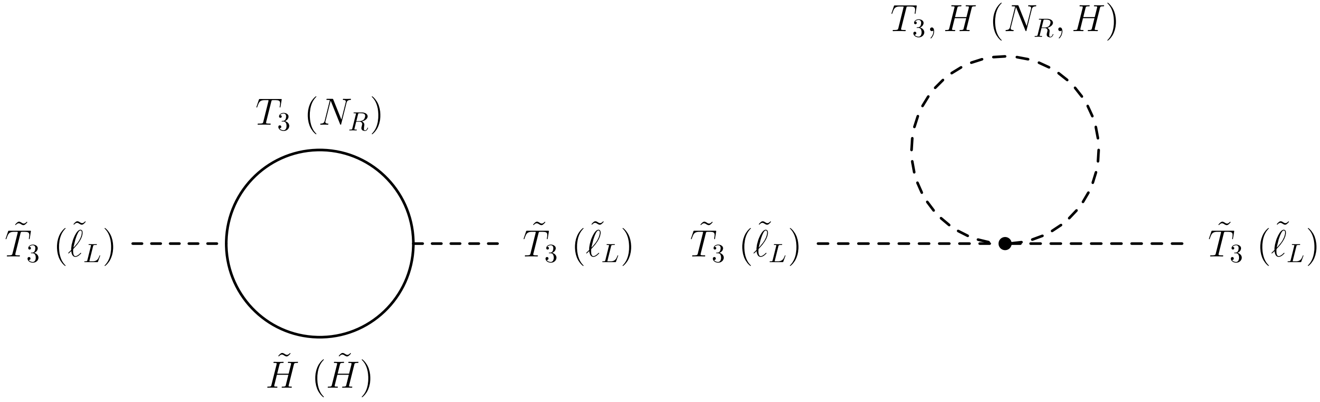

Figure 1.3: Radiative correction that gives rise to finite off-diagonal elements of slepton mass matrix[28]. Note that the Higgs in GUT is different from the Higgs in see-saw.

degenerate with those of SUSY partners, which is experimentally not the case. This contradiction can be explained by SUSY breaking, which gives larger masses to the SUSY partners so that they can escape from experimental detection. Various mechanisms are proposed for the SUSY breaking: gravity-mediated SUSY breaking [23, 24], gauge mediated SUSY breaking [25, 26, 27], and so on. At the Plank scale, most of these models predict a degenerate mass spectrum for sleptons (the SUSY partners of the leptons). This degeneracy results in a complete alignment between the slepton and lepton mass matrix, where no flavor mixing appears. When this is renormalized down to the electroweak scale, on the other hand, a finite sleptons' flavor mixing can be induced by radiative corrections; in particular, the GUT or see-saw can give rise to a sizeable effect. Hence, we expect a rare but finite $\mathcal{B}(\mu \to e\gamma)$, which is the key concept in theoretical calculations.

The flavor mixing in slepton induces $\mu \to e\gamma$ via the process shown in Fig.1.2, where the flavor transition takes place at the cross marker. This contribution is generally calculated as

$$\mathcal{B}(\mu \to e\gamma) \sim \left(\frac{m^2_{\tilde{\mu}\tilde{e}}}{m^2_{\tilde{\ell}}}\right)^2 \left(\frac{100\,\mathrm{GeV}}{m_{\tilde{\ell}}}\right)^4 10^{-6}, \tag{1.5}$$

where $m_{\tilde{\ell}}$ and $m^2_{\tilde{\mu}\tilde{e}}$ correspond to the diagonal and off-diagonal element of the slepton mass matrix, respectively [9, 18]. Though $m^2_{\tilde{\mu}\tilde{e}}$ is zero at the Plank scale, it becomes finite by radiative corrections in the GUT or see-saw mechanism. The diagram for such correction is drawn in Fig.1.3, where the GUT case assumes SU(5) unification and the see-saw case assumes the type-I model. The SU(5) SUSY-GUT gives rise to the flavor mixing in the right-handed sleptons as

$$(m^2_{\tilde{e}_R})_{ij} \sim -\frac{3}{8\pi^2} V_{i3} V^*_{j3} |(y_u)_{33}|^2 m_0^2 (3 + |A_0|^2) \log\left(\frac{M_P}{M_{GUT}}\right), \tag{1.6}$$

in a rough approximation. Here, V is the CKM matrix at the GUT scale, y is the Yukawa coupling, m_0 and A_0 are the SUSY breaking mass parameter and their coupling, and M_{GUT} is the GUT energy scale.

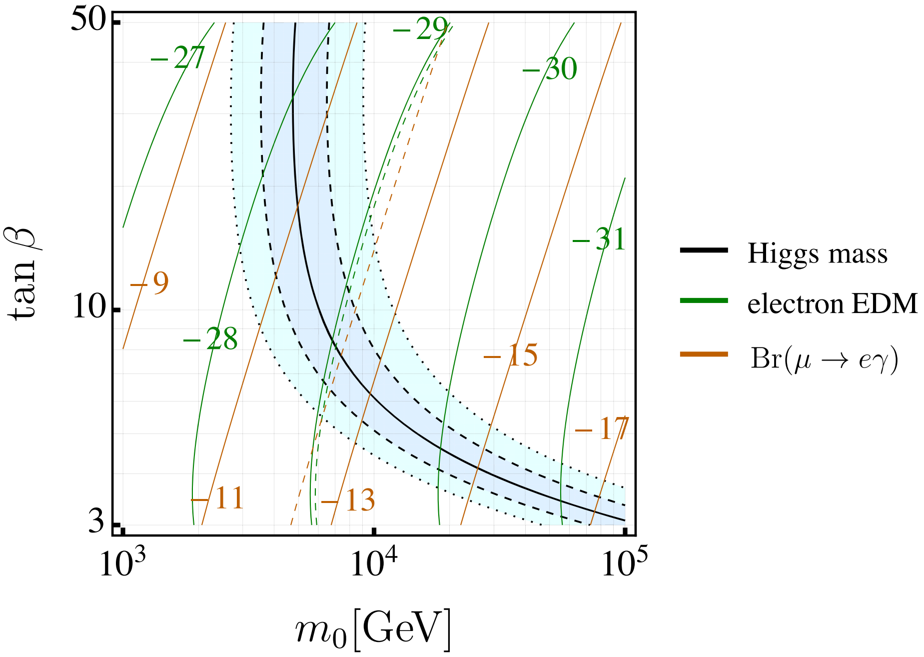

Figure 1.4: An expectation on $\mathcal{B}(\mu \to e\gamma)$ (orange contour lines) on as a function of m_0 (the universal scalar mass) and $\tan\beta$ (the VEV ratio between the two Higgs doublets) [32]. The blue band indicates the region where the Higgs mass is consistent with the experimentally measured one within the uncertainties.

In this equation, the flavor mixing in the quark sector affects the slepton mass matrix because the leptons and quarks are unified to the same gause multiplets. In SU(5), only the right-handed sleptons are hosted in **10** representation together with the top quark, which gives the largest radiative correction thanks to the largest $(y_u)_{33}$. This is why only the right-handed slepton can have a large flavor mixing in SU(5) model. Similarly, in the SUSY see-saw model, the left-handed sleptons acquire a finite flavor mixing as

$$(\Delta m^2_{\tilde{L}})_{ij} \sim -\frac{1}{8\pi^2}(y^*_\nu)_{ik}(y_\nu)_{kj} m_0^2 (3 + |A_0|^2) \log\left(\frac{M_P}{M_N}\right). \tag{1.7}$$

In models that incorporate both the GUT and see-saw [29, 30, 31, 32], both the left and right-handed slepton have flavor mixing, and even a larger contribution to $\mu \to e\gamma$ can be expected.

The $\mu \to e\gamma$ decay polarization appears differently between the following categories of models;

- Models with mixing only in right-handed sleptons,
- Models with mixing only in left-handed sleptons,
- Models with mixing both in right-handed and left-handed sleptons.

When only the right-handed sleptons are mixed, only the A_L term in Eq.(1.3) and Eq.(1.4) is sizeable and A_R is suppressed, whereas the opposite happens when only the left-handed slepton is mixed. When both the left and right-handed sleptons are mixed, both the A_R and A_L can have observable values. Therefore, when $\mu \to e\gamma$ decay is found, the angular distribution of the decay product will also be an important observable to discriminate the models from each other.

As an example of theoretical calculations for $\mathcal{B}(\mu \to e\gamma)$, Ref.[32] presents a calculation for a SUSY model that both includes the GUT and see-saw mechanism (Fig.1.4). Here, the GUT happens in SU(5) group and three generation right-handed neutrinos are introduced as singlets. The result indicates that the current upper limit on $\mathcal{B}(\mu \to e\gamma)$ is starting to exclude the large $\tan\beta$ region. At the same time, we can see that a search for a higher sensitivity around 10^{-14} is of high value for further exploration of the new physics parameter space.

1.2 Principle of experimental searches for $\mu \to e\gamma$ decay

1.2.1 Signal signature

Observed in the muon rest frame, $\mu \to e\gamma$ can be identified by the unique two-body kinematics of the decay products. The event signatures are

1. $t_{e\gamma} = 0$ (the time coincidence between positron and gamma)
2. $\Theta_{e\gamma} = 180^\circ$ (the back-to-back movement)
3. $E_e = E_\gamma = \frac{m_\mu}{2} \approx 52.8\,\mathrm{MeV}$ (monochromatic at half the muon mass).

The expected number of signal events can be expressed as

$$\begin{aligned} N_{\mathrm{sig}} &= k \times \mathcal{B}(\mu \to e\gamma) \\ k &= R_\mu \times T \times \Omega \times \epsilon_e \times \epsilon_\gamma \times \epsilon_{\mathrm{sel}}, \end{aligned} \tag{1.8}$$

where k corresponds to the number of effectively measured muon decay in an experiment. This is equivalent to the inverse of the single event sensitivity and is also called *the normalization factor* in this thesis. $R_\mu \times T$, the product of the muon rate and the total data taking time, corresponds to the total number of muons stopped during the experiment. The other parameters on the right hand side of k are the efficiency factors; Ω is the geometrical acceptance, $\epsilon_{e(\gamma)}$ is the detector's efficiency for positron (gamma), and ϵ_{sel} is the efficiency of the analysis.

To have a high statistical yield, we need to build an experiment with a high muon rate. At the same time, high efficiency of the detector is mandatory, which often gets more difficult with the increasing beam rate. Therefore, one experimental requirement is given in this respect, to keep a high efficiency even in a high-rate experiment.

1.2.2 Background from accidental coincidence

The main source of the background events is the coincidence of background positron and background gamma that accidentally mimics the signal signature. The former one comes from the normal muon decay $\mu^+ \to e^+\nu\bar{\nu}$, which we often call Michel decay. The latter mostly comes either from the radiative decay $\mu^+ \to e^+\nu\bar{\nu}\gamma$ or annihilation-in-flight of positrons from the normal decay.

The expected number of backgrounds follow

$$N_{\mathrm{Acc}} \propto R_\mu^2 \times (\sigma_{E_\gamma})^2 \times \sigma_{E_e} \times (\sigma_{\Theta_{e\gamma}})^2 \times \sigma_{t_{e\gamma}} \times T, \tag{1.9}$$

where σ-symbols in front of the variables stand for each resolution. The $R_\mu \times \sigma_{t_{e\gamma}}$ term corresponds to the rate of having a coincidence in the time axis, and the $\sigma^2_{\Theta_{e\gamma}}$ term corresponds to that in the angular axis. The σ_{E_e} and σ_{E_γ} contribution to the background can be evaluated by integrating their spectrum within the resolution, namely an integration over $[52.8\,\mathrm{MeV} - \sigma, 52.8\,\mathrm{MeV}]$. The spectrum is shown in Fig.1.5a and Fig.1.5b, and some formulas for them are given in Appendix.A. The linear scaling on σ_{E_e} in Eq.(1.9) comes from the integration of the finite spectrum around $52.8\,\mathrm{MeV}$. On the other hand, the gamma spectrum has a vanishing rate there, which results in the quadratic dependence when Fig.1.5b is linearly approximated in the integration over $[52.8\,\mathrm{MeV} - \sigma, 52.8\,\mathrm{MeV}]$.

As the accidental background has been the limiting factor of $\mu \to e\gamma$ sensitivity in experiments, its suppression is important. Eq.(1.9) gives several implications in this regard. Firstly, a continuous muon beam is better than a pulsed one, which is because the latter results in larger N_{Acc} with a higher instantaneous rate. In addition, four resolution parameters appear in Eq.(1.9) with the sixth power of total impact to N_{Acc}. Therefore, when experiments are designed, the resolution must be in consideration as well as the muon statistics.

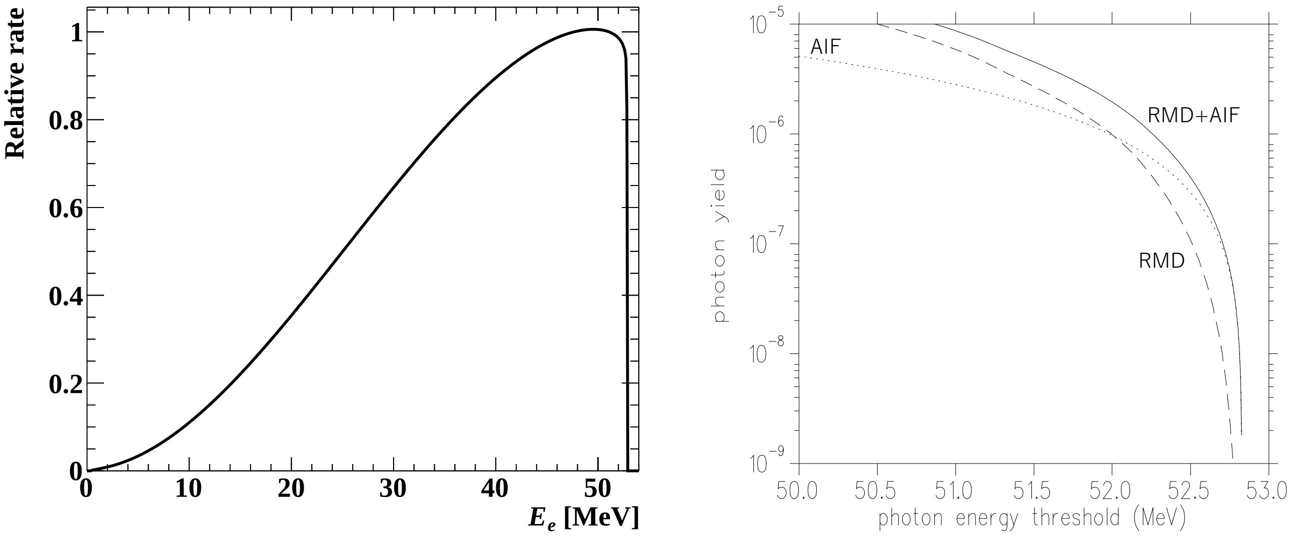

(a) E_e background spectrum.

(b) E_γ background spectrum.

Figure 1.5: E_e and E_γ spectrum in accidental background events [28]. (a) E_e background, from Michel decay, is calculated in [33]. (b) In the E_γ spectrum, two major sources are considered; the dashed line is that from radiative decay, the dotted line is that from annihilation in flight, and the solid line is their sum.

1.2.3 Background of physical origin

Another source of background events is the radiative muon decay (RMD) with the two neutrinos carrying small energies. The detail of its differential branching ratio is given in Appendix.A, and the effective branching ratio is shown in Fig.1.6. Here, the effective branching ratio is defined as

$$\int_{E_e}^{m_\mu/2} \mathrm{d}E_e \int_{E_\gamma}^{m_\mu/2} \mathrm{d}E_\gamma \frac{\mathrm{d}\mathcal{B}(\mu \to e\nu\bar{\nu}\gamma)}{\mathrm{d}E_e \mathrm{d}E_\gamma}, \tag{1.10}$$

which represents the integrated branching ratio of RMD decay above the corresponding E_e and E_γ thresholds. With a consideration that RMD events with $52.8\,\mathrm{MeV} - E_{e(\gamma)} < \sigma_{E_{e(\gamma)}}$ become background, realistic resolution of $\sigma_{E_e} \sim 100\,\mathrm{keV}$ and $\sigma_{E_\gamma} \sim 1\,\mathrm{MeV}$ gives an effective branching ratio below $\mathcal{O}(10^{-15})$. This contribution is much smaller than the accidental backgrounds and thus has only a minor impact on the $\mu \to e\gamma$ search.

1.2.4 Sign of muon charge

Experimentally, muons are stopped in a material and their decay products are measured. Here, the choice of negative muon (μ^-) is not favored because they form bound states in muonic atoms when captured by a nucleus in material. This induces the nuclear recoil effect in muon decays and spoils the simplicity of the two body $\mu \to e\gamma$ kinematics. Therefore, the use of positive muons is required in an experiment, namely $\mu^+ \to e^+\gamma$ is searched specifically.

1.3 Result of previous experiment and its limitations

The history of cLFV search results with muon is shown in Fig.1.7, where the latest point for $\mu \to e\gamma$ is based on the publication in 2016 [1]. This is a result of a search with the data collected by the MEG experiment during 2009–2013. As a result of this search with the sensitivity of 5.3×10^{-13}, an upper limit was set to be $\mathcal{B}(\mu \to e\gamma) < 4.2 \times 10^{-13}$ at $90\,\%$ confidence level.

The MEG experiment was constructed at πE5 beam line of Paul Scherrer Institute (PSI) to exploit the

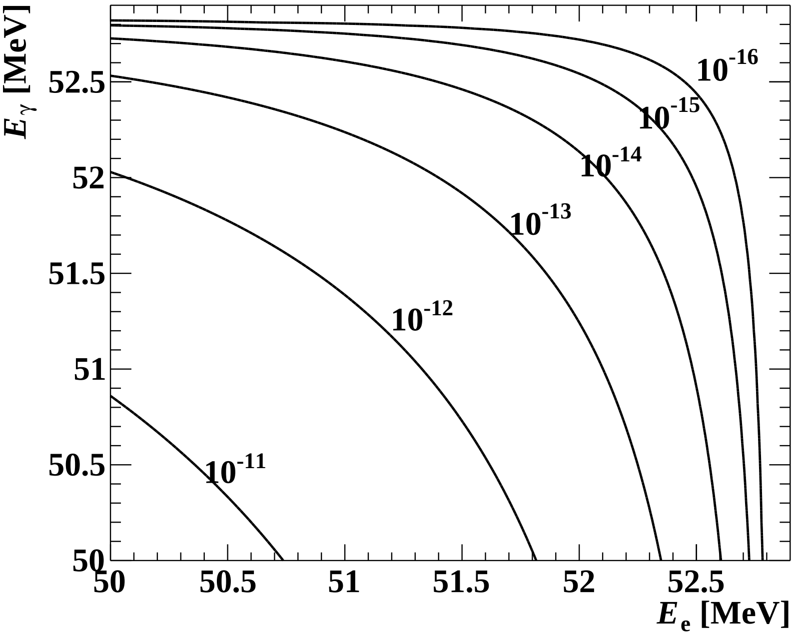

Figure 1.6: Effective branching ratio of the radiative decay when integrated over the phase space above the corresponding E_e and E_γ values. Given an experimental resolution of $\sigma_{E_e} \sim 100\,\mathrm{keV}$ and $\sigma_{E_\gamma} \sim 1\,\mathrm{MeV}$, the effective branching ratio of RMD background events is bounded below $\mathcal{O}(10^{-15})$.

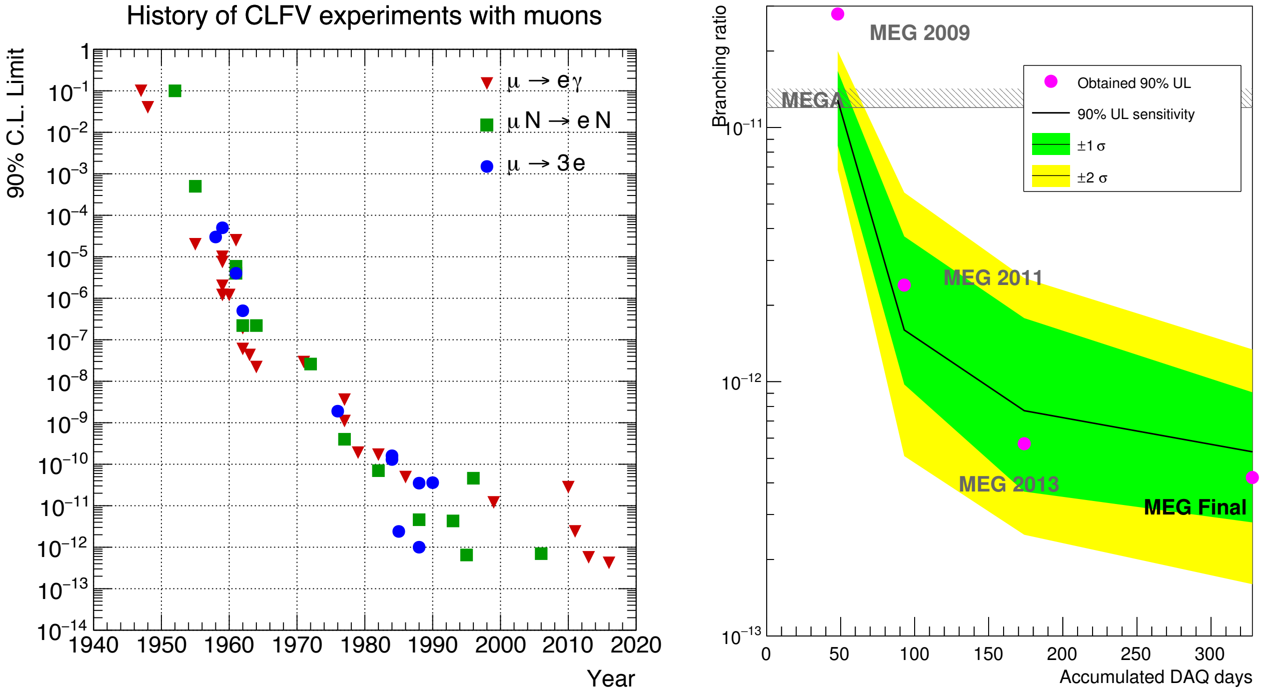

Figure 1.7: History of cLFV searches with muons [34] (left), and results of the previous experiment [35] (right).

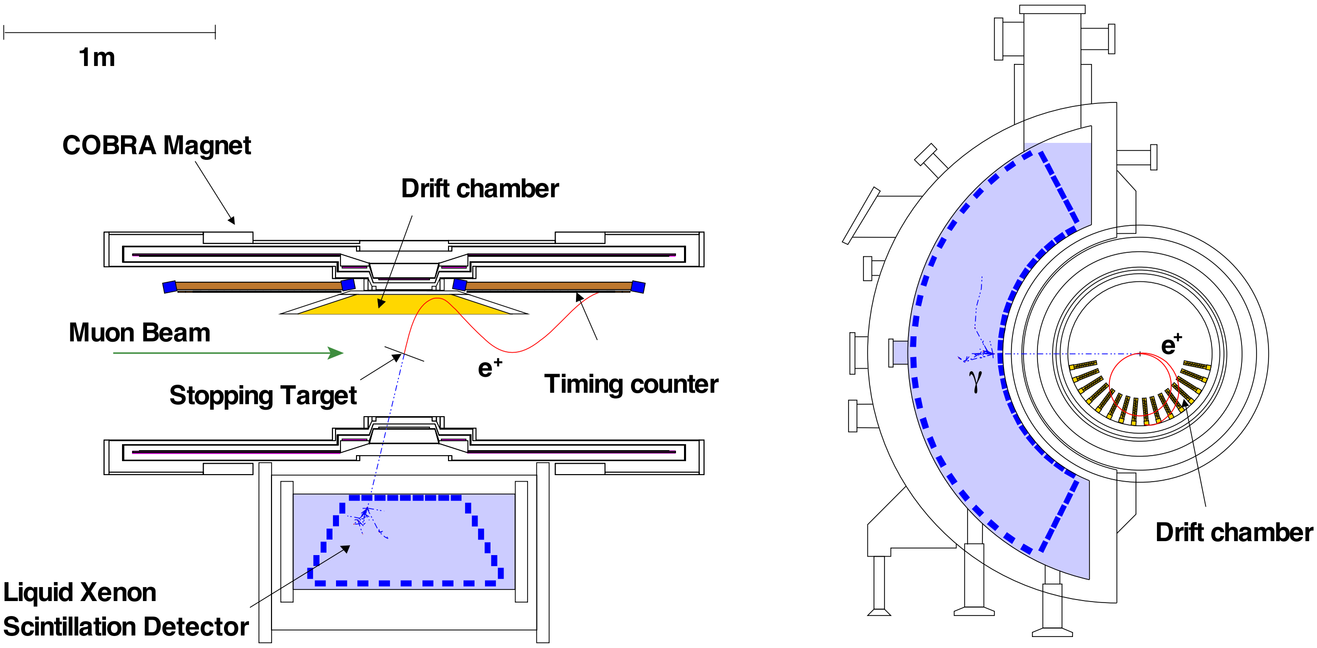

Figure 1.8: Schematic view of the MEG detector [36]. The red and blue lines are the simulated positron and gamma trajectories in a signal event.

world's most intense DC muon beam (Fig.1.8). The beam muons were stopped inside the target and then emitted the decay products. The trajectory of the decay positron was bent inside the magnetic field and was measured by the drift chamber. The magnetic field was provided by the *Constant Bending Radius* (COBRA) magnet, which produces a gradient magnetic field. The timing of the positron was measured by the timing counters in combination with the time of flight (TOF) measurement by the drift chamber. The position, timing, and energy of the gamma-rays were measured by the liquid Xenon scintillation detector (LXe). The performance achieved in the MEG experiment is summarized in Tab.1.1.

As can be seen in Fig.1.7, the sensitivity improves rapidly at the beginning of an experiment with the speed being proportional to the DAQ time. However, once a large statistics is accumulated and the background becomes non-negligible, the improvement slows down and behaves as the square root of the DAQ time. At this stage, an experiment becomes less efficient in sensitivity gain than at the beginning. In fact, the sensitivity improvement was limited between "MEG 2013" and "MEG Final" in Fig.1.7. Therefore, it was preferable to design an experiment with a smaller number of backgrounds rather than continuous data taking.

The background suppression can be achieved by improving the detector resolution as discussed in Sec.1.2. Ref.[34, 37] proposed an upgraded experiment with twice better resolution on average, resulting in a background reduction by a factor of ~ 30. The MEG experiment also suffered from the limited efficiency ($30\,\%$) in the positron reconstruction, whose improvement is another key concept of the upgrade. According to simulation studies and experiences in [1], these improvements can achieve an order of magnitude higher sensitivity. This improvement would never be feasible with the continuous data taking of the MEG, which would take > 100 years to achieve this sensitivity improvement.

1.4 Previous MEG II upgrade works

The MEG II experiment was first proposed in 2013 to realize the sensitivity improvement [37], and the concept of the upgrade is listed below.

- The positron tracking detector is updated to the cylindrical drift chamber (CDCH),
- The positron timing detector is updated to the pixelated timing counter (pTC),

Table 1.1: Resolutions and efficiencies achieved in the previous experiment and those achieved with this work.

Resoluition	MEG performance	MEG II achieved value with this work
E_e (keV)	380	90
θ_e (mrad)	9.4	7.2
ϕ_e (mrad)	8.7	4.1
z_e/y_e (mm) core	2.4/1.2	2.0/0.7
$E_\gamma(\%)$ (w<2 cm)/(w>2 cm)	2.4/1.7	2.0/1.8
$u_\gamma, v_\gamma, w_\gamma$ (mm)	5/5/6	2.5/2.5/5
$t_{e\gamma}$ (ps)	122	84
Efficiency (%)		
Trigger	≈ 99	~ 80
Gamma-ray	63	62
Positron	30	67

- The scintillation photon sensors for the liquid xenon detector (LXe) are replaced with novel SiPMs on the inner face,
- The radiative decay counter (RDC) is added to reduce background gamma-rays from radiative decay

Preparation works have been in place since the proposal, and the rest of this section reviews the previous works. The original works of this thesis will be summarized later in Sec.1.5.

The CDCH was assembled during 2016–2017 and delivered to PSI in 2018 for commissioning [38]. The commissioning aimed to find optimal working conditions, which continued during 2018–2021. Despite the difficulties in achieving a stable operation in the high-intensity muon beam, a stable operation was finally achieved at the beginning of 2021. Another difficulty was a wire-breaking problem, which happened a few times till the end of 2019. The cause was identified to be corrosion, and all the potentially problematic wires were successfully removed. In the meantime, studies progressed about the positron track reconstruction based on detector simulation [39, 40]. This is because studies on data have been impossible because of the absence of a full readout. Accordingly, the evaluated performance so far is also based on simulations, and its evaluation for the data has been left to be investigated.

The pTC assembly was finished in 2017 and integrated into the MEG II detector. Its calibration is already established [41] and the performance is presented in [40, 42]. The largest operational concern is the radiation damage, which results in resolution degradation [43]. This can be mitigated by installing a cooling system and its operation was also established by 2020 [40]. The estimated positron timing resolution was $35\,\mathrm{ps}$ before the radiation damage. It was also expected to become $41\,\mathrm{ps}$ after three years of damage accumulation [39].

The new SiPM development and its mass production for LXe was completed by 2016 [44], followed by installation works in 2017 [45]. SiPMs were aligned by laser scan and collimated X-ray data taken 2017–2018 [46, 47]. Ref.[48] presents the position reconstruction and its resolution evaluated on collimated $17.6\,\mathrm{MeV}$ gamma-rays. The energy reconstruction and calibration were also developed in [45, 48], and the resolution is presented in Ref.[48]. The time calibration was firstly developed in [45], and the resolution on $\pi^0 \to \gamma\gamma$ data was firstly evaluated to be $81 \pm 3\,\mathrm{ps}$ in [49]. This, however, included a large contribution of the vertex position spread of $\pi^0 \to \gamma\gamma$ decay, which was found to cause an additional $68\,\mathrm{ps}$ contribution [50, 51]. In addition, the above result was obtained for a limited readout configuration. Therefore, the time resolution evaluation should be revisited.

The RDC is planned to be installed in two places, both the downstream and upstream ends of the detector. The construction and installation of the downstream RDC were completed in 2016 [52, 53].

The upstream detector, on the other hand, is still under development, and the current status can be found in [54, 55, 56]. The calibration and the performance evaluation of the downstream detector were also established in [49].

1.5 Original works of this thesis

As the main theme of this thesis, this work establishes the analysis framework searching for $\mu \to e\gamma$ decay, which is discussed in Chap.6, and the result with the MEG II first year data is presented in Chap.7. This work describes a wide range of studies for the $\mu \to e\gamma$ analysis; formalism and evaluation of the probability density functions, the evaluation of the statistics of the dataset, validation of the analysis reliability, and estimation of the systematic uncertainties. This also involves the optimization of the event selection discussed in Sec.4.4.3. Ref.[57] is the publication based on these works.

In addition to the main analysis, this work is also devoted to the detector calibration and the optimization of the reconstruction. This work includes most of the data-driven studies of the CDCH: the optimization of the track reconstruction (Sec.4.1.8, Sec.4.1.9), calibration (Sec.5.8, Sec.5.9), and performance evaluation (Sec.5.13). As will be discussed in Sec.5.4.3, the LXe data taken with the full readout revealed the necessity of further improvement of time calibration and optimization of the time reconstruction. The LXe time resolution with the improved calibration is evaluated both with the $\pi^0 \to \gamma\gamma$ data (Sec.5.4.4) and the radiative muon decay events (Sec.5.6.3). This also includes works on the timing alignment between positrons and gamma-rays (Sec.5.6.1, Sec.5.6.2). The alignment between the different sub-detectors is also discussed in Sec.5.11. Ref.[58] and Ref.[59] are the publications based on these works.

With the above works, we achieved the detector performance presented in Tab.1.1. Given this achieved performance, the projected sensitivity of the MEG II experiment is also calculated, which is the first work based on a realistic scenario.

Chapter 2

MEG II apparatus

Fig.2.1 shows a schematic of the MEG II apparatus. The muons come from the right in Fig.2.1 and then stop inside the target. The decay positrons are bent inside the magnetic field produced by the COBRA magnet. The CDCH measures their helical trajectories from the hits on wires, and the pTC measures the timing from the hits on scintillation counters. The LXe detector absorbs the gamma-rays in the liquid Xenon, and the scintillation lights are measured by the photo-multiplier tubes (PMT) and silicon photo-multipliers (SiPM), which surround the whole volume. The downstream RDC measures the energy and timing of 1 – 5MeV positrons from RMD with a set of plastic and LYSO scintillation counters.

The global coordinate system of the MEG II is defined as the usual right-handed system, with the origin located at the center of the COBRA magnet. The z-axis is in the downstream direction (the left direction in Fig.2.1), the y-axis is in the upright direction, and thus, the x-axis points to the opposite of the LXe. The definition of r, θ and ϕ are also given as

$$\begin{aligned} r &:= \sqrt{x^2+y^2+z^2}, \\ \theta &:= \cos^{-1}\frac{z}{\sqrt{x^2+y^2+z^2}}, \\ \phi &:= \tan^{-1}\frac{y}{x}. \end{aligned}$$

In this thesis, r is often used to describe the detector geometry, and θ, ϕ is used for the emission angle of positron and gamma.

2.1 Muon beam line

As discussed in Sec.1.2, a direct current (DC) positive muon beam is necessary for the experiment. This is available at the πE5 beam line of PSI (Fig.2.2) with the highest DC intensity in the world. The muon beam originates from protons accelerated to $590\,\mathrm{MeV}$ by the main ring cyclotron at PSI (Fig.2.3), where the frequency is $50.7\,\mathrm{MHz}$, the bunch width is $0.3\,\mathrm{ns}$, and the beam current is up to $2.2\,\mathrm{mA}$. Protons are injected into a target of $4\,\mathrm{cm}$-thick graphite to produce pions, and muons can be obtained from the subsequent $\pi^+ \to \mu^+\nu_\mu$ process. The beam is then generated by collecting the muons from the surface of the pion production target (within a few µm), and called *surface muon* beam. This offers a good property of $\sim 28\,\mathrm{MeV}/c$ momentum with a good momentum-byte of $7\,\%$ (FWHM), which can later be stopped in a thin muon stopping target. The $50.7\,\mathrm{MHz}$ frequency of the accelerator is much higher than the muon lifetime of $2.2\,\mu\mathrm{s}$, and thus, the decay rate of muons (R_μ in Eq.(1.9)) behaves continuous as required. At $2.2\,\mathrm{mA}$, the maximum available beam rate can be set up to $10^8\ \mu^+/\mathrm{s}$, which is reduced to a smaller value in the experiment on demand.

A Wien-filter (also called separator), two quadrupole triplet magnets, and a superconducting beam transport solenoid (BTS) are installed to transport the beam from the πE5 to the detector. The Wien

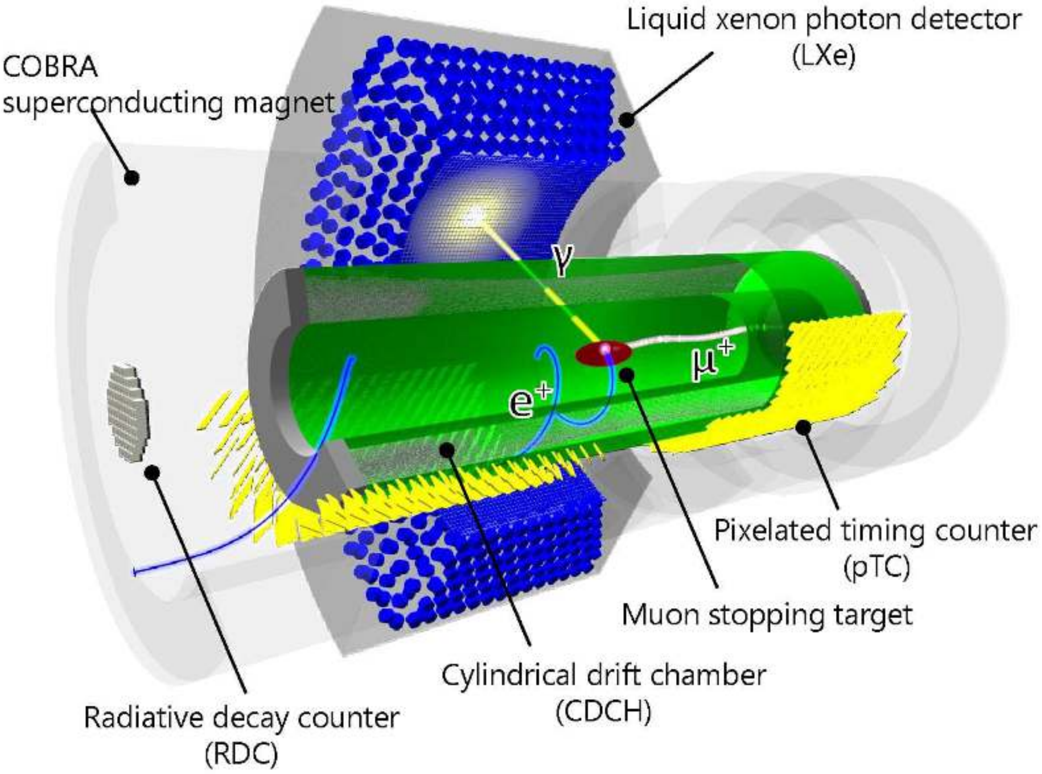

Figure 2.1: A schematic of the MEG II apparatus [34]. Beam muons (coming from the right) are stopped in the target (red) at the center. The decay positrons (blue helical line) are measured by the CDCH (green) and the pTC (yellow). The decay gamma-rays are measured by the LXe detector (blue C-shaped detector). Background events are identified by the RDC placed at the left end.

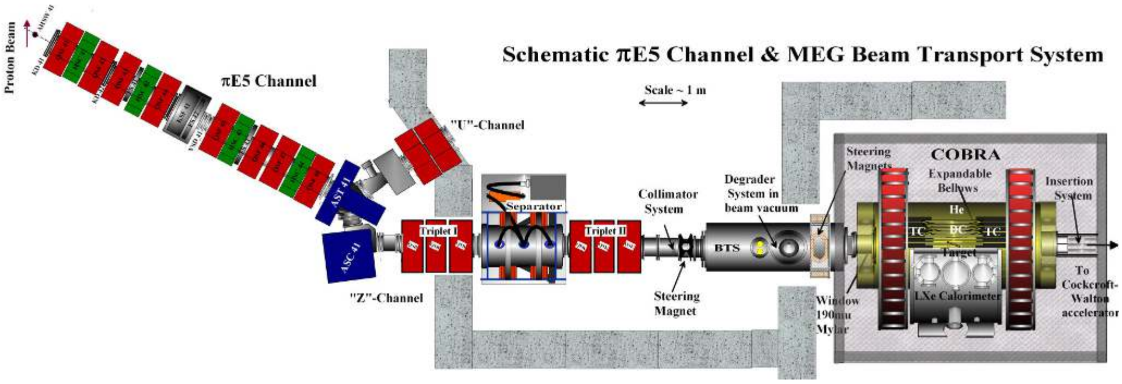

Figure 2.2: πE5 beam line in PSI [34]

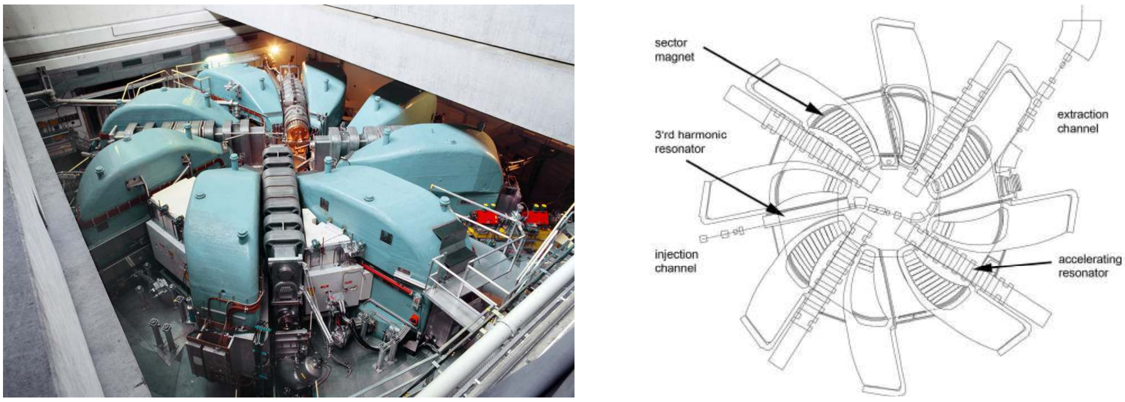

Figure 2.3: The main proton accelerator at PSI [60].

Figure 2.4: Muon stopping target for the MEG II experiment and a CCD monitoring camera [34, 61]. When projected in the global XY plane of the MEG II experiment, the ellipse shape results in a circle.

filter and the triplet magnets separate positron contamination in the muon beam, which comes from the Michel decay from a muon or pair creation of a gamma-ray from $\pi^0 \to \gamma\gamma$ process in the pion production target. Though the contamination initially accounts for eight times larger than the muons, the separation reduces it down to $< 1\,\%$ of the muons. The BTS, with a $0.36\,\mathrm{T}$ magnetic field, focuses the beam to the center of the muon stopping target. It also adjusts the momentum, with a $300\,\mu\mathrm{m}$-thick Mylar degrader placed in the middle, to maximize the stopping efficiency in the muon stopping target.

2.2 Muon stopping target

The muon beam is finally stopped in the muon stopping target at the center of the COBRA magnet. The target is required to have a high muon stopping efficiency, which motivates a thicker material. At the same time, it is required to be as thin as possible to suppress positrons' multiple scattering, annihilation, and bremsstrahlung inside. A $174\,\mu\mathrm{m}$-thick plastic scintillator is used as the stopping target (Fig.2.4) and is placed with a 15° slant angle from the beam axis. This geometry results in a long thickness seen from the muons while keeping a short path for the decay positrons. The target is supported by a carbon frame, which ensures the mechanical stability of the target shape.

The target alignment is important according to the experiences in the MEG experiment, in which the target uncertainties resulted in a $13\,\%$ degradation of the sensitivity. Four holes are on the long axis and two holes are on the short axis of the ellipse, which can be used to align the tracking detector and the target as will be presented later in Fig.5.11.2. Two CCD cameras are also introduced to monitor the time variation of the position and the shape [61, 62], which make use of the dot-shaped markers printed on the target.

2.3 Positron spectrometer

2.3.1 COBRA superconducting magnet

The COBRA magnet (Fig.2.5) is a superconducting magnet with a dedicated design for an efficient $\mu \to e\gamma$ detection. This was developed and installed in the MEG experiment and is reused in the MEG II. The magnetic field is provided by a composition of coils with three different radii: the central coil, the gradient coil, and the end coils. It generates a gradient magnetic field of 0.5–$1.7\,\mathrm{T}$, which is stronger at the center and weaker at the ends (Fig.2.6). In comparison with a uniform magnetic field, this is advantageous because the radius (projected on XY plane) of the decay positrons does not strongly depend on the θ-emission angle of positrons. In addition, this configuration sweeps out decay positrons more quickly than a uniform field. Therefore, only positrons with the energy of interest can leave a moderate number of hits on the detector, which is a good feature in association with the rate capability.

Co-existence with the LXe detector is another important requirement in its design. The material budget in the direction of the LXe detector is kept as small as $0.197\,X_0$, in order not to lose the gamma-ray

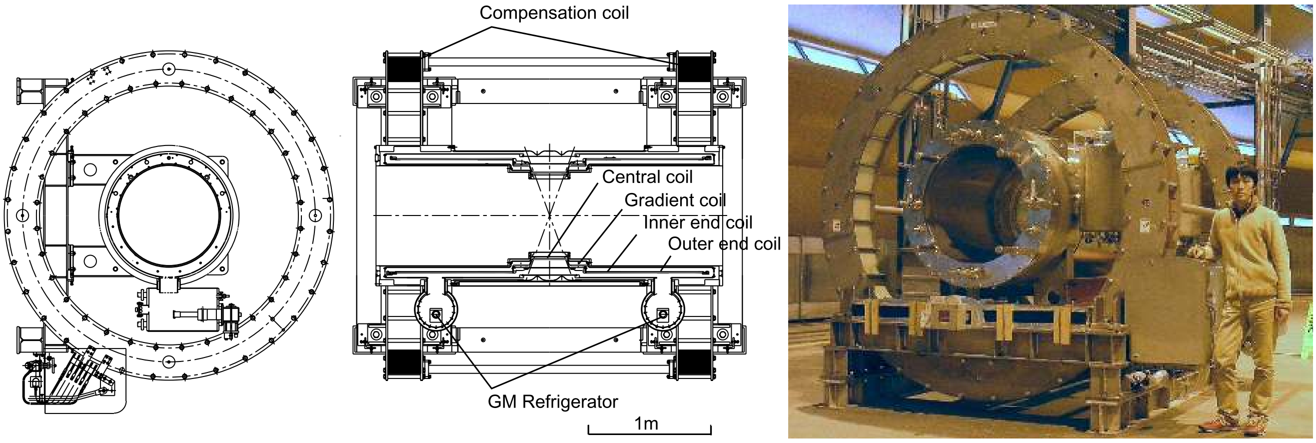

Figure 2.5: Schematic of the COBRA magnet (left for cross-section and middle for side view) and picture (right) [36, 63].

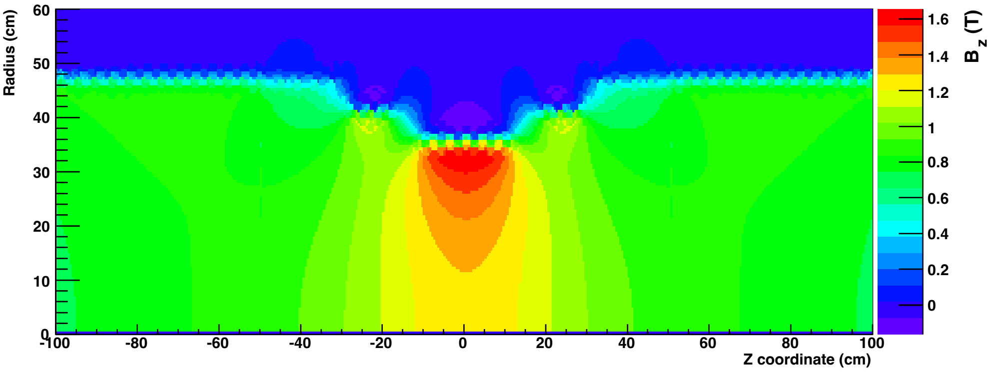

Figure 2.6: Map of magnetic field inside the spectrometer [63].

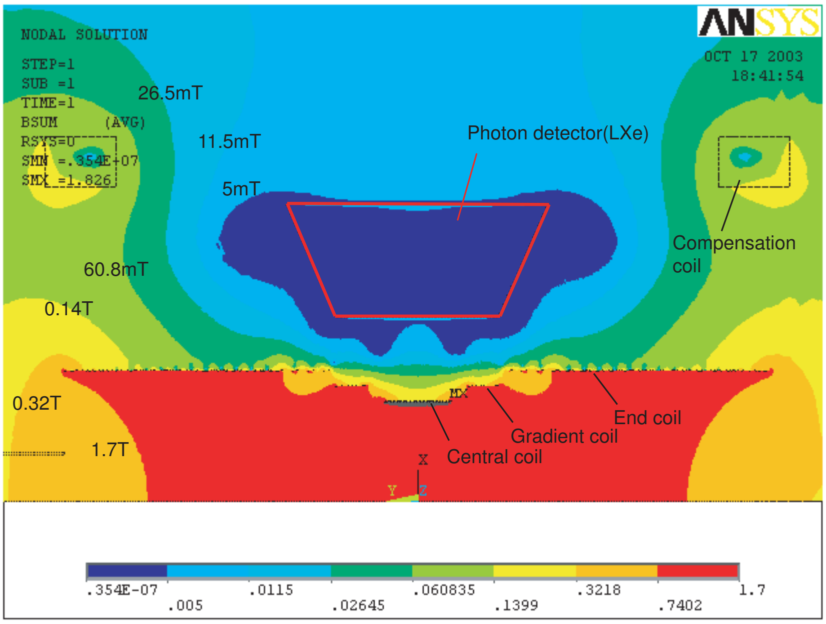

Figure 2.7: The compensated magnetic field inside the LXe [63].

Figure 2.8: Pictures of CDCH taken before the enclosure by the carbon support frame [34]. Left: Full picture of the entire drift chamber. The hyperbolic shape is visible. Right: A zoom-up picture showing the wire crossing in the stereo geometry.

detection efficiency. In addition, the compensation coil is introduced at the detector's end, which cancels the stray field in the LXe detector to keep the field strength to be $< 5\,\mathrm{mT}$ (Fig.2.7). Thanks to this compensation, the PMTs of the LXe detector can be operational.

2.3.2 Cylindrical drift chamber

A single-volume wire drift chamber is developed for the MEG II experiment (Fig.2.8), with the original inspiration from the KLOE experiment [64]. It has a geometry of $191\,\mathrm{cm}$ in the length, and $17\,\mathrm{cm}$ and $29\,\mathrm{cm}$ for the inner and outer radius (i.e. $17\,\mathrm{cm} < r_{\mathrm{CDCH}} < 29\,\mathrm{cm}$). This uses ~ 2000 sense wires and ~ 10000 field wires in total, which forms a nine-layer structure each with 192 drift cells of 5.8 – 8.7 cm size (Fig.2.9). The drift cells are defined by sense wires in a stereo configuration (Fig.2.10), with the θ_{stereo} ranging from $6.0°$ (the innermost layer) to $8.5°$ (the outermost layer). Two wires from neighboring layers have opposite directions, which enables a precise track reconstruction in the z-coordinate. This configuration results in a hyperbolic shape seen from the side, as is visible in Fig.2.8.

The sense wires are made of $20\,\mu\mathrm{m}$ diameter gold plated tungsten, and the field wires are made of $40\,\mu\mathrm{m}$ diameter silver plated aluminum. A gas mixture of He/iC_4H_{10}/O_2/2-propanol with each fraction of $88.5\,\%$/$9.8\,\%$/$0.5\,\%$/$1.2\,\%$ is used inside the active volume. The whole volume is enclosed by an inner

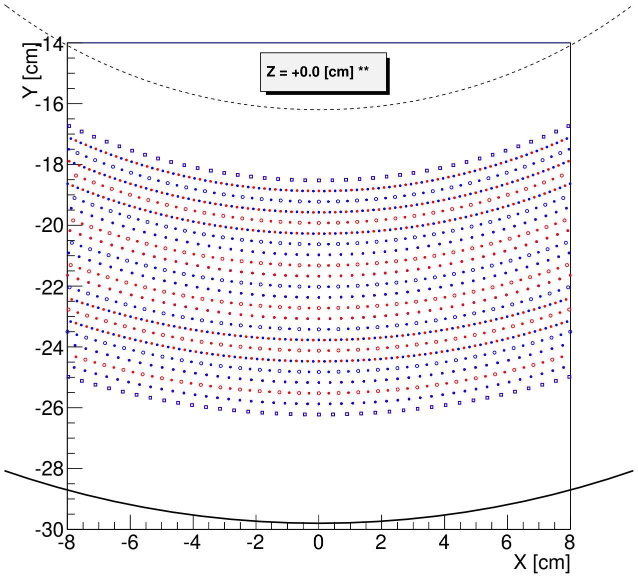

Figure 2.9: Drift cell configuration in the full layer [37]. Red and blue markers correspond to ± stereo angles (see Fig.2.10). The open circles are sense wires and the filled circles are field wires.

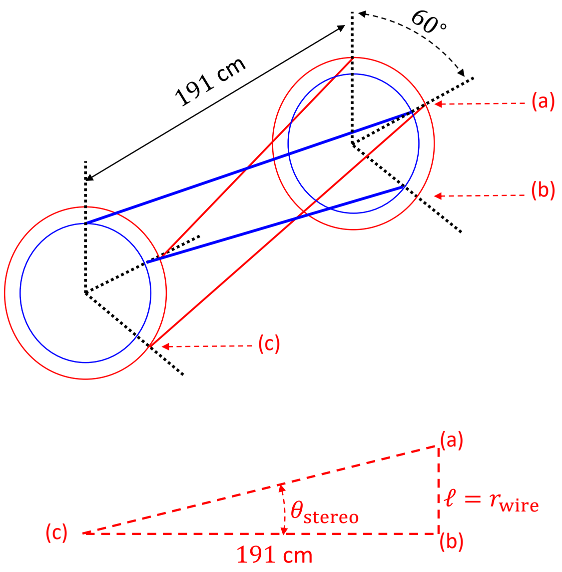

Figure 2.10: Illustration of the wiring scheme in the stereo geometry.

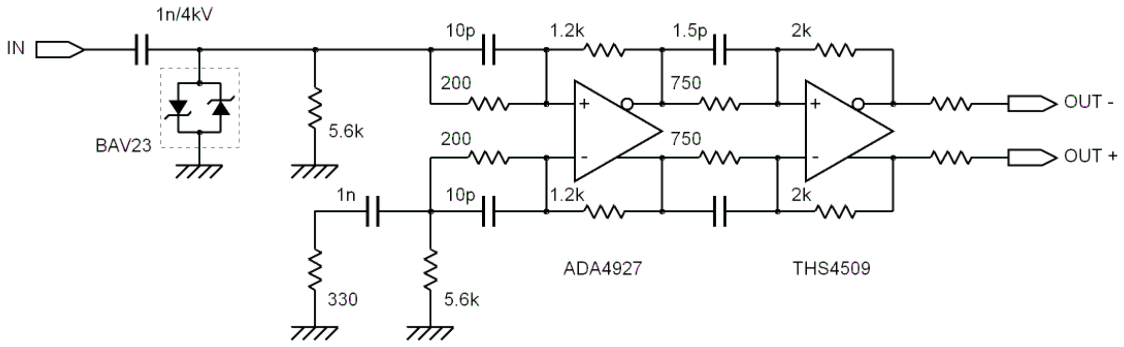

Figure 2.11: Circuit diagram of amplifier electronics for CDCH [34].

20 µm-thick one-side aluminized Mylar foil and an outer support structure made of 2 mm-thick carbon fiber. The whole material of the CDCH is highly transparent and positrons pass $1.58 \times 10^{-3}\ X_0$ in a single turn. This low-mass design reduces the multiple scattering and the generation of gamma-rays.

Only $2/3$ of the sense wires at the bottom are read out because it is enough to cover the full acceptance defined by the C-shaped LXe detector. A low-noise high-bandwidth front-end amplifier electronics is specially designed and connected to both ends of the wires (Fig.2.11). The high voltage, on the other hand, is applied to all of the sense wires (full $0 < \phi < 2\pi$) to have a homogeneous and symmetric electric field for the gas amplification.

2.3.3 Pixelated timing counter

The pixelated timing counter, a group of highly segmented plastic scintillation counters, is developed for the MEG II experiment for the positron timing measurement. It is placed just outside the CDCH with a minimum material in-between, which suppresses multiple scattering between the CDCH and the pTC. This ensures a high matching efficiency between the reconstructed track in the CDCH and the hits on the pTC, which was low and resulted in the largest inefficiency in the MEG experiment.

The pTC is divided into two sectors, downstream and upstream, with a geometrical separation by the

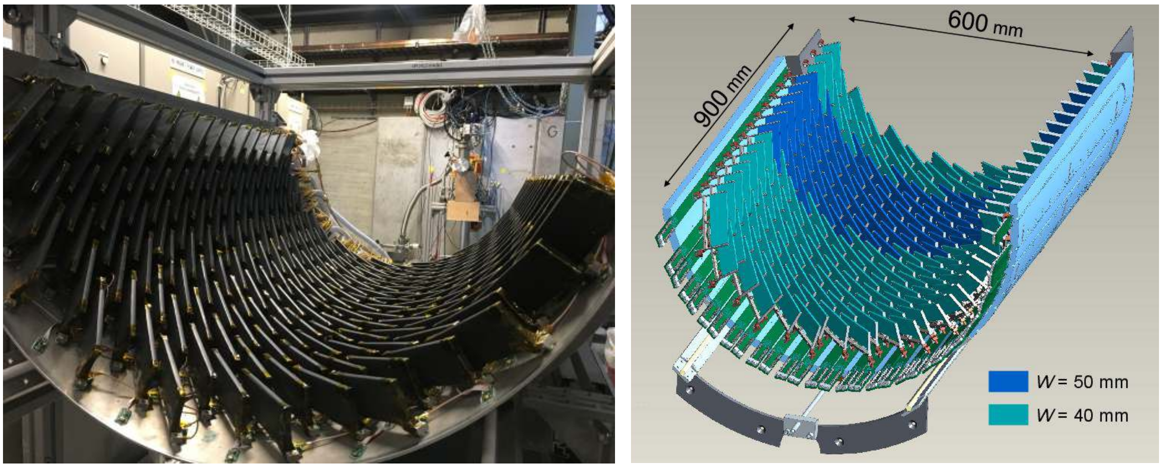

Figure 2.12: Picture (left) and schematic (right) of downstream pTC containing 256 scintillation counters [34, 48].

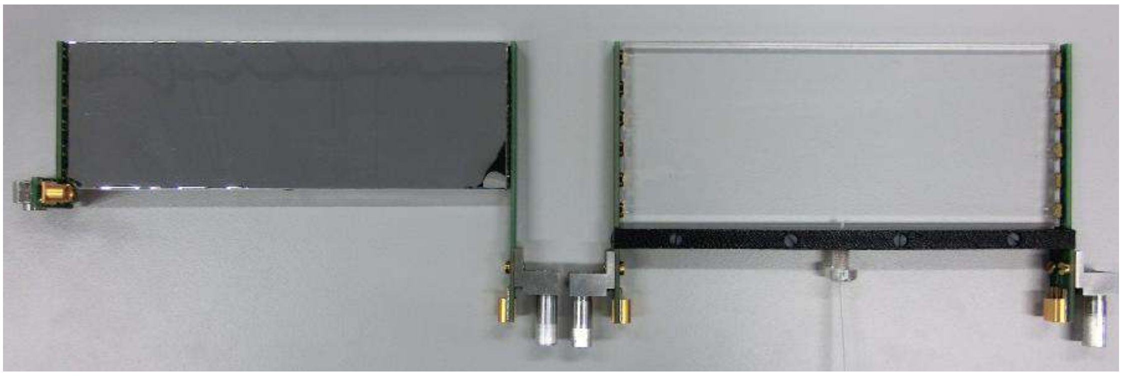

Figure 2.13: Picture for a $4\,\mathrm{cm}$ counter after wrapping (left) and a $5\,\mathrm{cm}$ counter before wrapping with optical fiber introduced from the bottom (right) [34].

central coil of the COBRA magnet. Fig.2.12 shows the picture and schematic of the downstream part, which hosts 256 scintillation counters. The upstream also hosts 256 counters, and 512 counters are used in total. Each counter is tilted by 45° to the beam, in order to be perpendicular to the incoming positron tracks. They are arranged to maximize the hit density, *i.e.* to maximize the number of hits, so that a good overall resolution can be achieved by a combination of multiple hits.

Fig.2.13 shows a picture of scintillation counters. Each counter is made of $120 \times 40/50 \times 5\,\mathrm{mm}^3$ BC422 (Saint-Gobain) scintillator with both ends coupled to six SiPMs from AdvanSiD (ASD-NUV3S-P-High-Gain). The six SiPMs are connected in series to have a reduced capacitance in the readout, which results in a good resolution thanks to the fast response. Each counter is wrapped by a reflector film to have a high scintillation light collection efficiency.

An optical fibers system is introduced to a part of the counters as a time calibration tool (Fig.2.14), which is complementary to another method using the reconstructed positron tracks (described later in Sec.5.5). Pulsed laser light is divided by the optical splitters to generate a synchronized signal, and it is then injected into the counters through optical fibers (Fig.2.13). With the optical length of the system measured in advance, this can be exploited to calibrate the counter time offsets.

The local coordinate is defined to express the hit position in the counter as shown in Fig.2.15. The w axis is defined in the direction between the two readout ends. The v axis is defined so that it points to the direction of decreasing r in the global MEG II coordinate.

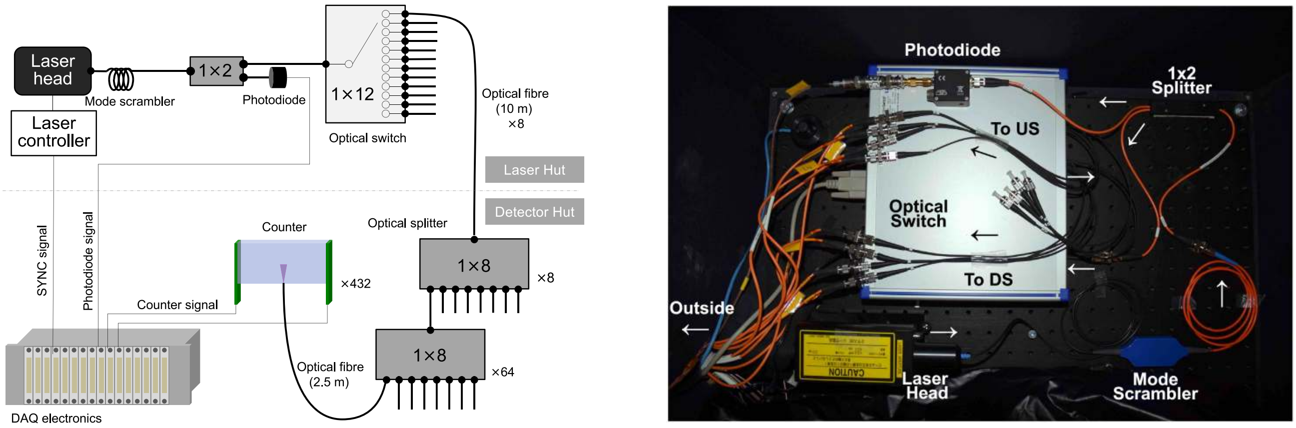

Figure 2.14: Schematic and picture of laser-based TC calibration system [41].

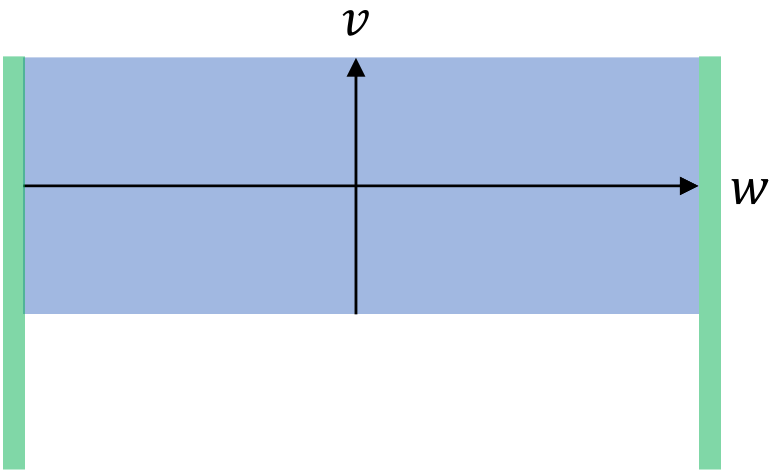

Figure 2.15: The local coordinate system on each counter of the pTC.

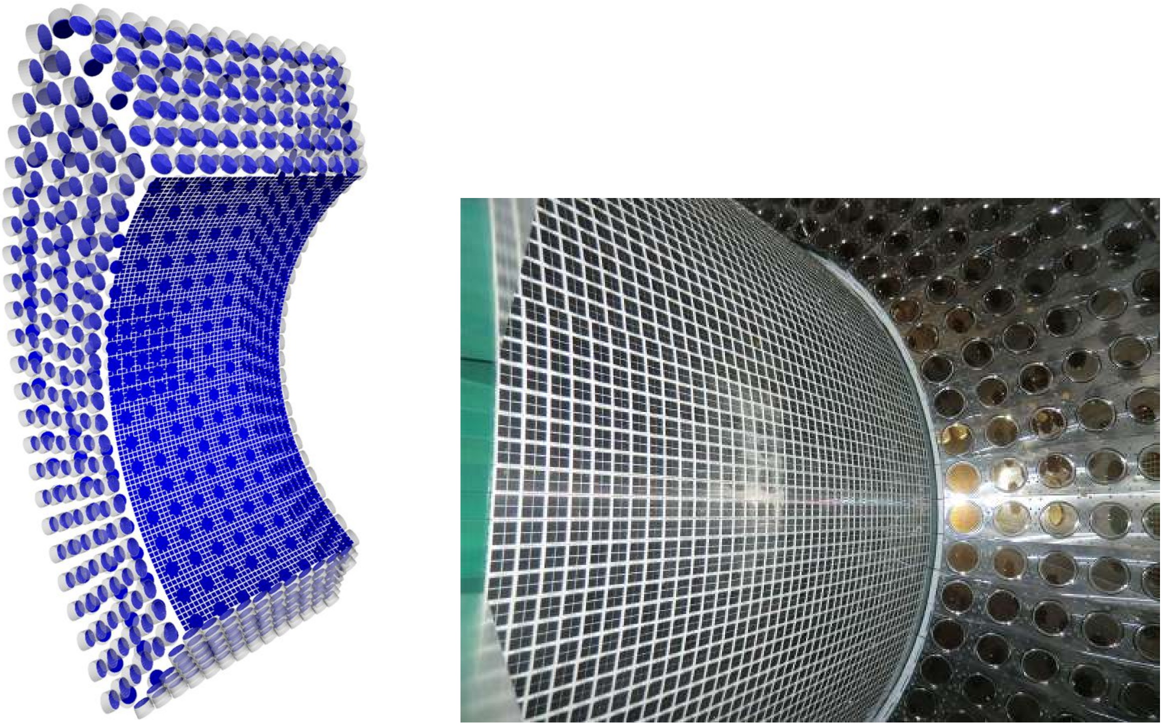

Figure 2.16: Scnitillation photon sensor layout (left) and picture (right) of the LXe detector [34, 45].

2.4 LXe gamma-ray detector

The gamma-ray detector uses $\sim 900\,\mathrm{L}$ liquid Xenon with the scintillation readout by SiPMs and PMTs (Fig.2.16). As the wavelength of the scintillation light lies in the vacuum ultraviolet (VUV) regime, special scintillation photosensors are used to be sensitive to VUV light. The photosensors of choice are VUV-MPPC (SiPMs) and R9869 (PMTs), both produced by Hamamatsu Photonics. The major upgrade from the MEG experiment is that the sensors on the inner face (originally PMTs) were replaced by VUV-MPPCs, while the PMTs in the other faces are reused from the MEG experiment.

The LXe detector is placed just outside the COBRA magnet and has a C-shaped geometry surrounded by six faces: inner, outer, upstream, downstream, top, and bottom face. The inner face has $r_{\mathrm{in}} = 64.97\,\mathrm{cm}$, and the local coordinate of the LXe detector (Fig.2.17) is defined as [1]

$$\begin{aligned} u &= z \\ v &= r_{\mathrm{in}} \cdot \tan^{-1}\left(-\frac{y}{x}\right) \\ w &= \sqrt{x^2 + y^2} - r_{\mathrm{in}}. \end{aligned} \tag{2.1}$$

2.4.1 Liquid xenon

When a gamma-ray around $52.8\,\mathrm{MeV}$ interacts with liquid xenon, an electromagnetic shower is formed inside. The elements contained in the showers ionize or excite the xenon atoms, which is followed by scintillation light emissions. The studies on its highly complex mechanism were initiated in the 1970s [65, 66, 67, 68], and a comprehensive review is given in [69]. Two different processes have been identified, a self-trapping process and a recombination process. The self-trapping is a process where

---

[1] Technical caution: This coordinate definition is for this analysis. It is planned to be changed in future publications.

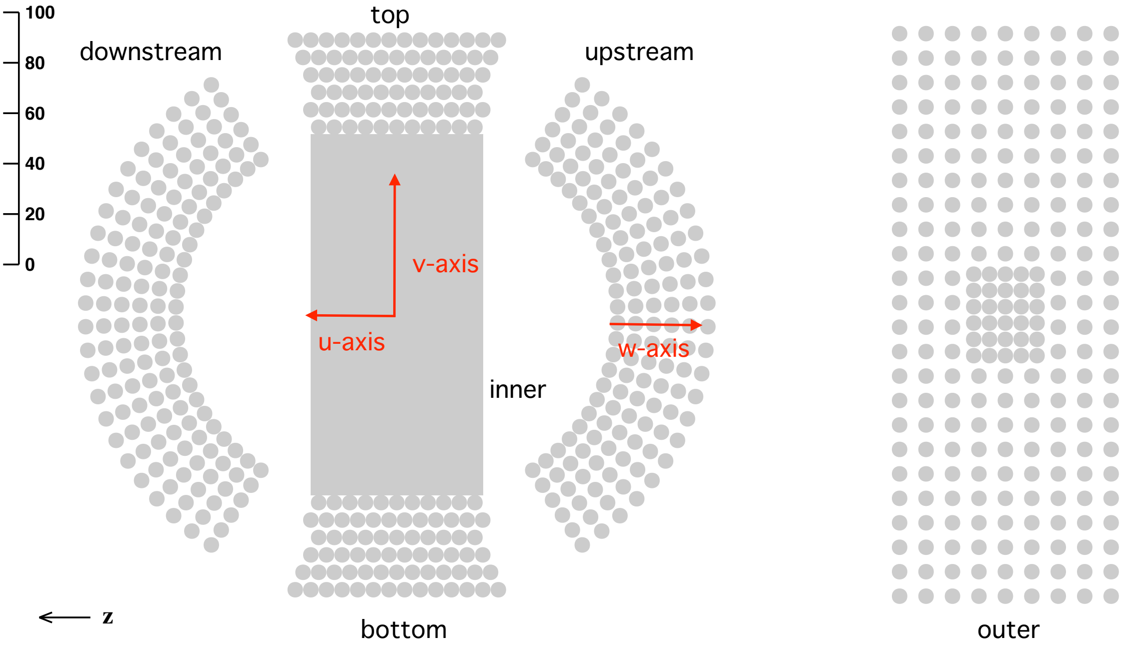

Figure 2.17: The local coordinate definition of the LXe detector [49].

excited xenon atoms are trapped,

$$\begin{aligned} \mathrm{Xe}^* + \mathrm{Xe} + \mathrm{Xe} &\rightarrow \mathrm{Xe}_2^* + \mathrm{Xe} \\ \mathrm{Xe}_2^* &\rightarrow 2\mathrm{Xe} + h\nu, \end{aligned} \tag{2.2}$$

where $h\nu$ has a VUV wavelength. There are singlet state and triplet state for the Xe_2^*, and they respectively have decay time of $4.2\,\mathrm{ns}$ and $22.2\,\mathrm{ns}$. The recombination is a process associated with the ionized xenon,

$$\begin{aligned} \mathrm{Xe}^+ + \mathrm{Xe} &\rightarrow \mathrm{Xe}_2^+ \\ \mathrm{Xe}_2^+ + e^- &\rightarrow \mathrm{Xe}^{**} + \mathrm{Xe} \\ \mathrm{Xe}^{**} &\rightarrow \mathrm{Xe}^* + \mathrm{heat} \\ \mathrm{Xe}^* + \mathrm{Xe} + \mathrm{Xe} &\rightarrow \mathrm{Xe}_2^* + \mathrm{Xe} \\ \mathrm{Xe}_2^* &\rightarrow 2\mathrm{Xe} + h\nu, \end{aligned} \tag{2.3}$$

where the decay time of this process is $45\,\mathrm{ns}$. The authors of [68] found that the $45\,\mathrm{ns}$ decay time component dominates when the liquid xenon is ionized by gamma-rays. This is not the case when the energy deposit density is larger, where $4\,\mathrm{ns}$ and $22\,\mathrm{ns}$ components become prominent.

As a scintillator, liquid xenon shows good properties for $\mu \to e\gamma$ detection. Thanks to its large atomic number and high density ($2.98\,\mathrm{g/cm^2}$), it has a high stopping power of $X_0 = 2.77\,\mathrm{cm}$. This results in a high detection efficiency of gamma-rays. It also has a high light yield of $46\,000\,\mathrm{photon/MeV}$, and a good resolution can be expected. Its fast response with the decay time of $45\,\mathrm{ns}$ is suitable in a high-rate environment, where the pileup becomes a severe problem. In addition, the liquid material contributes to a higher uniformity of the scintillation response than crystals.

In addition to the monetary cost, there exist three technical difficulties in the use of liquid xenon. The first difficulty is the narrow temperature range (161–169 K) of the liquid state, which poses a challenge for maintaining such precise temperature control in a 900 L detector. The second difficulty is that high-quality liquid purification is demanded because the scintillation light can be easily absorbed by contaminations such as oxygen and water. The final difficulty is the wavelength of the scintillation light lying in the VUV region ($175\,\mathrm{nm}$), which requires the scintillation photon sensors to be VUV-sensitive. The MEG experiment has already solved the first two difficulties [70, 71, 72], and the solution to the third difficulty is described in the next section.

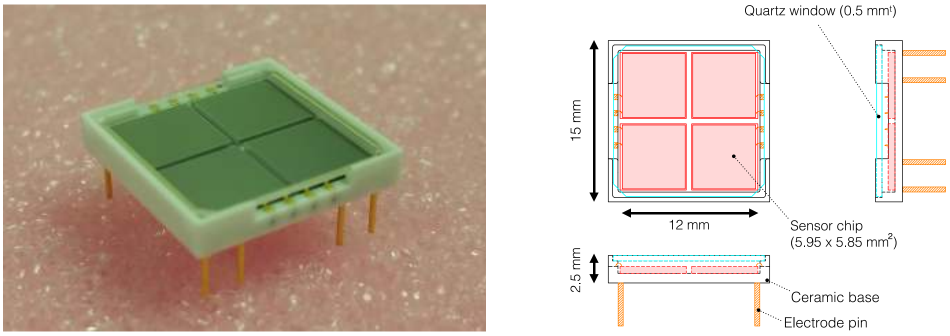

Figure 2.18: Picture and sketch of VUV-MPPC [44].

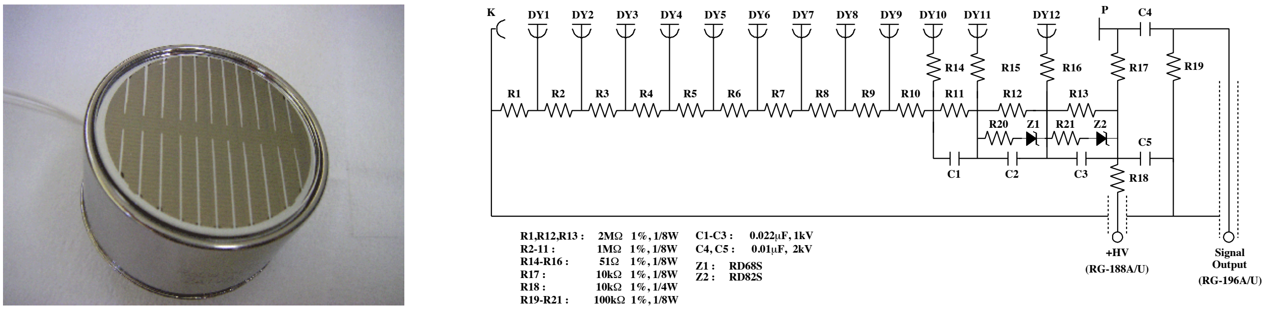

Figure 2.19: Picture of PMT (left) and diagram (right) [73].

2.4.2 Scintillation photon sensor

For the scintillation photon readout in the liquid xenon, the photosensors are required to be sensitive to VUV-light in $165\,\mathrm{K}$ and $5\,\mathrm{mT}$. These are fulfilled by specially developed VUV-MPPCs and R9869 PMTs, and 4092 VUV-MPPCs (Fig.2.18) are used on the inner face and 668 PMTs (Fig.2.19) are used in total on the other faces.

The PMTs use a VUV-sensitive photocathode made of Bialkali (K-Cs-Sb) and a quartz window of $\sim 75\,\%$ transparency for VUV light. As a result, a good quantum efficiency of $16\,\%$ was achieved for VUV light [34]. With an operation voltage of $\sim\,900\,\mathrm{V}$, an 10^6 gain can be obtained. Still, they have a problem with their round shape with the diameter of $46\,\mathrm{mm}$. This results in spatial gaps between adjacent PMTs, and the scintillation light cannot be uniformly readout. The non-uniformity results in a non-uniform light collection, which has a large impact on the energy and the position resolution. This is crucial on the inner face because most of gamma-rays are converted to a shower in the shallow region. Therefore, the PMTs are used only for the other five faces.

The VUV-MPPCs have the p-on-n structure as a semiconductor to deal with the short absorption length of VUV in silicon (Fig.2.20). To further suppress the VUV absorption, the protection layer is also

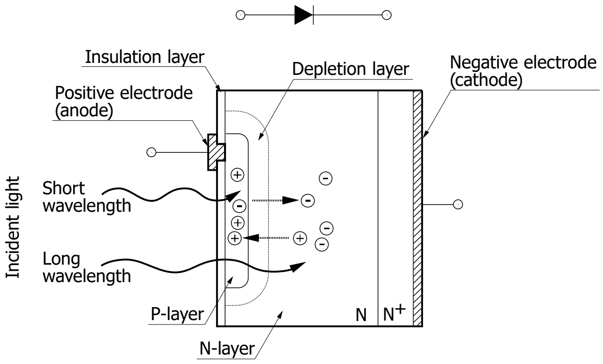

Figure 2.20: P-on-N structure of MPPC [74].

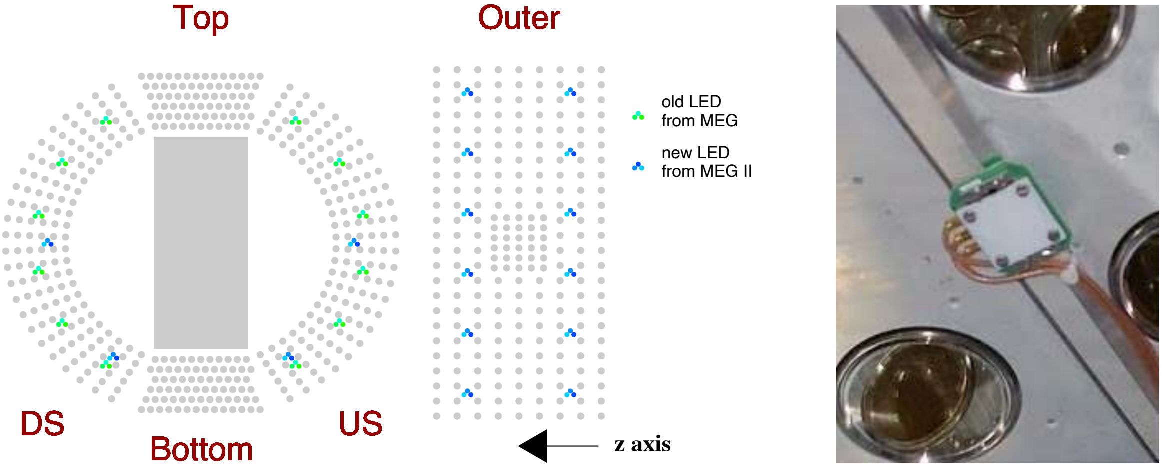

Figure 2.21: LED light sources installed on the outer and lateral faces [48].

optimized; it is made of VUV transparent quartz instead of the epoxy resin of the conventional SiPMs. As a result, the VUV-MPPCs have a sufficient photon detection efficiency (PDE) of $20\,\%$. Though a highly granular and uniform readout can be achieved thanks to its square shape, its use results in an increase in the number of readout channels. Four sensor chips of $6 \times 6\,\mathrm{mm}^2$, hosted in one package (Fig.2.18), are readout in series to mitigate this problem, which gives a $12 \times 12\,\mathrm{mm}^2$ coverage by each readout channel. This readout scheme is also advantageous because the smaller pulse width with the reduced capacitance helps to efficiently identify pileup pulses. Though SiPMs are known to have non-linearity, its impact on the $52.8\,\mathrm{MeV}$ detection is not expected to be severe thanks to the sufficient number of pixels (~ 13000 on each $6 \times 6\,\mathrm{mm}^2$ area).

Both sensors have operational difficulties and high calibration demands for long-term use in a high radiation environment. The PMT gain shows a decrease with a deterioration of dynodes in an accumulated multiplication. This demands a good and constant calibration of gain and a periodical adjustment of operation voltage. The MPPCs, on the other hand, are damaged during the operation in the muon beam, which results in a decrease of PDE [48]. This can be recovered by the thermal annealing method, which was completed at the beginning of 2022 and 2023.

2.4.3 Internal calibration sources — LED and alpha ray —

Blue light LED sources, Toyoda Gosei E1L49–3B1A–02 [75] and Kingbright KA-3021QBS-D [76], are installed inside the detector to calibrate the gain of the sensors. They are placed on the outer and lateral faces as shown in Fig.2.21. A Teflon sheet covers the LEDs to diffuse the light, which improves the overall stability of the light because the fluctuation of the light intensity reduces when the LEDs flash strongly.

Alpha-ray sources of $^{241}\mathrm{Am}$ are also installed to calibrate the light yield and the PDE of the MPPCs. Five gold-plated tungsten wires of $100\,\mathrm{\mu m}$ diameter are stretched between the upstream and downstream faces, each with five Am sources at $12.4\,\mathrm{cm}$ intervals (Fig.2.22) [77]. The activity of each Am source is $\sim 200\,\mathrm{Bq}$, which is a negligible rate in the data-taking with the muon beam.

2.4.4 $17.6\,\mathrm{MeV}$ gamma-ray calibration with proton beam and $\mathrm{Li_2B_4O_7}$ target

When $440\,\mathrm{keV}$ protons are injected to a $\mathrm{Li_2B_4O_7}$ target, gamma-rays are emitted from the ${}^7_3\mathrm{Li}(p,\gamma){}^8_4\mathrm{Be}$ reaction with a spectrum sharply peaked around $17.6\,\mathrm{MeV}$. Protons are accelerated by Cockcroft–Walton (CW) and injected from the downstream to the target at the COBRA center (Fig.2.23). A control system is implemented for the insertion and extraction of the muon stopping target and the CW equipment. This allows the whole operation to be completed within a few minutes, and thus, it does not heavily interfere

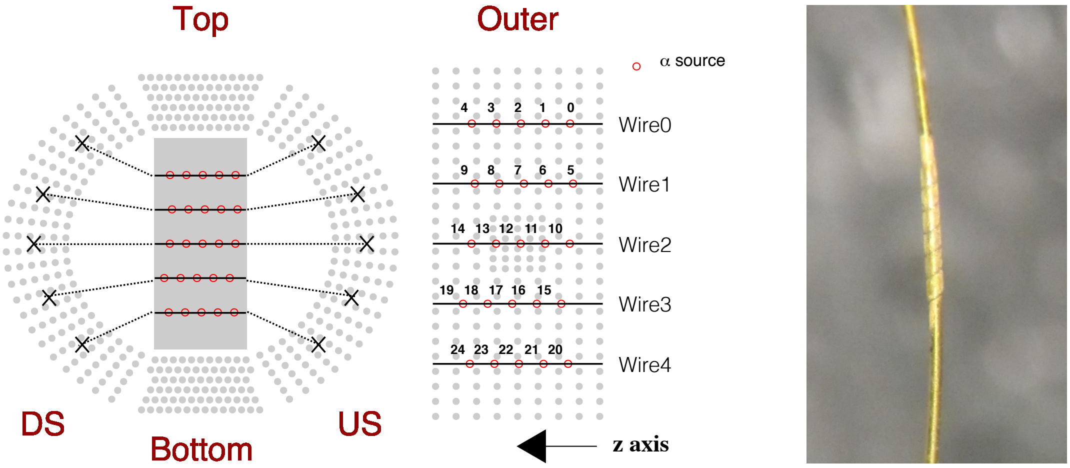

Figure 2.22: α-ray sources mounted in the LXe detector [48].

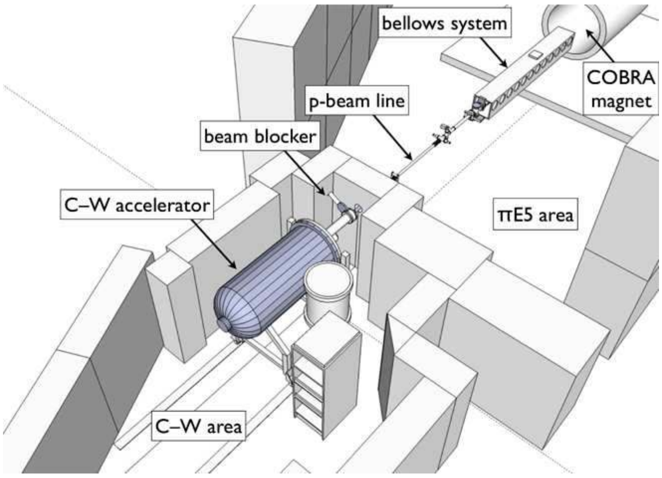

Figure 2.23: Layout of the apparatus for $17.6\,\mathrm{MeV}$ calibration gamma-ray data-taking [36]. The CW accelerator downstream of the MEG II detector injects protons to $\mathrm{Li_2B_4O_7}$ target at the center of the detector.

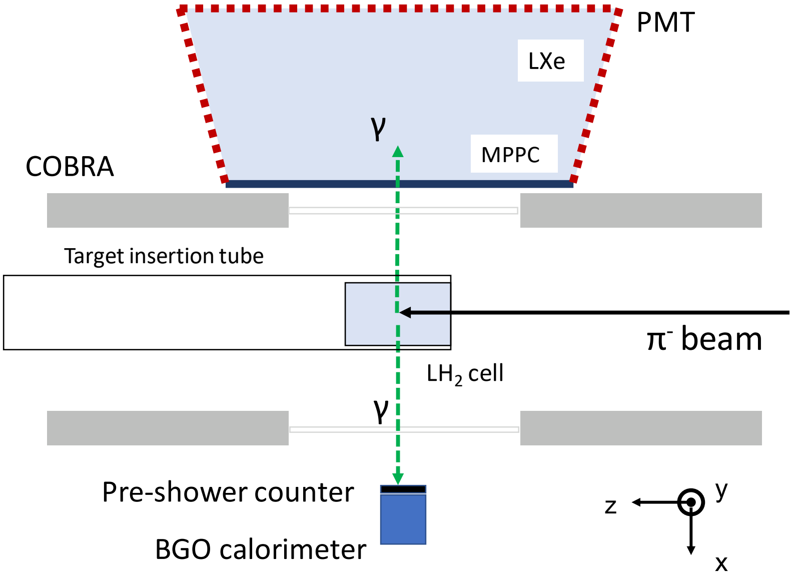

Figure 2.24: Setup of 55 MeV calibration data-taking [48].

with the physics data-taking.

2.4.5 55 MeV gamma-ray calibration with π^- beam and liquid hydrogen target

When π^- beam is injected into a liquid hydrogen target and stopped inside, π^0 are generated by $\pi^- + p \to \pi^0 + n$ reaction — called charge exchange reaction (CEX) —, which is immediately (π^0 lifetime is 8.5×10^{-17} s) followed by $\pi^0 \to \gamma\gamma$. Here, the energy of the emitted π^0 is

$$E_{\pi^0} = \frac{(m_{\pi^-} + m_p)^2 + m_{\pi^0}^2 - m_n^2}{2(m_{\pi^-} + m_p)} = 137.85\,\mathrm{MeV}, \tag{2.4}$$

where $m_{\pi^-} = 139.57\,\mathrm{MeV}$ is the π^- mass, $m_{\pi^0} = 134.97\,\mathrm{MeV}$ is the π^0 mass, $m_p = 938.27\,\mathrm{MeV}$ is the proton mass, and $m_n = 939.57\,\mathrm{MeV}$ is the neutron mass. Given the boosted π^0, the opening angle of the gammas ($\Theta_{\gamma\gamma}$) is correlated with the energy,

$$E_\gamma = \frac{E_{\pi^0}}{2} \pm \sqrt{\frac{E_{\pi^0}^2}{4} - \frac{m_{\pi^0}^2}{2(1 - \cos\Theta_{\gamma\gamma})}}. \tag{2.5}$$

In particular, when the decay gammas are completely back-to-back, the low energy gamma has 55 MeV and the high energy one has 83 MeV. This quasi-monochromatic gamma-ray close to the signal gamma energy is also used to calibrate the energy and evaluate the detector response.

As a by-product of this data-taking, a radiative capture reaction, $\pi^- + p \to \gamma + n$, is also expected with the cross-section being [78]

$$\frac{\sigma(\pi^- + p \to \pi^0 + n)}{\sigma(\pi^- + p \to \gamma + n)} = 1.533 \pm 0.021, \tag{2.6}$$

which is called “Panofsky ratio”. The 129 MeV gamma-rays from this reaction can be used to understand the linearity of the gamma-ray energy measurement.

The setup for the calibration data-taking is shown in Fig.2.24. The liquid hydrogen target is inserted from the downstream together with a cooling circuit. As we are interested in events close to the complete back-to-back kinematics, the opposite side is covered by another gamma-ray detector; the BGO calorimeter + pre-shower timing counter (Fig.2.25). The BGO calorimeter consists of 16 BGO crystals coupled to PMTs. The pre-shower counter consists of two plastic scintillation counters coupled

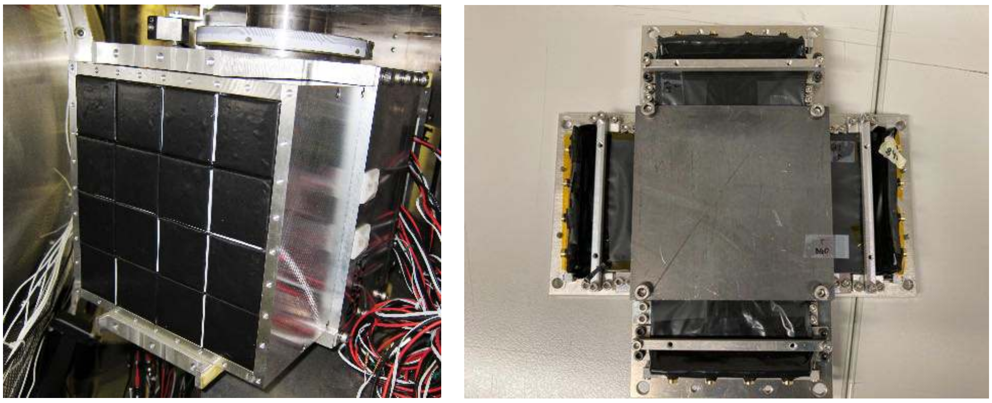

Figure 2.25: BGO crystal (left) + pre-shower timing counter (right) [35, 50].

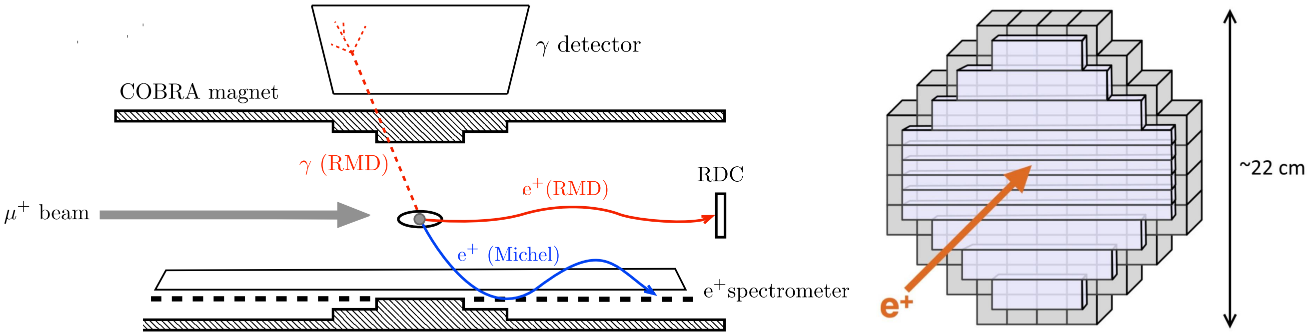

Figure 2.26: Downstream radiative decay counter at the endcap [34].

to SiPMs.

As a strong constraint on its calibration use, it takes a few days to install the special target and beam systems, which interrupts the physics data-taking. This gives the largest limitation to $55\,\mathrm{MeV}$ gamma calibration; we only have once-a-year opportunities with a limited time, and thus, the statistics are also limited.

2.5 Downstream radiative decay counter

The radiative decay counter is newly developed for the MEG II, which aims to identify background gamma-rays from the RMD. Most RMD gamma-rays close to $52.8\,\mathrm{MeV}$ are accompanied by a coincident low energy positron (typically $1 - 5\,\mathrm{MeV}$), which flies towards the detector ends along the beam axis in the COBRA field (Fig.2.26). About half of the RMD-associated low energy positrons are emitted in the downstream direction, and $\sim 90\,\%$ acceptance for them can be covered with a $\sim 20\,\mathrm{cm}$ size detector. Efficient identification of the RMD-associated low-energy positrons can be realized by measuring both the hit timing and energy (Fig.2.27).

The downstream RDC has two parts, one for the timing measurement part and the other for the calorimetry (Fig.2.28). The timing measurement part consists of 12 plastic scintillation counters (BC418, Saint Gobain) of different sizes; the thickness being $5\,\mathrm{mm}$ for all the counters, the height being $1\,\mathrm{cm}$ (the central six counters) or $2\,\mathrm{cm}$ (the outer counters), and the width is 7, 11, 15, and $19\,\mathrm{cm}$ (wider for inner counters). Both ends of the $1\,\mathrm{cm}$ ($2\,\mathrm{cm}$) high counters are coupled to two (three) SiPMs connected in series, where all the SiPMs are from Hamamatsu Photonics (S13360-3050PE). The calorimeter is located behind the plastic counters and hosts 76 LYSO crystals ($2 \times 2 \times 2\,\mathrm{cm}$), each of which is coupled to a SiPM from Hamamatsu Photonics (S12572-025P).

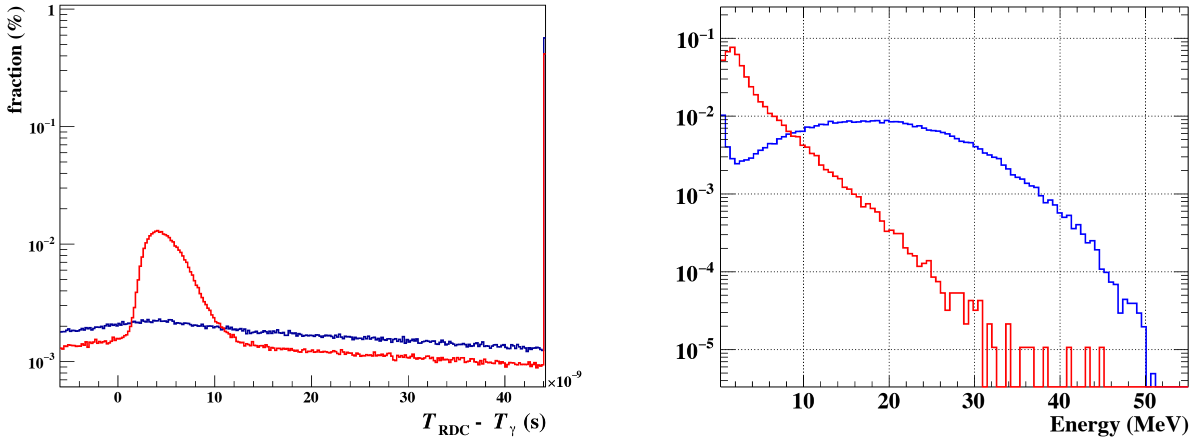

Figure 2.27: Timing (left) and energy (right) distribution of RDC hits [34]. The red (blue) line shows the distribution for the RMD-associated accidental gamma-rays (signal gamma-rays). In the timing plot, the time difference between the RDC hit and the LXe hit is shown. Here, the 4 ns offset corresponds to the TOF from the muon stopping target to the RDC.

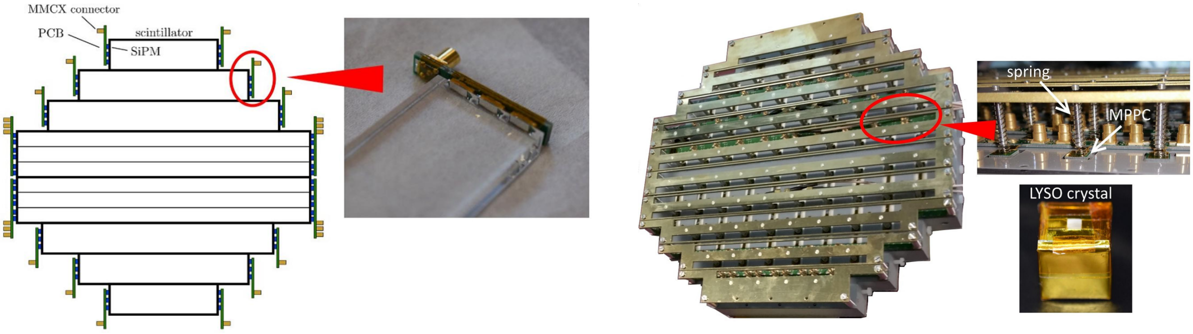

Figure 2.28: The picture of the downstream RDC components [34].

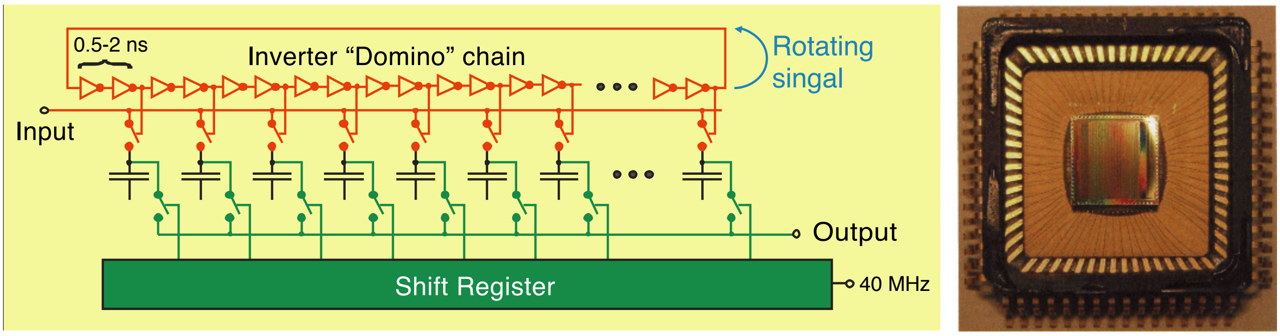

Figure 2.29: Schematic explaining the principle of DRS (left) and picture (right) [79, 80].

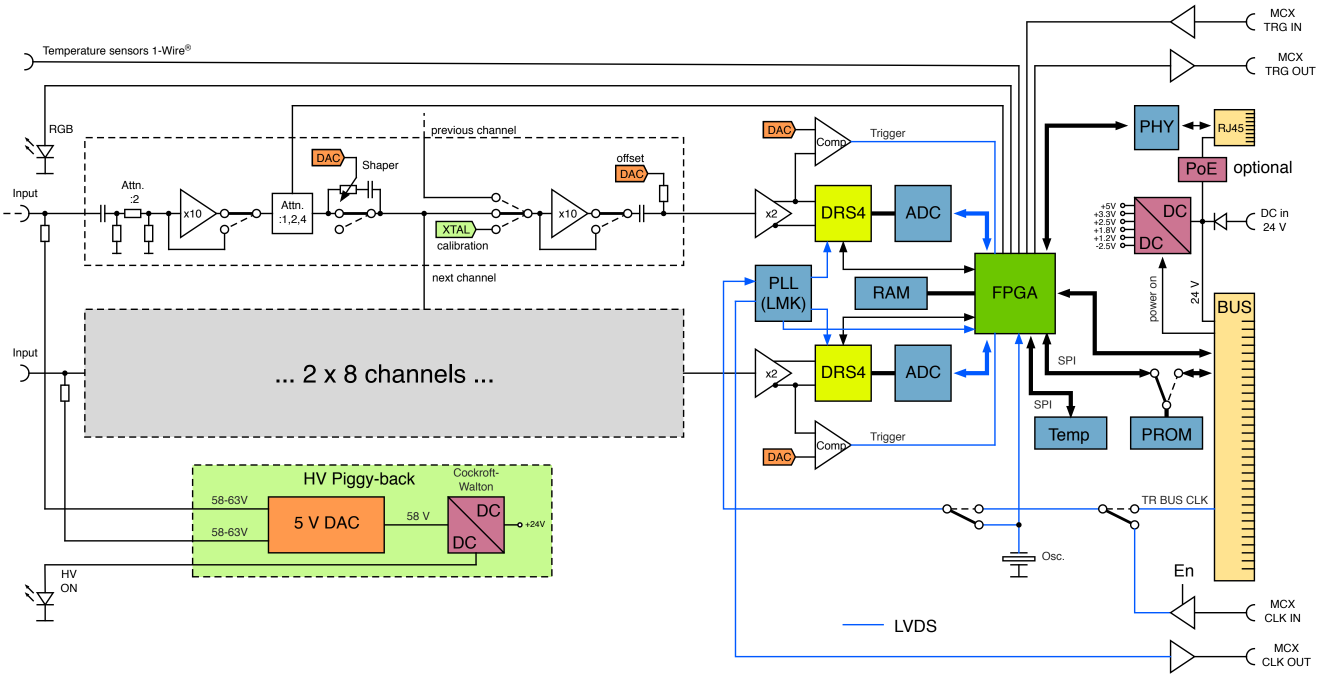

Figure 2.30: Structure of circuits in WaveDREAM board [34].

2.6 Electronics and data acquisition system

2.6.1 Integrated waveform data-taking system

In order to have a good resolution in the high pileup environment, the accessibility of the raw waveform is desired in the reconstruction. For this purpose, the waveform of all the detectors is digitized by the Domino Ring Sampler (DRS), which has a wide bandwidth of $\sim 1\,\mathrm{GHz}$ and a high sampling speed up to $5\,\mathrm{GSPS}$ [79, 80]. The DRS makes use of the switched capacitor arrays technique, where one DRS channel contains 1024 sampling cells. The sampling signal is generated by the inverter chain called "domino wave" (Fig.2.29), which is stopped when a trigger signal is issued. When the sampling signal stops, the cell array keeps the waveform at the most recent 1024 sampling points, which is then read out by the shift resistor and digitized. One DRS chip shown in Fig.2.29 contains eight digitizer channels.

Another requirement for the electronics is to be housed in a limited space. This is highly demanding with the necessity of pre-amplifiers and high-voltage application systems for the SiPMs as well as the trigger system and the waveform digitizers. A new DAQ module — called WaveDREAM Board (WDB) — is developed for the MEG II experiment (Fig.2.30), which integrates the above functionalities. One WDB has two DRS chips and can host 16 readout channels in total. The DRSs are operated in a way that it continuously samples the input waveform and sends its copy to the output. The DRS outputs are connected to the ADCs, which continuously digitize the waveform at $80\,\mathrm{MSPS}$. The ADC outputs are

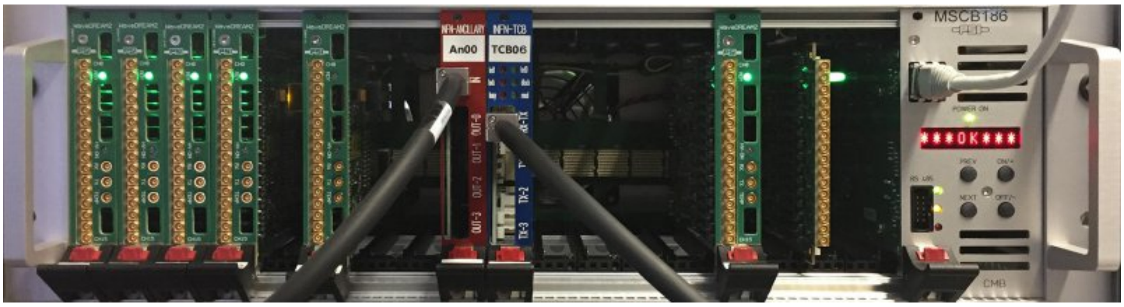

Figure 2.31: A WaveDREAM crate [34].

fed to the FPGA to finally build the trigger logic. The high voltage for the SiPMs (up to $\sim 240\,\mathrm{V}$) is provided by the Cockcroft-Walton multipliers, which can be further tuned on each channel by the $5\,\mathrm{V}$ DAC. The amplifiers before the DRS are combined with programmable attenuators and a programmable pole-zero cancellation circuit, giving flexibility in the gain (from $\times 0.5$ to $\times 100$) and the shaping.

The full communication between the ~ 9000 readout channels are designed on a crate basis (Fig.2.31), whose global control is taken by a DAQ computer hosting the MIDAS system [81]. A WaveDream crate hosts 16 WDBs, a trigger concentrator board (TCB), and a data concentrator board (DCB). The DCBs are responsible for the configuration of boards, the distribution of the master clock and trigger signals, merging and formatting the waveform data, and the interface to the DAQ computer. The TCBs gather the low (board) level information, perform online reconstruction, and generate trigger signals.

2.6.2 Trigger system

The trigger system has a strong constraint on the latency, which is determined by the depth of the waveform storage in DRS. Its typical value is a few hundred nanoseconds, which is 1024 (the number of cells) divided by the DRS sampling speed. Therefore, the trigger logic must be built within such a limitation. In particular, the CDCH information usually cannot be included in the logic with its drift time being up to $\sim 300\,\mathrm{ns}$.

The logic for the $\mu \to e\gamma$ is thus implemented based on the LXe and the pTC. Here, only $E_\gamma, t_{e\gamma}$, and $\Theta_{e\gamma}$ can be reconstructed online. The online gamma energy reconstruction uses a weighted sum of the waveform of scintillation photon sensors. Here, the weights are calculated from the sensor gain and PDE, and the overall energy scale is calculated from the $17.6\,\mathrm{MeV}$ gamma-ray calibration data. The online $t_{e\gamma}$ reconstruction uses the hit time difference between the pTC and the LXe, whose resolution is dominated by the positron time of flight (TOF) due to the absence of the full track reconstruction. It also received a non-negligible contribution from the t_γ time walk effect in the 2021 run, which has been mitigated in the 2022 run. This is because the online t_γ reconstruction relies on MPPCs (PMTs) in the 2021 (2022) run, where the time walk effect is stronger for the MPPC waveform. The online $\Theta_{e\gamma}$ reconstruction uses the first hit counter of the pTC and the peak position in the scintillation light distribution on the LXe inner face. The trigger judgment relies on a look-up table created from a detector simulation for the signal events, which is tight enough thanks to the highly segmented design of the pTC. The latency of the full trigger is $\sim 600\,\mathrm{ns}$ and the sampling speed of the DRS is $1.4\,\mathrm{GSPS}$ for the LXe, pTC, and RDC detector and $1.2\,\mathrm{GSPS}$ for the CDCH.

During the experiment, calibration data-taking is also required in addition to the main physics data-taking. Using the outputs of the dedicated calibration detectors, several different logics are also prepared for them as briefly summarized in Tab.2.1.

Table 2.1: List of trigger settings.

Logic	Aim
Cuts on $E_\gamma, t_{e\gamma}, \Theta_{e\gamma}$	Main physics data for $\mu \to e\gamma$
Self trigger on the pTC	Michel positron data
LXe hit $\wedge$ BGO + pre-shower counter hit	$\pi^0 \to \gamma\gamma$ calibration
Inputs from LXe LED	Sensor calibration
Inputs from pTC laser	Time offset calibration of each tile
α particle identification with waveform	α-ray calibration
Self trigger on RDC LYSO	Energy scale calibration for RDC
Random timing	Electronics noise calibration

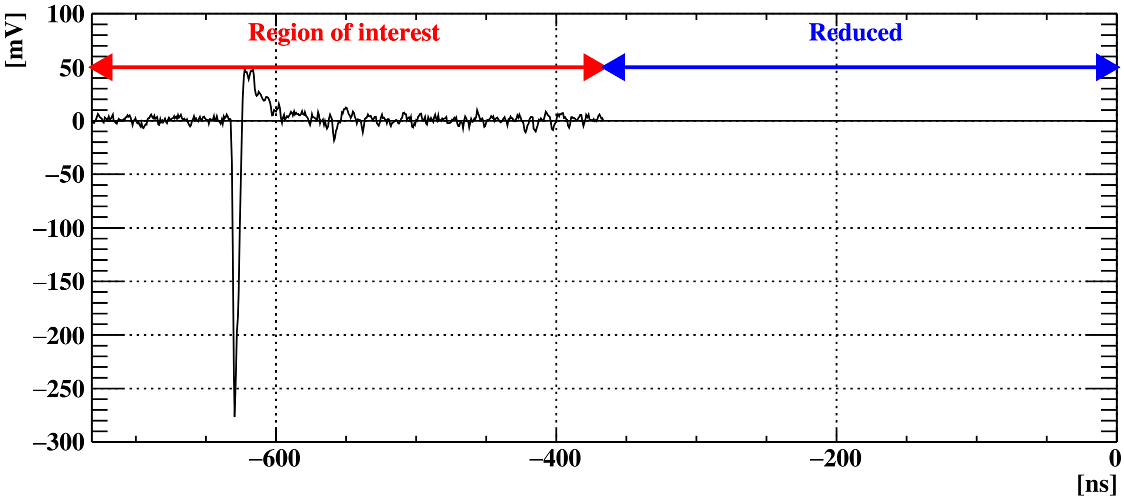

Figure 2.32: Recorded waveform after region of interest cut. The first half of the window is the region of interest and the waveform is stored, whereas the waveform in the later half of the window is dropped.

2.7 Data management

2.7.1 Reduction of waveform data size

When digitized waveform data is recorded by the DAQ system, the data size reduction is necessary for two reasons. The first one is to reduce the data rate to keep it below the data bandwidth of the whole system. In case of any overflow, some of the triggered events are not recorded and they become inefficient. Another purpose is to reduce the disk consumption of the storage system, which finally is required to store years of the MEG II dataset.

In addition to the file compression with bzip2, the data size is reduced by dropping some information from the recorded waveform. This scheme is optimized for each detector by combining three methods: zero-suppression, region of interest cut, and rebinning. The zero-suppression applies a threshold cut on the waveform amplitude, and channels below the threshold are dropped from the output file. The region of interest cut keeps the voltage information only in the important time region (Fig.2.32). The rebinning re-samples the waveform to have a sparse recording, where only averages of neighboring sampling points are stored (Fig.2.33). Here, the number of sampling points can be changed dynamically depending on the amplitude of the channel waveform.

2.7.2 Data storage and blinding scheme

During the offline reconstruction, the raw waveform data files are re-formatted into a ROOT [82] format which contains both the waveform information and the reconstructed kinematics. The blinding is also

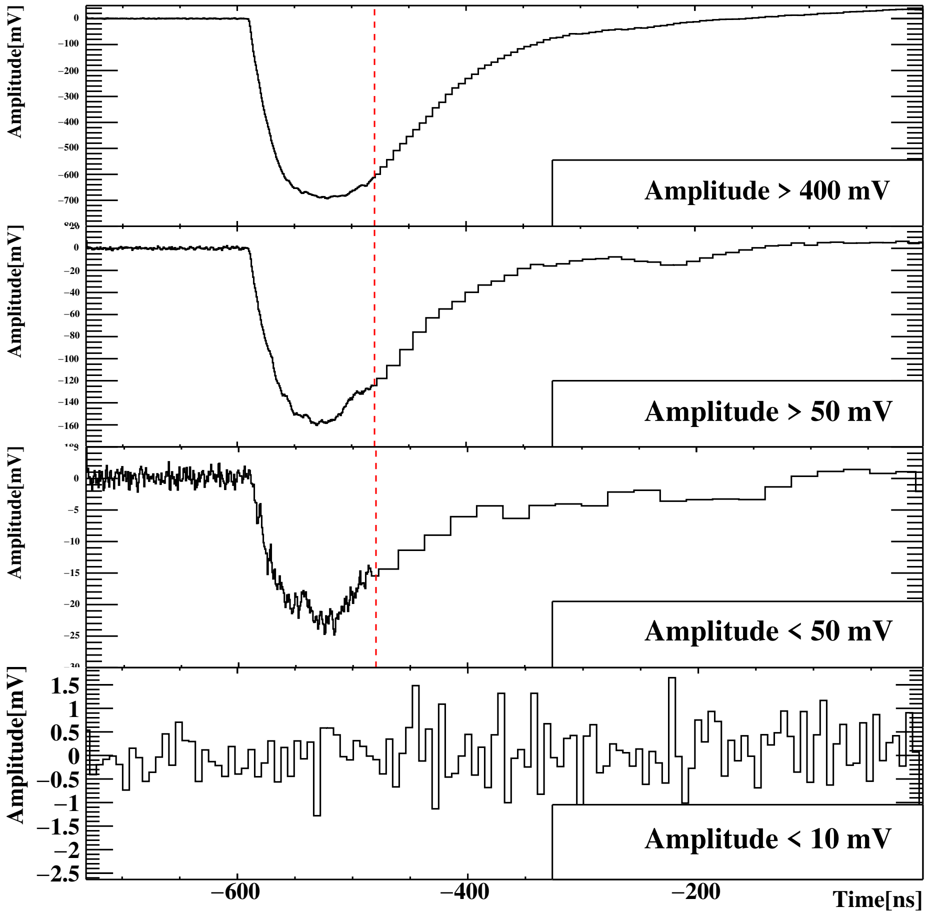

Figure 2.33: Recorded waveform for the LXe detector after rebinning [48]. The waveform tail region (after the vertical red dashed line) is rebinned, while the leading edge is fully preserved to keep a good time resolution. The number of sampling points in the rebinning is dynamically changed depending on the waveform amplitude.

applied here according to the criteria described later in Sec.6.2, which is to avoid psychological biases in the analysis [83]. After the blinding, the blinded events and the open events are written into different re-formatted files, and users are deprived of permission to access either the blinded files or the original format waveform files. *Data preselection* is also applied here to reduce uninteresting events in the re-formatted files. This is based on $t_{e\gamma}$ and E_γ with a similar logic as that used for the online trigger judgment, but makes use of the higher resolution in the offline reconstruction. Once the re-formatting ends, all the original files are moved to tape storage and fully preserved there.

2.8 Detector simulation

The final output of the detector simulation is a fully simulated waveform similar to the DRS data in the experiment, which ensures compatibility with the reconstruction framework. The simulation can be separated into three parts; the muon decay generation, the simulation of the particle transportation and ionization, and the simulation of pileup and waveform digitization.

In the event generation step, both the SM decay and the $\mu^+ \to e^+\gamma$ decay are simulated starting from muons. The muon polarization is also considered in the event generation according to the measured one in the MEG experiment [84]. Here, the angular distribution of $\mu^+ \to e^+\gamma$ decay is assumed to be isotropic, namely $A_R = A_L$ is assumed in Eq.(1.3) notation. Two different approaches are adopted regarding the simulation for the muon decay positions,

- Simulation starts from muons already stopped in the target, and the position is based on an assumption about the stopping position distribution,
- Simulation starts from muons during the transportation to the target in the beamline.

The latter case can simulate muons that decay in flight or the muons that are not stopped in the target but at the expense of the CPU time consumption. Though the choice of the approach changes case by case, simulations for background events generally adopt the latter approach.

The particle transportation and ionization are simulated with the Monte Carlo (MC) method based on the Geant4 package [85], which is a particle simulation framework to evaluate the particle trajectories and the energy deposit along them. This incorporates all the relevant electromagnetic reactions; pair creation and annihilation, bremsstrahlung, Compton scattering, photoelectric effect, ionization, and multiple scattering. After the detector hits are simulated, the detector's response to them is simulated in dedicated codes. The LXe simulation includes the scintillation photon absorption, scattering, and reflection in the detector material. The CDCH uses the Garfield++ [86] to simulate the gas ionization process in the drift cells.

The simulation of the full experiment requires simulations on the overlay of particle activities in a given event. This reads the results of the ionization simulation in the previous step and mixes them with the rate determined by the assumption on the beam. The timings of the mixed events are simulated according to the exponential decay time distribution. The waveform in the mixed events is simulated with a reliance on waveform templates, which are given as the impulse responses of the detectors. The templates of the pTC, LXe, and RDC are taken from the data samples while the template of the CDCH is based on SPICE [87] simulations. The noise is then added to the simulated waveform to include the observed noise situation in the data-taking. In the final step, the waveform is digitized including the sampling and the discretization of the DRS.

Chapter 3

Data taking

All the MEG II detector hardware was delivered to PSI by March 2021, followed by a commissioning period that lasted till the end of September. During the commissioning, a stable operation of the detectors was achieved and the signal check was also completed. The physics data-taking started at the end of September and continued till the middle of November. The $\pi^0 \to \gamma\gamma$ calibration data-taking system was then installed in late November, and its data-taking started at the beginning of December. During both the physics and $\pi^0 \to \gamma\gamma$ data-taking period, there were also daily short calibration routines. This chapter describes the condition of the data-taking activities relevant to this thesis.

3.1 Physics data taking

The physics data was taken during September 25th – November 18th, 2021, which is the first MEG II dataset. The total live time of the 2021 physics data-taking was $2.9 \times 10^6\,\mathrm{s}$. This is $63\,\%$ of the total elapsed time during the whole period, and its day-by-day breakdown is shown in Fig.3.1. The inefficiency came from the dedicated calibration data-taking — the difference between the black hatched graph and the red graph in Fig.3.1 corresponds to the fraction of calibration DAQ time (see Sec.3.3) — and the deadtime from the transitions related to the changes in recorded data files. In addition, there were a few occasions of short (up to 3 days) accelerator shutdowns, which entirely interrupted the physics data-taking.

During the physics data-taking, the beam intensity was risen step-by-step; we started from a lower intensity to validate a stable detector operation and then moved to a higher value. Here, the major concerns were the CDCH discharge and the PDE of the LXe MPPCs. As the CDCH discharge problem was expected to become severe at a higher intensity, detector conditioning works were performed carefully at lower intensities. The minimum requirement on the PDE value of the LXe MPPCs to keep a high energy resolution is $4\,\%$ as discussed in [45]. The PDE decrease speed was measured during the $3 \times 10^7\,\mu/\mathrm{s}$ period, and finally it was concluded that the experiment can survive the 2021 data-taking even with $5 \times 10^7\,\mu/\mathrm{s}$ intensity. As a result, four different muon beam intensities were adopted as summarized in Tab.3.1. The time evolution of the number of muons stopped in the target is shown in Fig.3.2, where the final value is 1.04×10^{14}.

Table 3.1: Beam rate during 2021 physics data taking.

Period	Beam rate
Sep/25 – Oct/15	$3 \times 10^7\,\mu/\mathrm{s}$
Oct/15 – Oct/28	$2 \times 10^7\,\mu/\mathrm{s}$
Oct/28 – Nov/2	$3 \times 10^7\,\mu/\mathrm{s}$
Nov/2 – Nov/10	$4 \times 10^7\,\mu/\mathrm{s}$
Nov/10 – Nov/18	$5 \times 10^7\,\mu/\mathrm{s}$

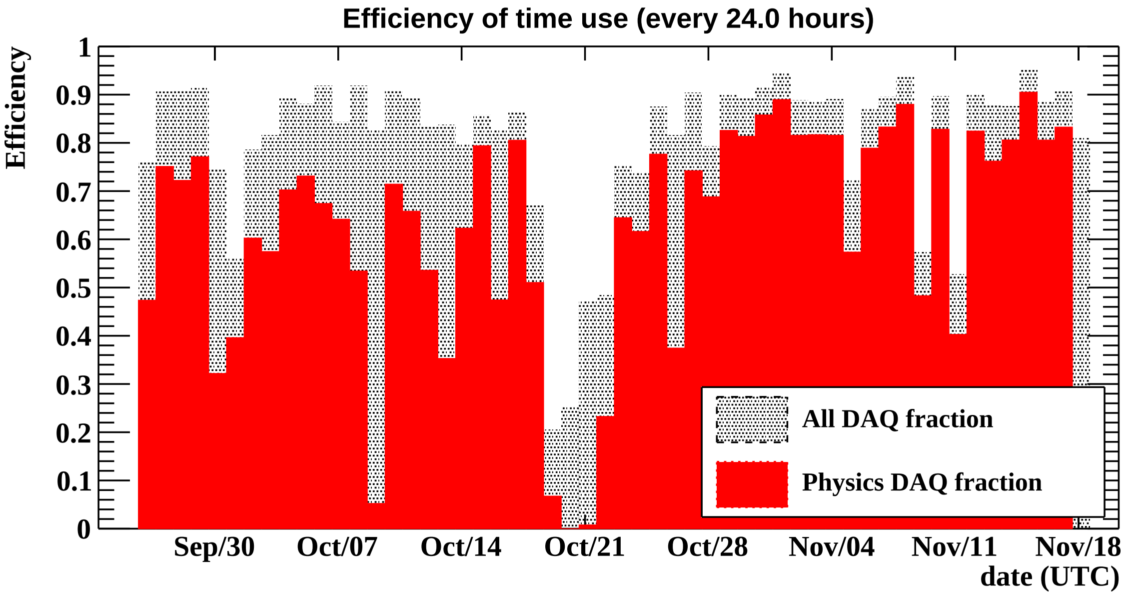

Figure 3.1: Efficiency of time use during the 2021 physics data-taking.

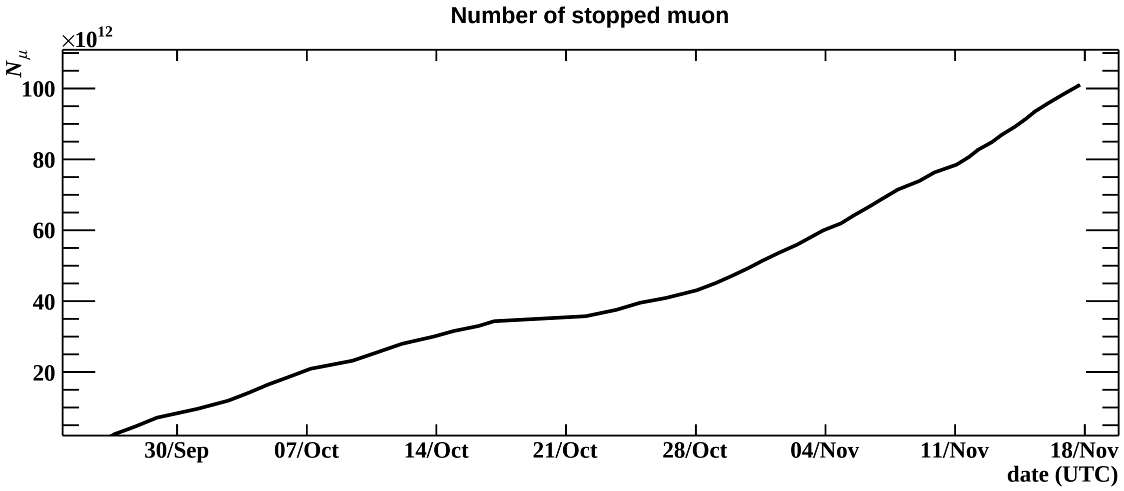

Figure 3.2: The number of muons stopped inside the target.

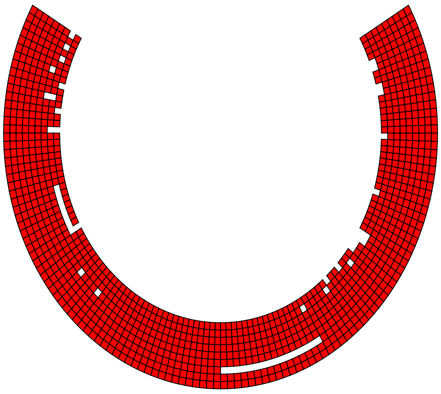

Figure 3.3: Map of active drift cells of CDCH in 2021.

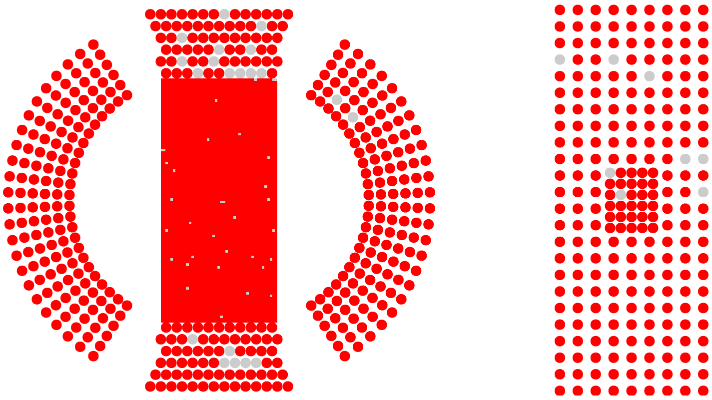

Figure 3.4: Map of active channels of LXe in 2021 [49].

3.2 Detector condition

The CDCH was stably operated during the whole physics data taking with few occasions of discharges. Only $\sim 3\,\%$ of all the CDCH readouts were found not active (Fig.3.3), which does not have any critical impact on the performance. Some of them come from detachments of high-voltage application systems and some others from problems in the front-end amplifier.

In the LXe detector, the liquid xenon was filled to $y = 83\,\mathrm{cm}$ level. This is below the position of some PMTs in the top region, which means that such PMTs could not efficiently collect scintillation lights. With a xenon purification system, the light yield was stable within a few percent [48]. The readout of the LXe detector also had a few problematic channels; 23 from the MPPCs and 22 from the PMTs (Fig.3.4). They came from problems in the circuit, malfunctions of the sensors, or malfunctions of the high voltage systems. Though the PDE of the VUV-MPPCs decreased as expected in the exposure to the muon beam, the final PDF value ($6\,\%$ [48]) was high enough.

The pTC was also operated in a stable condition, and only one counter was inactive during the data-taking. The readout had a large electronic noise at the beginning, which was reduced during the data-taking by removing problematic elements in the circuit.

The RDC detector kept a good condition for the data-taking with all the channels actively readout. However, its installation into the data-taking was delayed till the end of October. This is because of a safety problem; An interlock system was missing to avoid collisions between the RDC and the $17.6\,\mathrm{MeV}$ calibration system.

Two target cameras were installed during 2021 data-taking. One was in operation from the beginning until its stall in the middle of October. The other started its operation in the middle of October and ran till the end of the physics data-taking.

3.3 Daily calibration

The LXe and the pTC require daily calibration data-taking. Tab.3.2 shows the calibration routine in the final period of the physics data-taking. The LXe detector calibration, which requires frequent and precise calibration to correct for the time variations explained in Sec.2.4.2, dominates the calibration time consumption. As the requirements for the quantity of each calibration data were not clear at the beginning, we started with a scheme to collect conservatively large calibration statistics. Initially, the whole calibration data-taking consumed $20\,\%$ of the time (Fig.3.1), which was continuously reduced during the data-taking period. As a result, the calibration time consumption was finally reduced to $\sim 10\,\%$ at the end of the 2021 data-taking.

Table 3.2: Calibration data taking scheme.

Data	Frequency of data taking	Time consumption
Electronics noise data	2 / day	10 min
LXe LED data (long duration)	1 / day	40 min
LXe LED data (short duration)	1 / day	15 min
LXe alpha ray data	2 / day	20 min
LXe cosmic ray data	1 / day	20 min
$17.6\,\mathrm{MeV}$ gamma data	3 / week	1 hour
pTC laser data	1 / day	10 min

Table 3.3: Applied data reduction method (explained in Sec.2.7.1) for each detector.

Detector	Method
LXe (also see Fig.2.33)	Full waveform rebinned by 8 (when amplitude $< 10\,\mathrm{mV}$) Waveform tail rebinned by 32 (when $10\,\mathrm{mV} <$ amplitude $< 50\,\mathrm{mV}$) Waveform tail rebinned by 16 (when $50\,\mathrm{mV} <$ amplitude $< 400\,\mathrm{mV}$) Waveform tail rebinned by 8 (when $400\,\mathrm{mV} <$ amplitude)
CDCH	Full waveform rebinned by 2
pTC	Region of interest (first half) and zero-suppression
RDC plastic	Region of interest (first half) and zero-suppression
RDC LYSO	Region of interest (first half)

3.4 RMD-enhanced calibration

The full $t_{e\gamma}$ offset calibration requires RMD events, which are difficult to find in a high-rate condition. Hence, dedicated data-taking was performed at $\sim 1 \times 10^6\,\mu/\mathrm{s}$ to collect RMD events, where the statistics were enhanced by setting a low E_γ threshold of 10 – $20\,\mathrm{MeV}$. The data-taking was carried out twice; the first one on October 8th to optimize the trigger $t_{e\gamma}$ threshold, and the second one during November 18 – 21 (after the end of physics data-taking) to have sufficient statistics for the calibration in the offline reconstruction.

3.5 DAQ setting and performance

The data-taking condition was tuned in the first month of the physics data-taking to have a good DAQ performance. The data reduction scheme was optimized during this period as summarized in Tab.3.3. The trigger $t_{e\gamma}$ threshold was optimized based on the RMD-enhanced dataset taken in the middle of October (Sec.3.4). The trigger E_γ threshold was optimized based on the $17.6\,\mathrm{MeV}$ gamma-ray dataset.

The efficiency of the DAQ is defined as the number of recorded events divided by the number of triggered events, which is shown in Fig.3.5. In the beginning, both the trigger rate and the data size were too high (higher than the capacity) without the above optimization works. As a result, the trigger pre-scaling was applied at the beginning to drop a part of the triggered events, which was the main reason for the low efficiency until October 14th. The other inefficiencies came from the overflow of the data rate. They were solved by tightening the trigger thresholds of both $t_{e\gamma}$ and E_γ, namely by reducing the trigger rate. The overall trigger efficiency is discussed later in Sec.6.3.1.

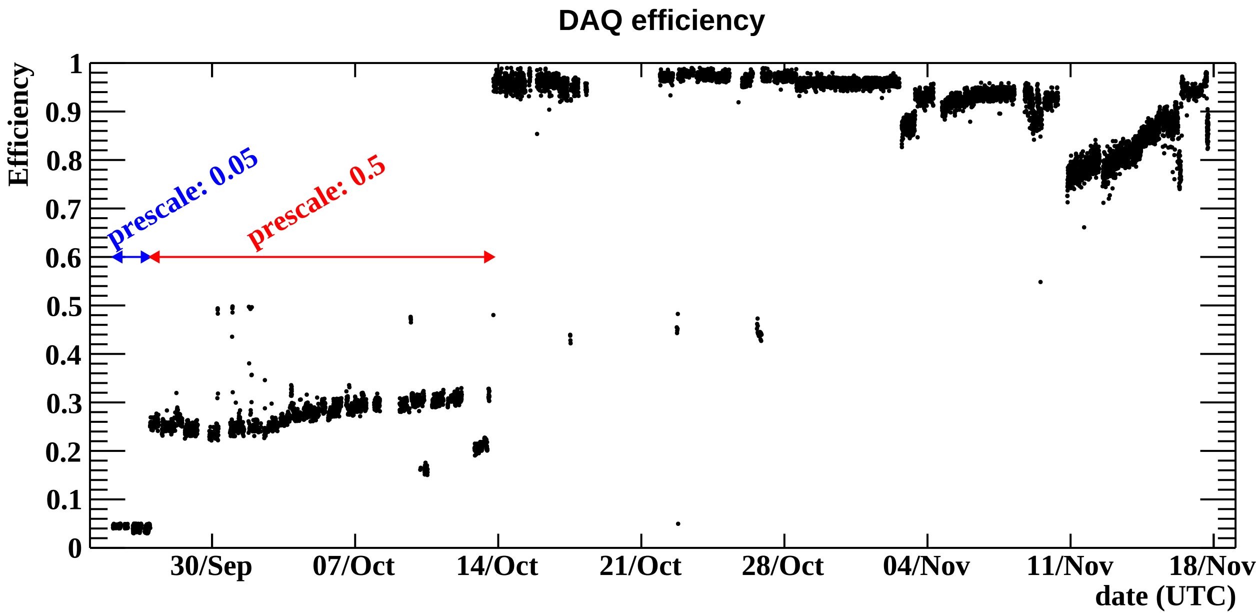

Figure 3.5: DAQ efficiency during the 2021 physics data-taking. The large inefficiency at the beginning of the data-taking came from the pre-scaling of the trigger, which was applied to keep the data rate below the capacity.

3.6 $\pi^0 \to \gamma\gamma$ data taking

The $\pi^0 \to \gamma\gamma$ data was taken during December 16th – December 22nd, after preparation works for the liquid hydrogen target. Though the $\pi^0 \to \gamma\gamma$ data with the MEG II LXe detector was first taken in 2020 [49], there were two additional important goals in 2021. The first one was the full scan of the whole LXe acceptance region, which was not possible in 2020 because of the limited number of readout channels. The second goal was to evaluate the geometrical spread of the $\pi^0 \to \gamma\gamma$ decay vertex with a dedicated measurement as proposed in [49]. Its importance was recognized in the previous time resolution evaluation with the 2020 data, which suffered from a large uncertainty coming from our ignorance about the decay vertex.

The liquid hydrogen target had a problem with insufficient cooling power to stably keep the hydrogen in a liquid state. This resulted in a time limitation for the data-taking. As a result, the full acceptance of the LXe detector was not covered as shown in Fig.3.6. On the other hand, the measurement of the spread of $\pi^0 \to \gamma\gamma$ decay vertex was successful though its statistics were close to the minimum requirement also due to the problem of the liquid hydrogen target.

3.7 Cosmic ray data taking for detector alignment

The cosmic ray data for the alignment was taken without a magnetic field to have linear tracks, which are triggered on energy deposits to the LXe detector. They are taken three times during the scheduled short accelerator shutdown periods: September 16 – 17th, October 19 – 20, and November 23rd.

3.8 Optical scanning for detector alignment

The COBRA magnet has a few optical markers to perform laser scans, which define the origin of the MEG II coordinate system. The CDCH wire scanning was performed before the chamber gas volume was closed [38]. Its global position in the MEG II apparatus was aligned by optical markers on the outer structure. The alignment of pTC combined optical markers on the support structure of the scintillation

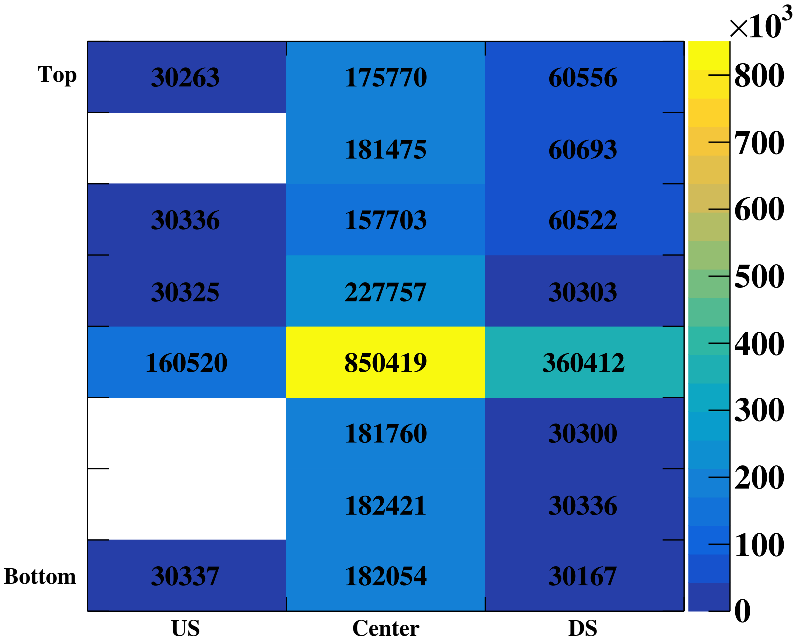

Figure 3.6: The number of acquired events for the $\pi^0 \rightarrow \gamma\gamma$ calibration [48]. Each sub-range of the acceptance is the region that can be covered by the finite-size BGO detector, which was moved to different positions to fully cover the acceptance.

counters and a full 3D scanning of all the counters. The LXe was aligned by combining a full scan of photosensors discussed later in Sec.5.2.1 and the time variation followed by optical markers on the outer structure of the detector. The alignment of the target relied on a combination of a CT scan and optical markers on the support frame. The CT scan data was taken before the installation to estimate its shape or deformation, and the position in the global coordinate was estimated from the optical markers.

3.9 Target camera operation and photograph

The target cameras were not fully operational during the 2021 data-taking, and special care is needed in the analysis. Firstly, no photograph was taken when an optical survey (an alignment method based on a laser scan) of the target position was performed, and the camera operation started after its position was moved from the position in the survey. Secondly, there was a period in November with several target movement operations for LXe calibration (Sec.2.4.4) but with no photograph to follow it (Fig.3.7).

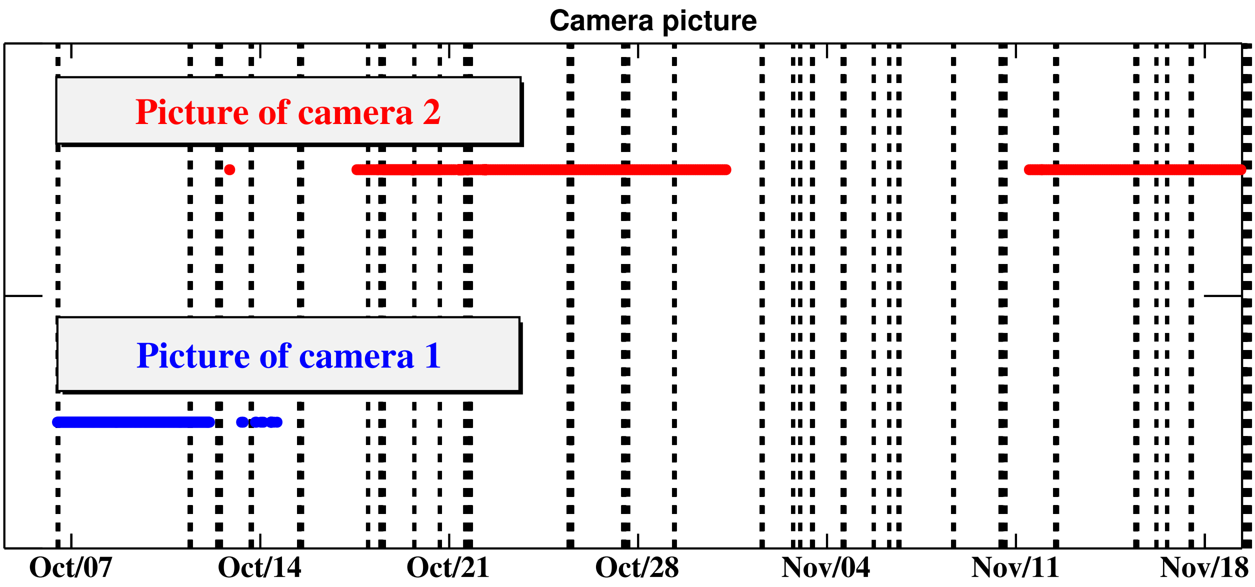

Figure 3.7: List of photographs taken by the target cameras. The blue markers correspond to photographs taken by the first camera and the red markers correspond to those by the second camera. The vertical lines correspond to target movements.

Chapter 4

Event reconstruction and selection

Fig.4.1 shows the reconstruction overview. The positron energy, vertex, and emission angle are estimated from reconstructed trajectories in the CDCH and their extrapolations to the target. The positron time is reconstructed from a cluster of pTC measurements with time-of-flight (TOF) corrections according to the measured trajectory. The gamma-ray energy, position, and timing at the hit position are directly measured by the LXe. The gamma reconstruction at the vertex relies on the reconstructed positron vertex, namely the gamma emission angle and the TOF are reconstructed by connecting the hit position in LXe with the positron vertex.

4.1 Positron reconstruction

The overview of the positron reconstruction algorithm is shown in Fig.4.2.

4.1.1 Hit reconstruction and clustering of pTC

The pTC hits are reconstructed by combining waveform analysis results from each edge of the counters. In the waveform analysis of the pTC, the pulses are detected by setting a threshold, and the time is evaluated from the constant fraction method. The reconstructed time at both ends, $t_{1,2}$, are then combined to reconstruct the hit on the counter. The hit time on the counter is reconstructed by averaging them,

$$t_{\text{hit}} = \frac{t_1 + t_2}{2} - t_{\text{counter}}, \tag{4.1}$$

where t_{counter} is the offset of the counter. The w position in the local coordinate (Fig.2.15) is reconstructed from the time difference between the ends,

$$w_{\text{hit}} = \frac{t_1 - t_2 - t_{\text{channel}}}{2} \cdot v_{\text{eff}}, \tag{4.2}$$

where t_{channel} is the offset between the two ends and v_{eff} is the velocity of the scintillation light propagation inside the scintillator.

The reconstructed hits are then grouped to separate those from pileup positrons. The clustering algorithm groups the hits by combining the timing with the counter position, whose principle is shown in Fig.4.3. The hit positions are ordered according to the depth from the innermost counter, which is used to roughly correct the TOF between the counters. After the rough TOF corrections, the hits can be clustered in the time coordinate with a 0.5 – $0.7\,\text{ns}$ wide window. In addition, a distance cut is also applied to separate hits further than $10\,\text{cm}$. This is to detect a small turn during the hits in the cluster; an example is shown in Fig.4.4. Here, the positron makes hits in the green region, makes a small turn, and then comes back in the orange region. The bottom right plot in Fig.4.4 shows that the hits in the green and the orange region can be successfully separated thanks to the distance cut. Though the two

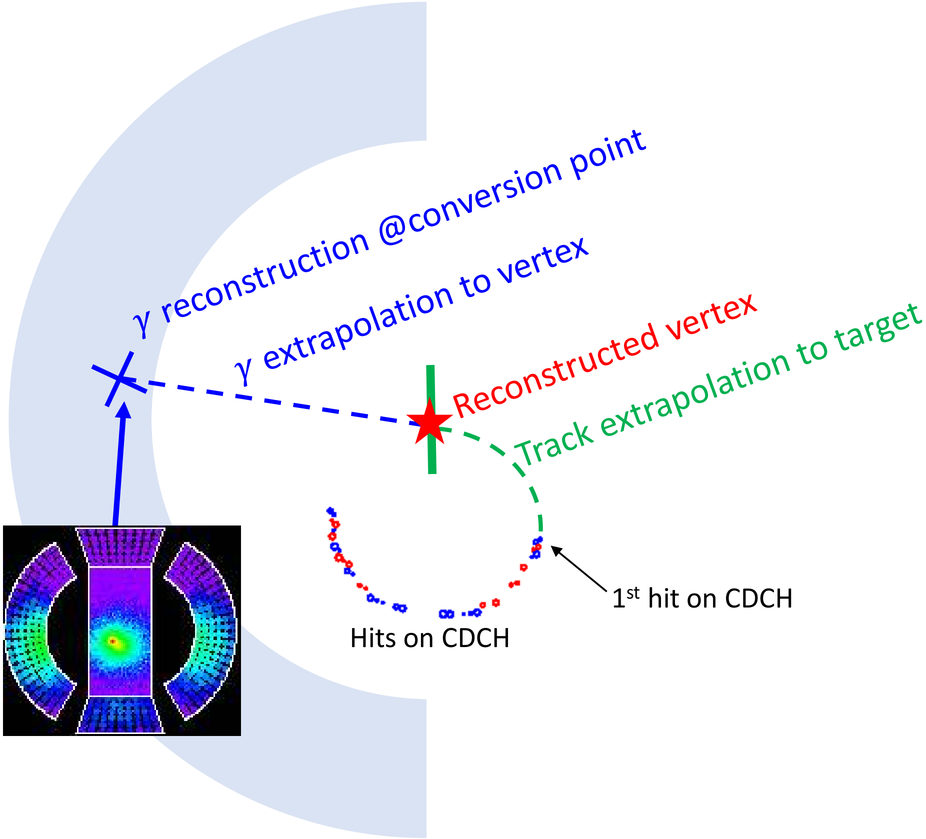

Figure 4.1: An overview of reconstruction procedure.

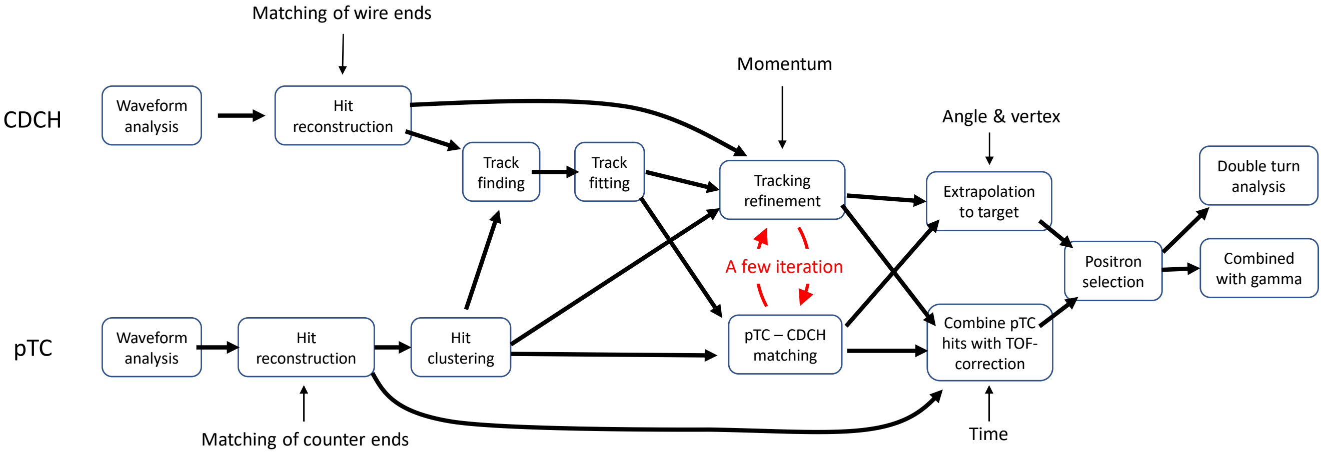

Figure 4.2: Flow chart of positron reconstruction.

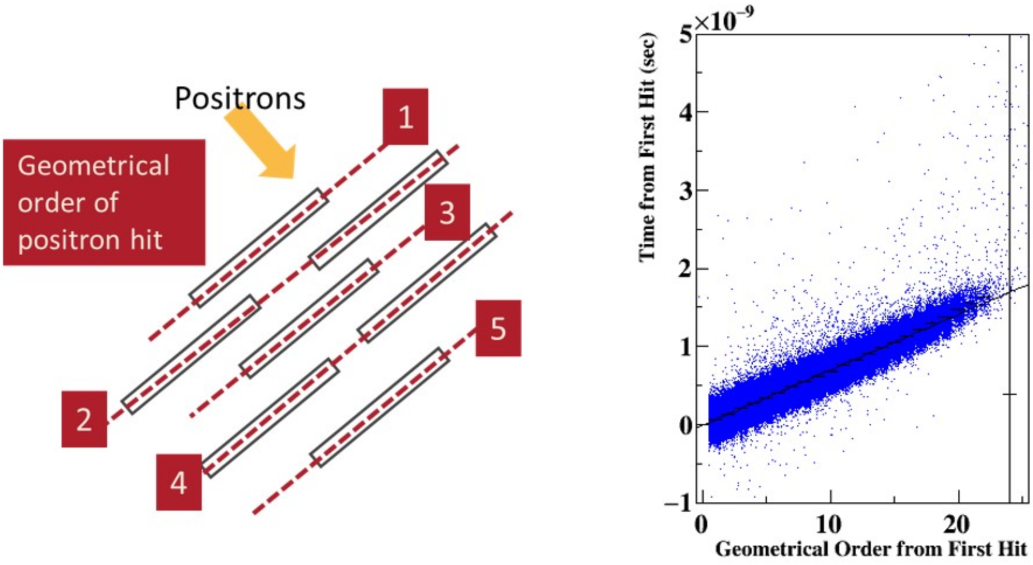

Figure 4.3: Principle of clustering of the pTC hits [42]. (Left) The counters are geometrically ordered according to the depth from the innermost counter. (Right) The correlation between the TOF and the index of the geometrical order.

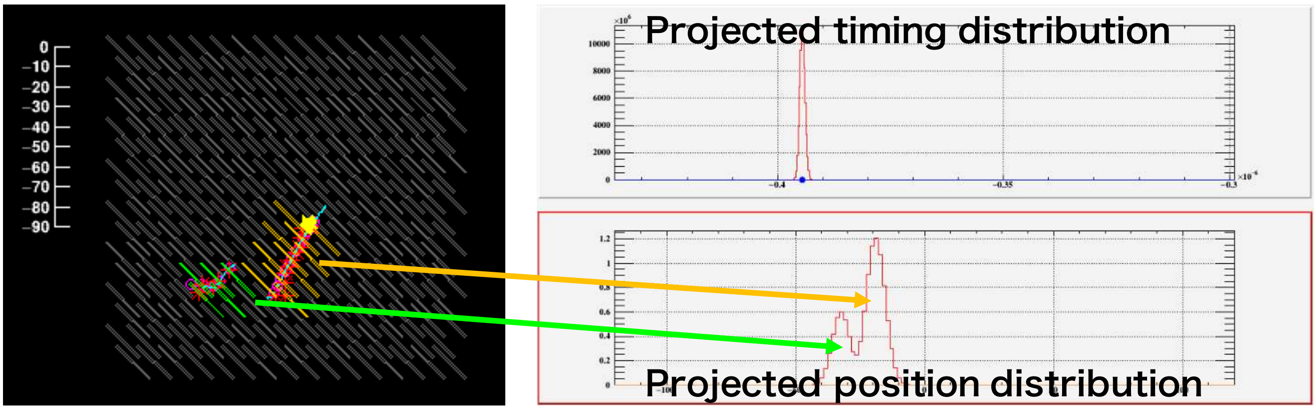

Figure 4.4: Purpose of distance cut shown in an example event display [40]. A small turn in the positron trajectory makes it difficult to separate two clusters only with timing. Instead, the counter position can be used to separate them.

peak structure in the timing is not visible at this stage with the limited TOF precision, the small turn in-between is harmful to the final reconstruction aiming at $50\,\mathrm{ps}$ precision.

4.1.2 Hit reconstruction of CDCH

Two waveform analysis algorithms are adopted to detect hits on the CDCH. One method detects hits by a simple threshold crossing after subtracting coherent noise, which appears on 16 adjacent wires corresponding to one front-end readout electronics. This coherent noise is extracted by averaging waveform on channels without pulses. Another method uses a more elaborate method based on a convolutional neural network, which is trained both to efficiently subtract coherent noise and detect signal pulses. The training samples are from simulated waveform; simulated signal waveform is overlaid with data-driven noise waveform (from data taken without beam).

By combining these two methods, a higher hit efficiency is achieved, but at the cost of a higher fake hit rate. As a result, it is found that the tracking efficiency is higher when two waveform analyses are combined. As a drawback of the increased fake hits, it is also observed that the resolution gets worse when tracks include hits from the second (machine learning-based) waveform analysis. Therefore, the positron track finding (discussed later in Sec.4.1.3) is first performed only with hits from the first method, and then additional track finding is repeated with all hits from both methods to recover missing tracks.

The waveform on both ends of wires for the detected hits is then proceeded to waveform cross-fitting. The waveform cross-fitting compares the waveform between the two ends, which are expected to be identical except for the difference in the amplitude and the timing. The waveform from the two ends, $f(t)$ for one and $g(t)$ for the other, are fitted to minimize

$$\int \Big(f(t) - A \times g(t+\tau) \Big)^2 \mathrm{d}t, \tag{4.3}$$

where two fit parameters A, τ are the amplitude difference parameter and the time difference parameter, respectively.

Once the cross-fit result is given, the hit position along the wire can be estimated by two methods: the charge division method and the time difference method. The charge division method makes use of the difference in the charge of the two ends ($Q_{1,2}$) as

$$z_{\mathrm{Q}} = \frac{G_{\mathrm{diff}} Q_1 - Q_2}{G_{\mathrm{diff}} Q_1 + Q_2} \left(\frac{Z}{\rho} + \frac{L}{2} \right), \tag{4.4}$$

where G_{diff} is the gain difference between the ends, $Z = 360\,\Omega$ is the input impedance of the amplifier, $\rho = 175\,\Omega/\mathrm{m}$ is the wire resistivity, and L is the wire length. The time difference method estimates the hit z position from the signal propagation speed on the wire (v_{eff}) and the time difference,

$$z_{\mathrm{T}} = \frac{t_1 - t_2 - t_{\mathrm{wireends}}}{2} \cdot v_{\mathrm{eff}}, \tag{4.5}$$

where t_{wireends} is the time offset between the two ends. The z position is finally estimated as a weighted sum of the two. The hit time is also reconstructed as the average of the two hits, namely $t_{\mathrm{hit}} = (t_1 + t_2)/2$.

4.1.3 Track finding

The track finding is the first step of the track reconstruction, which starts from the drift distance evaluation of CDCH hits. The drift distance is the track distance of the closest approach to the wire, and thus, is essential as the basis of the track finding. It is estimated from the wire hit time (t_{hit}) and the pTC cluster time (t_{pTC}) with a TOF correction (t_{TOF}) as

$$d_{\mathrm{drift}} = \zeta_{txy}(t_{\mathrm{hit}} - t_{\mathrm{pTC}} + t_{\mathrm{TOF}}), \tag{4.6}$$

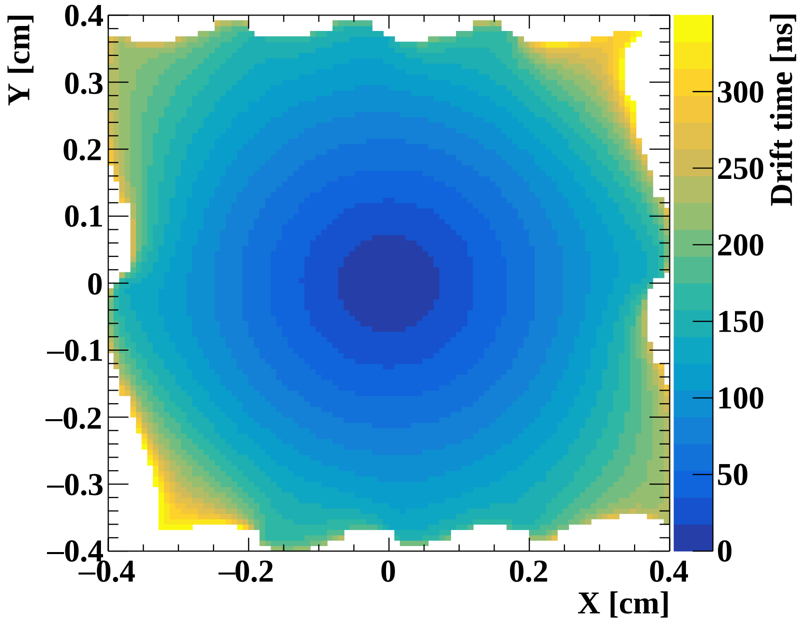

Figure 4.5: Time to drift distance relation in a drift cell.

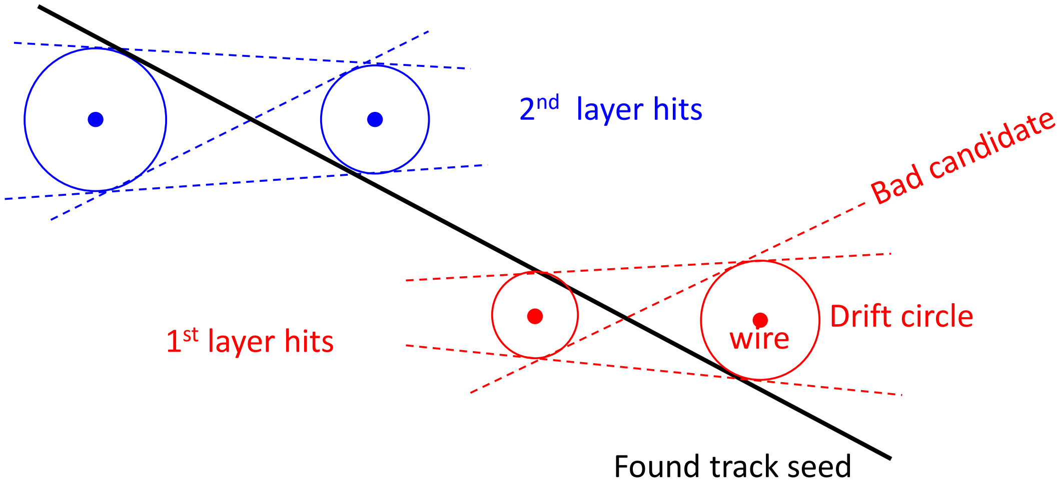

Figure 4.6: The seeding in the track finding. Different patterns of hit connections are tested and the consistent one is picked up as a track candidate.

where $\zeta_{txy}(t)$, shown in Fig.4.5, is the relation between the drift time and the drift distance and it. As we have an ambiguity in t_{TOF} at this stage because of the multiple-turn structure of the tracks, three typically expected values (0.5, 4, and $8\,\mathrm{ns}$) are used in parallel.

In the next step, track seeds are made by connecting four hits on the CDCH (Fig.4.6). Several different left-right patterns are tested here to connect the drift circles, and the consistent ones are selected as seeds. As there are many hits on the CDCH, it is impossible to try all the possible combinations. Therefore, the seeding attempts are made only for hits associated with the t_{pTC}, where the association is judged by the geometrical compatibility between the CDCH hit position and the pTC cluster position.

The seed is then further propagated and hits on different layers are added to form a *candidate track*. During this propagation, the hits belonging to the same *turn* are clustered, where the turn means a track segment from an out-moving point near the $z = 0$ axis to the returning point again getting close to the $z = 0$ axis.

4.1.4 Track fitting and matching with pTC

The candidate tracks are then fitted with the measurement of the drift distance in Eq.(4.6) and the z measurement in Eq.(4.4) and Eq.(4.5). The fitting algorithm uses the Kalman filter technique [88], which has widely been used in track fitting in high-energy physics [89, 90, 91]. In particular, the deterministic annealing filter (DAF), an extension of the Kalman filter, is adopted because of its high performance in a high noise and pileup environment [92, 93]. It removes outlier hits during the fit iteration, and thus, shows a good performance. Its implementation in the track fitting makes use of the GENFIT package [94]. Here, the overall track fitting uncertainty is provided including the effect of scattering inside the material.

The fitted track, which includes only hits on a single turn at this stage, is then merged with the segments belonging to the other turns. Each segment track is propagated in both back and forward directions to evaluate the kinematics at the turn start and end. The propagated kinematics are then compared between different segments, namely by trying to connect the turn-end of one and the turn-begin of the other. When the momentum and the position at the connection point agree within a pre-defined threshold, then two segments are merged into a single track.

The fitted tracks are then matched with a pTC cluster by extrapolating the tracks to each pTC hit. When the extrapolated position on the pTC detector plane is inside the real counter volume within a pre-defined margin, then the track and the pTC hit are matched. This is attempted from the innermost counter and the first match pTC hit is defined as the matched point.

The matching efficiency cannot be well-defined due to a strong dependence on the track quality; namely quality tracks have a large matching efficiency. Still, this is a clear indication that the matching inefficiency in the previous MEG experiment, which was due to the scattering effects, is significantly reduced.

4.1.5 Tracking refinement and missing hit recovery

Once the trajectories are connected from the CDCH region to the pTC region, the measurement on each hit should then be refined. Firstly, the TOF correction in Eq.(4.6) can be improved thanks to the connected trajectory to the matched point. In addition, Fig.4.5 shows that the drift time isochrone is not a complete circle, which can now be taken into account according to the estimated track angle at each CDCH hit. After updating the drift distance measurements, the track is better fitted.

The hits missed in the track-finding stage can also be recovered once we have a well-fitted track. All the possible wire crossing of the fitted trajectory are checked and some missed hits are found as a result. Those hits are added to the track and the track fitting is performed again. The refinement of the drift distance measurement is also iterated after the missing hit recovery.

4.1.6 Vertex and angle reconstruction

The fully reconstructed track is extrapolated to the muon-stopping target, which gives the muon decay vertex and the positron emission angle. The non-flat target shape and the time-varying target position (monitored by the cameras) are considered in this extrapolation. Fig.4.7 shows the impact of the non-flat target shape with bowing up to $1\,\mathrm{mm}$.

4.1.7 Time reconstruction

In the time reconstruction, the TOF to each pTC hit must be estimated when the pTC hit measurements are combined. This is realized by fitting the track in the pTC region starting from the extrapolated kinematics at the matched point. Here, each counter is treated as a two-dimensional detector of w and v, where the w estimation comes from Eq.(4.2) and the v estimation relies on the hit pattern (Fig.4.8). The hit pattern is the hit information on the forward and backward five counters in the ordering shown

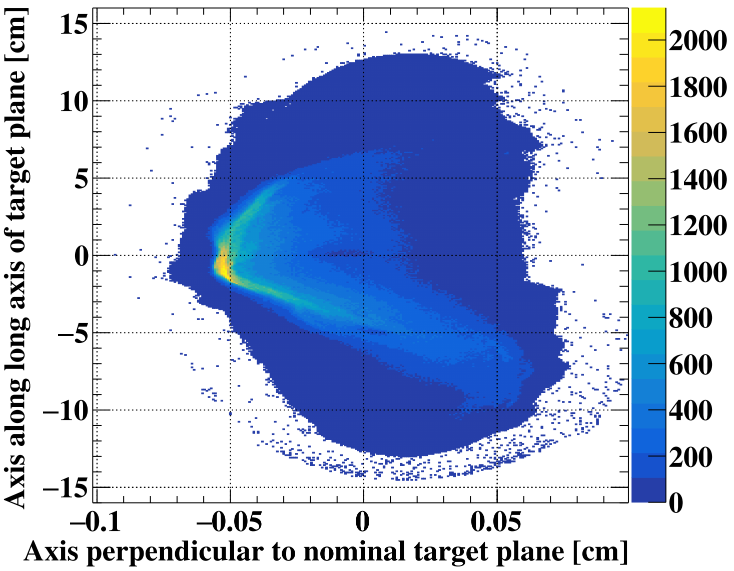

Figure 4.7: The reconstructed position distribution considering the deformed target shape. The horizontal axis of the plot corresponds to the coordinate along the axis perpendicular to the nominal (15°-slanted) target plane. The vertical axis of the plot corresponds to the coordinate along the long axis of the nominal target ellipse. The coordinate along the target short-axis is projected out in this plot.

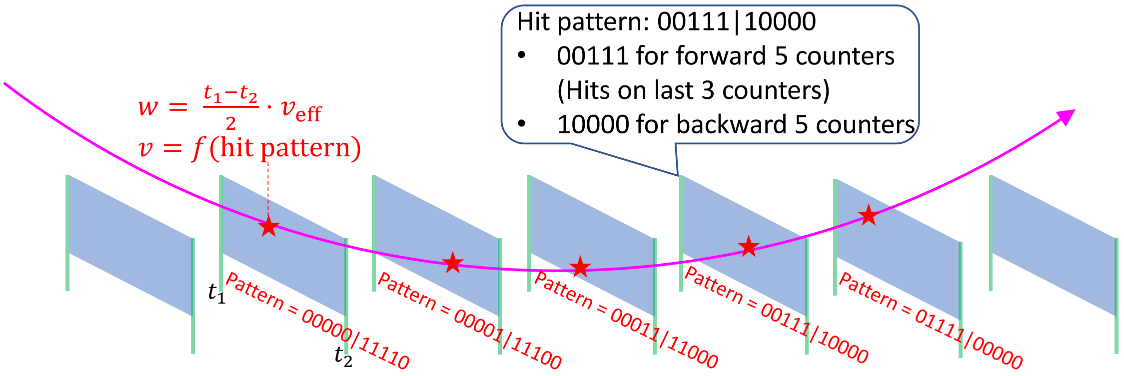

Figure 4.8: The tracking with the pTC hits.

in Fig.4.3, and the v estimation from the pattern is based on detector simulation samples. By fitting the track to v, w measurements again with the DAF algorithm, the TOF from the vertex to each i-th counter (t_{TOF_i}) is now reconstructed. The emission time at the target is then reconstructed by averaging the hit time on each counter with the TOF correction, namely

$$t_{\mathrm{decay}} = \frac{1}{n}\sum_{i=1}^{n}(t_{\mathrm{hit}_i} - t_{\mathrm{TOF}_i}), \tag{4.7}$$

where t_{hit_i} is the measured time on i-th counter.

4.1.8 Track selection

In the reconstruction, multiple tracks are reconstructed from one physical positron, which is called *ghosts*. To make one-to-one correspondence with the physical positron, track grouping is introduced. This grouping is associated with the index of the matched TC cluster, and its quality and purity are studied with MC samples and the results are as follows.

- $\lesssim 1\%$ positrons are lost by judging them as ghosts associated with different positrons, which is caused by highly coincident accidentals and hence the inefficiency depends on the beam rate.
- $\lesssim 0.1\%$ fraction of positrons are split into different ghost groups.

Tracks in the same ghost group are ranked and the highest rank track is selected. This ranking is based on a machine learning output making use of several input parameters: the number of hits used in the track fitting, the χ^2 value of the track fitting, the covariance matrix, and the track propagation length from the CDCH to the stopping target and the matched pTC counter. This is trained with Michel positron data to classify tracks into good and bad ones, where the training data samples are identified as good (bad) if the reconstructed momentum is larger (smaller) than $55\,\mathrm{MeV}$. This sample choice exploits the $52.8\,\mathrm{MeV}$ upper bound of the Michel positron spectrum; namely the "bad"-labelled training samples have E_e error of at least $2.2\,\mathrm{MeV}$.

After the best ghost selection, a quality cut is applied again making use of the machine learning output. This reduces low-quality background tracks, which account for $7\,\%$ of all, without introducing additional inefficiency for the signal positrons (evaluated to be $< 1\,\%$). This behavior is caused by the event selection for the physics analysis, where only samples with $52.2\,\mathrm{MeV} < E_e < 53.5\,\mathrm{MeV}$ and $|\theta, \phi_{e\gamma}| < 40\,\mathrm{mrad}$ are used (also see Sec.6.2). These kinematical cuts, requiring the error to be small, cannot be satisfied by low-quality signal positrons even without the above quality cut. Therefore, this quality cut does not cause any additional inefficiency of the signal. This mechanism is not the case for background positrons because the above cuts are not associated with the measurement error at all.

4.1.9 Dedicated double turn reconstruction

About $10\,\%$ of the tracks make two turns during their propagation from the target to the pTC. In addition to the full track reconstruction for the physics analysis, such tracks are also subject to *double-turn analysis*, which is useful for evaluating the position and angle resolution.

In the double-turn analysis, the full track is separated into the first turn track segment and the second one, and each is separately fitted (Fig.4.9). The first (second) turn is then extrapolated in the forward (backward) direction to a middle point, where a plane identical to the target is used. This choice of the middle point is to study the correlation between the errors, such as $\delta\phi_e$ vs δE_e, which is important in the physics analysis, as will be discussed later in Sec.6.7.4. The double-turn analysis becomes sensitive to the correlations in this way because the error correlation is geometrically produced by the track propagation to the muon stopping target plane.

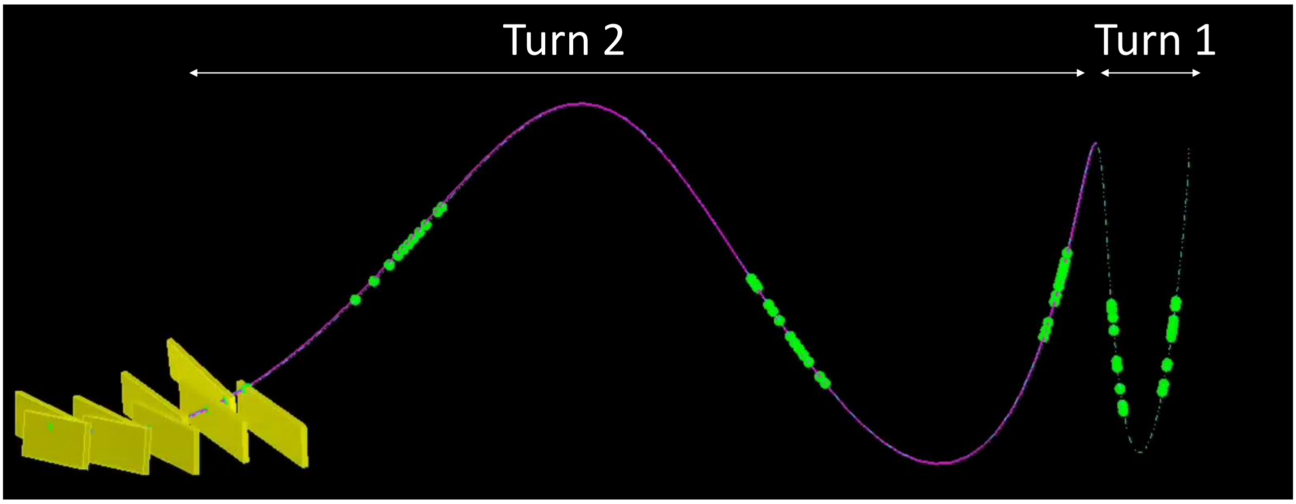

Figure 4.9: An example double-turn track. The first turn track (the dashed part) and the second turn track (the solid part) are fitted independently and compared at the border point. The green markers are hits used in the track fitting.

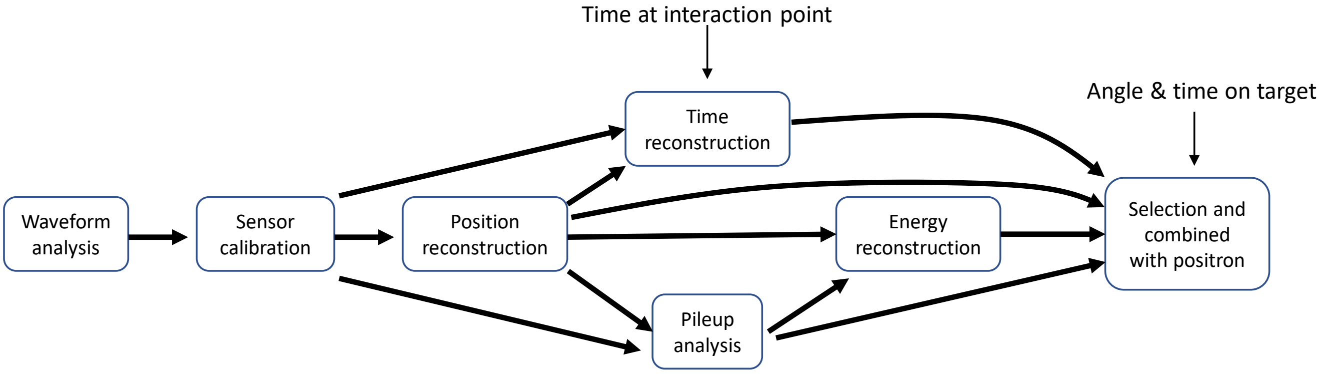

Figure 4.10: Flow chart of gamma-ray reconstruction.

4.2 Gamma-ray reconstruction

The overview of the gamma-ray reconstruction is shown in Fig.4.10.

4.2.1 Waveform analysis and sensor calibration

The first step of gamma-ray reconstruction is to evaluate the distribution of scintillation light and its arrival time measured by each scintillation photon sensor. The waveform analysis estimates the pulse timing (t_{pulse}) with the constant fraction method and the pulse charge (Q) with pulse integration over $150\,\text{ns}$.

The pulse charge is then converted into the light distribution according to calibrated sensor parameters. The number of detected photoelectrons is evaluated from the sensor gain (G) and the *excess charge factor* (F_{ECF}) defined in [95, 96],

$$N_{\text{phe}} = \frac{Q}{G \times F_{\text{ECF}}}. \tag{4.8}$$

The *excess charge factor* is calibrated for the MPPCs to correct the contribution of the correlated noise, cross-talk, and after-pulse. The number of scintillation photons (N_{pho}) is then evaluated by correcting N_{phe} with the quantum efficiency (QE) of the PMTs or the photon detection efficiency (PDE) of the MPPCs,

$$N_{\text{pho}} = \frac{N_{\text{phe}}}{\epsilon_{\text{QE(PDE)}}}. \tag{4.9}$$

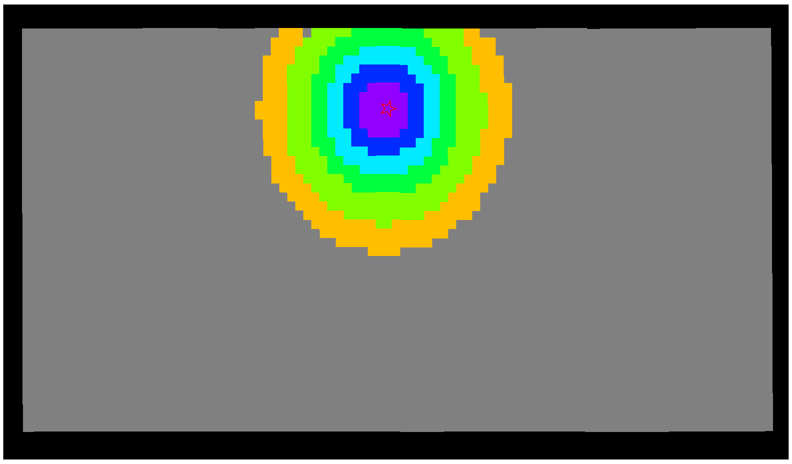

Figure 4.11: The MPPCs used for the position reconstruction in an example event [48]. The MPPCs in the circles (each color indicates N_{pho}) are used for the position fitting. The red cross marker at the center is the result of the pre-fitting based on the uv-projected light distribution, which is used to initiate the main fitting.

The pulse timing is also converted to the scintillation light arrival time at the sensor (t_{pm}) with two calibration parameters, the time walk parameter (t_{walk}) and the time offset parameter (t_{offset}) of each sensor,

$$t_{\text{pm}} = t_{\text{pulse}} - t_{\text{walk}} - t_{\text{offset}}. \tag{4.10}$$

Though the constant fraction method in the waveform analysis is a robust algorithm against the time walk effect, further correction is applied here to correct observed remaining dependences on N_{phe}.

4.2.2 Position reconstruction

The position of the gamma-ray interaction point in the liquid xenon is reconstructed from the light distribution measured by the MPPCs on the inner face. It starts from a pre-fitting based on the uv-projected N_{pho} distribution on the inner face. The estimated parameter in this step is then used to initiate the subsequent main fitting step, which minimizes

$$\chi^2_{\text{pos}}(\vec{x}) = \sum_{i \in \text{region}} \frac{\left(N_{\text{pho}_i} - C \times \Omega_i(\vec{x})\right)^2}{\sigma^2_{\text{pho}_i}}. \tag{4.11}$$

Here, C is the scale of the light distribution, $\Omega_i(\vec{x})$ is the solid angle of the i-th sensor seen from the position $\vec{x}$, and $\sigma_{\text{pho}_i} = N_{\text{pho}_i}/\sqrt{N_{\text{phe}_i}}$ is the uncertainty of N_{pho_i} assuming the Poisson fluctuation.

The set of MPPCs used in Eq.(4.11) is dynamically determined by the result of the pre-fitting with uv-projected light distribution. This is because the peak width of the light distribution gets larger with an increasing w, and the set of the used MPPCs needs to be optimized. The dynamical decision uses the distance between the MPPC position and the uv projected pre-fitted result (Fig.4.11), where the radius varies from $3\,\text{cm}$ (shallow events) to $15\,\text{cm}$ (deep events).

Though the electromagnetic shower has a finite size, the minimization in Eq.(4.11) corresponds to a model where the scintillation light comes from a point source. This incomplete modeling biases the fitted position in the direction of the shower development. This is solved by combining the following two corrections. The first one corrects the bias from the detector geometry; events with large $|u|$ tend to have a large incident angle to the inner face (Fig.4.12), which results in a position-dependent bias. This effect is evaluated on the detector simulations as a function of the position, which is thus used for its correction. The second one corrects the bias caused by the event-by-event fluctuation of the shower

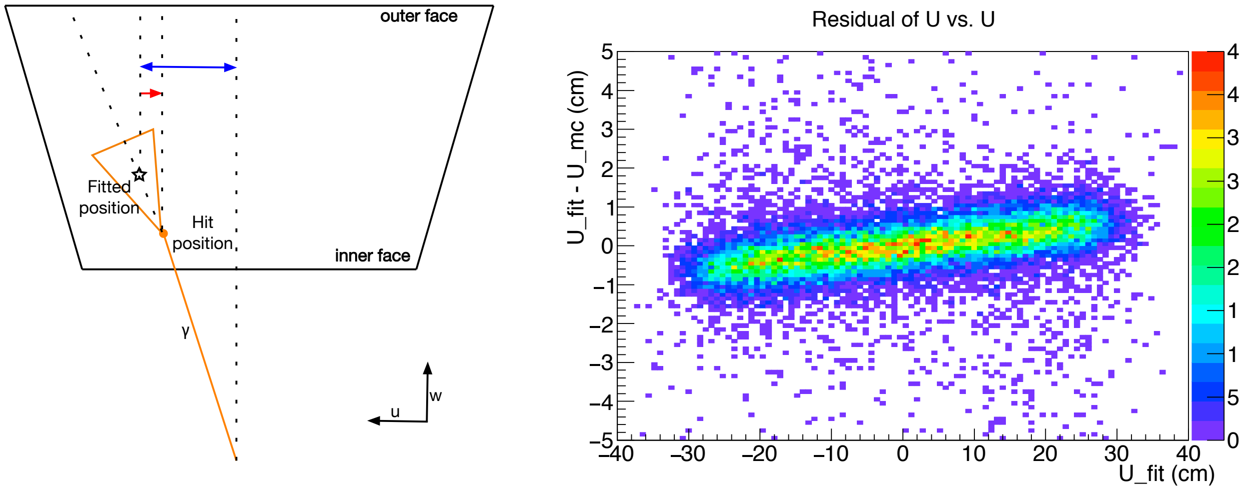

Figure 4.12: The global correction of the geometrical correlation between the shower incident position and the shower direction [45].

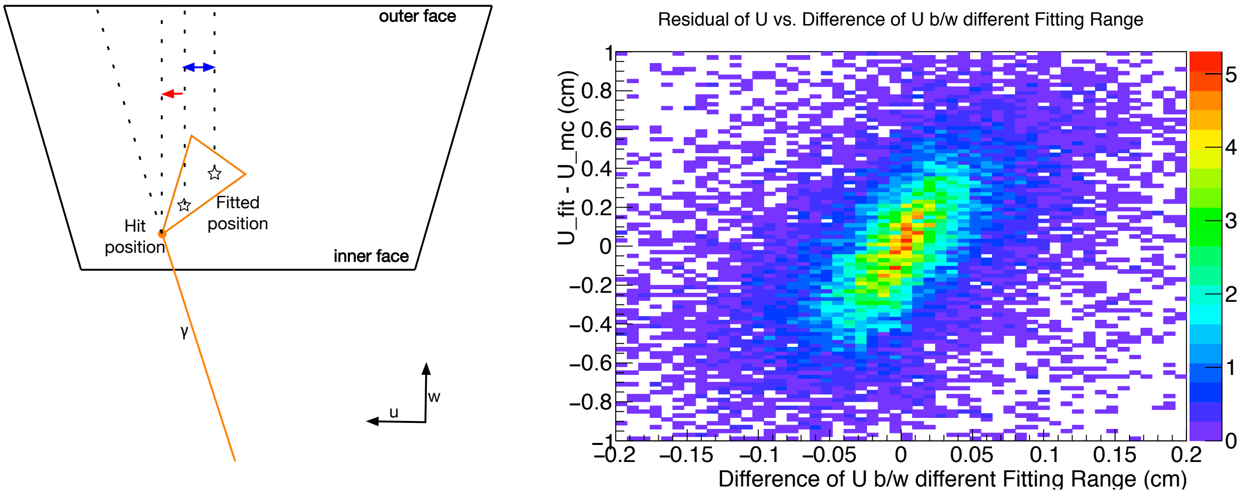

Figure 4.13: The correction of the event-by-event fluctuation of the shower direction [45].

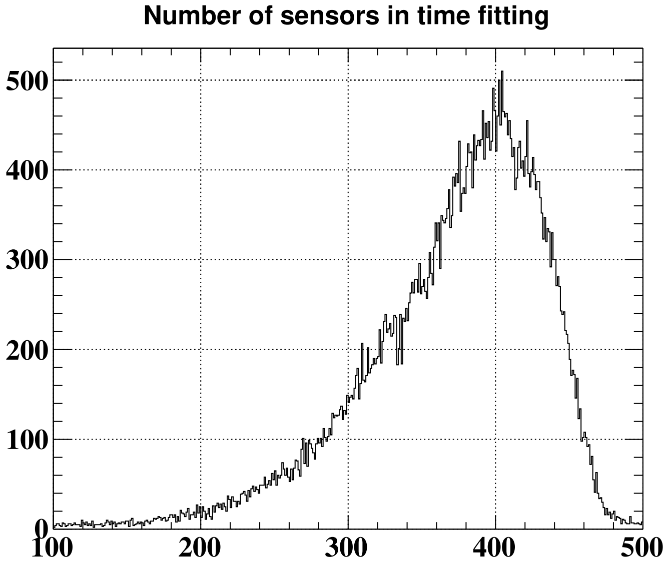

Figure 4.14: The number of sensors used in the time fitting.

direction (Fig.4.13). As this bias has a larger impact with a larger fit range, it can be estimated by comparing the main fit result with those from different ranges. This correction is also based on the detector simulations.

4.2.3 Time reconstruction

The gamma-ray conversion time in the liquid xenon scintillator is reconstructed from the measured arrival time of the scintillation light by both the MPPCs and PMTs. The best-fit time (t_{fit}) is obtained by minimizing

$$\chi^2_{\mathrm{time}}(t_{\mathrm{fit}}) = \sum_{N_{\mathrm{phe}_i} > N_{\mathrm{th}}} \frac{(t_{\mathrm{pm}_i} - t_{\mathrm{prop}_i} - t_{\mathrm{fit}})^2}{\sigma_i^2}, \tag{4.12}$$

where t_{pm_i} comes from Eq.(4.10), t_{prop_i} is the propagation time for scintillation light between the interaction position and the i-th sensor, and σ_i is the estimated time resolution there. The propagation time, t_{prop}, is estimated by dividing the distance from the conversion point to the sensor by the effective velocity of scintillation light propagation in liquid xenon.

The fitting is performed for sensors with N_{phe_i} larger than 50. In order to have robustness against the pileup gamma-rays, the fitting is iterated until it converges up to three times with outlier removal. The number of sensors finally used in the fitting is typically a few hundred for $\sim 52.8\,\mathrm{MeV}$ gamma-rays as shown in Fig.4.14.

As will be described later in Sec.5.4.3, calibration studies found that t_{fit} here shows position dependent biases. This is corrected to obtain the final estimation (t_{LXe}) as

$$t_{\mathrm{LXe}} = t_{\mathrm{fit}} - F_t(u, v, w). \tag{4.13}$$

4.2.4 Pileup analysis

There are two types of gamma-ray pileup events: *off-timing pileup* and *on-timing pileup*. The off-timing pileups come from accidental gamma-rays from different parent muons, and the on-timing pileup is from positron annihilation in flight (AIF) where both the created gamma-rays enter the LXe. The impact of pileup is limited for the position and time reconstruction thanks to the use of limited sensors in the fitting. The energy reconstruction, on the other hand, does receive a strong effect, and it results in a tail in the background energy distribution around $52.8\,\mathrm{MeV}$.

The purpose of the pileup analysis is firstly to identify the off-timing and on-timing pileups. In the off-timing case, it aims to remove the energy deposit from the pileup to have a clean reconstruction only for the main gamma-ray. When an event is identified to be the on-timing, on the other hand, it is discarded in the analysis because it is not likely from a signal event. The analysis is composed of two parts, *pileup clustering* and *pileup unfolding*.

The pileup clustering performs the pileup search in the spatial distribution of the scintillation light on the inner and the outer faces. When local maxima are found with the peak N_{pho} larger than a pre-defined threshold, they are identified as pileups. The on-timing pileup events can be identified with this algorithm.

The pileup unfolding to search for the off-timing pileups firstly makes the waveform sums for the MPPCs and the PMTs with channel-by-channel waveform normalization and time shifting as follows. In the normalization, the i-th channel waveform is scaled with correction factors to have an integral value of

$$B_i \times F_{\mathrm{face}}(u, v) \times N_{\mathrm{pho}_i}. \tag{4.14}$$

Here, B_i is a correction factor of the light collection efficiency, which considers the insensitive area around each sensor including the dead channels. $F_{\mathrm{face}}(u, v)$ is a *face factor*, which is introduced to improve the uniformity (see Sec.5.3.3 for detail). After the waveform normalization, the waveform is also shifted in the time coordinate to correct the channel-by-channel time offset and the scintillation propagation time.

The time differential of the summed waveform is searched for off-timing pileup pulses with an optimized threshold. By matching the pileups found in the waveform search with those found in the spatial search, a full list of candidate pileups becomes available.

The sum waveforms are then fitted with a sum of multiple templates,

$$g(t; \vec{\tau}, \vec{A}) = \sum_{i=1}^{N_{\mathrm{pulse}}} A_i \cdot h(t - \tau_i), \tag{4.15}$$

where τ_i, A_i are the timing and the amplitude of the overlaid waveforms and $h(t)$ is the waveform template, independently made for MPPCs and PMTs, describing a pulse that comes at $t = 0$. The vectors, $\vec{\tau}$ and $\vec{A}$, runs over the number of overlaid waveforms, N_{pulse}. The waveform fitting minimizes

$$\chi^2_{\mathrm{PL}}(\vec{\tau}, \vec{A}) = \int \frac{\left(f(t) - g(t; \vec{\tau}, \vec{A})\right)^2}{\sigma_g^2(t)} \mathrm{d}t, \tag{4.16}$$

where $f(t)$ is the observed sum of the waveform. The denominator in the integra, $\sigma_g(t)$, is the amplitude uncertainty of $g(t; \vec{\tau}, \vec{A})$, summing up the uncertainty of the template waveform according to Eq.(4.15).

The initial estimation of N_{pulse} in this fitting is based on the list of candidate pileup pulses. Here, additional discrepancies between $f(t)$ and $g(t)$ are sometimes found as a result of the fitting, which is identified according to the integral of $f(t) - g(t)$. In such cases, N_{pulse} is incremented and the fitting is iterated until it converges or it is iterated three times. An example of the template fitting is shown in Fig.4.15.

4.2.5 Energy reconstruction

After the waveform fitting in the pileup analysis, the amplitude of the main waveform, A_i, can then be interpreted as the number of original scintillation photons with the waveform normalization in Eq.(4.14). As the waveform sums are made separately for MPPCs and PMTs, we now have N_{MPPC} and N_{PMT}. The energy is then reconstructed as

$$E_\gamma = S_E(u, v, w) \times N_{\mathrm{sum}}, \tag{4.17}$$

where $S_E(u, v, w)$ is the position and period dependent energy scale and $N_{\mathrm{sum}} = R_{\mathrm{MPPC}} \cdot N_{\mathrm{MPPC}} + N_{\mathrm{PMT}}$ with R_{MPPC} correcting the time variation of $N_{\mathrm{MPPC}}/N_{\mathrm{PMT}}$.

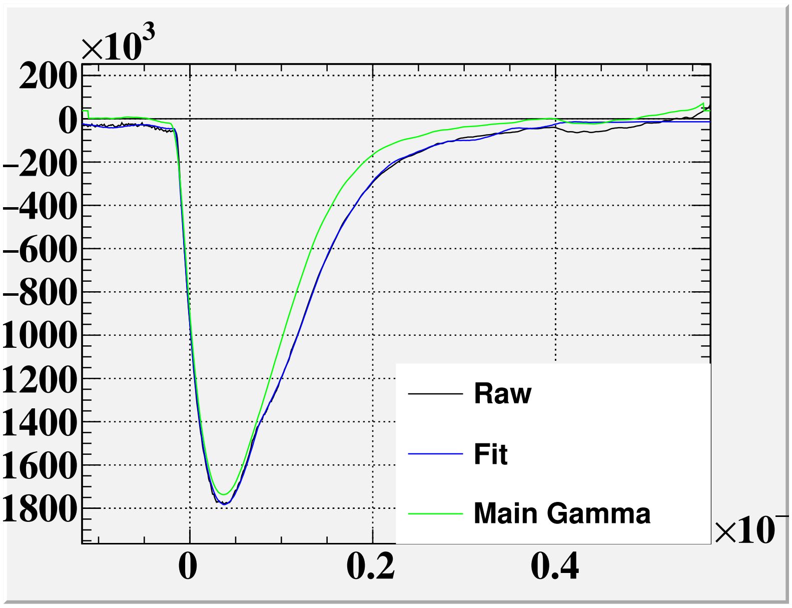

Figure 4.15: Fitted waveform in the pile-up unfolding algorithm [48].

4.2.6 Gamma-ray selection

The gamma-ray selection applies three cuts: the pileup rejection, the bad time fitting rejection, and the cosmic rejection. The first one selects events only if the event is judged not to have pileup gamma-rays or if it is judged to have only off-timing pileups that are successfully unfolded. Events are dropped when identified in the pileup clustering, but not unfolded in the waveform fitting, which are interpreted as on-timing pileups. Events are also dropped when the waveform fitting is bad in the unfolding (large χ^2_{PL} in Eq.(4.16)). The time-fitting cut checks the convergence of the time fitting during the iteration, and ill-converged events are dropped from the analysis, whose fraction is $< 1\,\%$. The convergence is judged by $\chi^2_{\mathrm{time}}(t_{\mathrm{fit}})$ value in Eq.(4.12), where the threshold is optimized to ensure a good time resolution according to a data-driven resolution evaluation with the $\pi^0 \rightarrow \gamma\gamma$ events. The cosmic rejection applies cuts on two dimensional w_γ vs $N_{\mathrm{MPPC}}/N_{\mathrm{PMT}}$ plane (Fig.4.16), which drops $\sim 50\,\%$ of cosmic-ray events while suppressing the signal inefficiency at $0.4\,\%$.

4.3 RDC reconstruction

The overview of the RDC reconstruction is shown in Fig.4.17.

4.3.1 Reconstruction

The RDC reconstruction is initiated by the waveform analysis for the plastic counters, which detects pulses by the threshold crossing. The pulse time of the plastic counter is then input to the subsequent LYSO waveform analysis. This procedure is beneficial when searching for associated LYSO pulses, integrating its charge for energy measurement, and then clustering the hits from the same positron.

There exist two inefficiencies of LYSO pulse finding in association with the plastic pulses. The first inefficiency is caused by the positrons leaving hits only to the plastic counter. The second comes from the reconstruction deadtime with pileups, which is the inefficiency for LYSO pulses immediately followed by a pileup. The deadtime depends on the amplitude of the pileup, which can be up to $30\,\mathrm{ns}$ in the worst case. If the LYSO pulse finding is successful, both the timing and the energy are reconstructed, while only the timing is reconstructed otherwise.

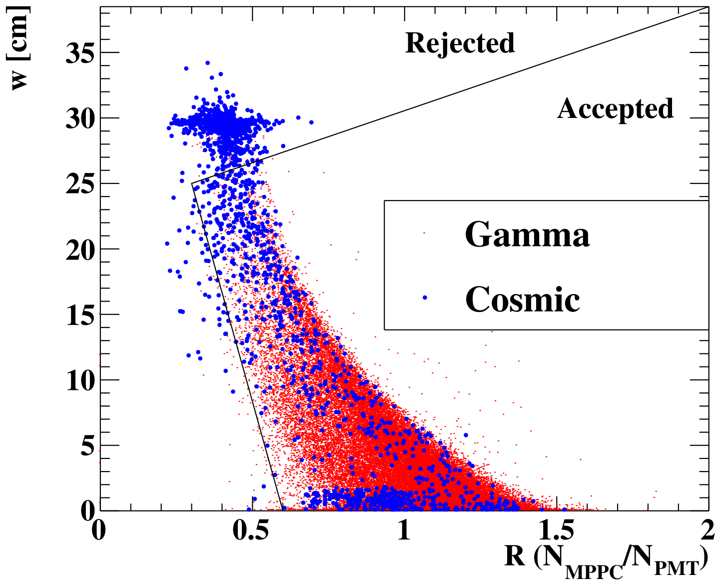

Figure 4.16: The distribution of gamma-ray data and cosmic-ray data on w_γ vs $N_{\mathrm{MPPC}}/N_{\mathrm{PMT}}$ plane. The black lines define the thresholds of the cosmic-ray rejection cut [48].

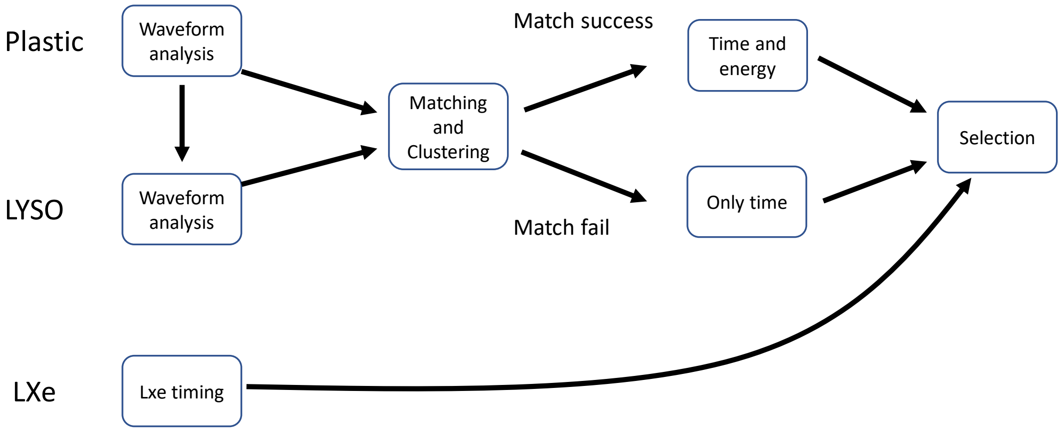

Figure 4.17: Flow chart of RDC reconstruction.

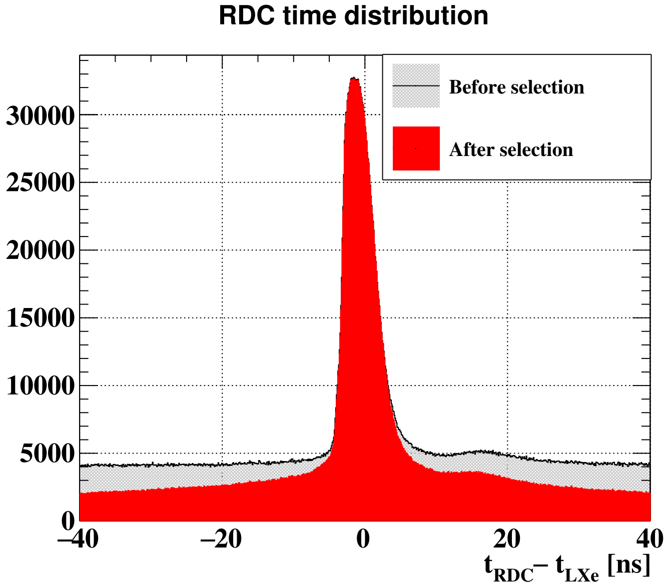

Figure 4.18: The RDC detection timing distribution before and after the selection with the offset from the LXe time. The offset peak position is intentionally introduced to maximize the RMD tagging efficiency in the asymmetric hit time distribution.

4.3.2 Selection with LXe time

Multiple hits are usually observed with the RDC, among which only one should be selected for the physics analysis. The selection is based only on the timing; the hit closest to the LXe time, t_{LXe}, is selected as shown in Fig.4.18.

4.4 Reconstruction of combined kinematics

4.4.1 Reconstruction of combined kinematics

The kinematics of the gamma-ray at the target is finally reconstructed when pairs are made with the reconstructed positrons. The gamma-ray angle is reconstructed as the direction of the reconstructed conversion position in the liquid xenon seen from the reconstructed vertex position. The TOF of the gamma-ray from the target to the conversion point is also estimated from the distance between them. The gamma-ray emission time is reconstructed accordlingly as $t_\gamma = t_{\mathrm{LXe}} - t_{\gamma-\mathrm{TOF}}$. The parameters for the combined kinematics are defined as follows,

$$\Theta_{e\gamma} = \text{opening angle between positron and gamma-ray}, \tag{4.18}$$
$$\theta_{e\gamma} = (\pi - \theta_e) - \theta_\gamma, \tag{4.19}$$
$$\phi_{e\gamma} = (\pi + \phi_e) - \phi_\gamma, \tag{4.20}$$
$$t_{e\gamma} = t_\gamma - t_e. \tag{4.21}$$

4.4.2 Fiducial volume of the detector

The fiducial volume of the LXe detector is defined such that reconstructed gamma-rays are accepted when the following conditions are satisfied.

$$\begin{aligned} |u_\gamma| &< 23.9\,\mathrm{cm} \\ |v_\gamma| &< 67.9\,\mathrm{cm} \\ 0 < w_\gamma &< 42\,\mathrm{cm}. \end{aligned} \tag{4.22}$$

On the other hand, the positron acceptance is defined on an angle basis; reconstructed positrons are accepted when the opposite of the positron emission direction points to the LXe fiducial volume.

4.4.3 Pair selection

Multiple positrons are reconstructed in general, and the combined kinematics is reconstructed for all the possible positron and gamma pairs. However, only a single pair must be finally selected so as not to bias the $\mu \rightarrow e\gamma$ search, which demands that the data samples be independent of each other. Therefore, single-pair selection is introduced at the end of the selection. Here, the selection criteria are optimized to keep the signal efficiency as high as possible as well as to avoid possible biases in the physics analysis.

The single pair selection is applied in the following steps;

1. Pre-selection of pairs with a wide window just to reduce the number of candidates
2. Selection of one pair from the pre-selected pairs

In the first step, cuts are applied on the angle, the positron momentum, and the time difference.

- $|t_{e\gamma}| < 3\,\mathrm{ns}$
- $45\,\mathrm{MeV} < E_e < 56\,\mathrm{MeV}$
- $\cos\Theta_{e\gamma} < -0.95$

After these cuts, $0.24\,\%$ of events have multiple candidate pairs. In the second step, the pair that has the largest opening angle ($\Theta_{e\gamma}$) is selected, which keeps the signal inefficiency as small as $\mathcal{O}(0.01\,\%)$.

Chapter 5

Calibration and performance evaluation

5.1 DRS calibration

5.1.1 Time calibration

The sampling interval between the DRS capacitor cells is calibrated beforehand by inputting sine wave signals. This calibration is applied to the waveform data used in the offline reconstruction. In addition, to correct event-by-event fluctuation of the time synchronization between different DRS chips, the $80\,\mathrm{MHz}$ master clock from the DCB (see Sec.2.6.1) is input to a dedicated DRS channel. The clock waveform is fitted with a sine function to evaluate the leading-edge point (Fig.5.1) closest to $-590\,\mathrm{ns}$, which corresponds to the trigger latency. The difference in the fitted zero-crossing time in different DRS chips is then used for the time alignment.

5.1.2 Voltage calibration

The voltage of each DRS cell is calibrated by measuring the response for different input DC voltages provided internally by the DRS module. Though this calibration is applied when the waveform data is written out, some additional calibrations are necessary offline. Fig.5.2 shows a comparison of the summed MPPC waveforms of the LXe detector before and after the offline calibration, where the noise situation significantly improves. Data samples for the offline voltage calibration are collected in the absence of the muon beam with a random-timing trigger. Four different sources are responsible for the remaining offline voltage miscalibration, and these are all calibrated with this random-trigger data.

The first calibration is further corrections of residual voltage offset of each DRS cell, which causes

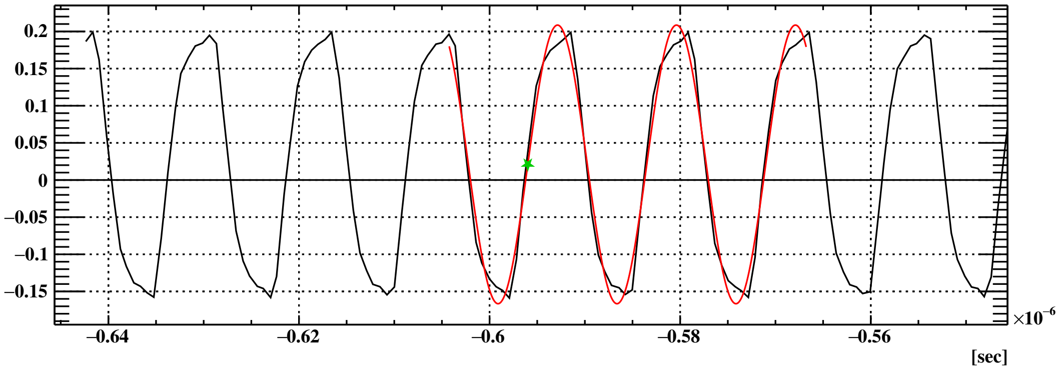

Figure 5.1: Display of clock analysis, which is used to align the DRS time offset. The red line is the fitted waveform and the green marker indicates the fitted leading-edge point of the sine wave. The green marker has $20\,\mathrm{mV}$ offset because of the voltage offset in the sine wave.

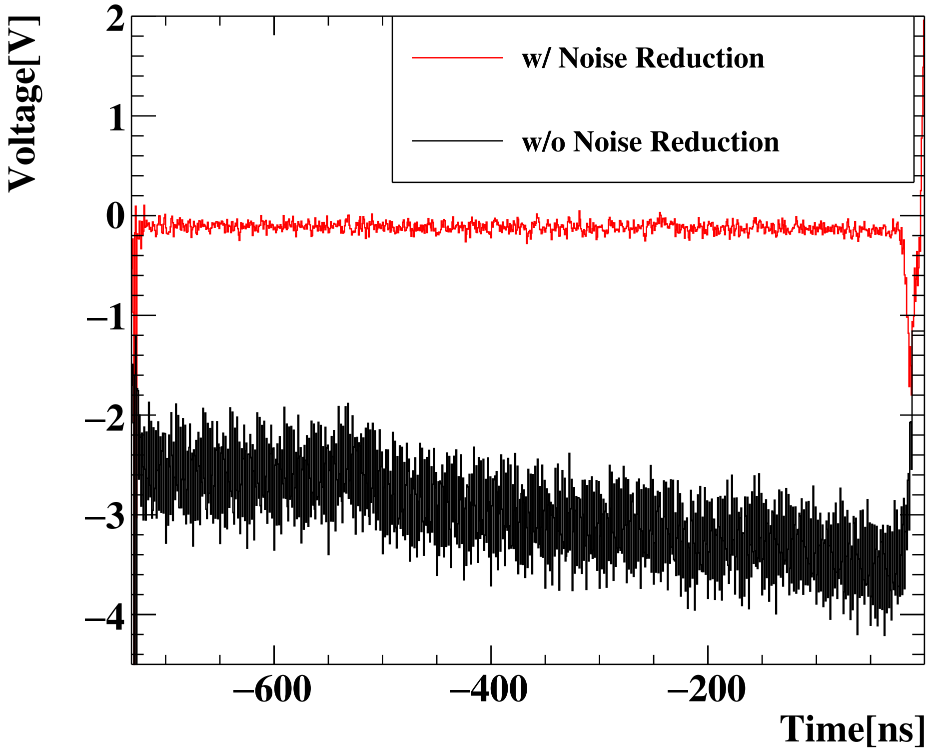

Figure 5.2: Effect of offline DRS voltage calibration for the summed waveform of the LXe detector channels [48]. The noisy black waveform before the calibration is corrected to get the red waveform. The noisy regions in the edges of the time window (caused by fluctuations of edge effects) are not included in the waveform analysis and thus are not harmful.

low-frequency noise. This comes from the incompleteness of the online voltage calibration. This is calibrated by averaging the voltage at each cell with the calibration samples.

The second calibration is a subtraction of high-frequency electronics noise, which is harmful to the time resolution. This noise comes coherently with the $80\,\mathrm{MHz}$ master clock signal of Fig.5.1 and can be reduced by subtracting typical noise templates. The templates are obtained by accumulating the waveform with a proper time alignment.

The third calibration is a correction of temperature-dependent noise, which originates from a leakage current of the DRS cells. Due to the accumulation of leakage current during the voltage hold time, this results in a slope in the recorded voltage. Furthermore, this slope value is also dependent on the temperature of the DRS chips. This is corrected with samples collected at different temperatures.

The final calibration is a correction of noise correlated with the first DRS cell of the waveform, whose origin has not been identified. This noise is found to have a large impact on the LXe energy reconstruction with the resolution contribution being $\mathcal{O}(\mathrm{MeV})$. This is calibrated by accumulating the waveform with a grouping on the first DRS cell index.

5.2 LXe sensor alignment and position resolution

5.2.1 MPPC alignment

Optical scan at room temperature

During the MPPCs installation into the detector, the surface of the MPPCs was scanned by a three-dimensional laser scanner (FARO Edge ScanArm [97]) as shown in Fig.5.3. The MPPC positions are reconstructed by fitting the scanned points with a model describing the package structure of four chips. The quality of the fitting was enough for 426 MPPCs, whereas the other low-quality data points (those

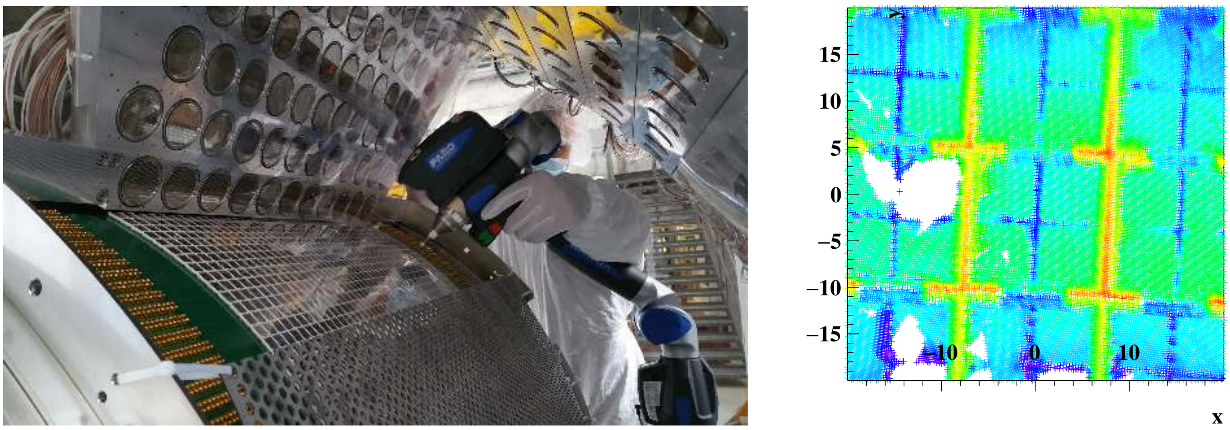

Figure 5.3: (Left) The surface of the MPPCs is scanned with the laser scanner [48]. (Right) An example of the measured height (perpendicular to the surface) distribution. The MPPC package structure (hosting four chips) is visible.

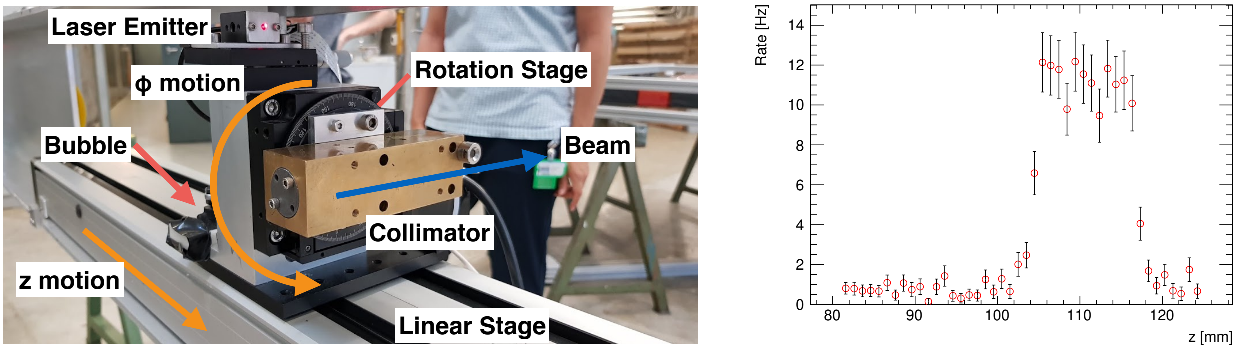

Figure 5.4: (Left) Gamma-ray source with a collimator used for the MPPC alignment [48]. (Right) A position scan of the event rate at an MPPC.

far from the reach of the scanner's support arm) come from diffused reflections of the laser. To have positions of unfitted MPPCs, the well-fitted ones are interpolated taking into account the PCB structure.

Alignment at liquid xenon temperature with gamma-rays

As the MPPC positions are changed by the thermal contraction, the optical scan at room temperature is complemented by a measurement at the liquid xenon temperature. In this measurement, collimated $120\,\mathrm{keV}$ gamma-rays from $^{57}\mathrm{Co}$ were injected into the liquid xenon from the outside of the detector cryostat. The shallow gamma-ray conversion within $3\,\mathrm{mm}$ is desirable for the alignment; only a few MPPCs located directly below the conversion point are illuminated with the scintillation light. The gamma-rays were collimated to have a spot size of $1.5 \times 40\,\mathrm{mm}$, whose direction was changed by a moving stage to cover the whole detector area (Fig.5.4). The distribution of the measured gamma-ray rate as a function of z in Fig.5.4 is fitted with a flat top and Gaussian tails at both ends. Here, the MPPC position is estimated to be at the center of the fit function with a $100\,\mathrm{\mu m}$ precision.

In addition to the main alignment measurement, validation measurements were also performed using 16 lead strips ($1 \times 1 \times 25\,\mathrm{mm}$) attached to the entrance face of the LXe detector (Fig.5.5). In the distribution of the gamma-ray conversion position, 16 defects are expected just behind the strips, which is the principle of this validation measurement. The consistencies between the reconstructed position of the lead strips and the optical survey were $\sigma_z = 0.43\,\mathrm{mm}$ and $\sigma_\phi = 0.68\,\mathrm{mrad}$.

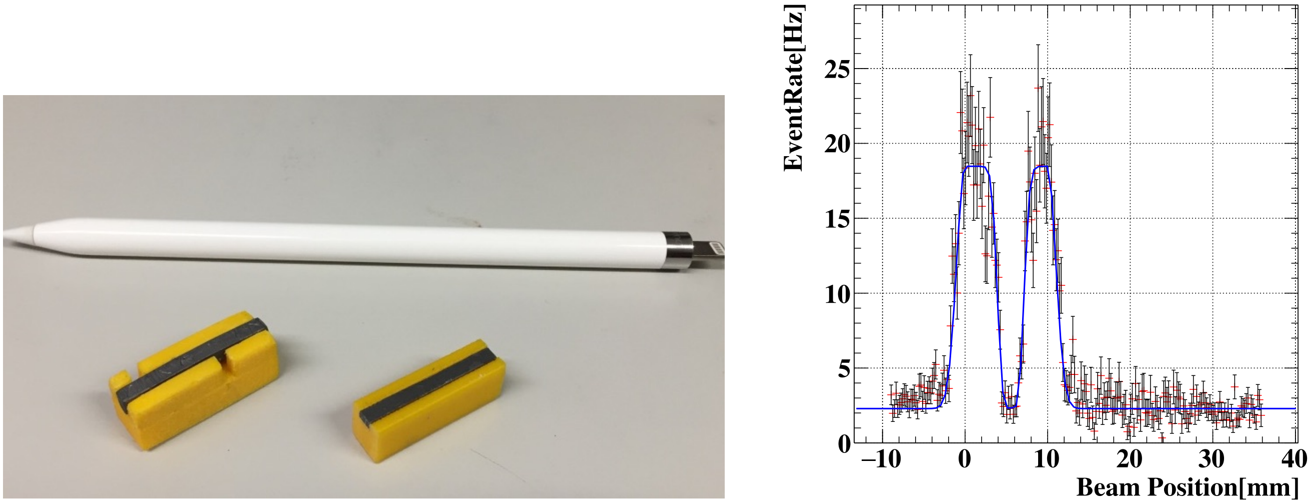

Figure 5.5: (Left) Lead strips used in the validation measurement [48]. (Right) A position scan of the event rate around a lead strip. The decreased rate around $5\,\mathrm{mm}$ corresponds to the lead position.

Combination of two alignment methods

The two methods, the optical scan and the collimated gamma-rays, are finally combined to have a full three-dimensional alignment. The optical scan can give a three-dimensional alignment, which is likely to change due to the thermal contraction. On the other hand, the collimated gamma-ray measurements were performed at the liquid xenon temperature but can provide information only in the uv plane. A combination of the above two methods complements each other accordingly.

The position at the liquid xenon temperature is assumed to be related to the position at the room temperature as,

$$\vec{x}_{\mathrm{fit}} = (1-a)R_{\mathrm{Eular}} \cdot \vec{x}_{\mathrm{room}} + \vec{x}_{\mathrm{offset}}, \tag{5.1}$$

where a is the scaling parameter for the thermal contraction, R_{Eular} is the Eular rotational matrix, $\vec{x}_{\mathrm{room}}$ is the measured position in the optical scan at the room temperature, and $\vec{x}_{\mathrm{offset}}$ is an additional offset term. The parameters of the coordinate transformations are estimated in a fitting to minimize the residual in the uv plane between the $\vec{x}_{\mathrm{fit}}$ and the estimation from the collimated gamma-rays.

The overall alignment uncertainties are $\sim 600\,\mu\mathrm{m}$ in the z coordinate and $\sim 0.7\,\mathrm{mrad}$ in the ϕ coordinate [48]. The z uncertainty is dominated by the reproducibility of the measurements with collimated gamma-rays, which are performed twice. The ϕ uncertainty is dominated by the slight inconsistency between the measurements with collimated gamma-rays and the cross-check measurements with the lead strips.

5.2.2 LXe position resolution evaluation

The position resolution of the LXe detector was measured with the $17.6\,\mathrm{MeV}$ gamma-rays which were collimated by a $25\,\mathrm{mm}$ thick lead collimator in front of the LXe inner face (Fig.5.6). The collimator has several $5\,\mathrm{mm}$ wide slits in $50\,\mathrm{mm}$ intervals. The reconstructed position distribution with this setup shows a peak corresponding to the slit position, which is smeared by the position resolution and the position spreading of $17.6\,\mathrm{MeV}$ gamma-ray origins (Fig.5.7). Here, the vertex size of the $17.6\,\mathrm{MeV}$ gamma-rays is as small as $0.6\,\mathrm{mm}$, which is small enough compared to the expected resolution. The resolution can thus be obtained from the smearing evaluation in the observed distribution. The collimated gamma-ray data was taken with two different slit rotations, one for the u resolution evaluation and the other for that of v.

In the resolution measurements, the observed position distribution was fitted with a simulated truth distribution smeared by the resolution parameter. Fig.5.8 shows the estimated resolution at $17.6\,\mathrm{MeV}$ as a function of the conversion depth, w. The observed resolutions are worse than the expected ones in

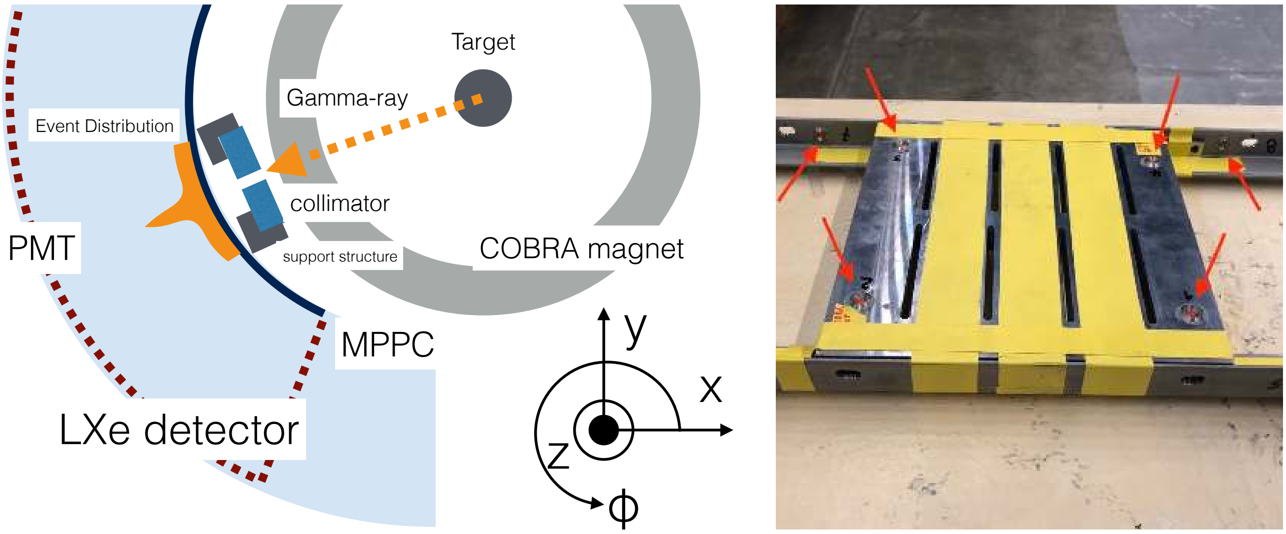

Figure 5.6: (Left) Setup for position resolution measurement with the $17.6\,\mathrm{MeV}$ gamma-rays [48]. (Right) Picture of the lead collimator used in the position resolution evaluation measurements.

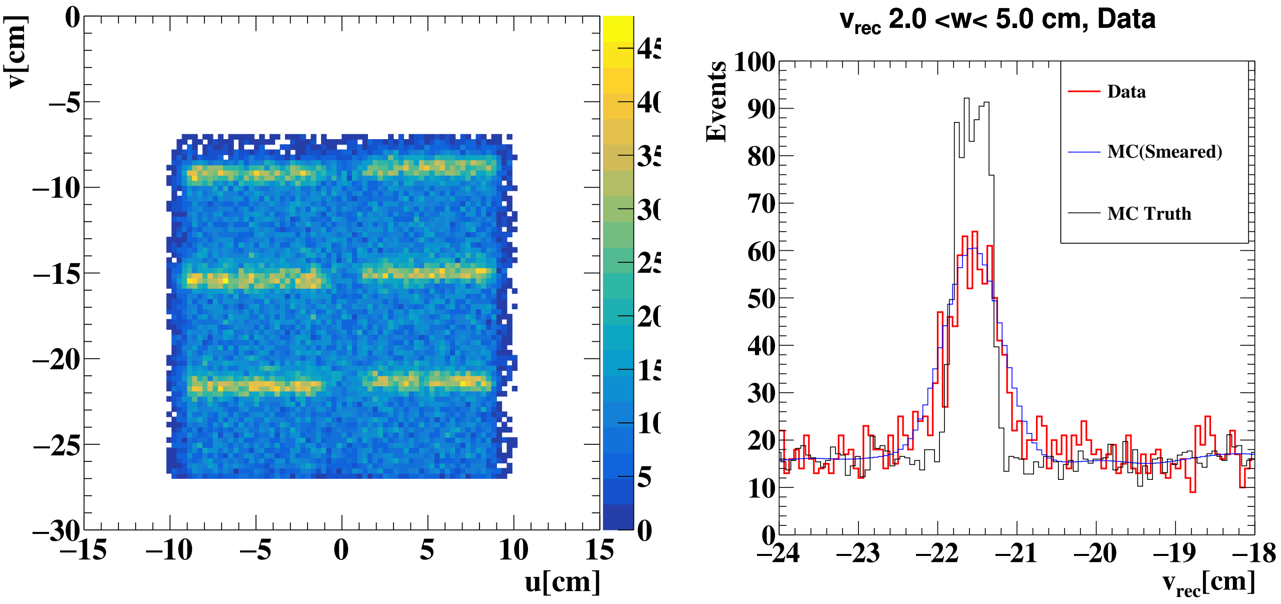

Figure 5.7: Observed position distribution in a σ_v measurement [48]. The observed distribution in the one-dimensional plot is fitted with a smeared MC distribution to evaluate σ_v.

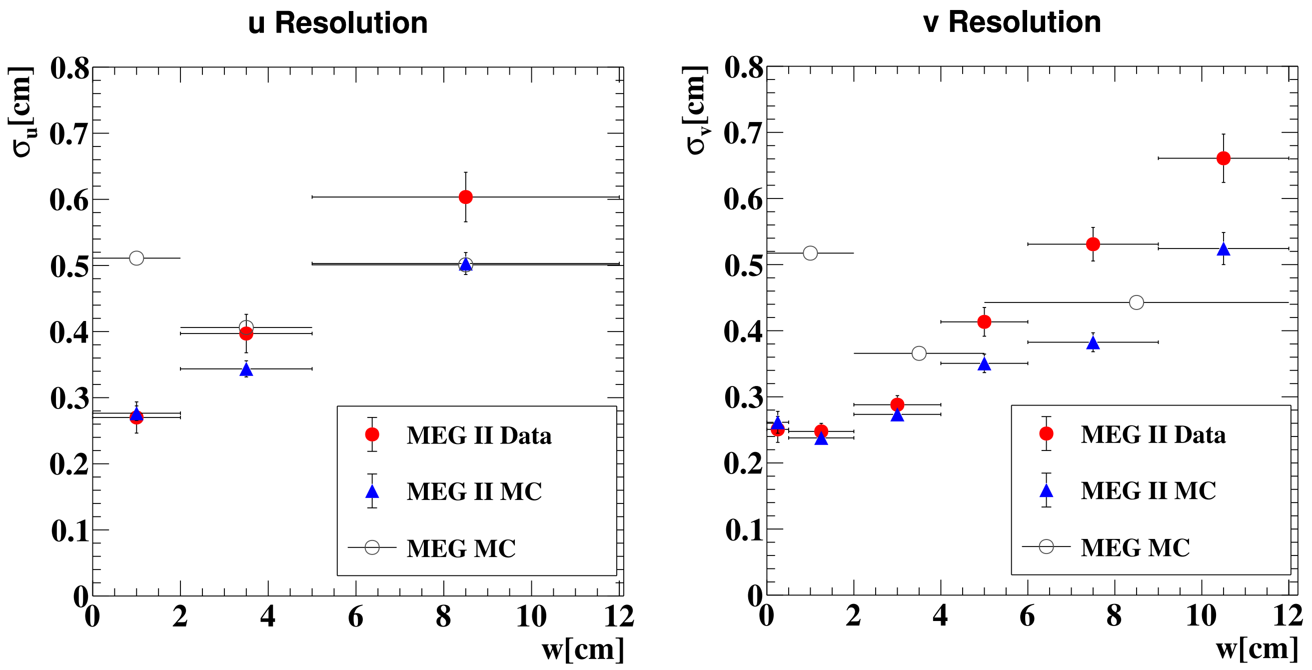

Figure 5.8: The estimated σ_u and σ_v values at $17.6\,\mathrm{MeV}$ as a function of w [48]. The measured and simulated resolutions for the MEG II detector are compared with the MEG resolution. The MEG II detector improved the position resolution especially in the shallow region thanks to the improved granularity of the photosensors on the inner face.

particular for deep events, whose cause is not understood.

The resolution for $52.8\,\mathrm{MeV}$ gamma-rays is expected to be different from that for $17.6\,\mathrm{MeV}$ gamma-rays. The resolution at $52.8\,\mathrm{MeV}$ was estimated with detector simulations, which is then corrected according to the observed resolution discrepancy between the data and the simulation for $17.6\,\mathrm{MeV}$. The results are shown in Fig.5.9.

5.3 LXe energy calibration and resolution

5.3.1 Sensor gain and excess charge factor

PMT calibration

The absolute PMT gain value is calibrated with the dedicated LED data, where the Poisson fluctuation of the number of photoelectrons plays a key role. When the mean of the number of photoelectrons is given as $\bar{N}_{\mathrm{phe}}$, the mean of the integrated charge can be expressed as

$$\bar{Q} = G \cdot \bar{N}_{\mathrm{phe}}, \tag{5.2}$$

where $\bar{Q}$ is the average of the charge and G is the gain. On the other hand, the Poisson fluctuation has a standard deviation of $\sqrt{\bar{N}_{\mathrm{phe}}}$, which gives a $G \cdot \sqrt{\bar{N}_{\mathrm{phe}}}$ contribution to the standard deviation of the charge. When the contribution from the electronics noise is included, the full standard deviation of the charge thus follows

$$\begin{aligned} \sigma_Q^2 &= G^2 \cdot \bar{N}_{\mathrm{phe}} + \text{noise term} \\ &= G \cdot \bar{Q} + \text{noise term}, \end{aligned} \tag{5.3}$$

where σ_Q is the standard deviation of the charge distribution in fixed $\bar{N}_{\mathrm{phe}}$ data.

As the noise term in Eq.(5.3) is independent of $\bar{N}_{\mathrm{phe}}$, the gain can be calibrated from a σ_Q^2 vs $\bar{Q}$

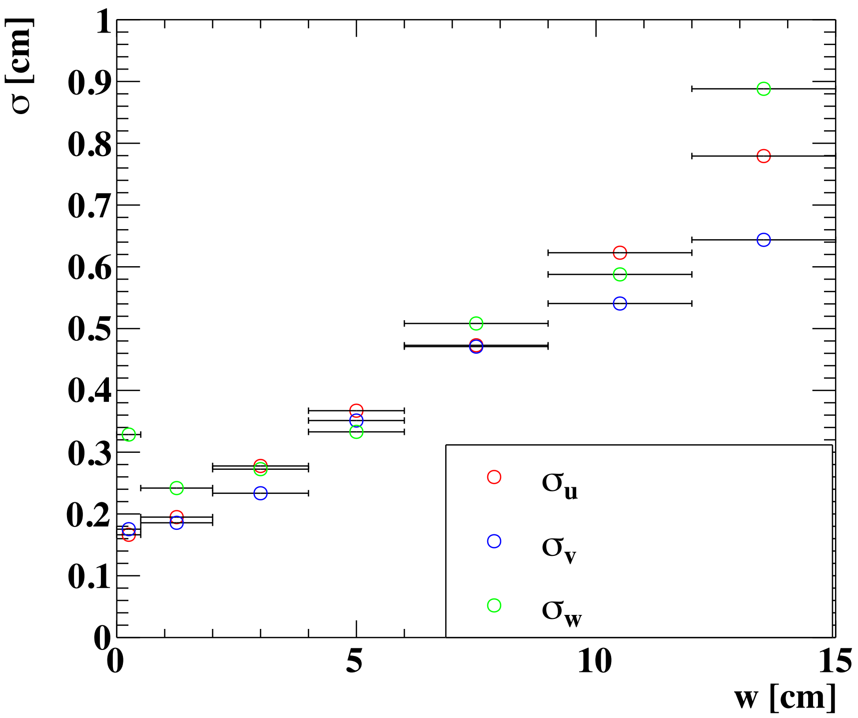

Figure 5.9: Estimated position resolution as a function of w for signal gamma-rays [48].

plot scanned over various $\bar{N}_{\mathrm{phe}}$ value. Fig.5.10 shows such an example, where the measurement points (each corresponds to one $\bar{N}_{\mathrm{phe}}$ value) are fitted with a linear line and the slope parameter corresponds to the gain. To have a high uniformity of the PMT gain, it was adjusted at the beginning of the 2021 run (Fig.5.11) by tuning the PMTs' high voltage.

Once the absolute gain value was estimated at a point in the middle of the 2021 run, the time variation was then followed with constant LED intensity data, which was collected also in the muon beam. The absolute gain value at a fiducial point was scaled to each point during the run according to the observed charge. The gain difference between the beam-off and beam-on conditions (Sec.2.4.2) can be corrected this way. It is also advantageous because the time variation can be followed in a short time scale (Fig.5.12).

The gain decrease explained in Sec.2.4.2 can be found in Fig.5.13, where two different gain calibration methods are compared in dedicated beam-off calibration dataset. The overall decrease during the whole period is around $10\,\%$. A small discrepancy between the two methods can also be seen in the gain decrease speed, which suggests a systematic uncertainty in the absolute gain value. This is suspected to come from the quality of Eq.(5.3); the LED light may not be completely stable or the gain itself may have a non-negligible contribution from the fluctuation in the multiplication. Still, the time variation is well followed by the method with constant LED light, and the above systematics are not expected to cause energy miscalibration. This is because the absolute gain uncertainty is finally absorbed in the later steps as long as the gain calibration is consistently applied.

MPPC calibration

The absolute gain value and the excess charge factor of the MPPCs are calibrated with LED data where the expected number of photoelectrons is adjusted to ~ 1. By resolving the single photoelectron peaks, the gain is estimated from the differences in the peak positions. Fig.5.14 shows the distribution of the MPPC charge on such data, which is fitted by a sum of two Gaussian functions with the mean difference corresponding to the gain. The excess charge factor, F_{ECF}, can be estimated by the Poisson photoelectron statistics [96]. The expectation value for the number of the incident photoelectrons, $\bar{N}_{\mathrm{phe}}$,

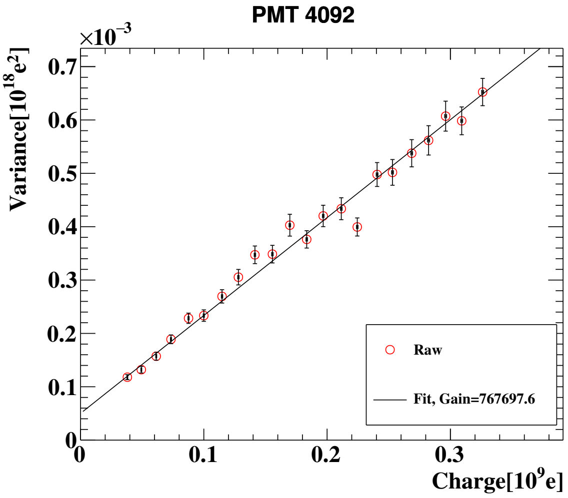

Figure 5.10: σ_Q^2 vs $\bar{Q}$ plot for a PMT [48].

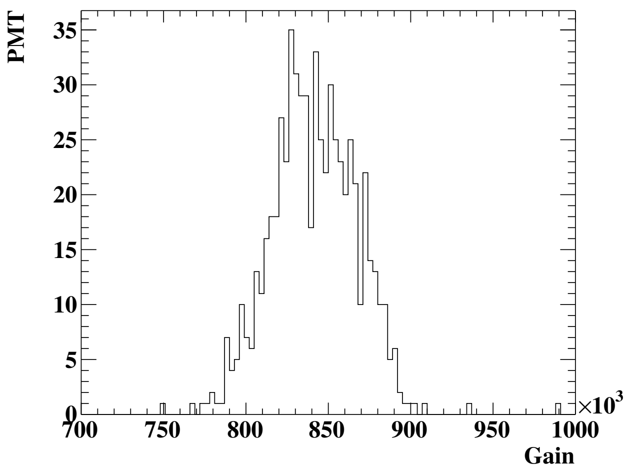

Figure 5.11: PMT gain distribution at the beginning of 2021 run [48].

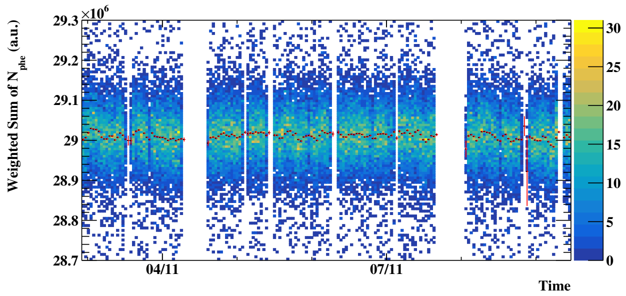

Figure 5.12: Time variation of PMT gain in beam-on condition [48].

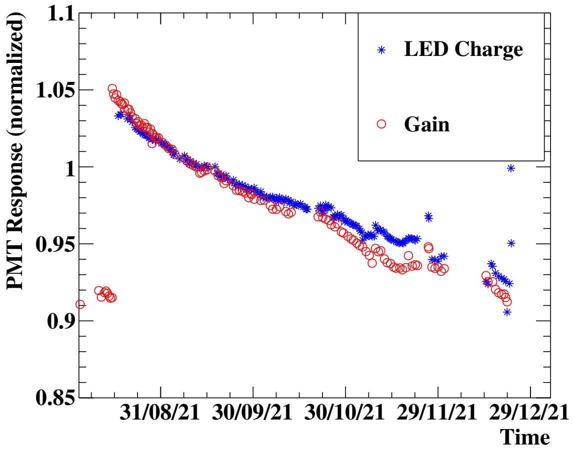

Figure 5.13: PMT gain decrease during the beam period [48].

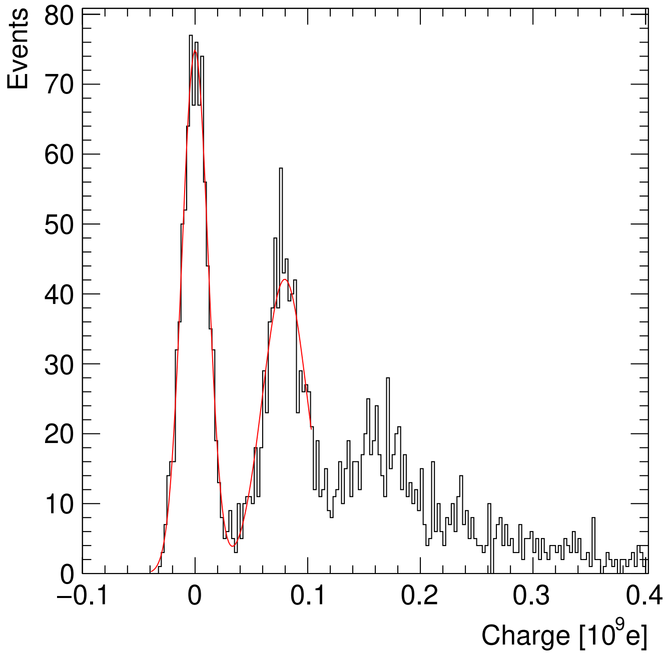

Figure 5.14: LED charge distribution on a MPPC [48].

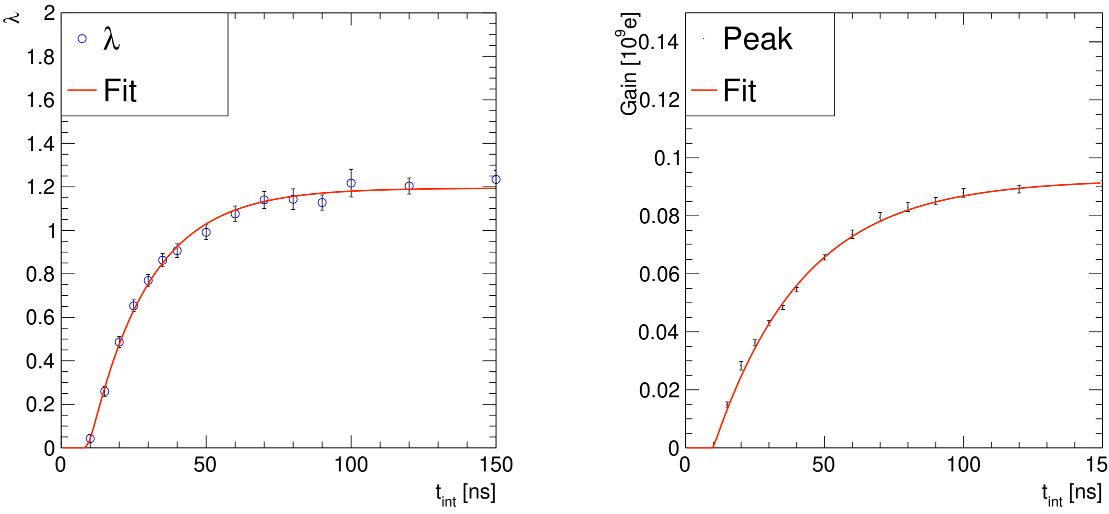

Figure 5.15: Integration range dependence of (left) the excess charge factor and (right) gain [48].

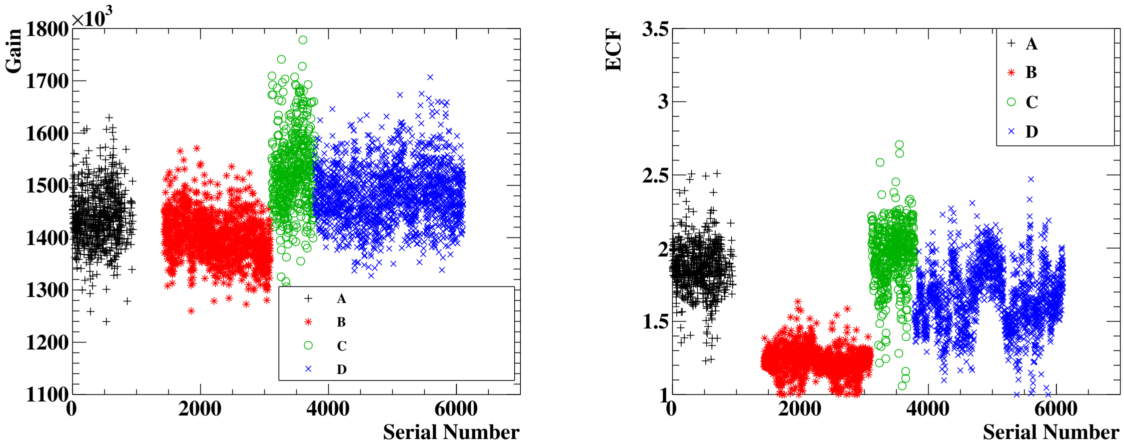

Figure 5.16: Distribution of the (left) gain and (right) the excess charge factor of MPPCs [48].

can be estimated from

$$\bar{N}_{\text{phe}} = -\log\left(\frac{N_{\text{zero}}}{N_{\text{all}}}\right), \tag{5.4}$$

where $N_{\text{zero}}/N_{\text{all}}$ is the fraction of the zero photoelectron events in the dataset. The correlated noise enhances the observed number of photoelectrons from the incident one as

$$F_{\text{ECF}} = \frac{\bar{N}_{\text{observed}}}{\bar{N}_{\text{phe}}}, \tag{5.5}$$

where $\bar{N}_{\text{observed}}$ is the average of the observed number of photoelectrons in Fig.5.14.

Though the MPPC charge is reconstructed in integration over $150\,\text{ns}$, such a long integration gives a large electronics noise contribution to the charge distribution and the single photoelectron peaks cannot be resolved. Therefore, the gain calibration was based on analyses with shorter integration ranges, t_{int}. The results from shorter integration ranges were then extrapolated to the parameters with $t_{\text{int}} = 150\,\text{ns}$ as

$$G(t_{\text{int}}) = G \times \left(1 - \exp\left(-\frac{t_{\text{int}} - t_0}{\tau_{\text{fail}}}\right)\right), \tag{5.6}$$

where G, t_0, and τ_{fail} were fitted to the shorter t_{int} results (Fig.5.15). The distribution of the calibrated gain and the excess charge factors as a function of the serial number are shown in Fig.5.16, where production lot dependences can be seen.

The time variation of the MPPC gain was also followed by the constant LED light data. Fig.5.17

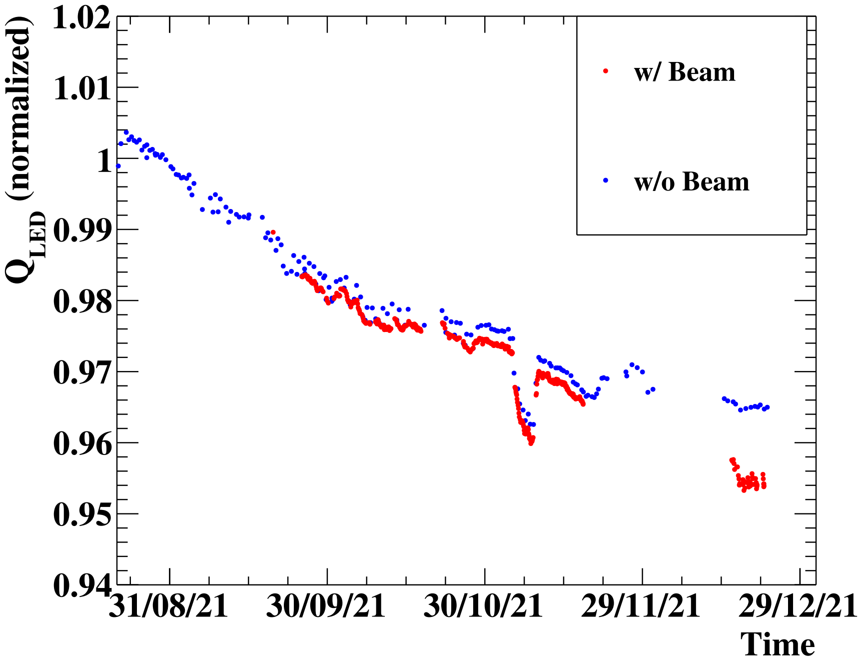

Figure 5.17: Time variation of the MPPC gain [48].

shows the time variation of the charge in constant LED data for beam-on and beam-off periods. The overall decrease during the beam time was $4\,\%$, which came from the PDE decrease due to the radiation damage (see Sec.2.4.2). The instability observed in early November came from a $\sim 1\,\mathrm{K}$ temperature fluctuation of the liquid xenon, which increased the MPPC breakdown voltage and thus decreased the gain. The discrepancy between the beam-off and the beam-on data likely came from the voltage drop by the current from the constantly illuminated MPPCs. This is a behavior discussed in [44], and the observed difference agrees with the expectation.

5.3.2 QE and PDE of sensors and liquid xenon light yield

The MPPC PDE and the PMT QE are estimated with alpha-ray events from $^{241}\mathrm{Am}$ sources. The number of photoelectrons on each sensor is estimated in simulation studies making use of the known position of the α-sources, the known energy deposit of the alpha-rays, and an assumption on the $\epsilon_{\mathrm{QE,PDE}}$. This simulation-based expectation is then compared with the observed number of photoelectrons to estimate the PDE or QE as

$$\epsilon_{\mathrm{QE,PDE}} = \frac{\epsilon_{\mathrm{MC\ assumed}} \cdot \bar{N}_{\mathrm{observed-phe}}}{\bar{N}_{\mathrm{simulated-phe}} \cdot F_{\mathrm{LY}}}, \tag{5.7}$$

where $\epsilon_{\mathrm{MC\ assumed}}$ is the assumed $\epsilon_{\mathrm{QE,PDE}}$ value in the simulation, $\bar{N}_{\mathrm{observed-phe}}$ is the observed average number of photoelectrons, $\bar{N}_{\mathrm{simulated-phe}}$ is the average in the simulation, and F_{LY} is the correction factor of the light yield. As this method directly observes the LXe scintillation light, it is not sensitive to the $\epsilon_{\mathrm{QE,PDE}}$ dependence on the wavelength.

In the calibration data analysis, the alpha-ray events are separated from cosmic backgrounds according to the difference in the amplitude vs charge ratio shown in Fig.5.18. This difference comes from the energy deposit dependence of the liquid xenon scintillation process described in Sec.2.4.1. The source of the incident alpha-ray is identified from the other 24 sources with the light distribution of the PMTs, whose separation power is shown in Fig.5.19. $\bar{N}_{\mathrm{observed-phe}}/\bar{N}_{\mathrm{simulated-phe}}$ is evaluated from a plot as shown in Fig.5.20. The light yield is determined with an assumption that the average of the PMT QE is stably at $16\,\%$ during the data taking, which is based on experiences in the MEG experiment.

The distribution of the observed QE value in 2021 is shown in Fig.5.21. Here, the PMTs with $y > 83\,\mathrm{cm}$ had lower QE values than the others because the liquid was not full in the detector and the

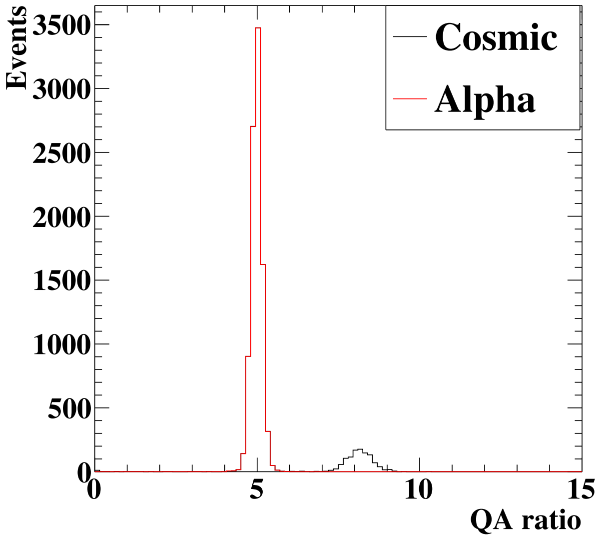

Figure 5.18: Charge vs amplitude ratio for cosmic-ray events and α-ray events [48].

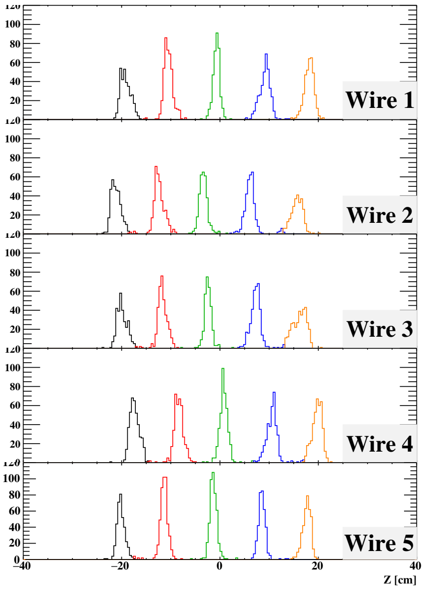

Figure 5.19: Identification power of alpha ray sources [48].

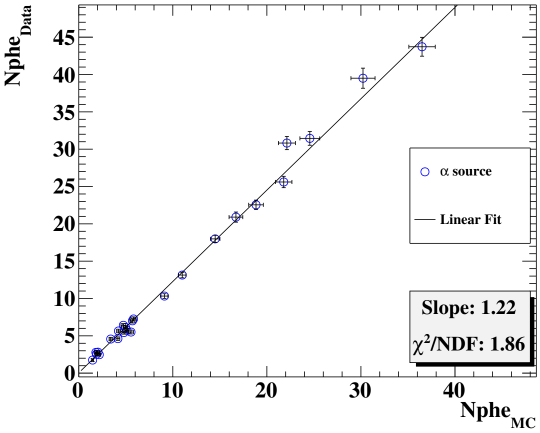

Figure 5.20: $\bar{N}_{\text{observed}-\text{phe}}$ vs $\bar{N}_{\text{simulated}-\text{phe}}$ plot for an MPPC [48].

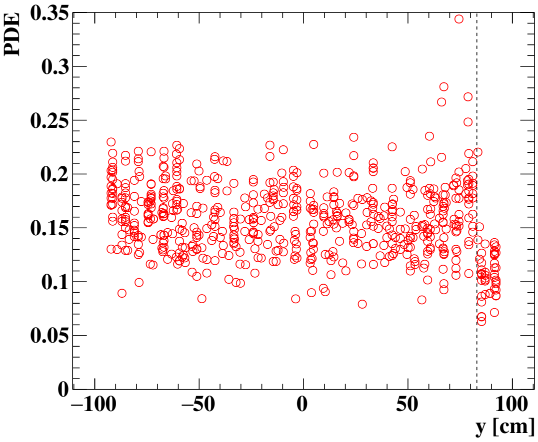

Figure 5.21: The PMT QE values as a function of y position of the PMTs [48].

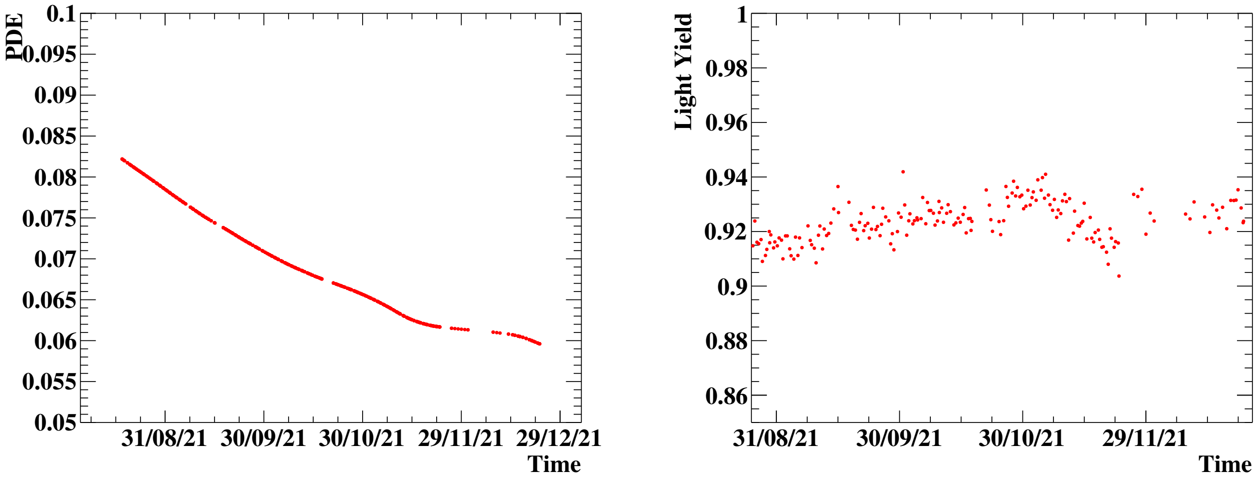

Figure 5.22: Time variation of the light yield and the PDE [48].

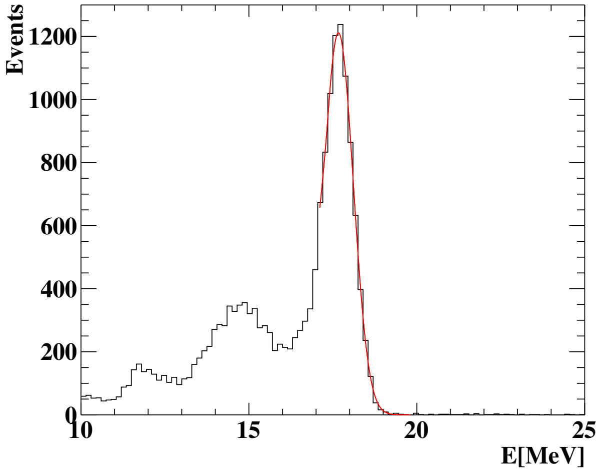

Figure 5.23: Reconstructed spectrum of 17.6 MeV gamma-ray data [48]. The fitted peak position at 17.6 MeV is used for energy scale calibration. The secondary peak is the 14.8 MeV gamma-ray byproducts of the ${}^{7}_{3}\mathrm{Li}(p,\gamma){}^{8}_{4}\mathrm{Be}$ reaction.

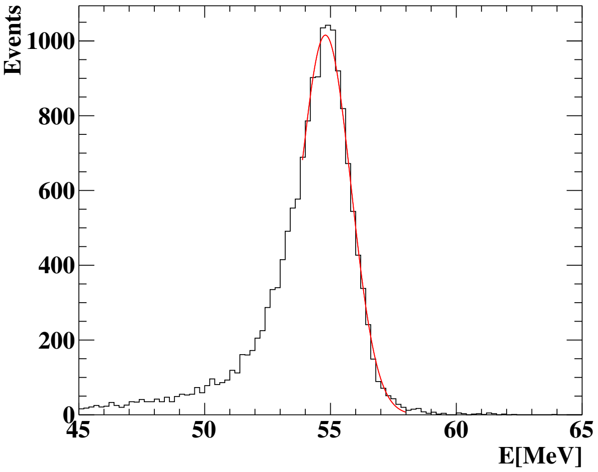

Figure 5.24: Reconstructed spectrum of 55 MeV gamma-rays [48].

sensors above the level were not fully sensitive to the energy deposit.

The time variation of the light yield and the PDE were also observed as Fig.5.22. The light yield was kept within $93 \pm 2\,\%$ during the data taking. The final PDE value at the end of the data taking was $6\,\%$, above the minimum required $4\,\%$. Though the absolute values of the PDE and QE also have uncertainties, they are absorbed in the next calibration of the energy scale.

5.3.3 Energy scale calibration

Several calibration tools are exploited for the energy scale calibration: α-particles, $17.6\,\mathrm{MeV}$ gamma-rays, $55\,\mathrm{MeV}$ gamma-rays, cosmic-rays, and background gamma-rays from muon decay. The calibration with $17.6\,\mathrm{MeV}$ gamma-rays and $55\,\mathrm{MeV}$ gamma-rays are straightforward; they use the peak in the energy spectrum shown in Fig.5.23 and Fig.5.24. The calibration with cosmic-rays uses the Landau distribution of the energy deposit with the peak value around $170\,\mathrm{MeV}$. Here, only cosmic-rays that cross the entrance face of the LXe detector are selected to have a uniform pass length, which drops the low-energy peak in Fig.5.25 of short-path length cosmic-rays. The calibration with background gamma-rays is based on a background spectrum fitting to the energy spectrum around $52.8\,\mathrm{MeV}$ (Fig.5.26), which is based

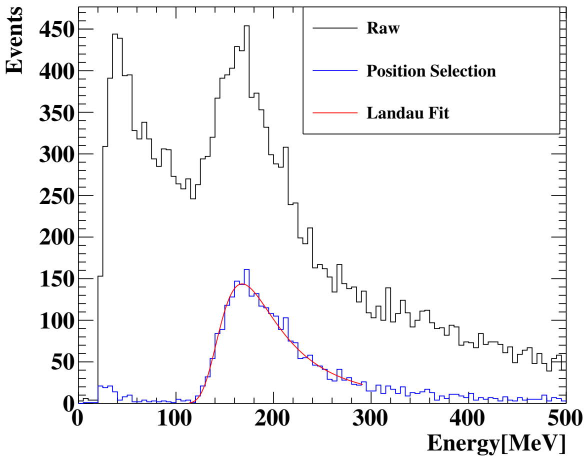

Figure 5.25: Reconstructed spectrum of cosmic-rays used for energy scale calibration [48]. The $170\,\mathrm{MeV}$ peak of the Landau distribution is used to calibrate the time variation of the energy scale.

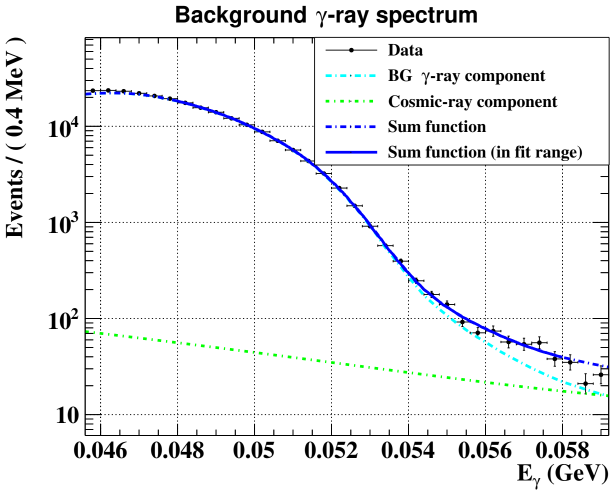

Figure 5.26: Fitting of background γ-ray spectrum around $52.8\,\mathrm{MeV}$. The solid line is the best-fit spectrum, which is modeled as a sum of the background gamma-ray component (cyan line) and cosmic-ray component (green line).

on a model detailed later in Eq.(6.15).

Time variation of energy scale

As introduced in Sec.4.2.5, N_{MPPC} and N_{PMT} are separatedly reconstructed. Here, the time variation of the energy scale and $N_{\mathrm{MPPC}}/N_{\mathrm{PMT}}$ value are corrected in the energy reconstruction. Accordingly, the time variation during the physics data taking was monitored with α-particles, $17.6\,\mathrm{MeV}$ gamma-rays, and cosmic-rays (Fig.5.27). Similar trends were observed between different calibration sources each for N_{MPPC} and N_{PMT}. They are understood to represent the time variation of the light yield of LXe caused by liquid impurities. The difference in the trend between N_{MPPC} and N_{PMT}, on the other hand, is understood to arise from the difference in the distance from the α-sources to the sensors, which can give different effects of scintillation light absorption to the PDE and QE calculations. In the energy reconstruction, this difference in the time variation is absorbed by the time-varying R_{MPPC} parameter introduced in Sec.4.2.5

Position dependence of energy scale

The u_γ, v_γ, and w_γ-dependence of the energy scale comes from several mechanisms: the position dependence of the light collection efficiency and the systematics in the sensor calibration. It is corrected by introducing $F_{\mathrm{face}}(u,v)$ in Eq.(4.14) and $S_E(u,v,w)$ in Eq.(4.17).

The face factor, $F_{\mathrm{face}}(u,v)$, was optimized to have the best resolution for $17.6\,\mathrm{MeV}$ γ-rays. The (u,v)-dependence was taken into account by dividing the calibration dataset into different subsets based on the position. The optimized $F_{\mathrm{face}}(u,v)$ values in different (u,v)-segments were then fitted with a symmetric function of u and v, and the result, shown in Fig.5.28, is used in the energy reconstruction. As an overall behavior, we can see that a larger weight is used when incident γ-rays are closer to the face.

The $S_E(u,v,w)$ factor was then calibrated with $17.6\,\mathrm{MeV}$ gamma-rays, background gamma-rays from muon decay, and $55\,\mathrm{MeV}$ gamma-rays. Here, the calibration with $17.6\,\mathrm{MeV}$ gamma-rays has systematics due to the energy dependence; the position dependence is found to have energy dependence both in data and MC samples. On the other hand, $55\,\mathrm{MeV}$ γ-rays are close to the signal energy, but they were not measured during the physics data-taking period. Therefore, possible time variation in the position dependence can cause systematic biases in the $55\,\mathrm{MeV}$ calibration. The background spectrum

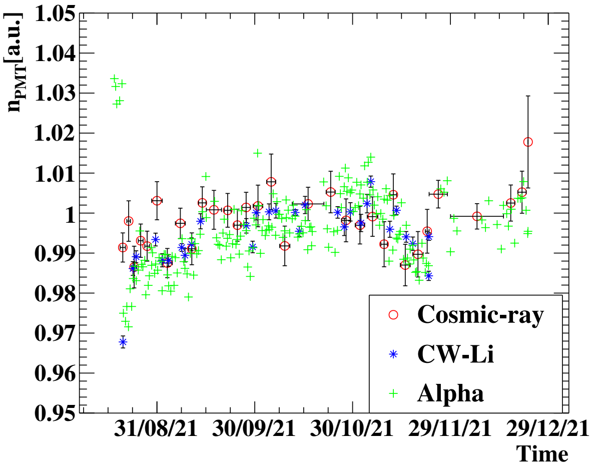

(a) (b)

Figure 5.27: Time variation of measured value of (a) N_{MPPC} and (b) N_{PMT} for different calibration sources. Three independent results show good agreements each other [48].

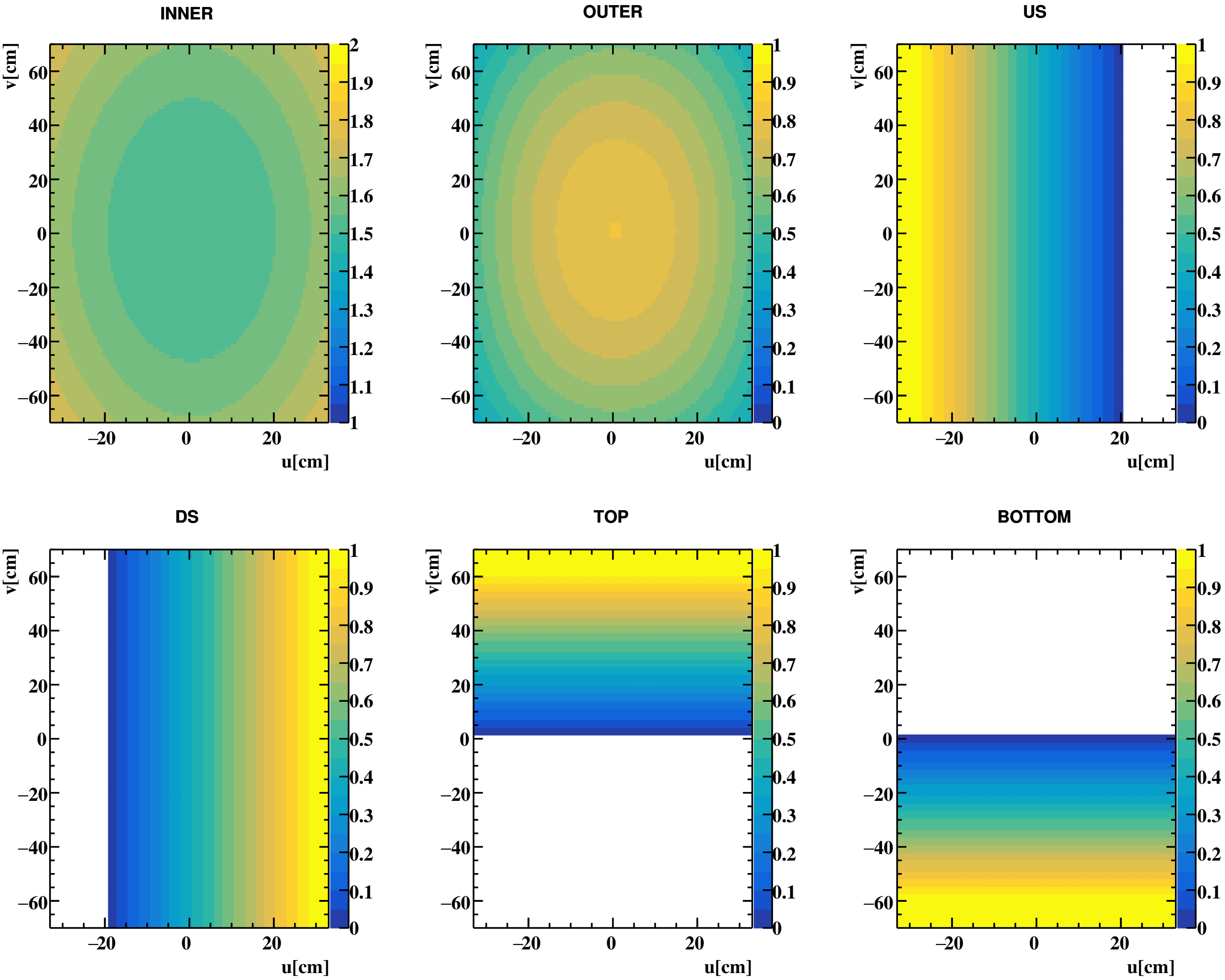

Figure 5.28: The position-dependent face factor $F_{\text{face}}(u, v)$ used in the energy reconstruction [48].

fitting also has its unique difficulty because of the use of the kinematical endpoint of the monotonically decreasing spectrum. This causes a large fit uncertainty due to the limited statistics around $52.8\,\mathrm{MeV}$, large error correlations between fit parameters, and large systematic uncertainties from the validity of the fit modeling. Given the different uncertainties in each method, the $S_E(u, v, w)$ was calibrated finally by combining three different methods with a weight optimization according to the uncertainties.

Energy scale uncertainty

The uncertainty of the energy scale has three contributions: the linearity of the energy response, the time variation of the energy scale, and the position dependence. The uncertainty from the energy response linearity, which originates from the small difference between $52.8\,\mathrm{MeV}$ and the calibration source ($55\,\mathrm{MeV}$), was evaluated to be $0.1\,\%$ according to the uncertainty in an extrapolation of a linearity plot between $55\,\mathrm{MeV}$, $83\,\mathrm{MeV}$, and $129\,\mathrm{MeV}$. The time variation uncertainty was evaluated to be $0.3\,\%$ from the agreement between the cosmic-ray calibration, 17.6 MeV gamma-ray calibration, and background gamma-ray spectrum fitting. The position dependence uncertainty was similarly evaluated to be $0.2\,\%$.

5.3.4 Energy resolution evaluation with $\pi^0 \to \gamma\gamma$ data

The energy resolution was evaluated with $55\,\mathrm{MeV}$ gamma-rays by fitting the reconstructed spectrum (as shown in Fig.5.24) with

$$f(E_\gamma) = \begin{cases} \exp\left[-\dfrac{\left(E_\gamma - \mu_{E_\gamma}\right)^2}{2\sigma_{E_\gamma}^2}\right] & (E_\gamma > \mu_{E_\gamma} + \tau), \\ \exp\left[\dfrac{\tau\left(\tau/2 - E_\gamma + \mu_{E_\gamma}\right)}{\sigma_{E_\gamma}^2}\right] & (E_\gamma \leq \mu_{E_\gamma} + \tau), \end{cases} \tag{5.8}$$

which represents a Gauss function smoothly connected with an exponential low energy tail. As a result, we obtained the $\sigma_{E_\gamma}/\mu_{E_\gamma}$ value of $2.0\,\%$ ($1.8\,\%$) for $w_\gamma < 2\,\mathrm{cm}$ ($w_\gamma > 2\,\mathrm{cm}$).

5.4 LXe time calibration and resolution

The time calibration and the resolution evaluation exploit the $\pi^0 \to \gamma\gamma$ events. Here, the fast pre-shower counters on the opposite side of the LXe detector are used as a reference. The pre-shower counter gives the interaction time at the LXe as

$$t_{\mathrm{ref}} = t_{\mathrm{preshower}} + t_{\gamma\gamma\mathrm{TOF}}, \tag{5.9}$$

where t_{ref} is the referenced value of the t_{LXe} in Eq.(4.13), $t_{\mathrm{preshower}}$ is the time measured at the pre-shower counter, and $t_{\gamma\gamma\mathrm{TOF}}$ is the TOF correction. The TOF correction here assumes that the two gamma-rays always originate from the center of the $\pi^0 \to \gamma\gamma$ decay vertex though the vertex itself has a finite spread in reality.

5.4.1 Time walk and offset

Compared with Eq.(4.12), the scintillation photon arrival time on each sensor can then be referenced as

$$t_{\mathrm{pmref}_i} = t_{\mathrm{ref}} + t_{\mathrm{prop}_i}. \tag{5.10}$$

From Eq.(4.10), the walk and the offset parameters thus follow

$$t_{\mathrm{walk}} + t_{\mathrm{offset}} = t_{\mathrm{pulse}} - t_{\mathrm{ref}} - t_{\mathrm{prop}}, \tag{5.11}$$

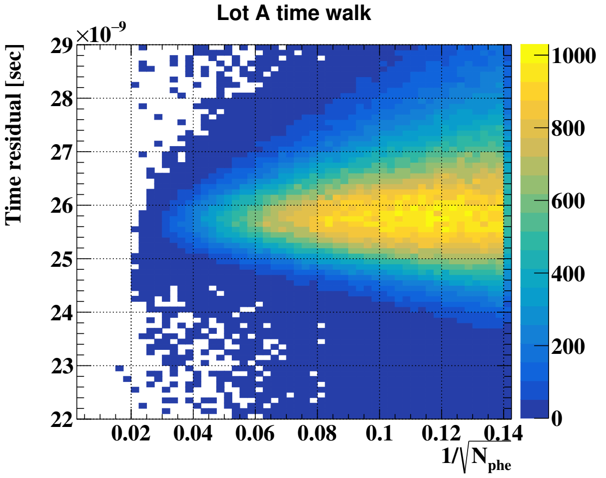

Figure 5.29: Distribution of $t_{\mathrm{pulse}} - t_{\mathrm{ref}} - t_{\mathrm{prop}}$ vs $1/\sqrt{N_{\mathrm{phe}}}$ for lot-A MPPCs. The offset dependence on N_{phe} is calibrated as the walk effect and the y-axis spread is used to evaluate the single sensor resolution.

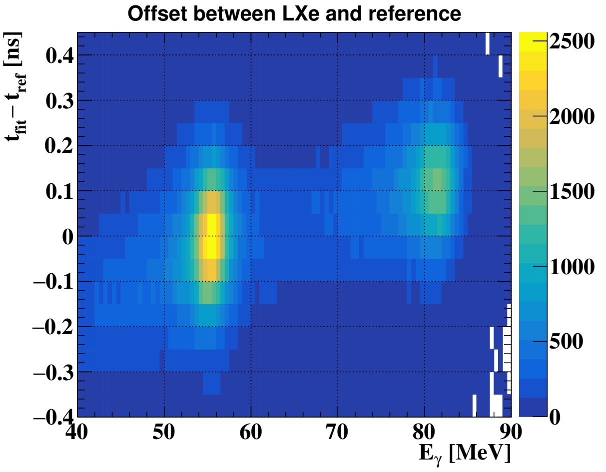

Figure 5.30: Comparison of $t_{\mathrm{LXe}} - t_{\mathrm{ref}}$ between the $55\,\mathrm{MeV}$ and $83\,\mathrm{MeV}$ with a not-optimized v_{eff}.

which is used in the walk and offset calibration.

When the walk parameter was calibrated, the sensors were separated into six groups: the PMTs on the outer face, the PMTs on the lateral face, and the MPPCs from four different production lots. This grouping was empirically determined according to the difference in the waveform shape; the typical waveforms for these six groups are different from each other. Though the walk and the offset are independent of each other, the calibration is entangled due to the above grouping. Therefore, the walk calibration and the offset calibration were iterated by updating the calibration of each other.

Fig.5.29 shows the $t_{\mathrm{pulse}} - t_{\mathrm{ref}} - t_{\mathrm{prop}}$ distribution as a function of N_{phe} for the lotA MPPCs. Here, $\mathcal{O}(100\,\mathrm{ps})$ dependence on the N_{phe} is found and corrected after the calibration. In addition, the same plot after the calibration was used to evaluate the σ_i in Eq.(4.12), which also depends on N_{phe} and the grouping. The single sensor resolution with large amplitude pulses was as good as $500\,\mathrm{ps}$ for both MPPCs and PMTs.

5.4.2 Effective velocity of scintillation light

The t_{prop} parameter also needs a calibration of the effective velocity of the scintillation light propagation in the liquid xenon, v_{eff}. When v_{eff} parameter is changed, the $t_{\mathrm{fit}} - t_{\mathrm{ref}}$ offset becomes inconsistent between $55\,\mathrm{MeV}$ and $83\,\mathrm{MeV}$ as shown in Fig.5.30. The effective velocity parameter was thus optimized to $8.4\,\mathrm{cm/ns}$ to minimize the time offset dependence on E_{γ}. Though this value is different from the correct physical propagation velocity of the scintillation light ($11\,\mathrm{cm/ns}$ group velocity), this choice of v_{eff} gives the best time resolution.

5.4.3 Position dependence of time offset

The fitted time in Eq.(4.12) showed a position-dependent bias and w dependence was especially strong as shown in Fig.5.31. This is corrected by introducing the correction term in Eq.(4.13), which was calibrated as a sum of three one-dimensional functions of u, v, w each

$$F_t(u, v, w) = F_{tu}(u) + F_{tv}(v) + F_{tw}(w). \tag{5.12}$$

The $F_{tw}(w)$ was the largest one among them and its value is as large as $400\,\mathrm{ps}$ peak-to-peak as shown in Fig.5.31.

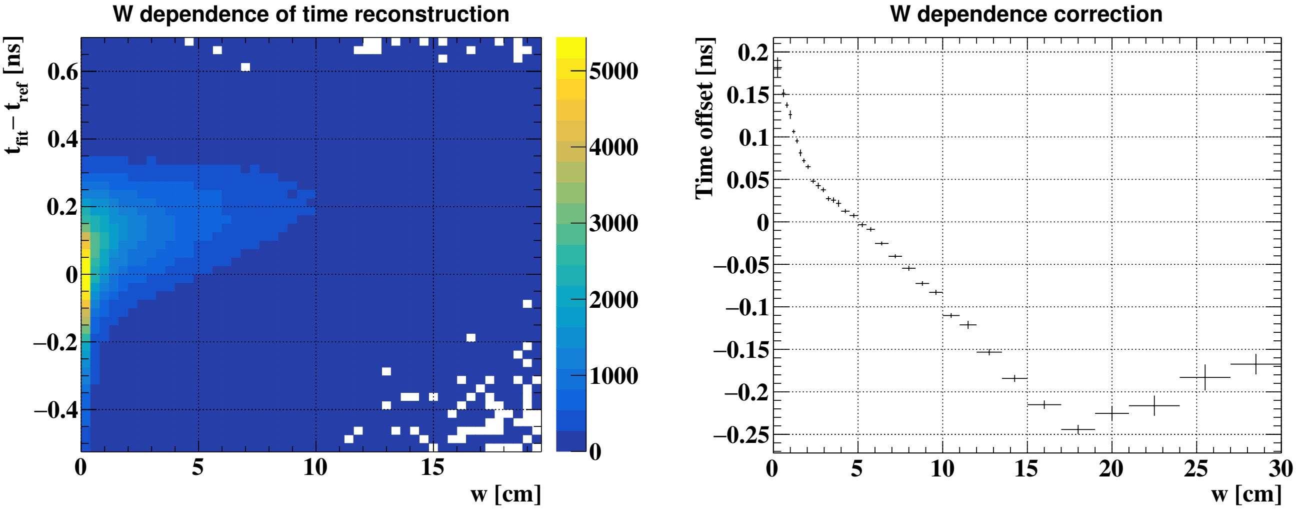

Figure 5.31: Calibration of w-dependent time offset, $F_{tw}(w)$. (Left) Distribution of $t_{\text{fit}} - t_{\text{ref}}$ vs w. (Right) Calibrated $F_{tw}(w)$ plot, which is obtained by profiling the left plot.

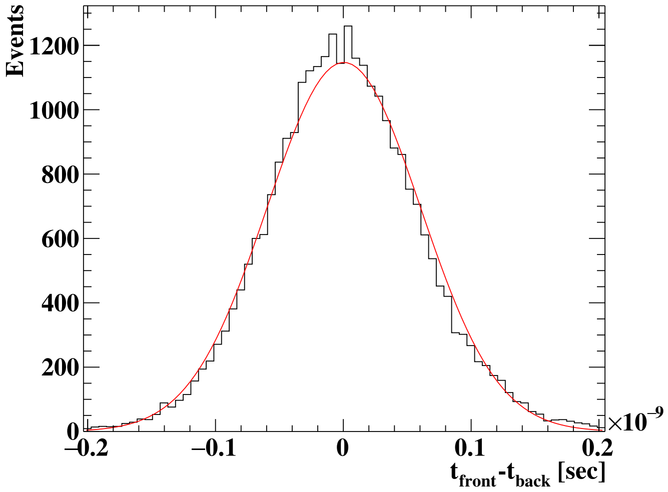

Figure 5.32: The front to back time difference of the pre-shower counter [48].

5.4.4 Time resolution in $\pi^0 \to \gamma\gamma$ events

In the reconstruction, $t_{\gamma\gamma\text{TOF}}$ measurements have large uncertainties due to the finite spread of the $\pi^0 \to \gamma\gamma$ vertex. Including this contribution, the $t_{\text{LXe}} - t_{\text{ref}}$ distribution has a standard deviation of $\sigma_{\text{LXe-preshower}}$ as

$$\sigma_{\text{LXe}-\text{preshower}} = \sigma_{\text{LXe}} \oplus \sigma_{\text{preshower}} \oplus \sigma_{\text{vertex}}, \tag{5.13}$$

where σ_{LXe} is the LXe time resolution, $\sigma_{\text{preshower}}$ is the pre-shower counter time resolution, and σ_{vertex} is the uncertainty contribution from the vertex spread.

The contribution from the pre-shower counter was estimated to be $28.2 \pm 0.2\,\text{ps}$ from the intrinsic time difference between the front counter and the back counter (Fig.5.32). The contribution from the vertex spread was measured with a dedicated measurement shown in Fig.5.33. Here, a counter consisting of two plastic scintillators was placed in front of the LXe detector, whose resolution was comparable to the pre-shower counter. The observed distribution between the opposite counters shown in Fig.5.33 indicates $\sigma_{\text{vertex}} = 68 \pm 6\,\text{ps}$. The uncertainty here mostly comes from the fact that the measured σ_{vertex} showed dependence on the liquid level in the hydrogen target.

The distribution of the $t_{\text{LXe}} - t_{\text{ref}}$ is shown in Fig.5.34. The core part of $\sigma = 98\,\text{ps}$ accounts for $95\,\%$ and the tail part of $\sigma = 290\,\text{ps}$ accounts for the other $5\,\%$. By subtracting the contribution from the σ_{vertex} and $\sigma_{\text{preshower}}$, the core resolution of the t_{LXe} was evaluated to be $65 \pm 6\,\text{ps}$.

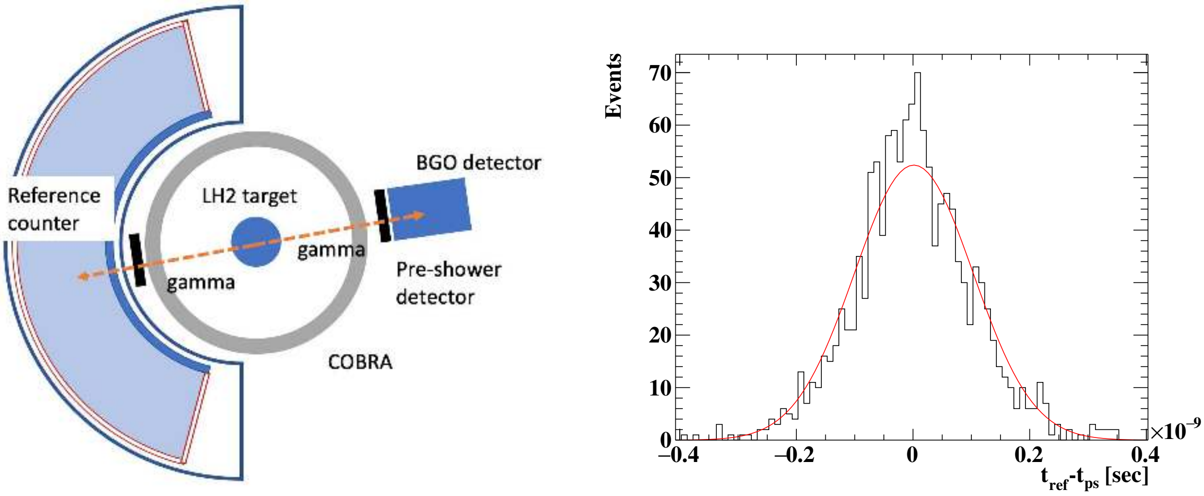

Figure 5.33: (Left) Setup to measure the vertex spread in the $\pi^0 \to \gamma\gamma$ data-taking. (Right) Time difference distribution between the pre-shower detector and the reference counter shown in the left sketch [48].

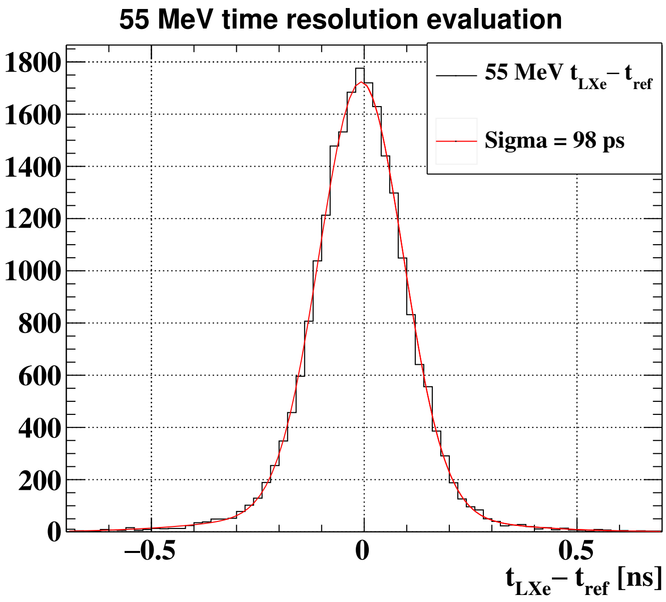

Figure 5.34: Time difference distribution of $t_{\mathrm{LXe}} - t_{\mathrm{ref}}$ in the $\pi^0 \to \gamma\gamma$ events. The overall spread of $98\,\mathrm{ps}$ includes the contributions of $\sigma_{\mathrm{preshower}} \oplus \sigma_{\mathrm{vertex}}$. After its subtraction, σ_{LXe} was evaluated to be $65 \pm 6\,\mathrm{ps}$.

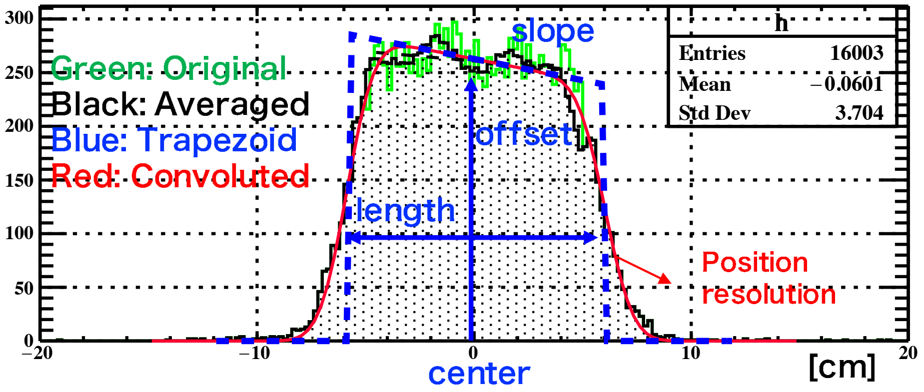

Figure 5.35: t_{channel} and v_{eff} calibrations in a pTC counter [40]. The original distribution (green) is smoothed (black), which is then fitted with a trapezoid function convoluted with a Gaussian (red). The best-fit trapezoid function (blue) gives t_{channel} from the trapezoid center and v_{eff} from the trapezoid width.

5.5 pTC time calibration and resolution

5.5.1 Internal time calibration

The hit reconstruction of the pTC in Eq.(4.2) requires v_{eff} and t_{channel} calibrations. In their calibration, the hit w distribution was modeled as a trapezoid function convoluted with a Gaussian as shown in Fig.5.35. The effective velocity was fitted so that the trapezoid length agrees with the $12\,\text{cm}$ counter geometry, which gave $v_{\text{eff}} = 12.4 \pm 0.4\,\text{ps}$. The end-to-end channel time offsets, t_{channnel}, were calibrated to have the center of the trapezoid at zero. The t_{channnel} calibration precision was $1.1\,\text{mm}$-equivalent, and the estimated resolution of the w reconstruction is $1.1\,\text{cm}$ according to the convoluted Gaussian function.

5.5.2 Track-based time calibration

The counter time reconstruction in Eq.(4.1) requires the calibration of the counter time offset, t_{counter}. It is calibrated with positron tracks by minimizing

$$\sum_{i \in \text{Track}} \sum_{j \in \text{Hit}} (t_{\text{hit}_{ij}} - t_{\text{TOF}_{ij}} - t_{\text{decay}_i} - t_{\text{counter}_j})^2, \tag{5.14}$$

where $t_{\text{hit}_{ij}}$ is the time measured at j-th counter in the i-th track, $t_{\text{TOF}_{ij}} + t_{\text{decay}_i}$ gives the j-th counter hit time of the i-th track, and t_{counter_j} is the offset parameter of the j-th counter. Eq.(5.14) is minimized with respect to all the t_{decay_i} and t_{counter_j} parameters, where t_{decay_i} (t_{counter_j}) gives N_{Track} (512) degrees of freedoms in total.

Though it has a large number of degrees of freedoms, the whole matrix that appears in the regression is sparse because each track can leave only up to ~15 counters. In addition, this minimization is an idealistic linear least square problem. Therefore, there exists an efficient algorithm, and it is implemented in the MillePede package [98], which was thus used in the calibration.

5.5.3 Laser based calibration

The track-based time calibration method discussed above is not sensitive to the global offset between the upstream and the downstream sectors. It is therefore complemented by the laser-based calibration method. In this method, the laser pulse gives the reference time with corrections on the optical length of the system, where the correction parameters were measured beforehand (Fig.5.36). The uncertainty of this method was evaluated to be $27\,\text{ps}$ overall [41].

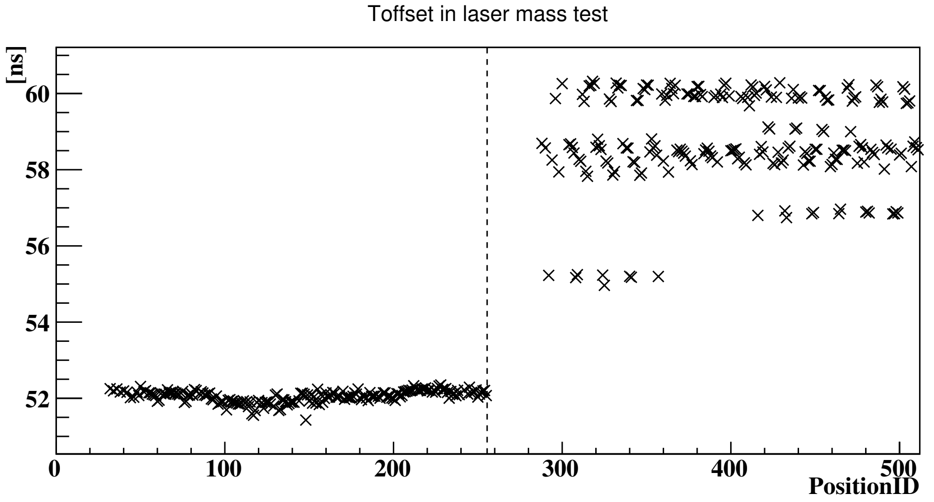

Figure 5.36: The measured time offset from the optical length of the laser system [42].

5.5.4 Performance evaluation with even-odd method

The pTC timing resolution was evaluated by the *even-odd method*, which splits hits into even hits and odd hits in Eq.(4.7) as

$$\begin{aligned} t_{\text{even}} &= \frac{1}{n}\sum_{i=1}^{n}(t_{\text{hit}_{2i}} - t_{\text{TOF}_{2i}}), \\ t_{\text{odd}} &= \frac{1}{n}\sum_{i=1}^{n}(t_{\text{hit}_{2i+1}} - t_{\text{TOF}_{2i+1}}). \end{aligned} \tag{5.15}$$

The resolution of $t_{\text{even}} - t_{\text{odd}}$ is then evaluated as a function of $2n$. With an assumption that the error of the counter time measurements is independent, the full resolution is expected to be the same as the resolution of $(t_{\text{even}} - t_{\text{odd}})/2$.

Fig.5.37 shows $(t_{\text{even}} - t_{\text{odd}})/2$ resolution as a function of $2n$, which is fitted with a model of $\sigma_{n-\text{hits}} = \sigma_{\text{single}}/\sqrt{n_{\text{pTC}}}$. This result indicates σ_{single} of $111.5 \pm 0.8\,\text{ps}$, which is worse than the $\sim 100\,\text{ps}$ result evaluated previously in 2017 [40]. This is understood to come from the accumulated radiation damage in these years.

5.6 Combined $t_{e\gamma}$ calibration and its resolution

5.6.1 Offset calibration

The offset between the position decay time and the gamma decay time was calibrated with RMD events observed in the $45\,\text{MeV} < E_\gamma < 48\,\text{MeV}$ region at a precision of $3\,\text{ps}$.

In addition to the offset between the positron and gamma, the residual offset between the upstream pTC and the downstream pTC was also observed. This was calibrated by combining the RMD events observed in the $45\,\text{MeV} < E_\gamma < 48\,\text{MeV}$ region and the RMD-enhanced calibration samples. The residual offset was corrected according to the observed residual of $32 \pm 3\,\text{ps}$. This suggests that the laser-based upstream vs downstream calibration was not perfect or had some biases, which is still not fully understood.

5.6.2 Calibration for trigger and data pre-selection

As described in Sec.2.7.2, $t_{\text{pTC}} - t_{\text{LXe}}$ without the TOF correction is used in the data pre-selection scheme. Therefore, the window for $t_{\text{pTC}} - t_{\text{LXe}}$ was optimized making use of the RMD events. Here,

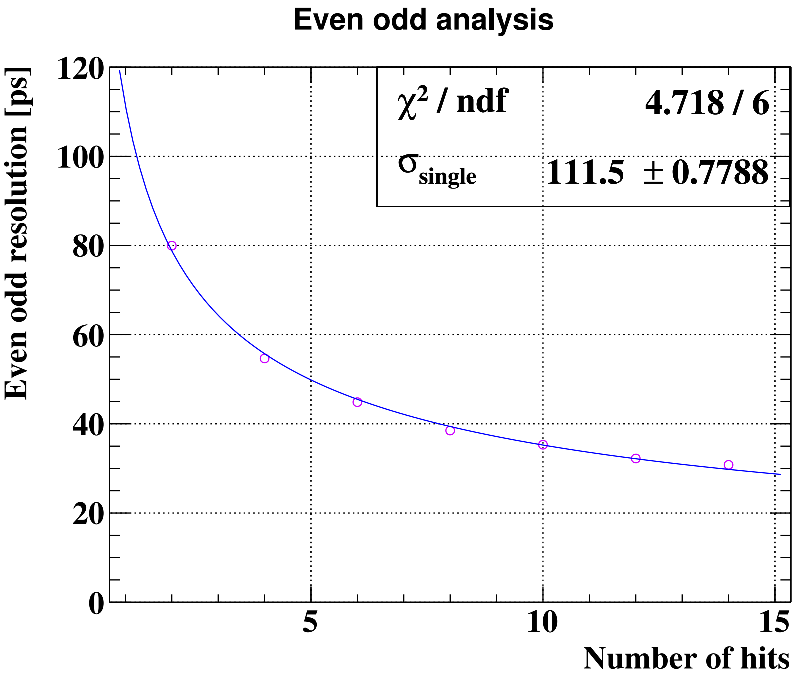

Figure 5.37: The time resolution evaluated with the even-odd method. The fitted value gives $\sigma_{\text{single}} = 111.5 \pm 0.8\,\text{ps}$.

events with $|t_e - t_\gamma| < 4\,\text{ns}$ were selected and the maximum and minimum value of $t_{\text{pTC}} - t_{\text{LXe}}$ defined the window. Similarly, the online time-coincidence trigger in Sec.2.6.2 was optimized at the beginning of the physics data taking.

5.6.3 Full evaluation of $t_{e\gamma}$ resolution

The $t_{e\gamma}$ resolution was evaluated by decomposing it into the pTC contribution and the others, where the pTC contribution is different event-by-event and the other contribution is constant. This is because the pTC average contribution becomes larger with a smaller E_e (presented later in Fig.6.10), which means that the average σ_{t_e} for RMD events is worse than that for the signal events. The decomposed resolution is estimated in a simultaneous fitting to the RMD-subsets categorized by the number of hits on the pTC (Fig.5.38). The RMD response in each category is modeled as $\sigma_{\text{TC}}/\sqrt{n_{\text{pTC}}} \oplus \sigma_{\text{const}}$, where $\sigma_{\text{TC}} = 112\,\text{ps}$ is from the even-odd analysis and σ_{const} is the estimated parameter. A naive fitting gave $\sigma_{\text{const}} = 73 \pm 4\,\text{ps}$ as a result. This term, expected to be dominated by the LXe time resolution, agrees with the $\pi^0 \to \gamma\gamma$ evaluation of $65 \pm 6\,\text{ps}$. By combining these two estimations, the full estimation of the $t_{e\gamma}$ resolution became

$$\frac{112\,\text{ps}}{\sqrt{n_{\text{pTC}}}} \oplus 70\,\text{ps}, \tag{5.16}$$

whose average over signal events is $\sigma_{t_{e\gamma}} \sim 85\,\text{ps}$.

5.7 RDC LYSO energy scale calibration

Though the resolution requirements for the RDC detector are not high, moderate optimization and calibration are still necessary. In particular, the LYSO counters need energy calibration in $\mathcal{O}(10\,\%)$ precision to have a uniform response to RMD-associated low-energy positrons. The RDC energy scale is calibrated with the intrinsic radioactivity of the LYSO crystals, which gives the total gamma-ray energy deposit of $596\,\text{keV}$. The peak in Fig.5.39 corresponds to the $596\,\text{keV}$ activity and the fitted parameter is used to calibrate the energy scale. The high voltage of the 76 MPPCs for the LYSO crystals is also

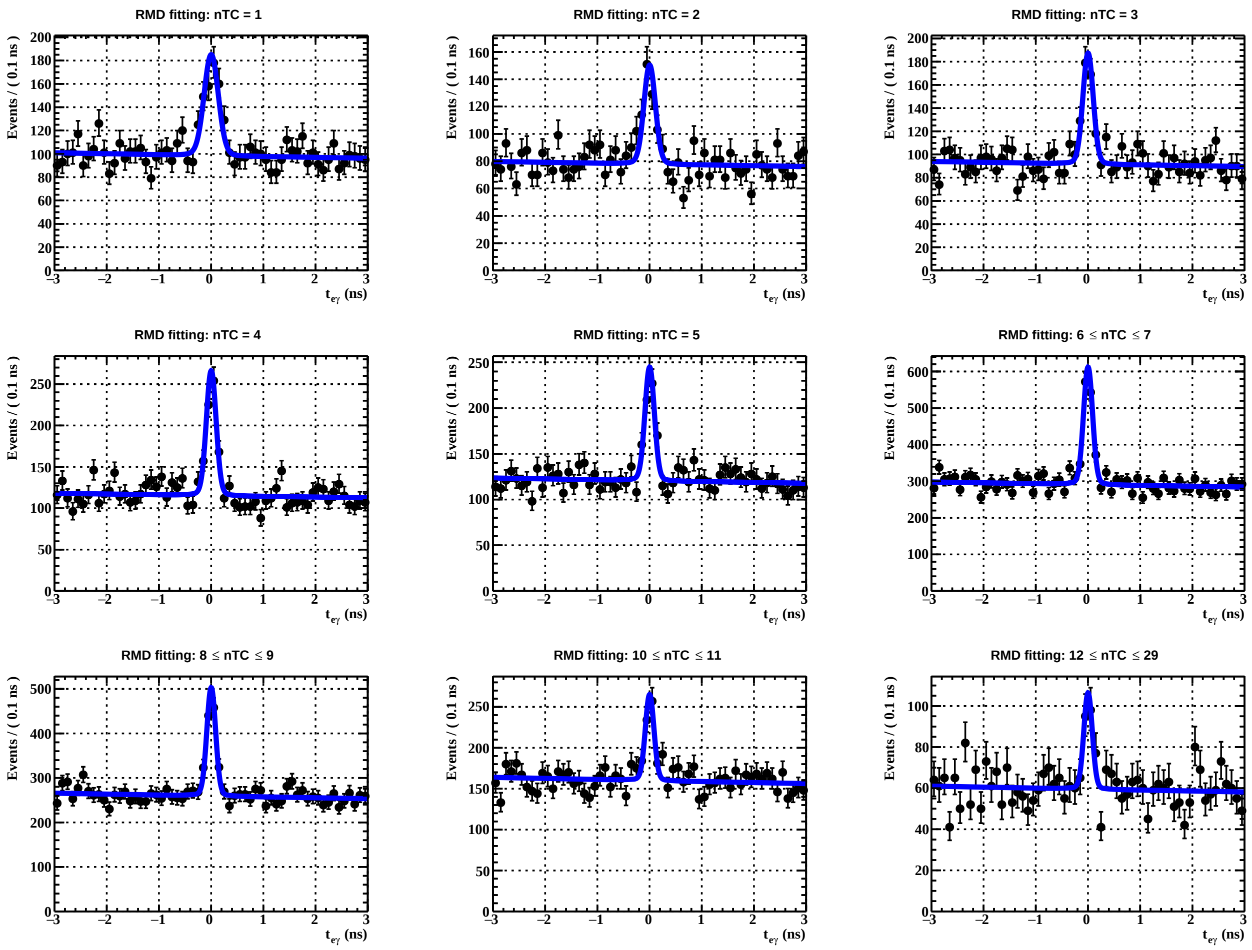

Figure 5.38: Time resolution evaluation in the peak fitting to RMD events. Event samples are divided into the shown 9 subsets according to the number of pTC hits and a simultaneous fitting is performed (blue lines in each subset). The data distribution indicates a resolution improvement with a larger number of n_{pTC}.

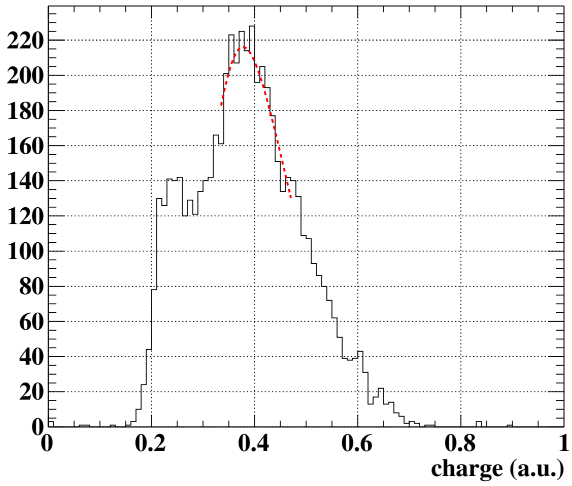

Figure 5.39: Spectrum of the observed LYSO self radiation [49]. The peak corresponds to $596\,\mathrm{keV}$, which is fitted (red line) to obtain the energy scale.

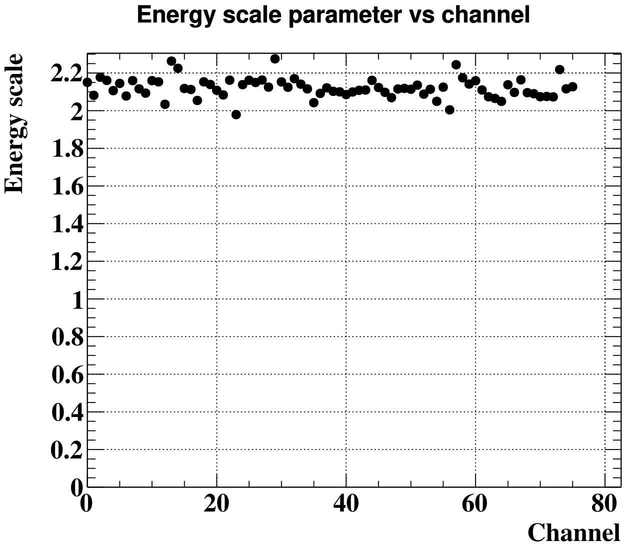

Figure 5.40: Energy scale distribution of LYSO channels in the 2021 run after a high-voltage adjustment.

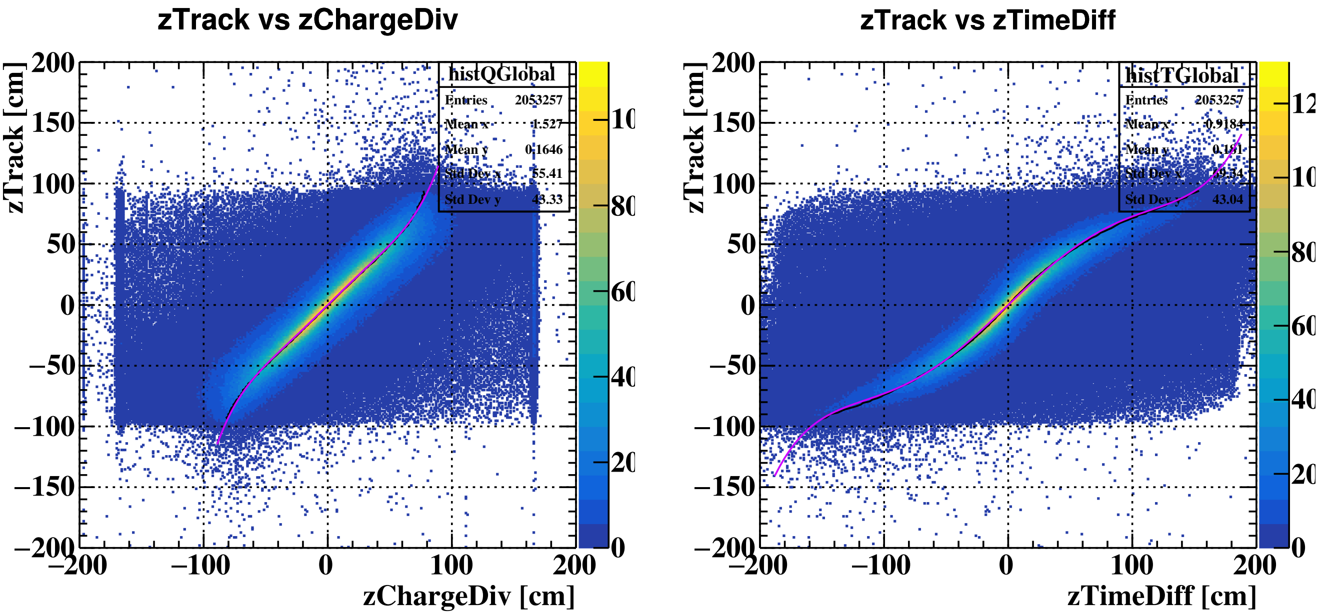

Figure 5.41: Observed nonlinearity of the z measurement in CDCH hit reconstruction for charge division method (left) and time difference method (right). The profile of each scatter plot is fitted with a polynomial (magenta curve).

adjusted to have a high uniformity in the energy scale (Fig.5.40). The overall precision of the energy scale calibration is a few percent, which is smaller than required.

5.8 CDCH calibration

5.8.1 CDCH Z measurement calibration

The CDCH z measurement in the hit reconstruction was calibrated by comparing the reconstructed track z position with the reconstructed hit position by Eq.(4.4) and Eq.(4.5). The G_{diff} and t_{wireends} were calibrated to eliminate the offset between the measured z and the track-fitted z position. In addition, non-linearity was found between the hit and the track (Fig.5.41), which were modeled with polynomials and calibrated by fitting the observed distribution accordingly.

Positron tracks leave most of the hits in the wire center region whereas many cosmic-ray track hits can be found also in the wire end region. The G_{diff} and t_{wireends} calibration, which does not require hits in the end region, can be calibrated both with the positron tracks and cosmic-ray tracks. On the other hand, the non-linearity calibration used cosmic-ray events because of the necessity of a higher hit occupancy in the wire end regions.

The z measurement resolution in the hit reconstruction was evaluated on the positron tracks as shown in Fig.5.42. Though both the time difference method and the charge division method have a core resolution of $9\,\text{cm}$, the charge division method has a larger tail in the measurement. Therefore, a higher weight is assigned to z_T in the full hit z reconstruction as $z_{\text{hit}} = 0.3 \cdot z_Q + 0.7 \cdot z_T$, giving an overall core resolution of $7.5\,\text{cm}$.

5.8.2 CDCH wire alignment

Though the CDCH wire positions were measured during the assembly, residual biases were observed between the fitted track position and the initially estimated hit position (Fig.5.43). This was corrected in an iteration of wire position shifting by the observed average of the residual. Due to the DAF algorithm in the track reconstruction, the hits used in Fig.5.43 are biased because hits are dropped from the track

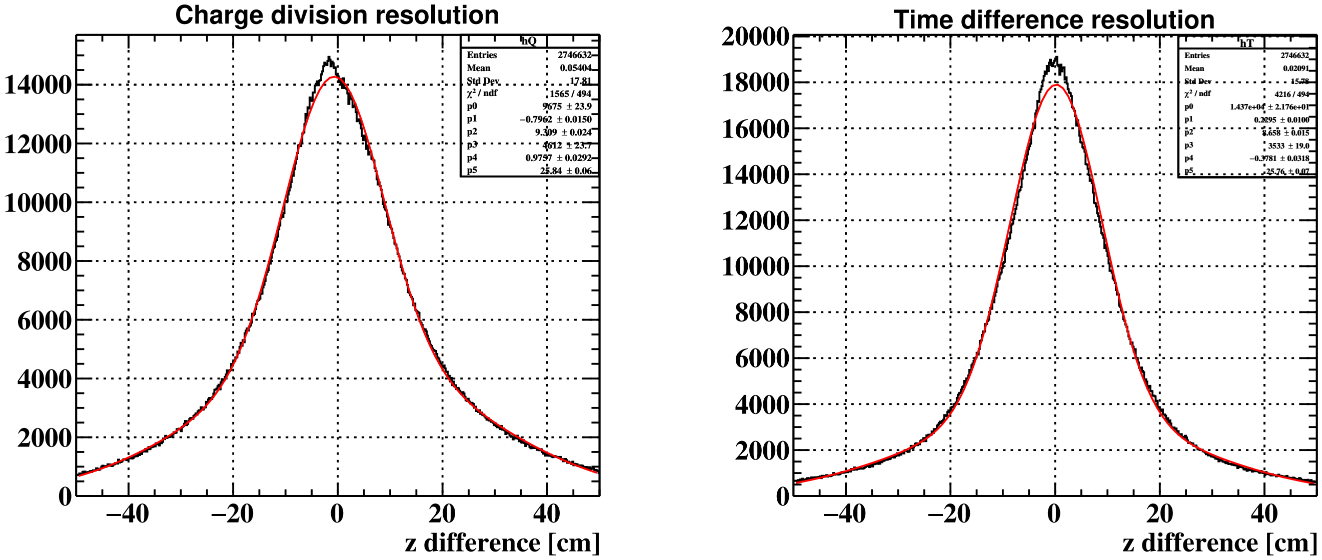

Figure 5.42: Estiamted z position difference between the measurement in hit reconstruction and the fitted track position for the charge division method (left) and the time difference method (right). The Gaussian fitting to each distribution indicates a $9\,\mathrm{cm}$ precision from each method, which gives $7.5\,\mathrm{cm}$ resolution when combined with an optimized weight.

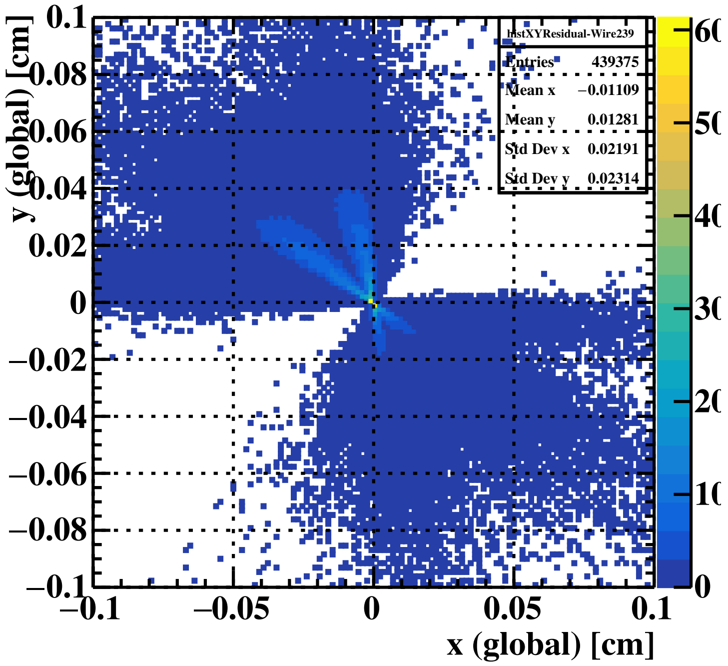

Figure 5.43: Distribution of the difference between the measured position of the hit reconstruction and the fitted track position on a wire. The asymmetry of the distribution is caused by a misalignment of the wire. Two line-shaped peaked regions are produced by the typical track crossing angle on the wire (one for tracks towards the inner direction and the other for those towards the outer direction).

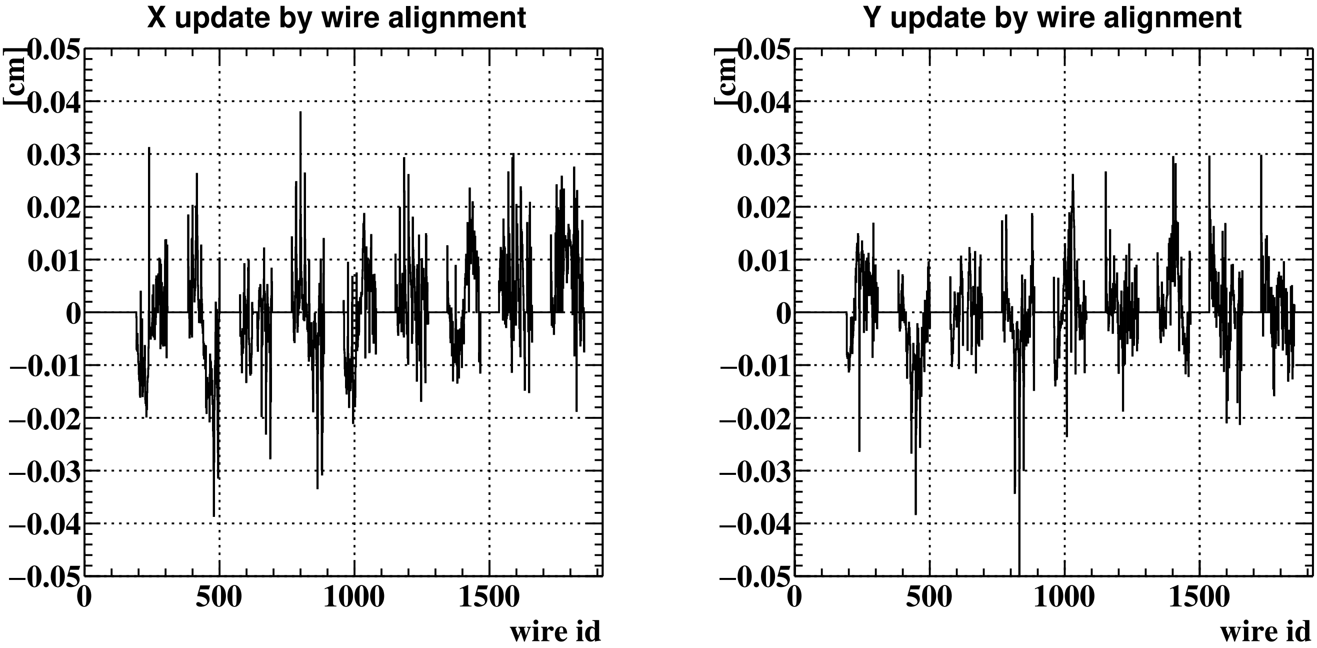

Figure 5.44: Wire position change before and after the wire alignment in x-coordinate (left) and y-coordinate (right). As indicated, typical misalignment is $\mathcal{O}(100\,\mu\mathrm{m})$.

fitting when the measured position is ill-consistent with the reconstructed track position. Furthermore, each track is not sensitive to the wire misalignments in the parallel direction to the track, which means that the averages of the residual are biased to give even smaller values than the actual ones. Therefore, the wire shifting by the residual average needs to be iterated until the update converges. Fig.5.44 shows the resulting x and y position shift before and after the track-based wire alignment. The final corrections (after the iteration) to the wire shown in Fig.5.43 were $\sim 300\,\mu\mathrm{m}$ for both x and y coordinates, which are larger than the observed average residual of $\sim 100\,\mu\mathrm{m}$ in Fig.5.43 because of the biases explained above.

5.8.3 CDCH drift time to distance calibration

The time-to-distance relation, $\zeta_{txy}(t)$ in Eq.(4.6), is based on Garfield++ simulation results. This simulation-based conversion can also be used to give a drift time estimation for each hit as

$$t_{\mathrm{drift}} = \zeta_{txy}^{-1}(d_{\mathrm{track}}), \tag{5.17}$$

where t_{drift} is the drift time estimated from the gas table, and d_{track} is the estimated drift distance according to the track reconstruction. The wire-to-wire time offset of the CDCH readout can then be aligned by

$$t_{\mathrm{wireoffset}} = t_{\mathrm{hit}} - t_{\mathrm{drift}} - t_{\mathrm{pTC}} + t_{\mathrm{TOF}}, \tag{5.18}$$

which compares the pulse time with the estimated arrival time of the gas cluster on the wire.

The full calibration refinement of the $\zeta_{txy}(t)$ itself, on the other hand, was performed by a machine learning-based approach, which was trained on the data. The machine learning model has several inputs to include different entangled dependencies: the layer index, the reconstructed hit time, and the amplitude of the waveform. The final resolution of the drift distance measurement is $150\,\mu\mathrm{m}$ as shown in Fig.5.45.

5.9 Positron momentum resolution and calibration

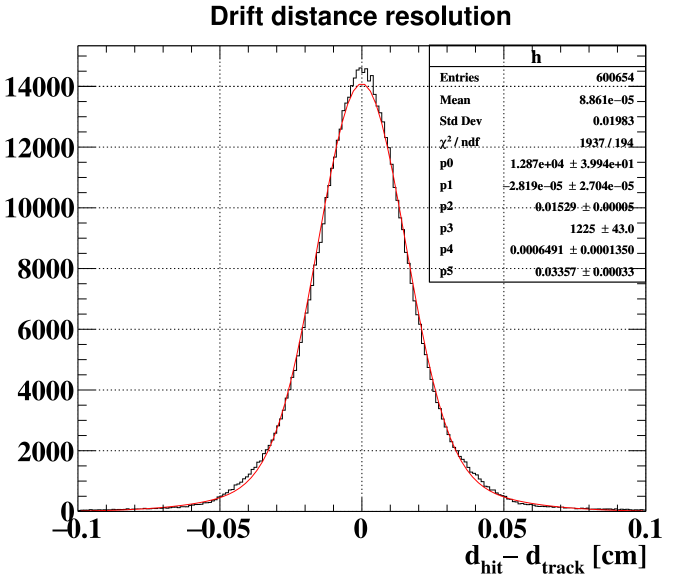

Figure 5.45: Distribution of the difference between the measured drift distance in the hit reconstruction and that of the fitted track. The Gaussian fitting to the distribution indicates a $150\,\mu\mathrm{m}$ precision.

5.9.1 Energy scale and response evaluation

To estimate the energy scale and the detector resolution, the energy spectrum of the Michel positron was fitted with the below model

$$\mathrm{Fit}(E_e) = \big(\mathrm{Theory}(E_e) \times \mathrm{Acceptance}(E_e)\big) \otimes \mathrm{Resolution}(E_e). \tag{5.19}$$

The theory spectrum uses the result in [33], which includes one-loop radiative corrections. The acceptance function, which describes the efficiency dependence on E_e, was modeled with error functions. The resolution function was modeled with a sum of three Gauss functions. Fig.5.46 shows the fit result for the reconstructed energy spectrum. The energy scale of the positrons was calibrated with a $0.01\,\%$ precision by correcting the offset of the response function. The momentum resolution was evaluated to be $90\,\mathrm{keV}$ from its resolution parameters.

In the positron tracking, the Kalman filter estimates the uncertainty for each fitted parameter. The estimated momentum uncertainty is shown in Fig.5.47, where the overall behavior agrees with the estimated average resolution of $90\,\mathrm{keV}$. The resolution dependence on the tracking uncertainty is also evaluated by fitting to the Michel edge of sliced data samples, which will later be shown in Fig.6.8. As a result, we found a clear correlation between the tracking uncertainty and the estimated resolution in the Michel fitting, as shown later in Fig.6.9. This, however, also indicates 5 – $10\,\%$ underestimation of the resolution by the track fitting, which likely suggests that some effects are missing when the tracking uncertainty is estimated. Though we have not yet reached any conclusion, one suspicious cause is that the scattering inside the wire material is not correctly taken into account.

In the distribution of momentum uncertainty, we see the lower bound at $\sim 55\,\mathrm{keV}$, which is understood to be dominated by the uncertainty due to the scattering in the material. On the other hand, the broader range of the uncertainty distribution reflects the quality of the track fitting. The peak around $60\,\mathrm{keV}$ is made by the double-turn tracks, which have abundant hits along its path in the CDCH. The small bump around $100\,\mathrm{keV}$ is made by tracks that are not efficient in finding hits in the last half-turn before entering the pTC.

5.9.2 Alignment of magnetic field

The gradient magnetic field requires a good alignment with the CDCH to have a good uniformity in the energy scale with respect to the positron emission angle. The impact of the magnetic field misalignment

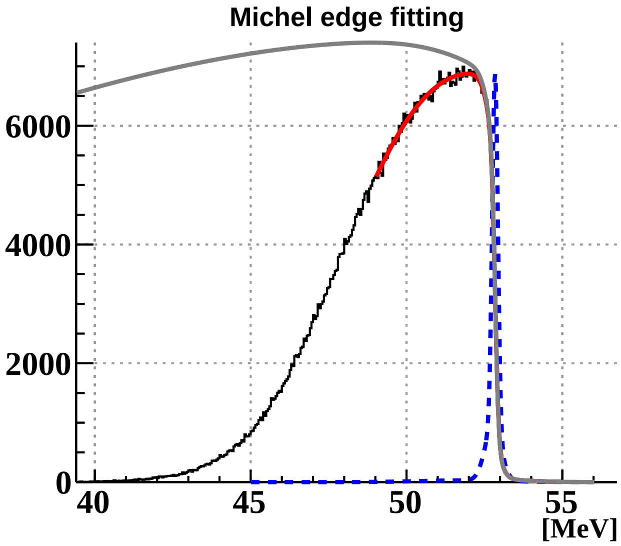

Figure 5.46: Observed positron momentum spectrum and the fit (red line) to evaluate the energy scale and resolution. The dashed blue line shows the estimated response to $52.8\,\mathrm{MeV}$ positron, giving the resolution value of $90\,\mathrm{keV}$. The gray curve is the expected spectrum without the acceptance function, i.e. the convoluted spectrum of the theory function with the resolution function.

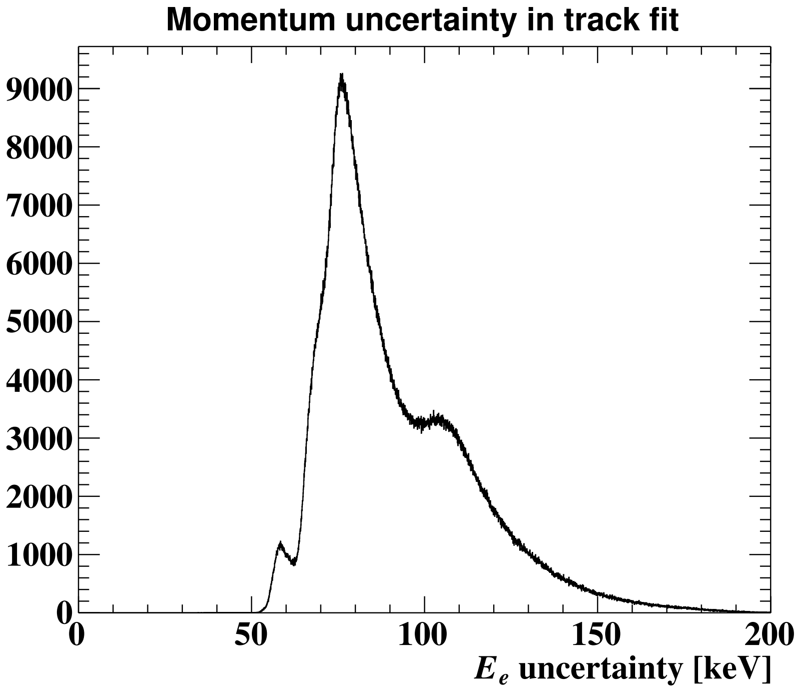

Figure 5.47: Distribution of positron momentum uncertainty estimated in the track fitting.

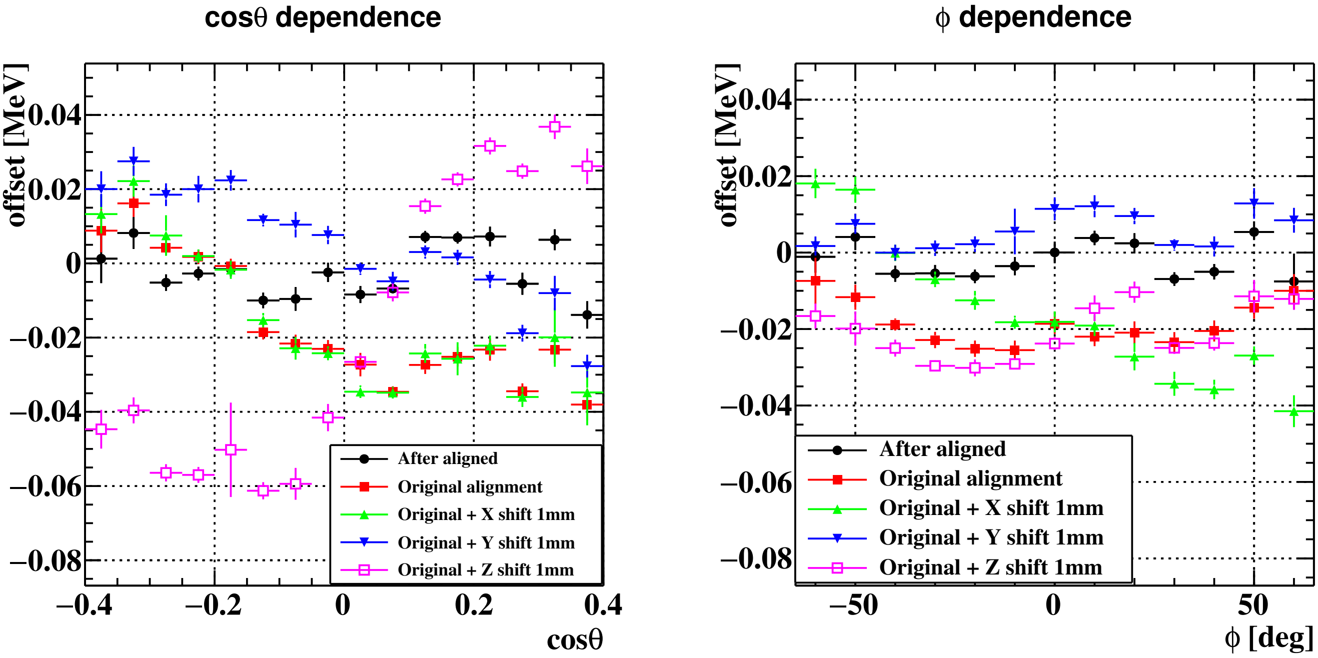

Figure 5.48: Magnetic field alignment with the angular dependence of the energy scale. The impact of misalignment in each direction is shown as well as the observed angular dependence. The y-axis indicates the bias on the positron momentum for $52.8\,\mathrm{MeV}$ tracks.

is illustrated in Fig.5.48, which shows θ_e and ϕ_e dependence of the energy scale evaluated from the Michel edge fitting to sliced data samples. The misalignment in the positive x direction results in a decreasing energy scale with an increasing ϕ_e. The misalignment in the positive y direction results in an energy scale maximized at $|\phi_e| = 0$. The misalignment in the positive z direction results in an increasing energy scale with an increasing $\cos\theta_e$.

The magnetic field was thus aligned to minimize the observed energy scale dependence on the emission angle. As a result, the magnetic field calculated from the COBRA design was shifted by 100 µm in x, 700 µm in y, and $300\,\mu$m in z, where the estimated alignment precision in x and z direction was 100 µm and that in y was 200 µm.

5.10 Positron resolution in double turn analysis

The vertex resolution and the angle resolution of the positron tracking were evaluated with double-turn tracks described in Sec.4.1.9, which account for $10\,\%$ of all the tracks. The first and the second turn tracks are separately fitted and the reconstructed position and angle are compared at the middle point. The difference receives the contribution of the first and second turn resolution. In addition, the first turn includes hits only in the first turn, which is less than the usual 1.5 turns included in most of the tracks. These effects were evaluated with MC samples, in which the true MC resolution ($\sigma^{\mathrm{MC\ truth}}$) can be evaluated as well as the MC double turn resolution ($\sigma^{\mathrm{MC\ DT}}$).

The data resolution was finally evaluated by scaling the data double turn resolution with this correction factor;

$$\sigma^{\mathrm{data}} = \sigma^{\mathrm{data\ DT}} \times \frac{\sigma^{\mathrm{MC\ truth}}}{\sigma^{\mathrm{MC\ DT}}}.$$

The estimated resolution on the data is $\sigma_{y_e} = 0.7\,\mathrm{mm}$, $\sigma_{z_e} = 2.0\,\mathrm{mm}$, $\sigma_{\theta_e} = 7.2\,\mathrm{mrad}$, and $\sigma_{\phi_e} = 4.1\,\mathrm{mrad}$.

The double turn resolution can also be evaluated on *pull*, which for θ_e is defined as $\delta\theta_e/\sigma'_{\theta_e}$. Here, $\delta\theta_e$ is the error of θ_e measurement and σ'_{θ_e} is the nominal θ_e uncertainty according to the track fitting. The resolution of the pull, denoted hereafter as $s_{\phi_e}, s_{\theta_e}, s_{z_e}, s_{y_e}$, was also evaluated with the double turn analysis as

$$s_{\theta_e}^{\mathrm{data\ DT}} = \frac{\theta_e^{\mathrm{first-turn}} - \theta_e^{\mathrm{second-turn}}}{\sqrt{\left(\sigma'^{\mathrm{first-turn}}_{\theta_e}\right)^2 + \left(\sigma'^{\mathrm{second-turn}}_{\theta_e}\right)^2}}, \tag{5.20}$$

which was then corrected with the correction factors estimated with MC samples. The correction factors, $s^{\mathrm{MC\ truth}}/s^{\mathrm{MC\ DT}}$, are introduced to correct the difference in the pull resolution between the double turn analysis and the MC truth, which were observed to be $\sim 10\,\%$ in MC samples. As a result, the estimated pull resolution is $s_{\phi_e} = 1.3, s_{\theta_e} = 1.2, s_{z_e} = 1.9$, and $s_{y_e} = 1.2$.

The double turn analysis can also be used to cross-check the momentum resolution evaluated in the Michel edge fitting (Sec.5.9) though the latter is more reliable because it is based on the full tracks (i.e. not based on tracks split into different turns). In particular, it is interesting to evaluate the pull resolution according to Eq.(5.20). The estimated values are $s_{E_e}^{\mathrm{data\ DT}} = 1.2$ and $s_{E_e}^{\mathrm{MC\ truth}}/s_{E_e}^{\mathrm{MC\ DT}} = 0.85$, which gives $s_{E_e} = 1.05$. This agrees with the result of Michel fitting to the sliced data samples (Fig.6.9), including the suggested 5 – $10\,\%$ underestimation of the resolution in the track fitting.

5.11 Global detector alignment

5.11.1 Target deformation and time shift of position

The target shape was measured by a CT scan before the installation, which was then combined with the optical marker position measurement after the installation. The time variation of the overall target rotation and translation was also followed by the printed dot markers reconstructed in the photograph data. Due to the absence of a photograph taken simultaneously with the optical marker measurement, the target position history is not fully known exactly. As a compromise, the position in the optical measurement was assumed to be the same as that in the first target photograph. The possible difference between them will be compensated by the target hole analysis described later in Sec.5.11.2. The position during the absence of the camera is assumed to be randomly distributed, and a large angular uncertainty is assigned to reconstructed positrons in those periods.

5.11.2 Alignment between CDCH and target

The target hole analysis evaluates the residual misalignment of the nominal hole position, which is obtained by combining the CT scan and target photographs. This analysis makes use of the holes in the reconstructed position distribution on the target (Fig.5.49). The y and z positions of each hole can be straightforwardly estimated from the dip position. The x misalignment geometrically produces an angle-dependent bias in the y-reconstruction as $\delta y \approx \tan\phi \cdot \delta x$. Therefore, x-coordinate can also be aligned as shown in Fig.5.50 from the dependence of the estimated y-position of each hole on the ϕ emission angle. With the nominal position given for each of the holes, this analysis independently estimates hole-by-hole residual misalignment. The full detail of the analysis method and its systematics are described in Appendix.D.

The estimated precision of the alignment at each hole was composed of 100 – $200\,\mathrm{\mu m}$ statistical uncertainty in each of x, y, z coordinate, and the systematic uncertainty of $(50\,\mathrm{\mu m}, 100\,\mathrm{\mu m}, 200\,\mathrm{\mu m})$ (see Tab.D.1 for the detail). The global translation and rotation were estimated by combining the results on different holes, and the uncertainty was $100\,\mathrm{\mu m}$ for the translations and $6\,\mathrm{mrad}$ $(1.4\,\mathrm{mrad})$ for the rotation around the target long (short) axis. The estimated shift, $(100\,\mathrm{\mu m}, 800\,\mathrm{\mu m}, 400\,\mathrm{\mu m})$, is attributed mostly to the CDCH misalignment, because a similar result was obtained also in CDCH vs COBRA alignment discussed in Sec.5.9.2.

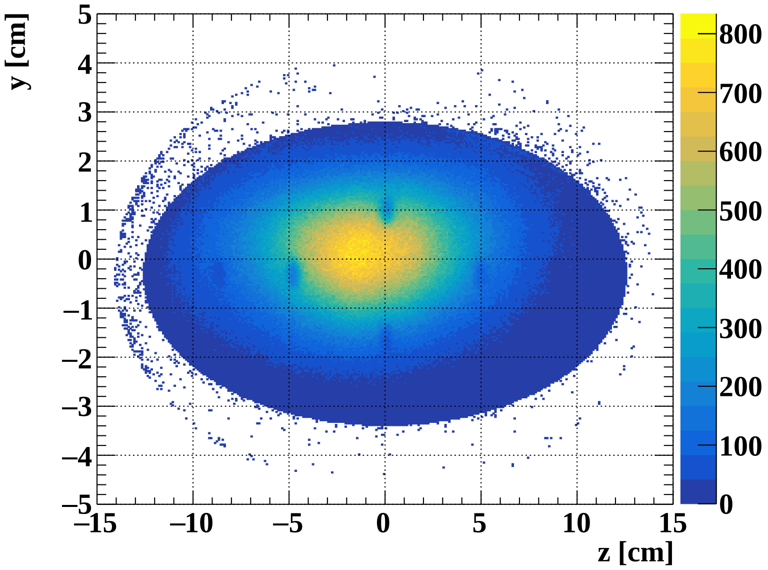

Figure 5.49: Reconstructed position distribution on the muon stopping target projected on the yz plane. Six holes are visible as the dips of the distribution.

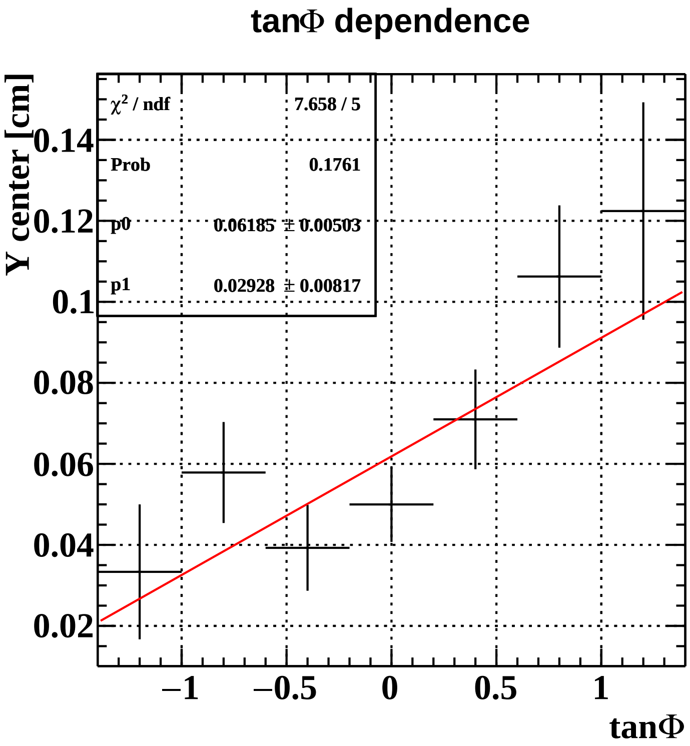

Figure 5.50: Estimated y position of a hole with positrons of different $\tan \phi$. The slope of the linear fit (300 µm) gives an estimate of x-misalignment, and the offset of the fit (600 µm) gives an estimate of y-misalignment.

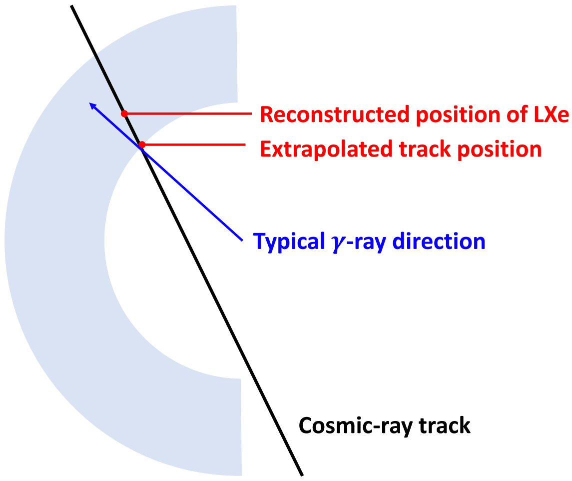

Figure 5.51: Illustration of alignment of the LXe detector and CDCH with linear cosmic-ray tracks with an indication of biases.

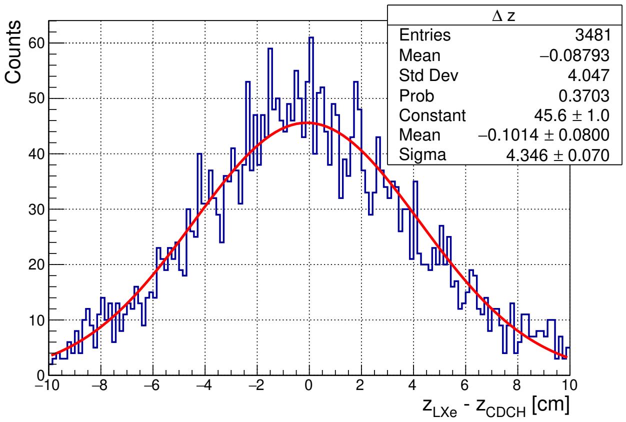

Figure 5.52: $z_{\mathrm{LXe}} - z_{\mathrm{track}}$ distribution and its fit with a Gauss function [58]. The fit indicates a $1\,\mathrm{mm}$ misalignment between the LXe and CDCH.

Table 5.1: Alignment summary. The estimated relative position with respect to the CDCH nominal position is tabulated.

Sub-detector	δx	δy	δz
Magnetic field (Sec.5.9.2)	$100 \pm 100\,\mu\mathrm{m}$	$700 \pm 200\,\mu\mathrm{m}$	$300 \pm 100\,\mu\mathrm{m}$
Muon stopping target (Sec.5.11.2)	$80 \pm 100\,\mu\mathrm{m}$	$860 \pm 100\,\mu\mathrm{m}$	$500 \pm 100\,\mu\mathrm{m}$
LXe detector (Sec.5.11.3)	no evaluation	no evaluation	$1000 \pm 800\,\mu\mathrm{m}$

5.11.3 Alignment between CDCH and LXe

The CDCH and the LXe were aligned with cosmic-ray tracks in data taken without a magnetic field. The reconstructed linear tracks in the CDCH were extrapolated to the inner face of the LXe ($r = 64.97\,\mathrm{cm}$), and the reconstructed position in the LXe was compared with that of the extrapolated track (Fig.5.51). Here, the position reconstruction in the LXe had a bias to give a deep point (not on the inner face), which biased the reconstructed u, v position according to the track direction. Because of this bias and the angle distribution of the cosmic-rays, the v-coordinate difference cannot be reliably aligned. On the other hand, the u-coordinate (or equivalently z-coordinate) can be aligned by exploiting the geometrical upstream vs downstream symmetry of the detector; namely, the bias, which cannot be eliminated track-by-track, was expected to be cancelled out in the overall $z_{\mathrm{LXe}} - z_{\mathrm{track}}$ distribution. Fig.5.52 shows its distribution suggesting a $1\,\mathrm{mm}$ misalignment between the LXe and CDCH.

5.11.4 Alignment summary

The results of detector alignment are summarized in Tab.5.1. Here, we see a good agreement between the target position and the magnetic field position within each uncertainty. However, both of them show large shifts in the y-axis with respect to the nominal CDCH position according to an optical survey of wire ends. The z misalignment also shows a similar trend; all three sub-detectors are offset in the positive direction and all the shifts agree with each other within the uncertainties. Though these are understood to be likely a real misalignment of the CDCH, they leave a $\sim 1\,\mathrm{mm}$ uncertainty in the absolute CDCH position. This uncertainty on the CDCH absolute position matters in the global CDCH vs LXe alignment because there was no direct alignment method between them in x and y directions.

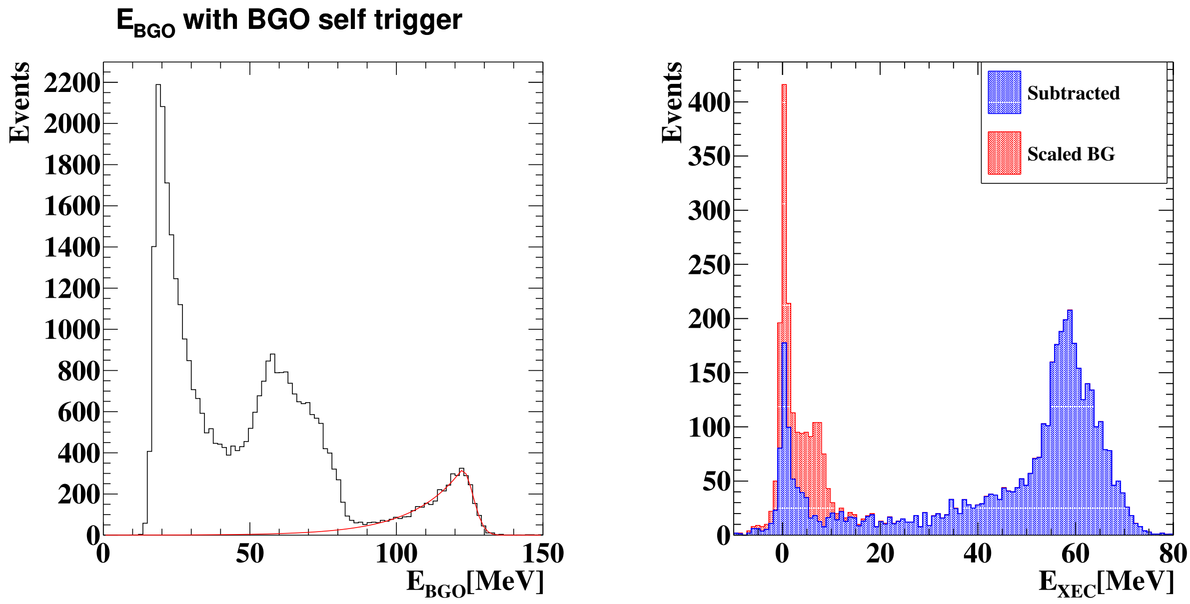

Figure 5.53: The background estimation in the efficiency measurement [48].

Final alignment uncertainty

With all the above considerations, the alignment uncertainties are concluded as below.

- The uncertainty on relative x-shift between the CDCH and the LXe is $100\,\mu\mathrm{m}$,
- The uncertainty on the shift between the CDCH and LXe is $1\,\mathrm{mm}$.

5.12 LXe efficiency evaluation

The detection efficiency of the LXe detector, defined as the fraction of the number of detected signal events out of those coming in the fiducial volume, was evaluated with the $\pi^0 \to \gamma\gamma$ events triggered by logic only on the BGO detector. By selecting BGO hits estimated to be from $83\,\mathrm{MeV}$ gamma-rays, $55\,\mathrm{MeV}$ gamma-ray samples emitted in the LXe direction can be obtained. By counting the efficient ones among them, the efficiency of the LXe gamma-ray detection can be evaluated.

In the efficiency measurement, there were background events associated with neutron capture events, $\pi^- p \to n\gamma$, with the final state gamma of $129\,\mathrm{MeV}$ (recall Panofsky ratio in Eq.(2.6)). The contamination in the BGO-based event tagging, which was evaluated from the spectrum fitting to the $129\,\mathrm{MeV}$ peak in the reconstructed BGO energy (Fig.5.53), gave an uncertainty of $\sim 1\,\%$.

In order to correct the difference in the material budget between the physics data and $\pi^0 \to \gamma\gamma$ data, the measured efficiency was compared with MC samples simulating $\pi^0 \to \gamma\gamma$ events that leave hits in the BGO detector as shown in Fig.5.54. There was an unexplained $2.9\,\%$ discrepancy between them, which is suspected to be from the wrong incorporation of the material budget either of the LXe detector components or the liquid hydrogen target components. Here, the former case results in a reduction of the efficiency also in the $\mu \to e\gamma$ detection while the latter has no impact on $\mu \to e\gamma$. This therefore gives an additional uncertainty to the efficiency evaluation for the signal gamma-ray detection. With all the uncertainties included, the estimated efficiency for the $52.8\,\mathrm{MeV}$ gamma-rays is $\epsilon_\gamma = 0.67 \pm 0.02$.

This, so far, considers only the efficiency associated with the gamma-ray interaction inside the material, which does not include the inefficiencies of the analysis. In reality, the final $\mu \to e\gamma$ analysis is also subject to the inefficiency of the gamma-ray selection described in Sec.4.2.6, which is dominated by the selection of the pileup analysis. This additional contribution was evaluated to be $93 \pm 2\,\%$, as will be detailed in Sec.6.3.1.

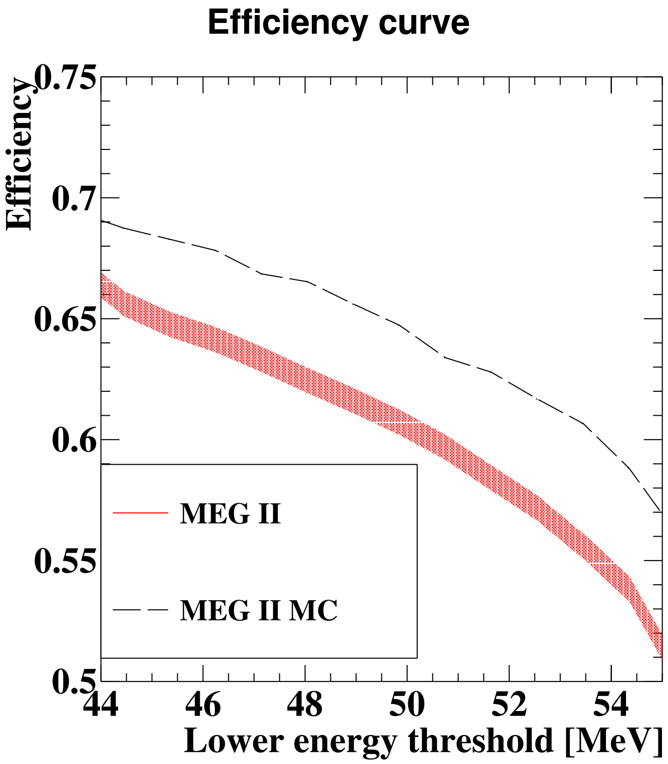

Figure 5.54: Data vs MC comparison of the efficiency analysis result [48]. $1.8\,\%$ out of the $4.9\,\%$ discrepancy is understood to come from inactive volume not included in the simulation.

Table 5.2: Results of hit efficiency evaluation of the CDCH both for MC and data.

Condition	Hit efficiency
Data at $3 \times 10^7\ \mu/\mathrm{s}$	$67 \pm 3\,\%$
Data at $5 \times 10^7\ \mu/\mathrm{s}$	$64 \pm 3\,\%$
MC simulation at $3 \times 10^7\ \mu/\mathrm{s}$	$70 \pm 3\,\%$

5.13 Positron efficiency evaluation

5.13.1 CDCH hit efficiency evaluation

The hit efficiency on a layer of CDCH was evaluated by tracking without the wires belonging to the layer and then extrapolating the tracks to the turned-off wires. This gave candidate hit positions on the turned-off wires with estimations of d_{drift}. These candidate hits were then matched, if existed, with reconstructed hits on the wires. In order not to pick up hits from pileup positrons, a consistency cut was applied on the difference between the measured drift distance and the track-estimated drift distance (Fig.5.55). The efficiency was measured from the fraction of consistently matched hits on the turned-off wires in all the candidate hits.

This analysis was performed both on data and MC simulation samples, and the results are summarized in Tab.5.2. The data and MC simulation agreed with each other within their uncertainty of $3\,\%$, which is dominantly from the ambiguities in the definition of pileup rejection. The degradation of the hit efficiency with an increased beam intensity is expected because pileups in the waveform analysis can make hits inefficient. This inefficiency, however, was found to be small in this analysis.

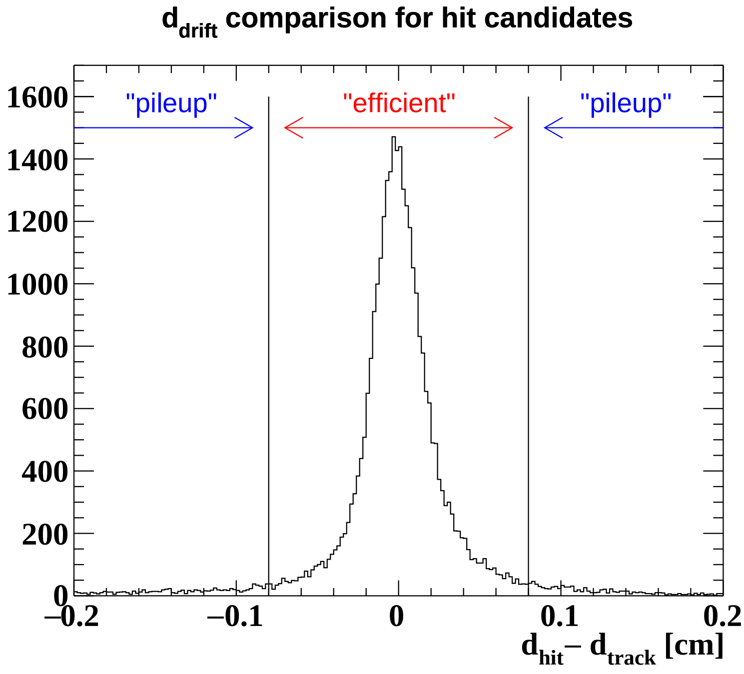

Figure 5.55: Distribution of drift distance difference between the wire-crossing position of tracks and found hits on the same wires. The peak is from hits that are really from interaction with the tested track, while a longer tail than the distribution in Fig.5.45 is also present because of pileup hits. Hits that happen in the peak region of the distribution are counted as efficient hits, which are defined by the cut range depicted in the plot.

Table 5.3: Results of positron tracking efficiency evaluation. Estimated efficiency with and without the use of the Machine Learning method in the hit reconstruction (introduced in Sec.4.1.2) is compared as well as the muon stopping rate dependence.

Condition	Tracking efficiency	Tracking efficiency (without ML hit finding in CDCH)
Data at $3 \times 10^7\,\mu/\mathrm{s}$	$67\,\%$	$60\,\%$
Data at $5 \times 10^7\,\mu/\mathrm{s}$	$60\,\%$	$48\,\%$

5.13.2 Positron tracking efficiency evaluation

The positron tracking efficiency is defined by the fraction of high-quality positron reconstruction out of all the $52.8\,\mathrm{MeV}$ positrons emitted in the opposite of the LXe fiducial region. It was evaluated with data samples triggered only on the pTC, which gives minimum-biassed samples of Michel positrons. The efficiency was estimated by dividing the counted number of Michel positrons by the expected number. The denominator in this calculation was evaluated as a product of the beam rate, geometrical acceptance of the LXe detector, and the trigger efficiency for the pTC-only trigger. The counting method for the numerator is used also in a normalization estimation method discussed later in Sec.6.3.1, and all details about the other necessary corrections will be described there.

The estimated efficiencies are summarized in Tab.5.3. The uncertainty of the evaluation is dominated by the muon-stopping rate estimation. It can also be seen that the ML hit finding method in the waveform analysis gives a higher efficiency; $\times 1.1$ higher at $3 \times 10^7\,\mu/\mathrm{s}$ and $\times 1.2$ higher at $5 \times 10^7\,\mu/\mathrm{s}$. We can also find an efficiency decrease with an increased beam rate. As the hit efficiency in Tab.5.2 is comparable even at a higher beam rate, this inefficiency is mostly attributed to algorithm inefficiency of the track finding in a high pileup environment.

Chapter 6

Analysis

6.1 Analysis framework

6.1.1 Likelihood function

An extended unbinned maximum likelihood fit to the data samples is performed to estimate N_{sig}, which is the expected number of signal events in the dataset. As nuisance parameters, $N_{\mathrm{Acc}}, N_{\mathrm{RMD}}, X_{\mathrm{TGT}}$ are also introduced in the fitting to incorporate part of systematic uncertainties in the fitting. Here, N_{Acc} is the expected number of accidental events (see Sec.1.2.2), N_{RMD} is that of RMD events (see Sec.1.2.3), and X_{TGT} is a parameter to incorporate uncertainties in the target alignment (see Sec.5.11).

The full likelihood function on these fit parameters is described as

$$
\begin{aligned}
& L(N_{\mathrm{sig}}, N_{\mathrm{RMD}}, N_{\mathrm{Acc}}, X_{\mathrm{TGT}}) \\
:= \quad & \exp\left(-\frac{(X_{\mathrm{TGT}})^2}{2\sigma_{\mathrm{TGT}}^2}\right) && (6.1\mathrm{a}) \\
& \times \exp\left(-\frac{(N_{\mathrm{RMD}} - \langle N_{\mathrm{RMD}}\rangle)^2}{2\sigma_{\mathrm{RMD}}^2}\right) \times \exp\left(-\frac{(N_{\mathrm{Acc}} - \langle N_{\mathrm{Acc}}\rangle)^2}{2\sigma_{\mathrm{Acc}}^2}\right) && (6.1\mathrm{b}) \\
& \times \frac{e^{-(N_{\mathrm{sig}}+N_{\mathrm{RMD}}+N_{\mathrm{Acc}})}}{N_{\mathrm{obs}}!} \prod_{i=1}^{N_{\mathrm{obs}}} \big(N_{\mathrm{sig}} S(\vec{x_i}|X_{\mathrm{TGT}}, \vec{q_i}) + N_{\mathrm{RMD}} R(\vec{x_i}|\vec{q_i}) + N_{\mathrm{Acc}} A(\vec{x_i}|\vec{q_i})\big), && (6.1\mathrm{c})
\end{aligned}
$$

where Eq.(6.1c) is the usual extended likelihood function [99], Eq.(6.1a) is an external constraint term for the detector alignment uncertainty, and Eq.(6.1b) is terms giving constraints to the number of the background events. These constraints are based on uncertainties from subsidiary measurements.

In the extended likelihood term, Eq.(6.1c), N_{obs} is the number of observed events. $S(\vec{x_i}|X_{\mathrm{TGT}}, \vec{q_i})$, $R(\vec{x_i}|\vec{q_i})$, and $A(\vec{x_i}|\vec{q_i})$ are probability density functions (PDF) for signal, RMD, and accidental events, respectively. Their details will be described in Sec.6.7 (for signal), Sec.6.8 (for RMD background), and Sec.6.6 (for accidental background). The $\vec{x_i}$ is a set of fit observables that discriminate signal from backgrounds, and $\vec{q_i}$ is a set of conditional observables, whose details will be discussed later in Sec.6.1.2. The implementation of this analysis is based on RooFit [100, 101], which is a dedicated toolkit for statistical data analysis and is widely used in high-energy physics experiments.

Conversion to branching ratio

As the likelihood analysis just estimates N_{sig}, we need to normalize it to obtain information about the branching ratio. As has already been introduced in Eq.(1.8), we obtain the branching ratio by a conversion of $\mathcal{B}(\mu \to e\gamma) = N_{\mathrm{sig}}/k$. Here, the k parameter corresponds to the effective number of measured muon decays. The estimation of this parameter in the 2021 data will be discussed in Sec.6.3.

Table 6.1: Values used in the fitting

Condition	Used t_{RDC} (ns)	Used E_{RDC} (MeV)
$\lvert t_{RDC}\rvert > 9.5\,\mathrm{ns}$	10	-1
$\lvert t_{RDC}\rvert < 9.5\,\mathrm{ns}\wedge$ Inefficient LYSO matching	t_{RDC}	-1
$\lvert t_{RDC}\rvert < 9.5\,\mathrm{ns} \wedge E_{RDC} > 20\,\mathrm{MeV}$	t_{RDC}	20
$\lvert t_{RDC}\rvert < 9.5\,\mathrm{ns} \wedge E_{RDC} > 20\,\mathrm{MeV}$	t_{RDC}	E_{RDC}

6.1.2 Observables of PDFs

Fit observables

The fit observables, $\vec{x_i}$, consist of the following parameters.

1. E_e; positron momentum
2. E_γ; gamma energy
3. $t_{e\gamma}$; time difference between positron and gamma
4. n_{pTC}; the number of positron hits on the pTC
5. $\theta_{e\gamma} = (\pi - \theta_e) - \theta_\gamma$; difference in θ
6. $\phi_{e\gamma} = (\pi + \phi_e) - \phi_\gamma$; difference in ϕ
7. t_{RDC}; timing of the selected RDC hit
8. E_{RDC}; energy of the selected RDC hit

Handling of RDC parameters

In the likelihood analysis, the RDC parameter ranges are defined as $-10\,\mathrm{ns} < t_{RDC} < 10\,\mathrm{ns}$ and $-1\,\mathrm{MeV} < E_{RDC} < 20\,\mathrm{MeV}$. When no RDC hit is found within the timing range of $|t_{RDC}| < 9.5\,\mathrm{ns}$, the event uses $t_{RDC} = 10\,\mathrm{ns}$, $E_{RDC} = -1\,\mathrm{MeV}$, which represents inefficient events. In the other events, the reconstructed time is filled in t_{RDC}. Among them, $E_{RDC} = -1\,\mathrm{MeV}$ is used if LYSO matching is inefficient, $E_{RDC} = 20\,\mathrm{MeV}$ is used when the reconstructed energy is larger than $20\,\mathrm{MeV}$, and the reconstructed energy is filled otherwise. Summarized in Tab.6.1 is the value used in the fitting in each condition. Note here that the RDC energy reconstruction is implemented so that the reconstructed E_{RDC} value is always numerically positive.

Handling of n_{pTC} parameter

When the reconstructed n_{pTC} is larger than 16, $n_{\mathrm{hit}} = 16$ is used instead and the overall timing resolution of the pTC measurement is also calculated accordingly. This is because such a large number of hits is from rare tail events, which may occasionally cause a large bias in the fitting. Another reason is that the σ_{t_e} resolution improvement as $\sigma_{\mathrm{single}}/\sqrt{n_{\mathrm{pTC}}}$ saturates there.

Conditional observables for per-event PDFs

The conditional observables, $\vec{q_i}$, are introduced to build the PDFs considering event-by-event differences of detector response (*per-event PDFs*). They consist of the following parameters

1. v_γ and ϕ_e; the gamma conversion point in XEC local v coordinate, or equivalently the positron ϕ angle.
2. w_γ; the gamma conversion point in XEC local w coordinate
3. $\vec{\sigma}_e$; the tracking uncertainties estimated by the Kalman filter on positron angle, position, and momentum.

6.1.3 Toy MC simulation

Once we have a full set of PDFs for the fitting, it can also be used to simulate experiments by generating events. This simulation method, often called *toy MC*, is a powerful tool to study the statistical behavior of the experiment. Note that this simulation is distinguished from the full simulation described in Sec.2.8. The toy MC simulates experiments based on an already estimated detector response, which is incorporated in the PDFs. The full simulation, on the other hand, aims to understand the detector response itself.

As we build per-event PDFs, the toy MC event generation depends on the conditional observables, which themselves must be generated with correct weights. This is achieved by directly sampling them from observed events in data, which ensures that all the complications (such as correlations) of the conditional observables are correctly taken into account. Each toy MC experiment is generated by making a set of events taking into account the Poisson fluctuation according to N_{sig}, N_{Acc}, and N_{RMD}.

6.1.4 Frequentists-based statistical method

This analysis gives a result based on the frequentists approach, where the confidence interval on N_{sig} is constructed based on the Feldman-Cousins approach [102]. The test statistic is built from the profile likelihood ratio, $\lambda(N_{\mathrm{sig}})$, which is given by

$$\lambda(N_{\mathrm{sig}}) = \begin{cases} \dfrac{L\Big(N_{\mathrm{sig}}, \hat{\hat{N}}_{\mathrm{Acc}}(N_{\mathrm{sig}}), \hat{\hat{N}}_{\mathrm{RMD}}(N_{\mathrm{sig}}), \hat{\hat{X}}_{\mathrm{TGT}}(N_{\mathrm{sig}})\Big)}{L\Big(\hat{N}_{\mathrm{sig}}, \hat{N}_{\mathrm{Acc}}, \hat{N}_{\mathrm{RMD}}, \hat{X}_{\mathrm{TGT}}\Big)} & (\mathrm{when}\ \hat{\mathrm{N}}_{\mathrm{sig}} > 0) \\ \dfrac{L\Big(N_{\mathrm{sig}}, \hat{\hat{N}}_{\mathrm{Acc}}(N_{\mathrm{sig}}), \hat{\hat{N}}_{\mathrm{RMD}}(N_{\mathrm{sig}}), \hat{\hat{X}}_{\mathrm{TGT}}(N_{\mathrm{sig}})\Big)}{L\Big(0, \hat{\hat{N}}_{\mathrm{Acc}}(0), \hat{\hat{N}}_{\mathrm{RMD}}(0), \hat{\hat{X}}_{\mathrm{TGT}}(0)\Big)} & (\mathrm{when}\ \hat{\mathrm{N}}_{\mathrm{sig}} < 0). \end{cases} \tag{6.2}$$

Here, the single hat variables — $\hat{N}_{\mathrm{sig}}, \hat{N}_{\mathrm{Acc}}, \hat{N}_{\mathrm{RMD}}$, and $\hat{X}_{\mathrm{TGT}}$ — are the values that maximize the likelihood, and the double hat variables — $\hat{\hat{N}}_{\mathrm{Acc}}(N_{\mathrm{sig}}), \hat{\hat{N}}_{\mathrm{RMD}}(N_{\mathrm{sig}})$, and $\hat{\hat{X}}_{\mathrm{TGT}}(N_{\mathrm{sig}})$ — are the values that maximize the likelihood with a fixed value of N_{sig}. Eq.(6.2) is split into two lines because the best-fit value in the denominator is searched for within the physical region, namely $N_{\mathrm{sig}} \geq 0$. This test statistic offers a good property for a statistical test; a larger $-\log\lambda(N_{\mathrm{sig}})$ suggests that the tested value of N_{sig} is less likely the case.

We then introduce $CL(N_{\mathrm{sig}})$, which is the probability of $-\log\lambda(N_{\mathrm{sig}})$ being smaller than the observed $-\log\lambda(N_{\mathrm{sig}})$ value when the tested value of N_{sig} is correct [1]. This probability is directly calculated from an ensemble of toy MCs simulated with the given N_{sig}. Note that the asymptotic formula of $-\log\lambda(N_{\mathrm{sig}})$ distribution presented in [103], which is widely used in many other experiments, is not used in this analysis because this formula is known not to be precise in a limited statistics regime.

The confidence interval is set by requiring $CL(N_{\mathrm{sig}})$ to exceed the defined threshold; $CL(N_{\mathrm{sig}}) > 0.9$ is required in this analysis to set a $90\,\%$ confidence interval. This interval of N_{sig} is finally translated into the interval of $\mathcal{B}(\mu \to e\gamma)$ with a multiplication of $1/k$.

6.1.5 Theory independence of the analysis

The theory uncertainty on the signal polarization appears in θ_e distribution. In this analysis, however, θ_e is not included as an observable — neither as a fit observable nor as a conditional observable —, which means any θ_e dependencies are integrated out from all the PDFs. In particular, the signal PDF is

---

[1] Note here that (by definition) $1 - CL(N_{\mathrm{sig}})$ is identical to the p-value of the hypothesis that the true value is N_{sig}.

formalized as

$$S(\vec{x}|\vec{q}) = \int S(\vec{x}|\vec{q}, \theta_e) S(\theta_e) \mathrm{d}\theta_e. \tag{6.3}$$

Here, thanks to the upstream vs downstream symmetry of the detector and the anti-symmetry of the θ_e-dependence in Eq.(1.4), the $S(\vec{x}|\vec{q})$ is polarization independent; namely

$$\int S(\vec{x}|\theta_e) S_R(\theta_e) \mathrm{d}\theta_e = \int S(\vec{x}|\theta_e) S_L(\theta_e) \mathrm{d}\theta_e, \tag{6.4}$$

where $S_{R(L)}(\theta_e)$ is the θ_e distribution in the full right (left) polarization case. Thus, any models with an arbitrary $|A_R|/|A_L|$ ratio can be consistently tested with a single PDF obtained as Eq.(6.3).

6.1.6 Incorporation method of systematic uncertainties

The systematic uncertainties are included in two methods. The first one randomly samples uncertain parameters during the toy MC generation (analogous to [104, 105]), which broadens the distribution of $-\log\lambda$. As this distribution is used in the CL evaluation, the broader distribution results in a reduction of CL value at each N_{sig} giving an enlarged confidence interval. The other method includes uncertain parameters as fitted nuisance parameters in the likelihood functions; the X_{TGT} parameter in Eq.(6.1), for example. As stated in Wilk's theorem [106], it is expected not to change the $-\log\lambda$ distribution calculated by the toy MC production. Instead, when it is adapted to data, the profiling reduces $-\log\lambda$ at non-best N_{sig} points. Therefore the CL value compared at the same $|N_{\mathrm{sig}}^{\mathrm{test}} - N_{\mathrm{sig}}^{\mathrm{best}}|$ gets smaller than the case without profiling, which broadens the confidence interval.

As a general behavior, the profiling method is more robust in particular when the signal strength is finite. Its drawback is a large increase in the CPU cost, and it is a serious problem, especially in the fitting with unbinned PDFs or per-event PDFs; in our case, the fitting takes $\times 4$ or more if one nuisance parameter is added to incorporate PDF uncertainties. Therefore, only important parameters can be profiled in the analysis. Such parameters are roughly identified by the relative uncertainty level with respect to the resolution parameters used in the signal PDFs. Among the uncertainties, the largest relative uncertainty is on the signal $\phi_{e\gamma}$ PDF due to the large contributions from alignment uncertainty. The introduced nuisance parameter, X_{TGT} is an approximate combination of target x misalignment and LXe misalignment in (x, y) plane. The other uncertainties are incorporated in the first method, namely the numerical sampling of uncertainties in the toy MC generation.

The profiled X_{TGT} parameter changes the center of the $\phi_{e\gamma}$ PDF as

$$S(\phi_{e\gamma}|X_{\mathrm{TGT}}, \theta_{e\gamma}, E_e \cdots) = \mathcal{G}(\phi_{e\gamma}, \Phi(X_{\mathrm{TGT}}) + \mathcal{F}(\theta_{e\gamma}, E_e \cdots), \Sigma(\theta_{e\gamma}, E_e \cdots)), \tag{6.5}$$

where $\mathcal{G}$ represents a Gaussian function and Φ is a function that geometrically transforms X_{TGT} into event by event change in $\phi_{e\gamma}$ value. The other parameters appearing in the equation, $\mathcal{F}(\theta_{e\gamma}, E_e \cdots)$ and $\Sigma(\theta_{e\gamma}, E_e \cdots)$, will be fully given in Sec.6.7.4.

6.2 Analysis window

After applying the selections described in Sec.4.4.3, data samples in the analysis window defined below are finally used in the likelihood analysis;

- $|t_{e\gamma}| < 0.5\,\mathrm{ns}$
- $52.2\,\mathrm{MeV} < E_e < 53.5\,\mathrm{MeV}$
- $48\,\mathrm{MeV} < E_\gamma < 58\,\mathrm{MeV}$
- $|\theta_{e\gamma}| < 40\,\mathrm{mrad}$
- $|\phi_{e\gamma}| < 40\,\mathrm{mrad}$

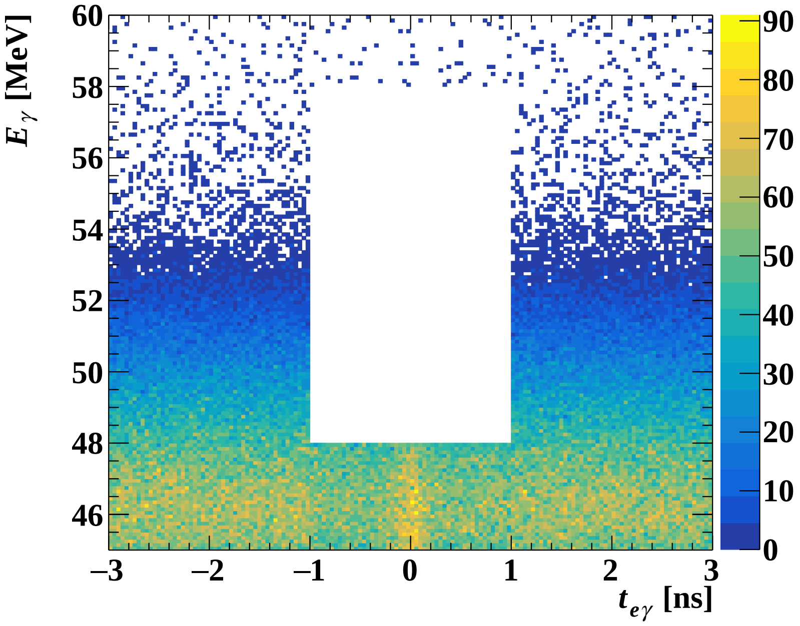

Figure 6.1: Distribution of accessible events before the unblinding on $(t_{e\gamma}, E_\gamma)$ parameter space. $48\,\mathrm{MeV} < E_\gamma < 58\,\mathrm{MeV}$ and $|t_{e\gamma}| < 1\,\mathrm{ns}$ region is null because of the blinding.

In order to avoid psychological human biases, events that satisfy both $48\,\mathrm{MeV} < E_\gamma < 58\,\mathrm{MeV}$ and $|t_{e\gamma}| < 1\,\mathrm{ns}$ were blinded until the final fit in the analysis region as can be seen in Fig.6.1, which is a projection of events onto E_γ vs $t_{e\gamma}$ plane. In addition to the main analysis window, *energy sideband* $(45 < E_\gamma < 48\,\mathrm{MeV})$ and *timing sideband* $(1 < |t_{e\gamma}| < 3\,\mathrm{ns})$ regions are used to examine background events.

6.3 Normalization

6.3.1 Michel positron counting method

One method to evaluate the normalization factor, k, is based on a Michel positron counting, where the number of positrons with $E_e > 50\,\mathrm{MeV}$ is counted in the dataset taken by the pre-scaled self-trigger on the pTC. The parameter is estimated as

$$k_{\mathrm{Michel}} = \frac{N^{e\nu\bar{\nu}}}{\mathcal{B}^{e\nu\bar{\nu}}} \cdot \frac{\epsilon_{\mathrm{trg}}^{e\gamma}}{\epsilon_{\mathrm{trg}}^{e\nu\bar{\nu}}} \cdot \frac{\epsilon_{e}^{e\gamma}}{\epsilon_{e}^{e\nu\bar{\nu}}} \cdot \frac{P^{e\nu\bar{\nu}}}{P^{e\gamma}} \cdot \epsilon_\gamma \cdot A_\gamma^{e\gamma} \cdot \epsilon_{\mathrm{sel}}^{e\gamma}. \tag{6.6}$$

Here, $N^{e\nu\bar{\nu}}$ is the counted number of Michel positrons, which amounts to 114739 in total. $\mathcal{B}^{e\nu\bar{\nu}} = 0.101$ is the branching ratio of decay with $E_e > 50\,\mathrm{MeV}$. P factors are the pre-scaling factor of the physics trigger and pTC self-trigger. The pre-scaling for the physics trigger, which ideally should be 1, was not 1 at the beginning of the data taking as was presented in Fig.3.5. The pre-scaling factor for the pTC self-trigger ranged between $P^{e\nu\bar{\nu}} = 2 \times 10^6$ – 7×10^6, also depending on the period. ϵ and A factors, of which detail is discussed in the next paragraphs, are introduced to correct efficiencies and detector fiducial volume. The numbers are summarized also in Tab.6.2.

Trigger efficiency correction

The trigger inefficiency of the pTC self-trigger was caused by the deadtime of the trigger logic ($\tau_{\mathrm{dead}} = 50\,\mathrm{ns}$), which causes a paralysis of the trigger functionality. Its correction factor, $\epsilon_{\mathrm{trg}}^{e\nu\bar{\nu}}$, is thus evaluated

Table 6.2: Parameters used in the k-estimation with the Michel positron counting method.

$\mathcal{B}^{e\nu\bar{\nu}}$	0.101
$\epsilon_{\mathrm{trg}}^{e\gamma}$	0.77 – 0.79
$\epsilon_{\mathrm{trg}}^{e\nu\bar{\nu}}$	$\sim$ 0.9 depending on beam rate (Eq.(6.7))
$\epsilon_{\mathrm{e}}^{e\gamma}/\epsilon_{\mathrm{e}}^{e\nu\bar{\nu}}$	1.09
$P^{e\nu\bar{\nu}}$	2×10^6 – 7×10^6 depending on periods
ϵ_γ	0.67 (detection efficiency) $\times$ 0.93 (analysis efficiency)
$A_\gamma^{e\gamma}$	0.97
$\epsilon_{\mathrm{sel}}^{e\gamma}$	0.93

from the measured rate of fired trigger (r_{fired}) by solving

$$\begin{aligned} r_{\mathrm{fired}} &= r_{\mathrm{true}} \exp(-\tau_{\mathrm{dead}} \cdot r_{\mathrm{true}}) \\ &= \frac{r_{\mathrm{fired}}}{\epsilon_{\mathrm{trg}}^{e\nu\bar{\nu}}} \exp\left(-\tau_{\mathrm{dead}} \cdot \frac{r_{\mathrm{fired}}}{\epsilon_{\mathrm{trg}}^{e\nu\bar{\nu}}}\right), \end{aligned} \tag{6.7}$$

where $r_{\mathrm{true}} = r_{\mathrm{fired}}/\epsilon_{\mathrm{trg}}$ is the true rate of the events that meet the trigger logic. The estimated correction factor from this inefficiency is ~ 1.1 depending on the muon stopping rate.

The trigger efficiency of the physics data, $\epsilon_{\mathrm{trg}}^{e\gamma}$, was estimated by comparing the $t_{e\gamma}$, E_γ, $\Theta_{e\gamma}$ distribution with that in data taken with a looser trigger threshold; namely wide timing logic, low E_γ threshold logic, and wide-angle logic. As a result, $\epsilon_{\mathrm{trg}}^{e\gamma}$ was estimated to be 0.77 – 0.79 depending on the data-taking period, which reflects the difference in the trigger threshold optimization.

Positron efficiency correction

The positron efficiency correction, $\epsilon_{\mathrm{e}}^{e\gamma}/\epsilon_{\mathrm{e}}^{e\nu\bar{\nu}}$ was evaluated from the energy spectrum fitting of the Michel positrons, which was introduced in Eq.(5.19). Here, the fitting was performed on the pTC self-trigger data because the efficiency dependence on E_e is different between the timing sideband data (i.e. the data collected by the physics trigger) and the pTC self-trigger data. This difference is understood to be from the direction match logic of the physics trigger. The estimated correction factor is $\epsilon_{\mathrm{e}}^{e\gamma}/\epsilon_{\mathrm{e}}^{e\nu\bar{\nu}} = 1.09$.

Gamma efficiency correction

One contribution to the gamma efficiency is from the shower leakage or the absorption of gamma-rays in the material in front of the detector. This was evaluated to be $67 \pm 2\,\%$ with BGO-single dataset taken during the $\pi^0 \to \gamma\gamma$ calibration as presented in Sec.5.12.

The other contribution to the gamma efficiency is from the reconstruction efficiency with the pileup analysis. This was evaluated with signal MC samples and corrected according to a data vs MC comparison. The data and MC were compared with the background gamma-rays; i.e. the data in the timing sideband is compared with the MC simulation for the background gamma-rays. As a complementary method to a direct comparison of the behavior for background gamma-rays, we also studied the pileup analysis results for gamma-rays tagged by the RDC, which are supposed to be less contaminated by the AIF background. The estimated value of the reconstruction efficiency is $93 \pm 2\,\%$, and the uncertainty is dominated by the data vs MC correction.

Acceptance correction

The acceptance correction factor, $A_\gamma^{e\gamma}$, corrects the definition difference in the acceptance region between that in the Michel counting and that for the $\mu \to e\gamma$ signal (Fig.6.2). In the Michel counting, all the

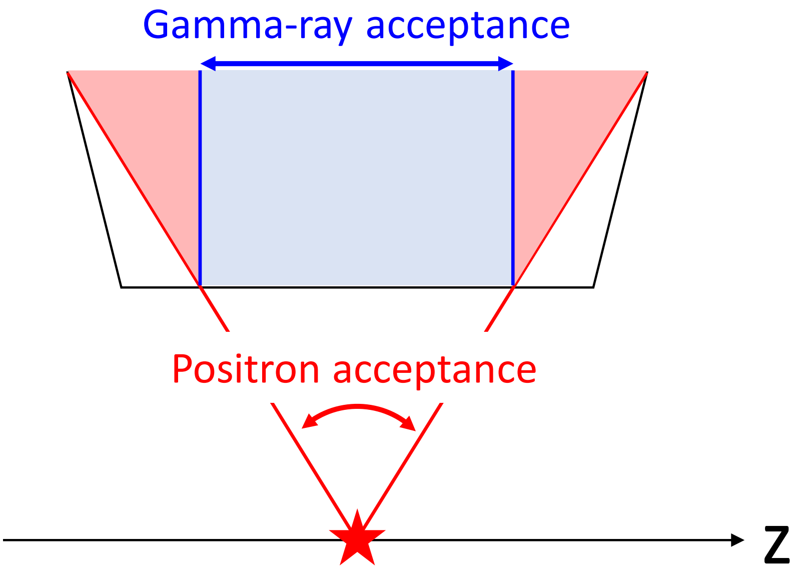

Figure 6.2: Difference in the definition of acceptance between positron and gamma-ray. The red region in the triangular lines corresponds to the positron acceptance and the blue rectangular region corresponds to the gamma-ray acceptance. The gamma-ray acceptance is smaller than the positron acceptance, which is taken into account in $A^{e\gamma}_{\gamma}$.

positrons are accepted if the opposite of their direction at the target points to the acceptance region defined at the inner face of the LXe detector. In the $\mu \to e\gamma$ signal events, however, the gamma-rays can convert in a deeper region, which can be outside of the acceptance even if the positron direction is accepted. The $|\theta_{\gamma}|$ dependence of the acceptance correction factor was evaluated as shown in Fig.6.3, which is then weighted by the signal positron efficiency dependence on $|\theta_e|$. Thig gave an overall correction factor of $A^{e\gamma}_{\gamma} = 97\,\%$.

Selection efficiency correction

The selection efficiency is introduced to correct inefficiencies that are relevant for the likelihood analysis but cannot be included in the Michel counting. The estimated efficiency is $93\,\%$ with two major effects taken into account;

1. Positron missing-turn tracks that are dropped in the pair timing selection
    - This gives $4\,\%$ inefficiency.
2. Tails in angular and momentum measurements that are dropped in angle or momentum cuts according to the analysis window explained in Sec.6.2.
    - $0.6\,\%$ inefficiency from E_e tail,
    - $2\,\%$ from $\theta_{e\gamma}$ tail,
    - $0.4\,\%$ from $\phi_{e\gamma}$ tail.

Estimated k_{Michel} value and uncertainty

The uncertainty of the Michel counting method mostly comes from the selection efficiency estimations. The uncertainty of ϵ_{γ} is $3\,\%$; $2\,\%$ from the evaluation with the $\pi^0 \to \gamma\gamma$ data and $2\,\%$ about the reconstruction efficiency evaluation. The ϵ_{sel} uncertainty is also $3\,\%$, which also includes the uncertainty about the efficiency of the likelihood fitting itself (i.e. PDF efficiency). This is included because there may exist missing effects in the PDF uncertainty evaluation, which will be later discussed in Sec.6.10.

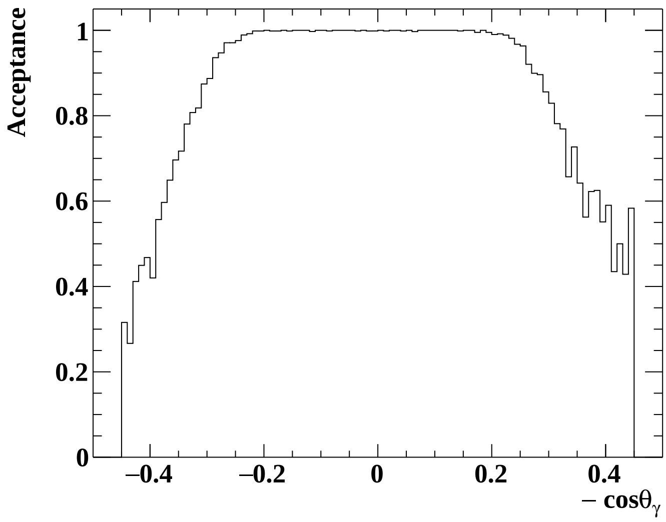

Figure 6.3: Gamma-ray acceptance correction factor as a function of θ_γ emission angle evaluated with MC samples. The acceptance gets smaller at large $\cos\theta_\gamma$ because gamma-rays are accepted only if they are converted in the shallow region.

Table 6.3: The results of k-estimation with RMD events with analyses performed in different angle ranges.

$\Theta_{e\gamma}$ range [deg]	Estimated $k_{\mathrm{RMD}} \pm (\mathrm{stat})$
164 – 168	$(3.05 \pm 0.36) \times 10^{12}$
168 – 172	$(2.73 \pm 0.17) \times 10^{12}$
172 – 176	$(3.60 \pm 0.24) \times 10^{12}$
176 – 180	$(3.47 \pm 0.28) \times 10^{12}$

The other contributions are small, giving up to $1\,\%$ uncertainties each. The total uncertainty about k_{Michel} was thus evaluated to be $\sim 5\,\%$. With all these taken into account, the k-estimation from the Michel positron counting method is

$$k_{\mathrm{Michel}} = (2.55 \pm 0.13) \times 10^{12}. \tag{6.8}$$

6.3.2 RMD normalization

In the RMD normalization, the number of RMD events in the energy sideband, estimated by a time fitting, is scaled as

$$k_{\mathrm{RMD}} = \frac{N^{e\nu\bar{\nu}\gamma}}{\mathcal{B}^{e\nu\bar{\nu}\gamma}} \cdot \frac{\epsilon_{\mathrm{trg}}^{e\gamma}}{\epsilon_{\mathrm{trg}}^{e\nu\bar{\nu}\gamma}} \cdot \frac{\epsilon_{e}^{e\gamma}}{\epsilon_{e}^{e\nu\bar{\nu}\gamma}} \cdot \frac{\epsilon_{\gamma}^{e\gamma}}{\epsilon_{\gamma}^{e\nu\bar{\nu}\gamma}} \cdot \frac{\epsilon_{\mathrm{sel}}^{e\gamma}}{\epsilon_{\mathrm{sel}}^{e\nu\bar{\nu}\gamma}}, \tag{6.9}$$

where the definitions of parameters are similar to those in Eq.(6.6). In this analysis, events in $E_e > 45\,\mathrm{MeV}$, $45\,\mathrm{MeV} < E_\gamma < 48\,\mathrm{MeV}$, and $164° < \Theta_{e\gamma} < 180°$ were used. The angle range was further divided into four sub-ranges as tabulated in Tab.6.3 and k_{RMD} was estimated independently in each sub-range.

As the RMD samples used in this analysis were triggered on the main trigger for $\mu \to e\gamma$, the difference in the kinematics gives rise to the difference in the trigger efficiency between the $\mu \to e\gamma$ events and the RMD events, $\epsilon_{\mathrm{trg}}^{e\gamma}/\epsilon_{\mathrm{trg}}^{e\nu\bar{\nu}\gamma}$. It consists of additional inefficiencies from direction match and the E_γ threshold logics, which make RMD event collection less efficient. The direction match effect is evaluated in an analysis of $\Theta_{e\gamma}$-dependent efficiency with accidental events. The E_γ-threshold effect is evaluated in the background spectrum fitting with a model described later in Eq.(6.15). In the estimation of positron efficiency correction ($\epsilon_{e}^{e\gamma}/\epsilon_{e}^{e\nu\bar{\nu}\gamma}$), the acceptance function from the Michel fit result is again

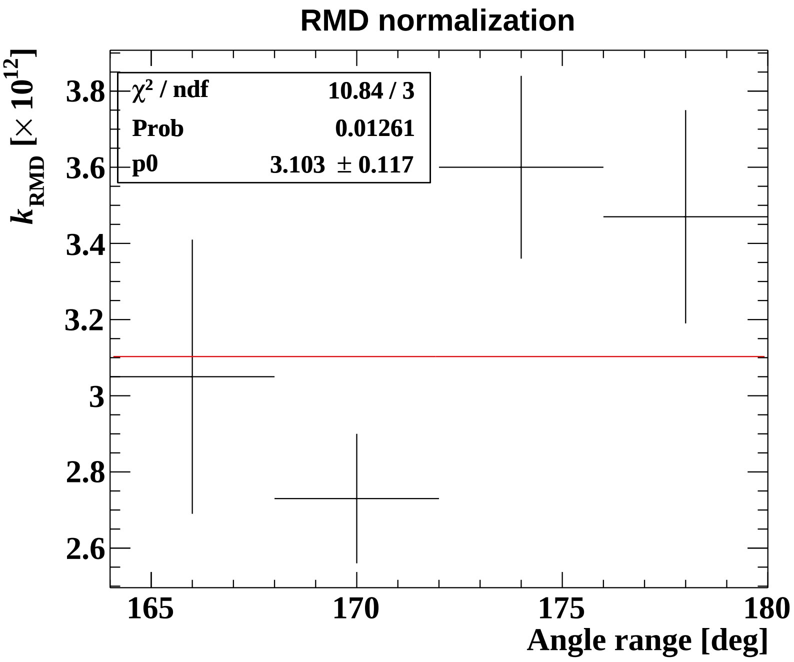

Figure 6.4: The combined estimation of k_{RMD} in a χ^2 fitting to the results in different angle sub-ranges.

used. In the gamma-ray efficiency difference ($\epsilon_{\gamma}^{e\gamma}/\epsilon_{\gamma}^{e\nu\bar{\nu}\gamma}$) estimation, the counting of events with the $45\,\mathrm{MeV} < E_{\gamma} < 48\,\mathrm{MeV}$ cut on the reconstructed energy has both inefficiencies ($E_{\gamma}^{\mathrm{true}}$ inside the range but $E_{\gamma}^{\mathrm{reco}}$ outside the range) and overestimations (vise versa) due to the finite resolution. The correction factor for these effects is evaluated by convoluting the RMD spectrum with the expected energy response, which is the same as the E_{γ} PDF for the $\mu \to e\gamma$ events (see Sec.6.7.1). In the selection efficiency difference ($\epsilon_{\mathrm{sel}}^{e\gamma}/\epsilon_{\mathrm{sel}}^{e\nu\bar{\nu}\gamma}$), the missing turn positron tracks are irrelevant because they are inefficient in both of $\mu \to e\gamma$ and RMD events. Therefore, we considered only the inefficiencies due to the kinematical tails, which are smaller in the $N^{e\nu\bar{\nu}\gamma}$ estimation because of the wider cut ranges and the continuous spectrum.

The result of k_{RMD} estimation in each angle sub-range is presented in Tab.6.3, and the combined result is shown in Fig.6.4. The uncertainty presented in the table includes only the statistical uncertainty in $N^{e\nu\bar{\nu}\gamma}$ estimation. The slight disagreements between the results in different angle sub-ranges can be due to systematic effects in the evaluation of angle cut effects though it is not fully concluded. However, such systematic effects, if exist, likely yield an anti-correlation between the errors in different angle subranges. Therefore, its contribution to the uncertainty of the combined result is estimated as $< 3\,\%$, which is smaller than the observed $\sim 10\,\%$ disagreement between different angle sub-ranges. The systematic uncertainty that is common in all the four angle sub-ranges was estimated to be $10\,\%$ in total. The dominant contribution is from $\epsilon_{\gamma}^{e\gamma}/\epsilon_{\gamma}^{e\nu\bar{\nu}\gamma}$, with the uncertainty evaluated to be close to $10\,\%$ because of its high impact on the k_{RMD} estimation. This evaluation comes from a comparison of the results with different (but within the calibration uncertainties) assumptions on the shape of the response function; a E_{γ} spectrum based on that in $\pi^0 \to \gamma\gamma$ events fully calibrated with the $\pi^0 \to \gamma\gamma$ dataset gave a $\sim 10\,\%$ higher k_{RMD}, whereas a spectrum that strongly considers disagreements between different calibration sources gave a $\sim 10\,\%$ smaller result. The systematics of $N^{e\nu\bar{\nu}\gamma}$ estimation was evaluated to be $3\,\%$. This is an outcome of the uncertainty in the time response function for RMD events, which was used to fit the data in the energy sideband. The other correction factors — $\epsilon_{\mathrm{e}}^{e\gamma}/\epsilon_{\mathrm{e}}^{e\nu\bar{\nu}\gamma}$, $\epsilon_{\mathrm{trg}}^{e\gamma}/\epsilon_{\mathrm{trg}}^{e\nu\bar{\nu}\gamma}$, and $\epsilon_{\mathrm{sel}}^{e\gamma}/\epsilon_{\mathrm{sel}}^{e\nu\bar{\nu}\gamma}$ — were evaluated to have $\sim 2\,\%$ uncertainties respectively. With all the above discussions considered, the final estimation of the RMD normalization is as follows,

$$k_{\mathrm{RMD}} = (3.1 \pm 0.11\,(\mathrm{stat}) \pm 0.3\,(\mathrm{syst})) \times 10^{12}. \tag{6.10}$$

6.3.3 Combined result and uncertainty

From Eq.(6.8) and Eq.(6.10), the discrepancy between k_{Michel} and k_{RMD} is $\sim 1.7\sigma$. The combined normalization is also given as

$$k_{\text{combined}} = (2.64 \pm 0.12) \times 10^{12}. \tag{6.11}$$

6.4 Background estimation

6.4.1 Number of accidental background

The number of accidental backgrounds was directly counted in the timing sideband region; $1\,\text{ns} < |t_{e\gamma}| < 3\,\text{ns}$. Here, the angle cut was widened to $|\theta_{e\gamma}| < 100\,\text{mrad}$ and $|\phi_{e\gamma}| < 100\,\text{mrad}$ to have an enriched control sample, which improves the statical uncertainty at a cost of introducing a systematic uncertainty from the angle scaling according to the different cut range. With the widened sideband region, the uncertainty of N_{Acc} was ± 3.5, which is better than ± 4 statistical uncertainty that we would have with the nominal angle range. The final estimated number of accidental background events were

$$N_{\text{Acc}} = 68 \pm 3.5. \tag{6.12}$$

6.4.2 Number of RMD background

The number of RMD background events was estimated by extrapolating the RMD normalization. As was the case in the RMD normalization, the extrapolation again had a large uncertainty $(10\,\%)$ due to the E_γ energy response uncertainty. In addition, the $\sim 10\,\%$ disagreement between different angle subranges in Tab.6.3 is fully relevant in the N_{RMD} estimation. Note that the impact of this disagreement in the RMD normalization was concluded to be smaller because it is likely from anti-correlated systematics in different angle sub-ranges (see Sec.6.3.2). This suppression of systematics thanks to the anti-correlation, however, is not the case here because N_{RMD} is estimated in the narrow angle-range, namely $|\phi_{e\gamma}| < 40\,\text{mrad}$ and $|\theta_{e\gamma}| < 40\,\text{mrad}$. Therefore, $\sim 15\,\%$ uncertainty was assigned to N_{RMD} giving the estimation as

$$N_{\text{RMD}} = 1.2 \pm 0.2. \tag{6.13}$$

6.5 Period-dependent event weight

In the 2021 data-taking, the beam intensity was changed several times, ranging between 2×10^7 – $5 \times 10^7\,\mu/\text{s}$. As the accidental background rate gets larger with larger beam intensity, the signal-to-background ratio is dependent on the period. Therefore, the whole dataset is divided into different periods according to the beam intensity, and period-dependent weights are included in the fitting. Hereafter, we will use the following period index; $\text{id} = 0$ for $3 \times 10^7\,\mu/\text{s}$, $\text{id} = 1$ for $2 \times 10^7\,\mu/\text{s}$, $\text{id} = 2$ for $4 \times 10^7\,\mu/\text{s}$, and $\text{id} = 3$ for $5 \times 10^7\,\mu/\text{s}$.

The weight for the accidental background events is evaluated by counting the accidental events in the timing sideband for each period. The weight for the signal events is obtained from the Michel positron counting result in each period (Sec.6.3.1). Since the RMD rate is expected to be proportional to the normalization factor, the weight assigned for the RMD events is identical to that for the signal.

6.6 Accidental background modeling

The accidental background PDF is decomposed as

$$\begin{aligned} & A(E_\gamma, E_e, t_{e\gamma}, \theta_{e\gamma}, \phi_{e\gamma}|\vec{q}) \\ = \quad & A_1(E_\gamma|v_\gamma, w_\gamma)\times \\ & A_2(E_e|\sigma_e)\times \\ & A_3(t_{e\gamma}, n_{\mathrm{pTC}}|E_e, w_\gamma)\times \\ & A_4(\theta_{e\gamma})\times \\ & A_5(\phi_{e\gamma}|v_\gamma)\times \\ & A_6(t_{\mathrm{RDC}}, E_{\mathrm{RDC}}|E_\gamma). \end{aligned} \tag{6.14}$$

6.6.1 Accidental gamma-ray energy PDF: $A_1(E_\gamma|v_\gamma, w_\gamma)$

The accidental E_γ PDF is modeled as

$$A_1(E_\gamma|v_\gamma, w_\gamma) = \left((\mathrm{Spectrum}_{\mathrm{MC}} \otimes \mathcal{G}_{\mathrm{additional}}) + r \cdot \mathrm{Spectrum}_{\mathrm{cosmic}}\right) \times \mathrm{Acceptance}_{\mathrm{trigger}}, \tag{6.15}$$

where $\mathrm{Spectrum}_{\mathrm{MC}}$ is a spectrum of reconstructed energy in background simulations, $\mathcal{G}_{\mathrm{additional}}$ is a Gaussian term to additionally smear it, $\mathrm{Spectrum}_{\mathrm{cosmic}}$ is a cosmic-ray spectrum, r is a factor to account for the cosmic-ray fraction, and $\mathrm{Acceptance}_{\mathrm{trigger}}$ is an acceptance function to represent the trigger E_γ threshold window. The parameters in this model were estimated by fitting to the background spectrum (see also Fig.5.26).

The background MC simulation has AIF, RMD, and decay in flight (DIF) gamma-rays, which are mixed according to the muon beam rate. In the calculation of the fraction of each source, we use the branching ratio of $0.579\,\%$ for $E_\gamma > 20\,\mathrm{MeV}$ RMD and from the stopping efficiency at the target of $83\,\%$ for DIF. As the reconstructed spectrum on the MC samples is used, the effect of shower leakage, which can cause a low-energy tail, is already included. Therefore, an additional Gaussian smearing is intended to account for the resolution difference between the data and the MC.

The cosmic-ray component is introduced in the background spectrum. It gives a non-negligible contribution in the high E_γ region, where the gamma-ray contribution is vanishing. The spectrum was directly estimated from the data taken with the beam-off condition, which was fitted with a polynomial. Its contribution can be seen in Fig.5.26.

The trigger acceptance function is represented as

$$\mathrm{Acceptance} = \frac{1}{4}\left(1 + \mathrm{erf}\left(\frac{E_\gamma - \mu_{\mathrm{acc}}}{\sqrt{2}\sigma_{\mathrm{acc}}}\right)\right)\left(1 + \mathrm{erf}\left(\frac{-E_\gamma + \mu_{\mathrm{acc-high}}}{\sqrt{2}\sigma_{\mathrm{acc-high}}}\right)\right), \tag{6.16}$$

where $\mathrm{erf}(x)$ is the error functions, $\mu_{\mathrm{acc}} \sim 44\,\mathrm{MeV}$ corresponds to low energy trigger threshold, and $\mu_{\mathrm{acc-high}} \sim 100\,\mathrm{MeV}$ corresponds the high energy trigger threshold. The shape of the trigger window is based on an evaluation with E_γ-single trigger data.

The PDF dependence on the conditional observables, v and w, are included by dividing the fiducial volume into 14 segments as shown in Fig.6.5(a); the top and bottom edges are separately treated because of the worse resolution than in the central regions and the increased contamination of cosmic-ray events. As the PDF dependence on the beam intensity is found, it is also included by evaluating the PDFs period-dependently.

As the accidental energy PDF was evaluated directly with the data, its uncertainty evaluation is straightforward. The only contribution to the PDF uncertainty is the fitting uncertainty due to the statistical limitation of the data samples.

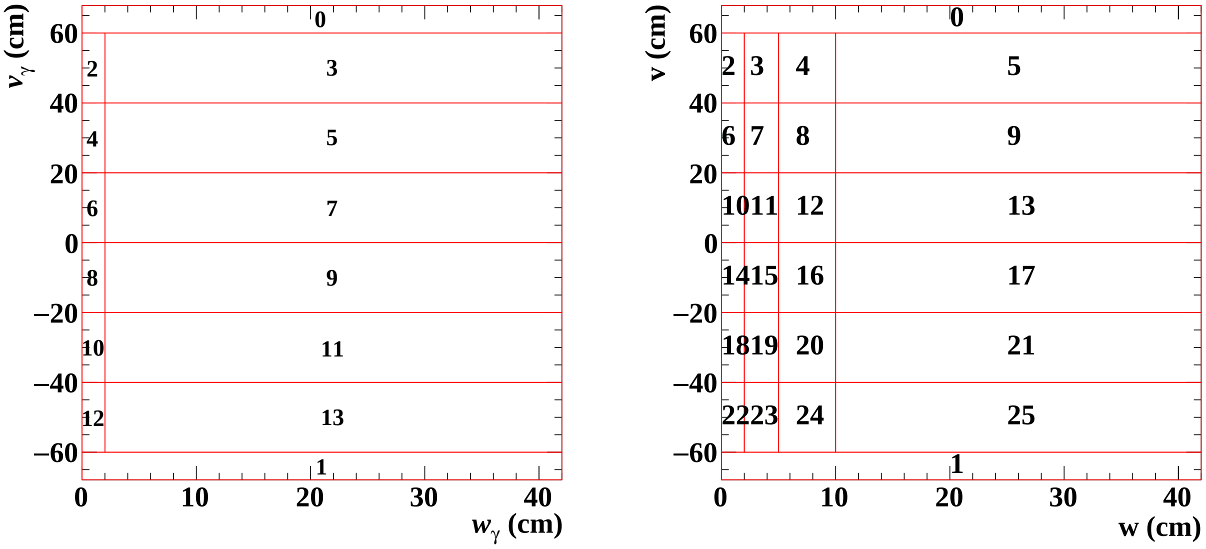

(a) Accidental E_γ PDF

(b) Signal E_γ PDF

Figure 6.5: E_γ PDF segmentation according to the conditional observables, v, w.

6.6.2 Accidental positron momentum PDF: $A_2(E_e|\sigma_e)$

The accidental positron energy PDF is based on the Michel spectrum fitting with the below parametrization,

$$A_2(E_e|\sigma_e) = \big((\text{Michel}) \times (\text{Acceptance})\big) \otimes \text{Resolution}. \tag{6.17}$$

Here, the per-event PDF is based on a categorization according to the covariance ($\vec{\sigma}_e$) of the fit uncertainties estimated by the Kalman filter.

The acceptance function introduces inefficiencies in both low and high momentum sides with a parametrization as

$$\text{Acceptance} = \frac{1}{4}\left(1 + \text{erf}\left(\frac{E_e - \mu_{\text{acc}}}{\sqrt{2}\sigma_{\text{acc}}}\right)\right)\left(1 + \text{erf}\left(\frac{-E_e + \mu_{\text{acc-high}}}{\sqrt{2}\sigma_{\text{acc-high}}}\right)\right). \tag{6.18}$$

The small acceptance on the low-energy side arises from the geometrical coverage of the positron spectrometer, where positrons can be reconstructed only when they have a large radius that can leave hits on the CDCH and pTC. The introduction of the acceptance function in the high E_e side is motivated by a comparison of the Michel MC spectrum of the E_e-truth with the true theoretical spectrum (Fig.6.6). Here, we can see that the high E_e inefficiency is especially large for tracks that have small tracking uncertainties. This behavior is understood to be from the detector material distribution, which affects the tracking uncertainty via scattering.

A sum of three Gaussian is used to describe the resolution function, which is motivated by observed distributions of $E_e^{\text{reco}} - E_e^{\text{true}}$ in detector simulation (Fig.6.7). Because of the kinematical upper limit of $E_e^{\text{true}} < 52.8\,\text{MeV}$, $E_e^{\text{reco}} > 53.5\,\text{MeV}$ data samples cannot be explained within a 2σ discrepancy by the core ($100\,\text{keV}$ resolution) or the first tail ($300\,\text{keV}$ resolution). Therefore, the introduction of the long-tail component ($\sigma \gtrsim 1\,\text{MeV}$) is especially important when $E_e > 53.5\,\text{MeV}$ is included in the range of background fitting.

Fig.6.8 shows distributions of background data samples and their fit in each Kalman-covariance-based category. The best-fit values for some representing parameters are also shown in Fig.6.9, where higher resolution and smaller fractions of long-tail components can be seen for tracks with smaller tracking uncertainties. These parameter dependences were studied also with MC samples to validate this method, and we found that the data and the MC agree within the fit uncertainties.

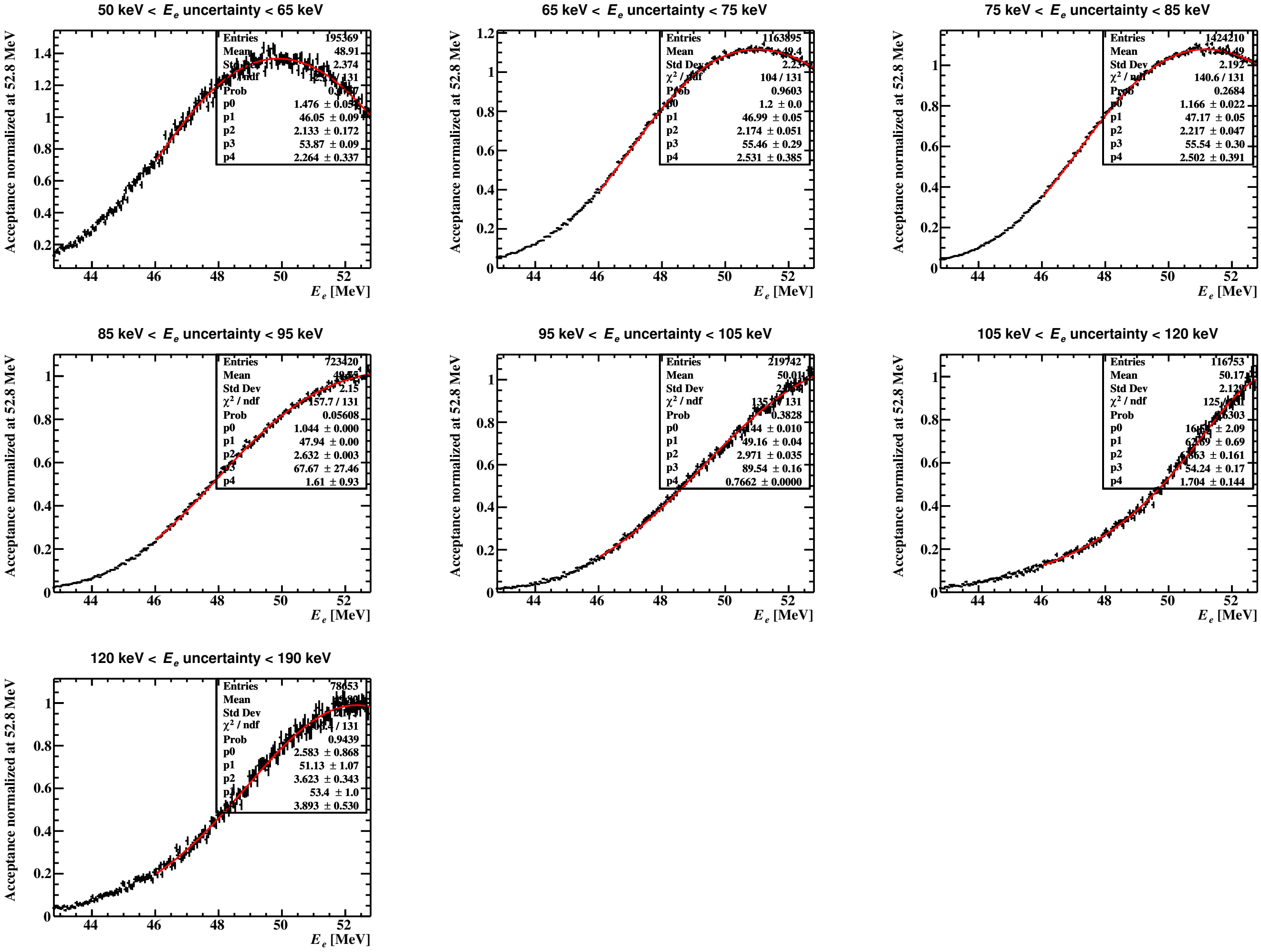

Figure 6.6: Positron acceptance function in Michel MC samples for different σ_{E_e} value estimated in the track fitting. The top-left plot shows the acceptance curve for tracks estimated to be $\sigma_{E_e} < 65\,\mathrm{keV}$, for example.

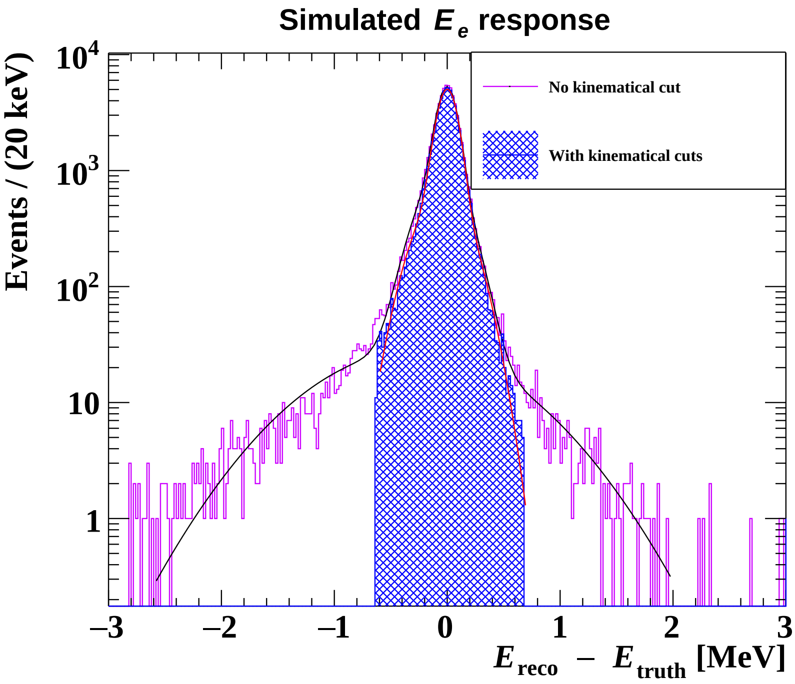

Figure 6.7: Positron response function in detector simulation. The violet histogram is a distribution without any kinematical cuts and is fitted with triple Gaussian (black line). The hatched blue histogram is a distribution after applying angle and momentum cuts and fitted with double Gaussian (red line). The long tail component reduction, visible around $\delta E_e = \pm 0.6\,\mathrm{MeV}$, originates from angle cut, which affects the momentum spectrum due to the δE_e vs $\delta \phi_e$ correlation.

6.6.3 Accidental time PDF: $A_3(t_{e\gamma}, n_{\text{pTC}}|E_e, w_\gamma)$

The n_{pTC} distribution for the accidental background was evaluated from the timing sideband samples. With the observed correlation shown in Fig.6.10, the n_{pTC} parameter is conditioned by the positron momentum. The accidental $t_{e\gamma}$ distribution was not perfectly flat due to a time walk effect in the timing-coincident logic of the trigger, which was parametrized with a linear function (Fig.6.11). The slope parameter was correlated only with w_γ, and it was confirmed to be independent (or have negligible dependence even if correlations exist) of the other fit or conditional observables. Hence, the PDF is further decomposed as $A_3(t_{e\gamma}, n_{\text{pTC}}|E_e, w_\gamma) = A_{3\text{a}}(t_{e\gamma}|w_\gamma) \times A_{3\text{b}}(n_{\text{pTC}}|E_e)$.

6.6.4 Accidental angle PDF: $A_4(\theta_{e\gamma})$ and $A_5(\phi_{e\gamma}|v_\gamma)$

The accidental angle PDFs were directly evaluated from the timing sideband data. We found weak correlations between $\theta_{e\gamma}$, $\phi_{e\gamma}$, and E_e, which is understood to come from the direction-matching logic of the trigger. These, however, are weak enough that we can approximate them to be independent of each other as long as we study the PDFs within a narrow window. Its correlation with E_γ, on the other hand, was not observed, which suggests that we can enlarge the E_γ range to have larger statistics to study the accidental distribution. Therefore, the angle PDFs were studied in the range of $52.2 < E_e < 53.5\,\mathrm{MeV}$, $42 < E_\gamma < 58\,\mathrm{MeV}$, $|\theta_{e\gamma}| < 200\,\mathrm{mrad}$, and $|\phi_{e\gamma}| < 200\,\mathrm{mrad}$.

Both the $\theta_{e\gamma}$ and $\phi_{e\gamma}$ PDFs are parametrized with polynomials up to fourth order (Fig.6.12). The $\phi_{e\gamma}$ PDF was evaluated after slicing the full acceptance range into five v ranges. The observed strong dependence on v_γ is due to the edge effect of the acceptance cut defined in Eq.(4.22). The overall non-flat distribution is understood to be an efficiency curve that comes from the direction-matching algorithm of the trigger. The PDF uncertainty is dominated by the fitting uncertainty of the polynomial modeling due to the statistical limitation of the data samples.

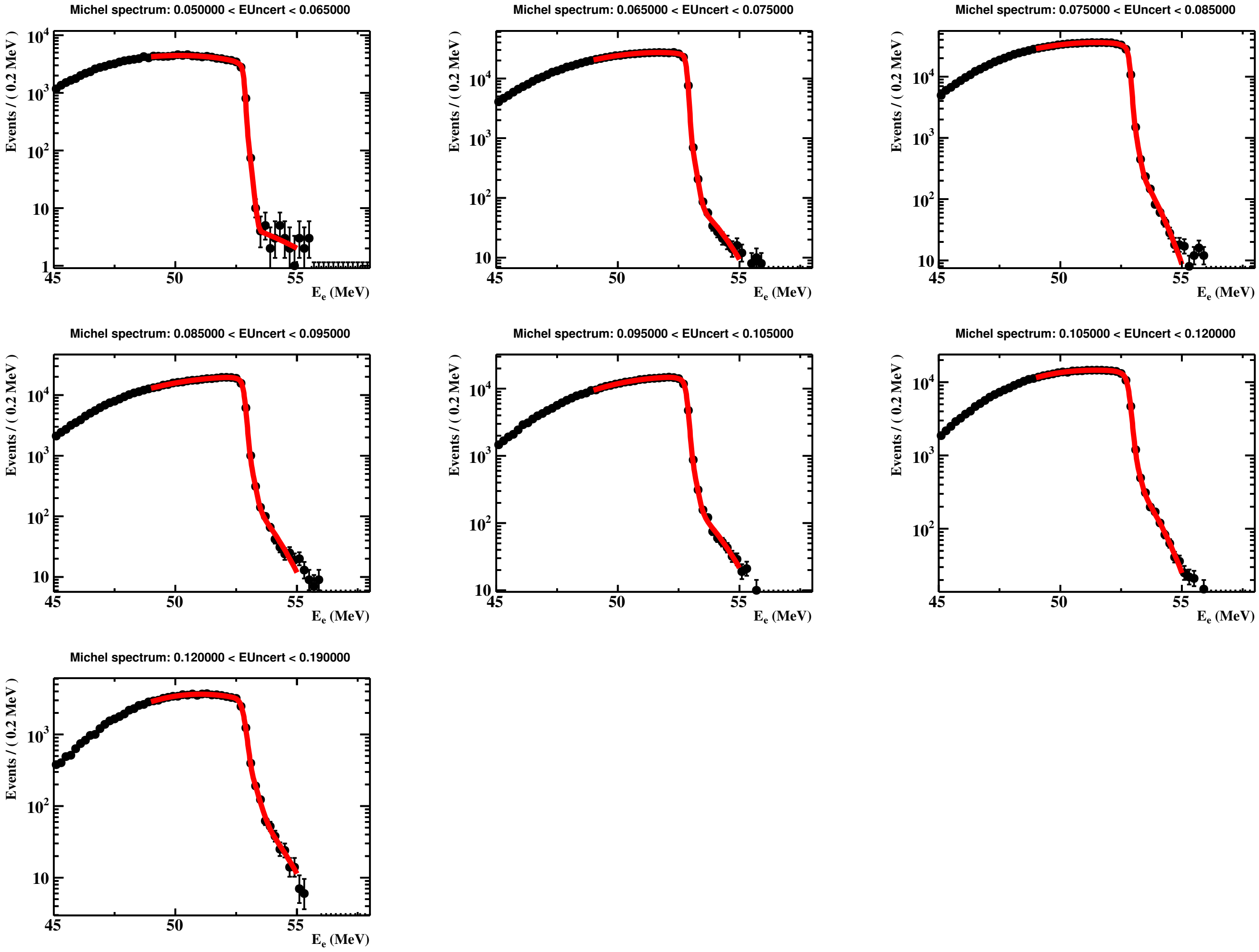
Michel spectrum: 0.050000 < EUncert < 0.065000

Michel spectrum: 0.065000 < EUncert < 0.075000

Michel spectrum: 0.075000 < EUncert < 0.085000

Michel spectrum: 0.085000 < EUncert < 0.095000

Michel spectrum: 0.095000 < EUncert < 0.105000

Michel spectrum: 0.105000 < EUncert < 0.120000

Michel spectrum: 0.120000 < EUncert < 0.190000

Figure 6.8: Evaluation of accidental positron momentum PDF, with the same σ_{E_e}-based categorization as that in Fig.6.6. The increased trend in the fraction of the long-tail resolution component ($\sigma \gtrsim 1\,\mathrm{MeV}$) can be seen with a larger σ_{E_e} value.

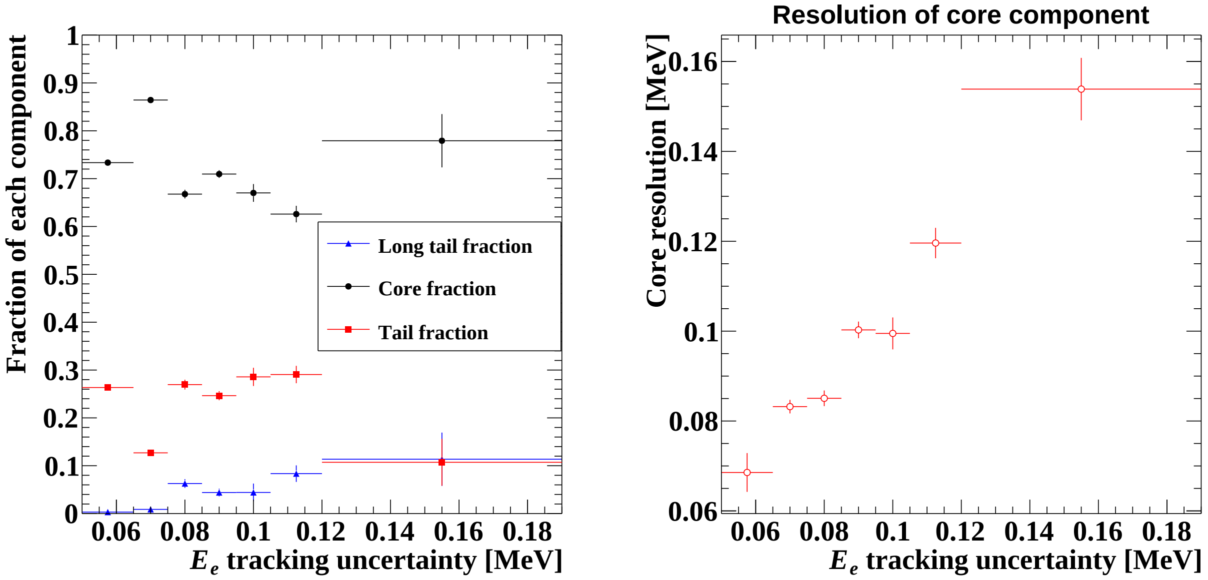

(a) Core to tail fraction parameter in the response function.

(b) E_e resolution parameter for the core part of the response function.

Figure 6.9: Parameters for the E_e response as a function of the tracking E_e uncertainty parameter (σ_{E_e}), which is estimated by the Michel spectrum fitting.

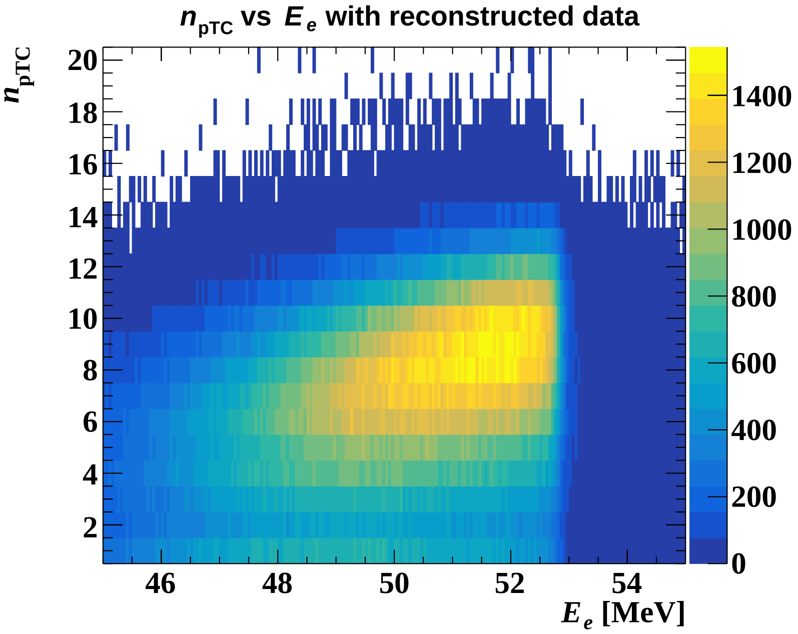

Figure 6.10: Dependence of the n_{pTC} parameter on E_e, observed for background positrons.

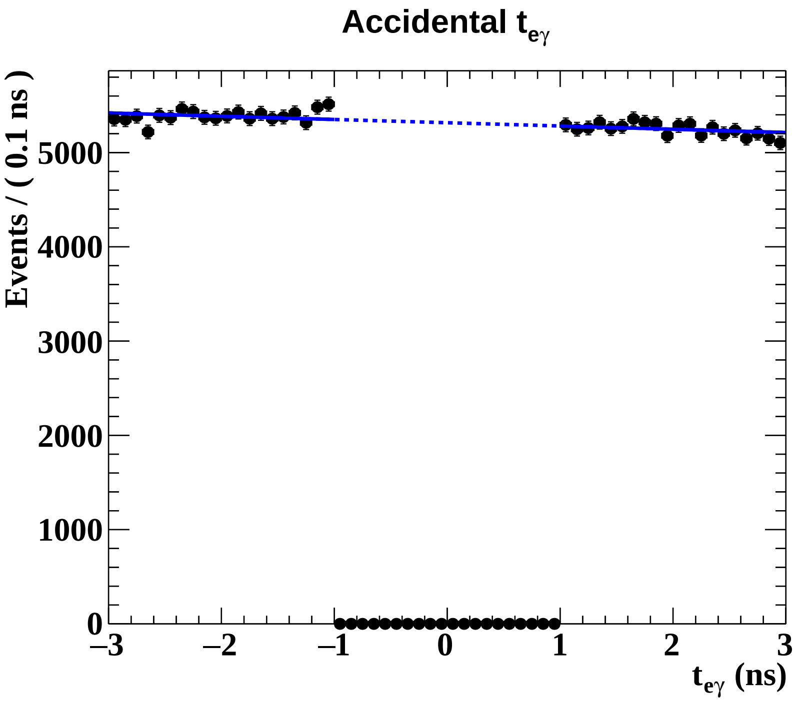

Figure 6.11: Time distribution for the accidental background events and its fit with a linear function (blue line). No events are found in the $|t_{e\gamma}| < 1\,\mathrm{ns}$ region due to the blinding.

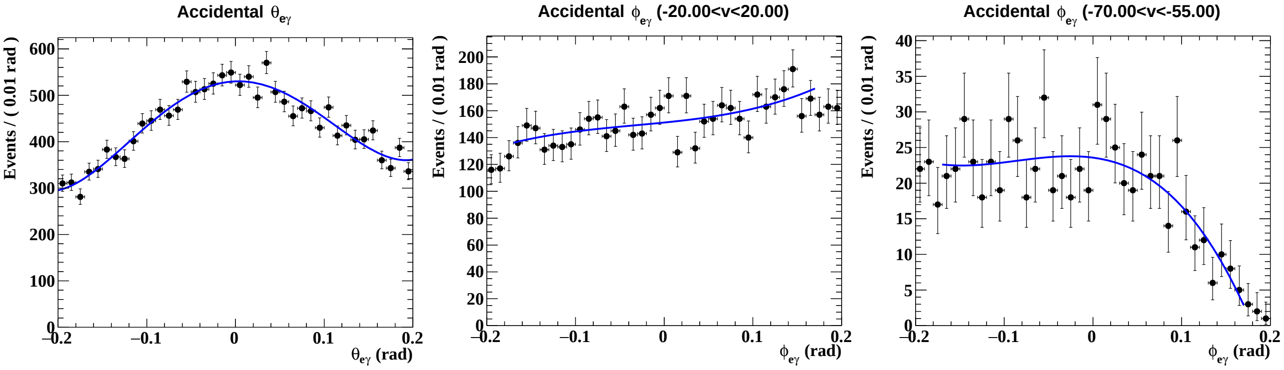

(a) Accidental $\theta_{e\gamma}$ PDF.

(b) Accidental $\phi_{e\gamma}$ PDF for $|v| < 20\,\mathrm{cm}$ region.

(c) Accidental $\phi_{e\gamma}$ PDF for $v < -55\,\mathrm{cm}$ region.

Figure 6.12: Evaluation of angle PDFs for accidental events. (a): The accidental $\theta_{e\gamma}$ PDF is not conditioned by other parameters; the u_γ dependence is integrated out, and the other dependencies are weak enough and approximated to be independent. (b): $\phi_{e\gamma}$ distribution for the central region in the acceptance range of v. (c): That in the edge region. The difference in (b) and (c) indicates a strong dependence of $\phi_{e\gamma}$ distribution on v, which is included in the conditional PDF, $A_5(\phi_{e\gamma}|v_\gamma)$.

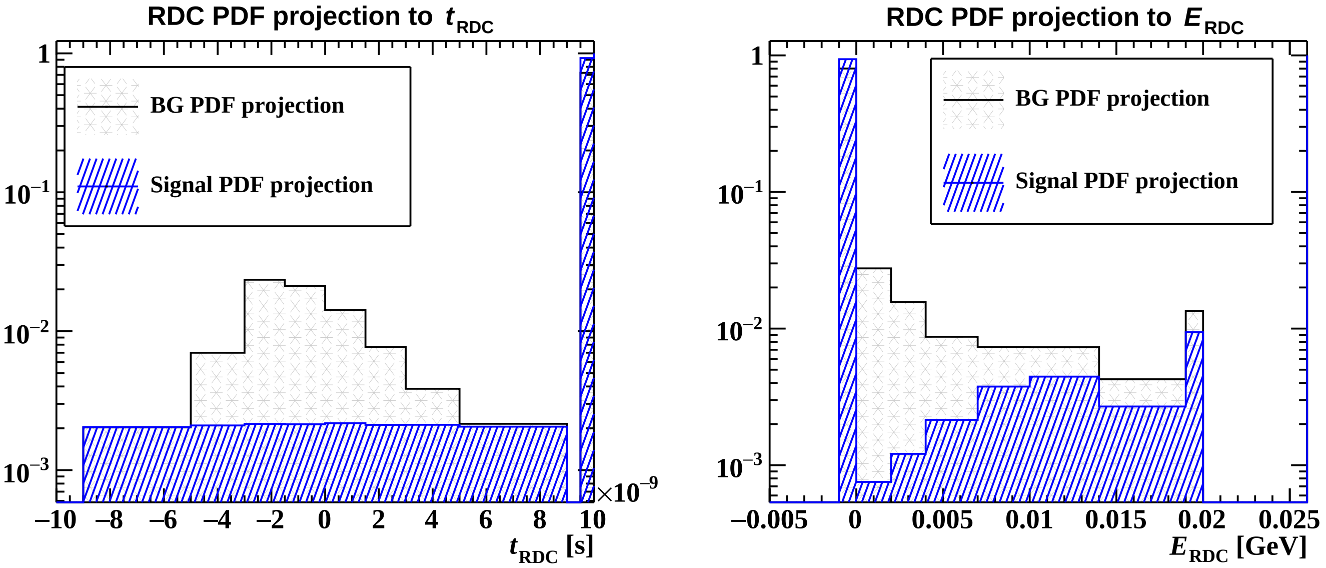

Figure 6.13: RDC PDF projected on t_{RDC} axis (left) and E_{RDC} axis (right) for $49.5 < E_\gamma < 51.5\,\mathrm{MeV}$ events. The rightmost (leftmost) bin in the t_{RDC} (E_{RDC}) projection corresponds to events with no hit detection in the RDC.

6.6.5 Accidental RDC PDF: $A_6(t_{\mathrm{RDC}}, E_{\mathrm{RDC}}|E_\gamma)$

The accidental RDC PDF was estimated with the samples in the timing sideband region. Here, the PDF is conditioned by E_γ because its dependence is induced by the difference in the E_γ spectrum between the RMD-originated background gamma-rays and AIF-originated ones. In the PDF extraction, the dataset was divided into E_γ-based subsets with the thresholds at $E_\gamma = 48, 49.5, 51, 53, 58\,\mathrm{MeV}$.

The PDF was parametrized in a histogram-based format, which, in the unbinned likelihood fitting, means the use of a step function. The parameter width in the step function was flexibly changed according to the tradeoff between the available statistics and the importance of having detailed information within each step width. The RDC PDF projected on t_{RDC}-axis and E_{RDC}-axis are shown in Fig.6.13.

The RDC PDFs are strongly period-dependent for two reasons. The first one is from the hit rate of accidental positrons, which is mostly determined by the muon stopping rate on the target. This makes a difference in the probability of having events in the off-peak region of the timing distribution. The other period dependence comes from the fact that the RDC was not installed at the beginning of the beam time for safety reasons.

The uncertainty of the PDF comes from the used statistics in the PDF evaluation. The bin-by-bin uncertainties are assigned according to the Poisson fluctuation.

6.7 Signal modeling

The full signal PDF is decomposed as follows,

$$\begin{aligned}
& S(E_\gamma, E_e, t_{e\gamma}, \theta_{e\gamma}, \phi_{e\gamma}, t_{\mathrm{RDC}}, E_{\mathrm{RDC}}, n_{\mathrm{pTC}}|\vec{q}) \\
= \quad & S_1(E_\gamma|v_\gamma, w_\gamma)\times \\
& S_2(E_e|\vec{\sigma}_e)\times \\
& S_3(t_{e\gamma}, n_{\mathrm{pTC}}|E_\gamma, E_e)\times \\
& S_4(\theta_{e\gamma}|E_e, v_\gamma, w_\gamma, \vec{\sigma}_e, X_{\mathrm{TGT}})\times \\
& S_5(\phi_{e\gamma}|E_e, \theta_{e\gamma}, v_\gamma, w_\gamma, \vec{\sigma}_e, \phi_e, X_{\mathrm{TGT}})\times \\
& S_6(t_{\mathrm{RDC}}, E_{\mathrm{RDC}}).
\end{aligned} \tag{6.19}$$

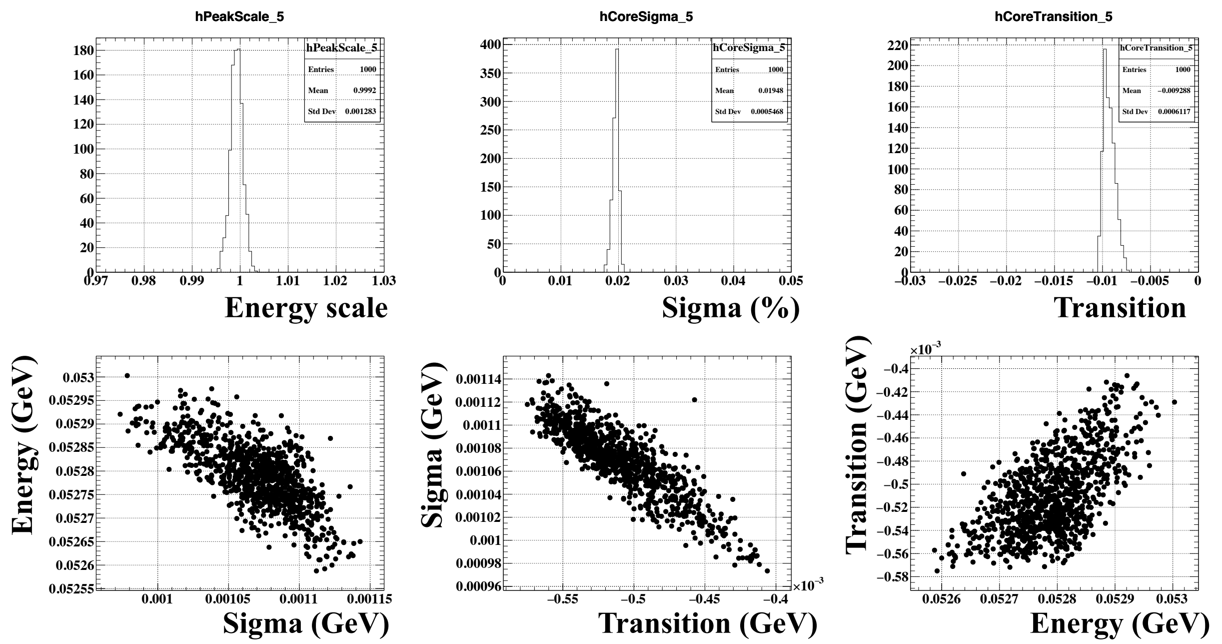

Figure 6.14: Parameters of signal E_γ parameters in a segment. The top three plots are the distributions of energy scale, sigma, and transition. The bottom three are scatter plots between two parameters out of three.

6.7.1 Signal gamma-ray energy PDF: $S_1(E_\gamma|v_\gamma, w_\gamma)$

The signal PDF modeling is based on the function introduced in Eq.(5.8); the sum of two such functions is used for the PDF. Dependences on the conditional observables (v_γ and w_γ) were included by dividing the fiducial volume into 26 segments shown in Fig.6.5(b). Though the segmentation must be identical to that for the accidental in principle, the signal PDF segmentation has a larger number of segments. This, however, is based on a data-driven reasonable approximation that the accidental spectrum does not show strong correlations with v and w, and hence does not cause biases in the fitting.

As the PDF is not conditioned by u_γ, the u_γ dependence is integrated out as discussed in Sec.6.1.5. Still, we may have energy-scale non-uniformities in u sub-segments of each v, w-based segment if its calibration is not correct. This energy-scale misalignment broadens the shape of the spectrum when u dependence is integrated out. Such an effect should be taken into account in the PDF according to the uncertainties in the u-dependent non-uniformity calibration. This was evaluated by making an ensemble of u-integrated PDFs, in which each sampled PDF models different u-dependent energy scale miscalibration.

The full procedure of making a signal PDF in the ensemble is

1. extract the spectra in different u regions obtained in the $\pi^0 \to \gamma\gamma$ data,
2. randomize the energy scale according to its uncertainty in each segment,
3. simulate (MC) the θ_γ distribution of signal events including efficiencies,
4. integrate u_γ-segmented spectra with a weight according to the simulated θ_γ distribution.

In segments that do not have enough $\pi^0 \to \gamma\gamma$ statistics in the first step (see Fig.3.6), the spectra in neighboring segments are interpolated.

By iterating the above procedure, an ensemble of 1000 PDFs was generated in each of 26 segments divided by v, w. The distribution of the PDF parameters in this ensemble is shown in Fig.6.14. Here, the mean of each distribution corresponds to the best estimate of PDF parameters considering the energy scale calibration uncertainty effects in u integration. On the other hand, the covariance of each distribution gives the uncertainty of PDF parameters.

Uncertainty of signal gamma-ray energy PDF

The uncertainty of the E_γ scale has two contributions, a global uncertainty that is common among all the segments and segment-by-segment uncertainty. The global E_γ scale uncertainty comes from the uncertainty of energy scale parameters calculated in background E_γ spectrum fitting ($0.2\,\%$), a disagreement with the energy scale calculated from $\pi^0 \to \gamma\gamma$ ($0.2\,\%$), and statistical uncertainty in $\pi^0 \to \gamma\gamma$ ($0.1\,\%$). The overall global E_γ scale uncertainty is $0.3\,\%$ in total. The segment-by-segment uncertainty comes from different trends of energy scale among different calibration sources, which is $0.23\,\%$ on average.

In addition to the global energy scale, uncertainties of the PDF shapes are included. The distribution in Fig.6.14, which spans the PDF parameter uncertainties, is used to quantify the impacts.

6.7.2 Signal positron momentum PDF: $S_2(E_e|\sigma_e)$

The signal positron momentum PDF has the tracking momentum uncertainty as a conditional observable. The Michel fit technique for the background spectrum presents a good agreement with response studies based on $E_e^{\mathrm{reco}} - E_e^{\mathrm{true}}$ in MC samples. Therefore, both the energy scale and the resolution parameters are based on the best-fit value of the background spectrum fitting.

In the signal PDF, however, the angle cuts of $|\phi_{e\gamma}| < 40\,\mathrm{mrad}$ and $|\phi_{e\gamma}| < 40\,\mathrm{mrad}$ must be taken into consideration. These cuts reduce the long tail component of the response function because $\delta\phi_e$ and δE_e are correlated as will be discussed later in Sec.6.7.4. This mechanism does not apply to the backgrounds because such an angle cut is not associated with the real $\delta\phi_e$ when combined with accidentally coincident gamma-rays. Therefore, the resolution function estimated in the Michel fit is further corrected to obtain the signal PDF.

The effect of the angle cuts was evaluated with the detector simulations. It was found there that the signal PDF can be parametrized as a sum of two Gaussian functions (the hatched distribution and its fit in Fig.6.7). Here, the differences before and after the angle cuts are found only in the fraction parameters and no systematic effect was found in the resolution. Therefore, only the corrections on the core-to-tail fraction were applied when the response function from the Michel fit was transformed into the signal PDF. The fraction of the core component is $\sim 80\,\%$, which is 5 – $10\,\%$ larger than that for the background response function.

Uncertainty of signal E_e PDF

The PDF uncertainty is based on the fit uncertainty of the resolution function parameters in the Michel fitting, which was summed with additional uncertainties from the corrections based on MC samples. The MC-based corrections were adopted to the core to tail fraction of the double Gaussian response function, which yields a $3\,\%$ additional uncertainty to the parameter.

6.7.3 Signal time PDF: $S_3(t_{e\gamma}, n_{\mathrm{pTC}}|E_\gamma, E_e)$

The n_{pTC} distribution for the signal was evaluated from MC samples, which was parametrized independently of the reconstructed E_e because no correlation was found among them. Therefore, the signal PDF is further decomposed as $S_3(t_{e\gamma}, n_{\mathrm{pTC}}|E_\gamma, E_e) = S_{3\mathrm{a}}(t_{e\gamma}|n_{\mathrm{pTC}}, E_\gamma, E_e) \times S_{3\mathrm{b}}(n_{\mathrm{pTC}})$.

The $t_{e\gamma}$ PDF, $S_{3\mathrm{a}}(t_{e\gamma}|n_{\mathrm{pTC}}, E_\gamma, E_e)$, uses a sum of two Gaussian functions, which considers event-by-event positron time resolution of $\sigma_{t_e} = \frac{\sigma_{\mathrm{single}}}{\sqrt{n_{\mathrm{pTC}}}}$. The full time response is thus parametrized as $\sigma_{t_{e\gamma}} = \sigma_{t_e} \oplus \sigma_{\mathrm{const}}$, where σ_{const} part is decomposed into two Gaussian functions. The σ_{single} parameter, the averaged single counter resolution of the pTC, was evaluated to be $112\,\mathrm{ps}$ by the even-odd analysis (Sec.5.5.4). The σ_{const} response term was then evaluated to be $\sigma_{\mathrm{const}} = 70 \pm 3\,\mathrm{ps}$ ($220 \pm 30\,\mathrm{ps}$) for core (tail), which accounts for $94 \pm 3\,\%$ (the remaining $6\,\%$) of the full response. This was evaluated by fitting to the RMD events in the energy sideband (Sec.5.6.3) with fit parameters constrained by the resolution in

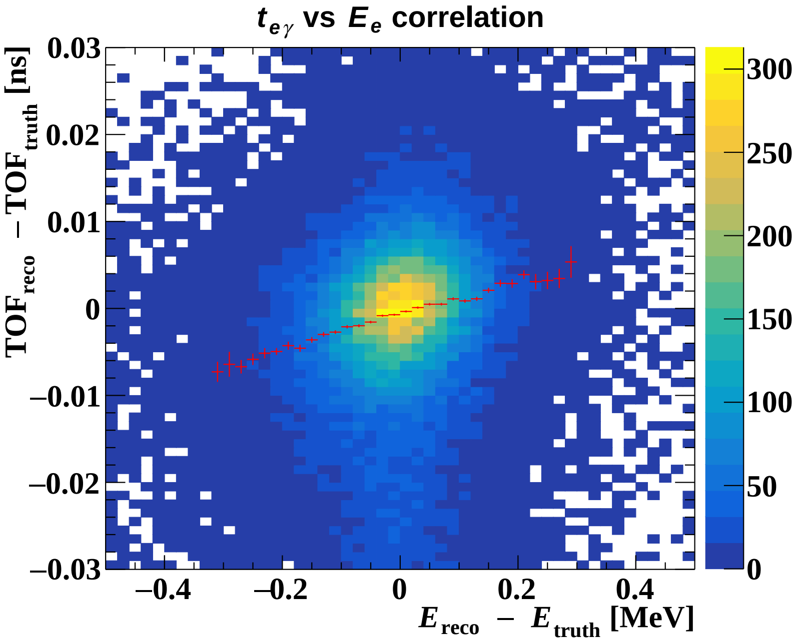

Figure 6.15: Correlation between positron TOF reconstruction error and E_e reconstruction error evaluated with signal MC events.

the $\pi^0 \rightarrow \gamma\gamma$ dataset (Sec.5.4.4). Here, the constraints from the $\pi^0 \rightarrow \gamma\gamma$ resolution exploit the fact that the σ_{const} is dominated by the LXe resolution, and the contribution from the positron TOF measurement is small ($\sim 10\,\mathrm{ps}$). This additional constraint reduces the uncertainty of the time response estimation.

There is a correlation between $t_{e\gamma}$ and E_e because E_e reconstruction error results in TOF measurement error. This small effect of $18.9 \pm 0.5\,\mathrm{ps/MeV}$ is included in the signal PDF. The correlation between $t_{e\gamma}$ and E_γ is also included as a resolution dependence on E_γ, which was evaluated with the $\pi^0 \rightarrow \gamma\gamma$ dataset.

Uncertainty of signal timing PDF

The uncertainty of the n_{pTC} PDF comes from the statistical uncertainty of the used data samples, which is thus evaluated according to the Poisson statistics. The uncertainty of the σ_{single} is dominated by the systematic uncertainty of the even-odd analysis, which gives $5\,\%$ uncertainty to its scale. As the σ_{const} evaluation uses σ_{single} as an input, their uncertainties are correlated, which was evaluated by profiling σ_{single} parameter in the RMD fitting. This correlation changes the σ_{const} value by $-1\,\mathrm{ps}$ when σ_{single} is overestimated by $5\,\%$. The uncertainty in the global time offset and the shape of $t_{e\gamma}$ resolution function come from the fit uncertainty in the RMD peak fitting. Here, the uncertainty in the shape is suppressed also by the $\pi^0 \rightarrow \gamma\gamma$ data because of its use as a fit constraint.

6.7.4 Signal angle PDF: S_4 and S_5

The signal angle PDF is parametrized based on the combination of the positron angle and vertexing resolutions and the gamma position resolution. The gamma position resolution, as discussed in Sec.5.2.2, depends on w_γ, which is included as the event-by-event gamma position resolution. The positron resolution is parametrized by multiplying the pull sigma with the event-by-event tracking uncertainty, which is based on the evaluation with the double-turn analysis presented in Sec.5.10.

Correlations are also considered in the signal PDF as is evident in Eq.(6.19); the $\theta_{e\gamma}$ PDF is conditioned also by E_e, and the $\phi_{e\gamma}$ PDF is conditioned by E_e and $\theta_{e\gamma}$. The ϕ_e dependence of the PDF represents the dependence of $\phi_{e\gamma}$ vs E_e correlation on ϕ_e, which will be discussed later in this section.

To describe the angle resolution and correlation, we introduce the following notations,

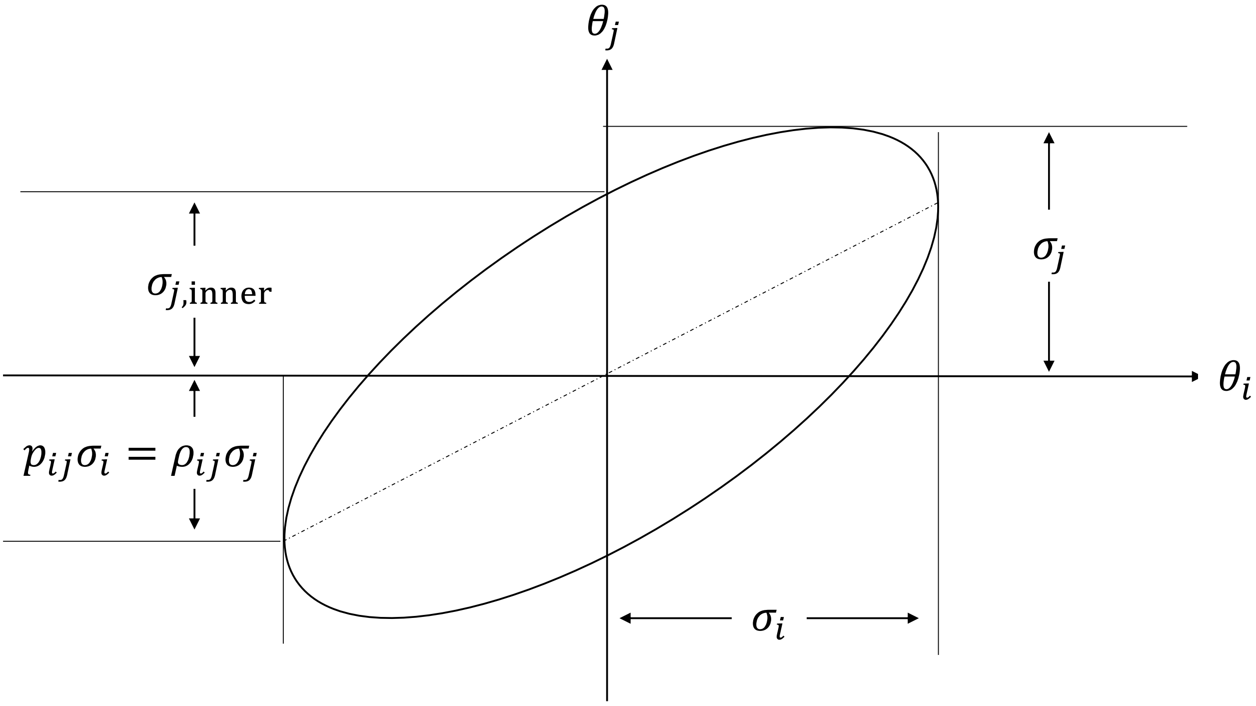

Figure 6.16: Parametrization of correlation (Original figure from Figure 40.5 of [2], modified to include only necessary parameters and to have a consistent notation).

δ: error; $\delta\phi_e$ represents the difference between the reconstructed and the true value,
μ describes center of PDF; $\mu_{\phi_{e\gamma}}$ represents the center of the $\phi_{e\gamma}$ PDF,
σ: true resolution,
σ': nominal reconstruction uncertainty,
s: resolution of pull, namely $s \times \sigma' = \sigma$,
p_{ij}: slope parameter to describe correlation between variables (see Fig.6.16),
ρ: correlation coefficient between variables, $\rho = p_{ij} \cdot \sigma_i/\sigma_j$,
p': correlation slope parameter between pull, namely $p'_{ij} = p_{ij} \cdot \sigma'_i/\sigma'_j$,
σ_{inner} and s_{inner}: inner pull resolution after correlation correction (see Fig.6.16), which follow

$$\sigma_{y,\text{inner}} = \sqrt{\sigma_y^2 - p_{xy}^2\sigma_x^2},$$
$$s_{\text{inner}} = s \cdot \sqrt{1-\rho^2}.$$

Handling of $\delta\phi_e$ vs δE_e correlation

An error of E_e is equivalent to an error in the estimated track radius, which changes the back-propagated trajectory between the CDCH and the target. This geometrically results in an error of ϕ_e as illustrated in Fig.6.17. Note here that the correlation parameter, $p_{E_e\phi_e}$, also depends on ϕ_e because of the geometrical mechanism.

The ϕ_e dependent correlation is parametrized as

$$p'_{E_e\phi_e} = \frac{c_\phi - k_\phi \tan\phi_e}{\sqrt{\sigma^2_{\phi_e}(0) + (k_{\phi_e}\tan\phi_e)^2}}. \tag{6.20}$$

The denominator parametrization is motivated by the fact that the track fitting uncertainty (σ'_{ϕ_e}) is evaluated including the effect of σ'_{E_e} and this correlation, namely the $\sigma^2_{\phi_e}(0)$ is introduced to represent the ϕ_e uncertainty at $\phi_e = 0$. As the true positron momentum is known for signal events, the ϕ_e shift

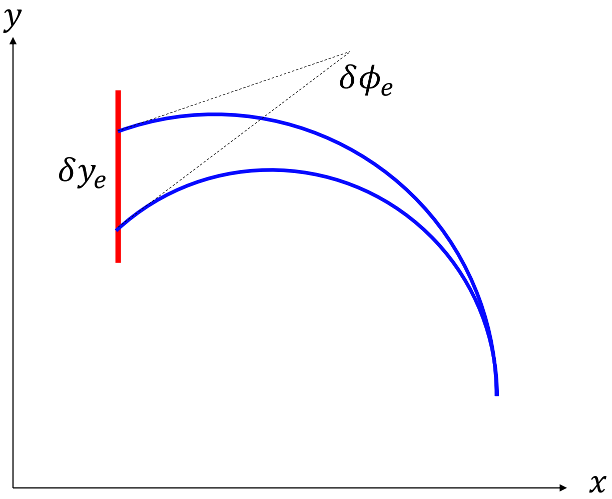

Figure 6.17: Mechanism of correlation of $\delta\phi_e$ vs δE_e and δy_e vs δE_e. An error of δE_e is equivalent to an error of track radius estimation, which geometrically results in ϕ_e and y_e error during the track back-propagation to the target.

is evaluated straightforwardly by multiplying $p'_{E_e\phi_e}$ with $\delta E_e = E_e - 52.8\,\mathrm{MeV}$. As $\delta\phi_e$ shifts the $\phi_{e\gamma}$ accordingly, the center of the $\phi_{e\gamma}$ PDF is dependent on E_e.

After subtracting this correlation, the inner pull resolution of ϕ_e becomes

$$s_{\phi_e,\mathrm{inner}} = s_{\phi_e}\sqrt{\frac{1-(c_\phi^2 - 2c_\phi k_\phi \tan\phi_e)/\sigma_{\phi_e}^2(0)}{1+\left(\frac{k_\phi}{\sigma_{\phi_e}(0)}\tan\phi_e\right)^2}}. \tag{6.21}$$

This is one of the contributions to the $\phi_{e\gamma}$ resolution, which will be summed up with the other contributions discussed hereafter.

Handling of δy_e vs δE_e correlation

The δy_e vs δE_e correlation also arises from the geometrical mechanism in Fig.6.17. Here, $p_{E_e y_e}$ is used instead of $p'_{E_e y_e}$ because the former was found to better describe the observed correlation in data. The $p_{E_e y_e}$ value was evaluated to be $280\,\mathrm{cm/GeV}$ from the double-turn analysis. This is used to shift the center of $\phi_{e\gamma}$ PDF according to the measured E_e by geometrically converting δy_e to $\delta\phi_{e\gamma}$. The inner y_e resolution after the correlation correction is also added to the $\phi_{e\gamma}$ resolution.

Handling of δz_e vs $\delta\theta_e$ correlation

The z_e and θ_e measurements are both relevant to the $\theta_{e\gamma}$ measurement. The correlation between these two parameters enhances the error of $\theta_{e\gamma}$ measurement because $\delta\theta_e$ induces δz_e in a way that $\delta\theta_e$ and $\delta\theta_\gamma$ have the same sign contribution to $\delta\theta_{e\gamma}$ (Fig.6.18). When the positron resolution, δz_e vs $\delta\theta_e$ correlation, and u_γ resolution are all included, the full $\theta_{e\gamma}$ resolution follows

$$\sigma_{\theta_{e\gamma}} = \sqrt{s_{\theta_e}^2\sigma'^2_{\theta_e} + C_z^2 s_{z_e}^2\sigma'^2_{z_e} + 2C_z p'_{\theta_e z_e} s_{\theta_e}^2 \sigma'_{\theta_e}\sigma'_{z_e} + C_u^2\sigma_{u_\gamma}^2}, \tag{6.22}$$

where C_z (C_u) is a factor that converts δz_e (δu_γ) into $\delta\theta_{e\gamma}$. This conversion factor is simply calculated considering the geometry of the detector. The full derivation of this formula is based on a tedious algebra described in Appendix.B.

The value of the $p'_{\theta_e z_e}$ parameter was evaluated to be 1.1 from signal MC samples. Here, the double-turn analysis method cannot be used because it is insensitive to θ_e vs z_e correlation. This is because

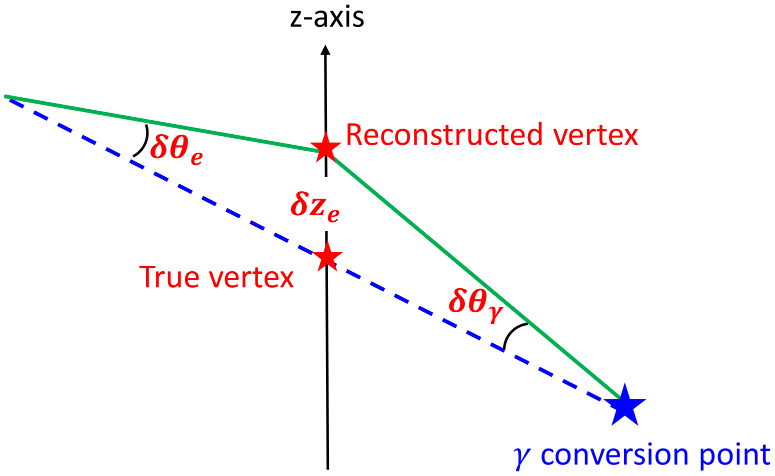

Figure 6.18: An illustration of the effect of δz_e vs $\delta\theta_e$ correlation in the combined error of $\delta\theta_{e\gamma}$. Positive $\delta\theta_e$ likely produces positive δz_e, which geometrically results in an enhancement of $\delta\theta_{e\gamma}$. (The drawing ignores the target slant angle for simplicity.)

the sign of the correlation is opposite between the first turn track (forward propagated to the virtual target plane) and the second turn track (backward propagated to the same plane), which cancels out the correlation effects in the double-turn analysis. The sign difference between two turns can be intuitively understood with a replacement of $\delta_{\theta_\gamma} \to -\delta_{\theta_{e(\text{first-turn})}}$ in Fig.6.18.

Handling of correlations between $\delta\phi_e$, δz_e, and $\delta\theta_e$

The $\delta\phi_e$ vs δz_e and $\delta\phi_e$ vs $\delta\theta_e$ are both correlated mainly because of the propagation length change due to the slanted target geometry (Fig.6.19). The double-turn analysis method is found to be sensitive only to $\delta\phi_e$ vs δz_e correlation among them, which is again because of the correlation sign difference between the first and second turns. Therefore, $\delta\phi_e$ vs δz_e correlation was evaluated first with the double-turn method. The $\phi_{e\gamma}$ vs $\theta_{e\gamma}$ correlation was then evaluated with signal MC samples after correcting the $\delta\phi_e$ vs δz_e correlation. As they were both found to depend on ϕ_e, their dependence was modeled with quadratic functions.

Note here that the δz_e and $\delta\theta_e$ are also correlated. This means that the $\delta\phi_e$ vs δz_e correlation receives a contribution of a combined effect of the $\delta\phi_e$ vs $\delta\theta_e$ correlation and δz_e vs $\delta\theta_e$ correlation. Therefore, this additional contribution has to be carefully considered, whose full detail is given in Appendix.B.

Handling of $\delta\phi_{e\gamma}$ vs $\delta\theta_{e\gamma}$ correlation

The correlation of $\delta\phi_e$ with $\delta\theta_e$ and δz_e results in $\phi_{e\gamma}$ vs $\theta_{e\gamma}$ correlation. Both of these, however, receive the contribution from the LXe position resolution, namely σ_{u_γ} in $\sigma_{\theta_{e\gamma}}$ and σ_{v_γ} in $\sigma_{\phi_{e\gamma}}$. Therefore, a further transformation from the positron correlations into $\phi_{e\gamma}$ vs $\theta_{e\gamma}$ is necessary. This transformation, as shown around Eq.(B.23), is given as

$$p_{\theta_{e\gamma}\phi_{e\gamma}} = \frac{s^2_{\theta_e}\sigma'_{\theta_e}\sigma'_{\phi_e}}{\sigma^2_{\theta_{e\gamma}}}(q'_{\theta_e\phi_e} + q'_{z_e\phi_e}\cdot p'_{\theta_e z_e}) + C_z\cdot\frac{s^2_{z_e}\sigma'_{z_e}\sigma'_{\phi_e}}{\sigma^2_{\theta_{e\gamma}}}q'_{z_e\phi_e}. \tag{6.23}$$

The $\delta\phi_{e\gamma}$ vs $\delta\theta_{e\gamma}$ correction in the $\delta\phi_{e\gamma}$ inner resolution is specifically shown in Eq.(B.24). After correcting both the $\delta\phi_{e\gamma}$ vs $\delta\theta_{e\gamma}$ and $\delta\phi_{e\gamma}$ vs δE_e correlations, the inner resolution of $\phi_{e\gamma}$ is finally given as

$$\sigma^2_{\phi_{e\gamma},\text{inner}} = s^2_{\phi_{e,\text{inner}-E_e}}\sigma'^2_{\phi_e} - p^2_{\theta_{e\gamma}\phi_{e\gamma}}\sigma^2_{\theta_{e\gamma}} + C_v^2\sigma_v^2 + C_y^2 s^2_{y_e,\text{inner}}\sigma'^2_{y_e}. \tag{6.24}$$

The complicated correlation handling discussed above was cross-checked by comparing the $\phi_{e\gamma}$ vs $\theta_{e\gamma}$

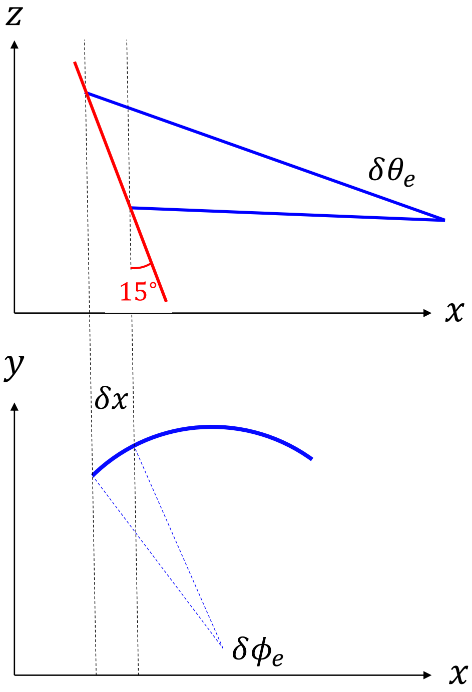

Figure 6.19: An illustration of the mechanism for $\delta\phi_e$ vs δz_e and $\delta\phi_e$ vs $\delta\theta_e$ correlations. The δz_e, which can be also from $\delta\theta_e$ via z_e vs θ_e correlation, results in $\delta\phi_e$ because δz_e on the 15° slanted target plane changes the track propagation length.

signal correlation between toy MC and full detector simulation. Fig.6.20 compares the $\mu_{\phi_{e\gamma}}$ parameter as a function of $\theta_{e\gamma}$, where we can see a good agreement between them.

Uncertainties of signal angle PDF

The uncertainty of the PDF comes both from the detector alignment and the correlation and pull parameters. A wrong choice of the correlation and pull parameters changes only the shape of the PDFs. The alignment, on the other hand, results in a shift of the peak positions of the PDFs.

The uncertainties on the correlation and pull parameters are different depending on their estimation methods. Some of the correlation parameters and all the pull parameters were estimated on data with the double-turn analysis, and $5\,\%$ uncertainties are expected. Here, the double-turn analysis on data showed that the agreement between the data and the MC is $\sim 10\,\%$ level. Therefore, $10\,\%$ uncertainties are assigned for those estimated only from MC samples.

As discussed in Sec.5.11, the uncertainty of the alignment between the LXe detector and CDCH is $1\,\mathrm{mm}$ in all x, y, and z coordinates. This misalignment changes the reconstructed θ_γ and ϕ_γ. In addition, the target alignment uncertainty in the x coordinate also affects the ϕ_e reconstruction because of the change in the track propagation (recall Fig.6.19). The target alignment uncertainty is $100\,\mu\mathrm{m}$ for the translation and $6\,\mathrm{mrad}$ for the rotation around the target long axis.

During the period without a camera photograph, there were several insertion and extraction operations (see Fig.3.7) and the true target position likely changed in each operation. The angle PDF in the period is likely an overlay of multiple Gaussians that have different peak positions, and this can be represented by increasing the resolution parameter of the PDFs. Its contribution to the overall resolution, however, is negligible and has little impact on the likelihood analysis.

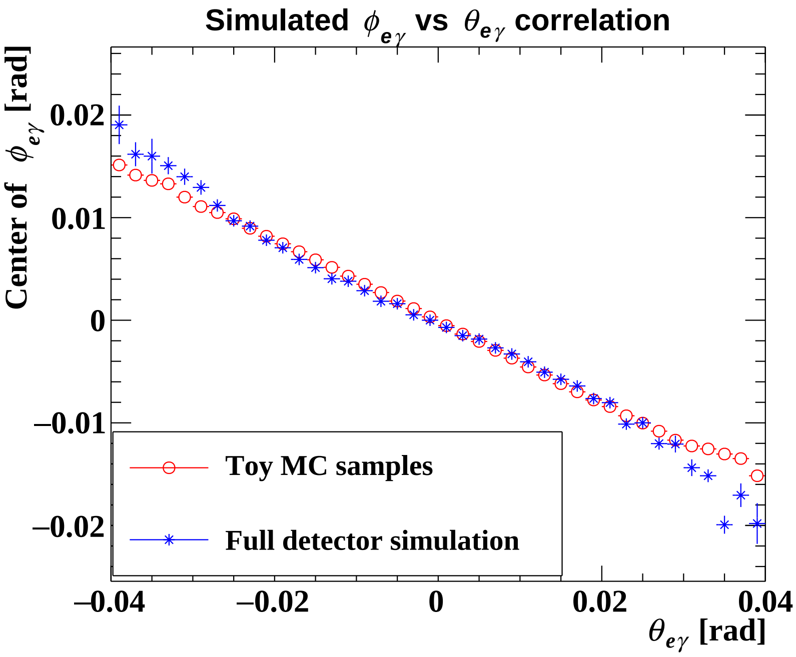

Figure 6.20: Simulated correlation between $\phi_{e\gamma}$ error vs $\theta_{e\gamma}$ error, which is compared between toy MC samples and full detector simulation. The center (peak position) of $\phi_{e\gamma}$ PDF at each $\theta_{e\gamma}$ slice is shown.

6.7.5 Signal RDC PDF: $S_6(t_{\rm RDC}, E_{\rm RDC})$

The signal RDC PDF was estimated with the samples in the timing sideband making use of the off-peak region in Fig.4.18. The t_{RDC} vs E_{RDC} correlation is fully considered here because they are not independent even in the signal PDF. This is because the single-hit selection makes t_{RDC} correlated with the pileup situation[2] and thus correlated with E_{RDC}.

6.8 RMD background modeling

The RMD background PDF is decomposed as

$$\begin{aligned}&R(E_\gamma, E_e, t_{e\gamma}, \theta_{e\gamma}, \phi_{e\gamma}|\vec{q})\\ =\quad & R_1(E_\gamma, E_e, \phi_{e\gamma}, \theta_{e\gamma}|v_\gamma, w_\gamma)\times\\ & R_2(t_{e\gamma}, n_{\rm pTC}|E_\gamma, E_e)\times\\ & S_6(t_{\rm RDC}, E_{\rm RDC}).\end{aligned} \tag{6.25}$$

Here, the RDC PDF is shared with the signal because they are identical; the detected RDC hit is accidental and not associated with the detected gamma-ray in both signal and RMD events.

6.8.1 Incorporation of RMD kinematics in R_1

The differential branching ratio of RMD events is a function of the angle, the positron energy, and the gamma-ray energy. Therefore, the PDF building starts from its theoretical formula given in [28], which is shown in Appendix.A. Here, the opening angle parameter of the formula is transformed into the $(\theta_{e\gamma}, \phi_{e\gamma})$ parameter space. This is further modified to include the detector responses (efficiency and resolution) in the following way:

---

[2] If $t_{RDC} = -5\,\rm ns$ for example, it means there is no hit during $10\,\rm ns$ after that hit.

- The differential branching ratio is multiplied by the E_e acceptance (efficiency) curve presented in Eq.(6.18). It is then convoluted with the E_e resolution function used in Eq.(6.17), which includes the long tail component. Note here that the $|\theta_{e\gamma}| < 40\,\mathrm{mrad}$ and $|\phi_{e\gamma}| < 40\,\mathrm{mrad}$ cuts have little effect on the response function of the RMD positrons because the original RMD angle spectrum is wider than the cut range.

- The two dimensional angle spectrum of $(\theta_{e\gamma}, \phi_{e\gamma})$ is convoluted with the angle resolution. It is then multiplied by the angular efficiency estimated from the non-flatness of the background angle distribution.

- The E_γ spectrum is convoluted with the signal PDF, which is then multiplied by the E_γ acceptance curve estimated in the background spectrum fitting.

6.8.2 RMD timing PDF: R_2

The RMD timing PDF is further decomposed into

$$R_2(t_{e\gamma}, n_{\mathrm{pTC}}|E_\gamma, E_e) = R_{2\mathrm{a}}(t_{e\gamma}|n_{\mathrm{pTC}}, E_\gamma) \times A_{3\mathrm{b}}(n_{\mathrm{pTC}}|E_e).$$

Here, the same n_{pTC} distribution is used as that for the accidental backgrounds. $R_{2\mathrm{a}}(t_{e\gamma}|n_{\mathrm{pTC}}, E_\gamma)$ is similar to the signal PDF, with the resolution parametrized as $\sigma_{\mathrm{const}} \oplus \frac{\sigma_{\mathrm{single}}}{\sqrt{n_{\mathrm{pTC}}}}$. The only difference is that the E_e dependence is removed, as is evident in the $R_{2\mathrm{a}}(t_{e\gamma}|n_{\mathrm{pTC}}, E_\gamma)$ formalism. This is because the RMD positron has a continuous spectrum, and E_e is therefore negligibly correlated with the TOF error.

6.9 Properties of PDFs

Overall PDF shape

The projected distribution of the observables in a toy MC with $N_{\mathrm{sig}} = 2500$, $N_{\mathrm{RMD}} = 0$, and $N_{\mathrm{Acc}} = 2500$ and its fit are shown in Fig.6.21 and Fig.6.22. Here, the true number of the generated signal events is 2574, and that for the accidental events is 2469, and the best-fit values (fitted without external constraints) are consistent within the uncertainties.

In the "ϕ after correlation correction" plot, the $\phi_{e\gamma}$ value is corrected for each data point considering the correlations in the signal PDFs. Here, the measured $\phi_{e\gamma}$ is shifted to cancel the expected signal $\phi_{e\gamma}$ center, which is calculated with the measured E_e and $\theta_{e\gamma}$. As we cannot know the true event type (signal, accidental, or RMD) for the data, this correction is applied also to background events. Here, events are dropped from the plot if the corrected value is outside the $\phi_{e\gamma}$ window. The ϕ-corrected background PDFs are calculated by shifting the original PDF according to the event-by-event correction and their overall average is drawn as the fit line. This ϕ-corrected plot thus shows the inner $\phi_{e\gamma}$ resolution for the signal PDF.

In the 2021 data taking, the RDC was not installed in the first half of the whole period. Therefore, the efficiency of background tagging became lower for this reason. Note that this inefficiency shall not be the case in the future dataset.

Event-by-event resolution parameters for signal PDFs

The distribution of important resolution parameters of the PDFs, which are different event-by-event, are shown in Fig.6.23. The positron resolution parameters — σ_{E_e}, σ_{y_e}, σ_{z_e}, σ_{θ_e}, and σ_{ϕ_e} — are conditioned by the uncertainty of the track fitting. Fig.6.23 shows the raw positron resolution before correlation corrections, and the visible σ_{ϕ_e} dependence on ϕ_e comes from the stronger $\delta\phi_e$ vs δE_e correlation at larger $\tan\phi_e$. The gamma resolution parameters — σ_{E_γ}, σ_{u_γ}, σ_{v_γ}, and σ_{w_γ} — are conditioned by v_γ and

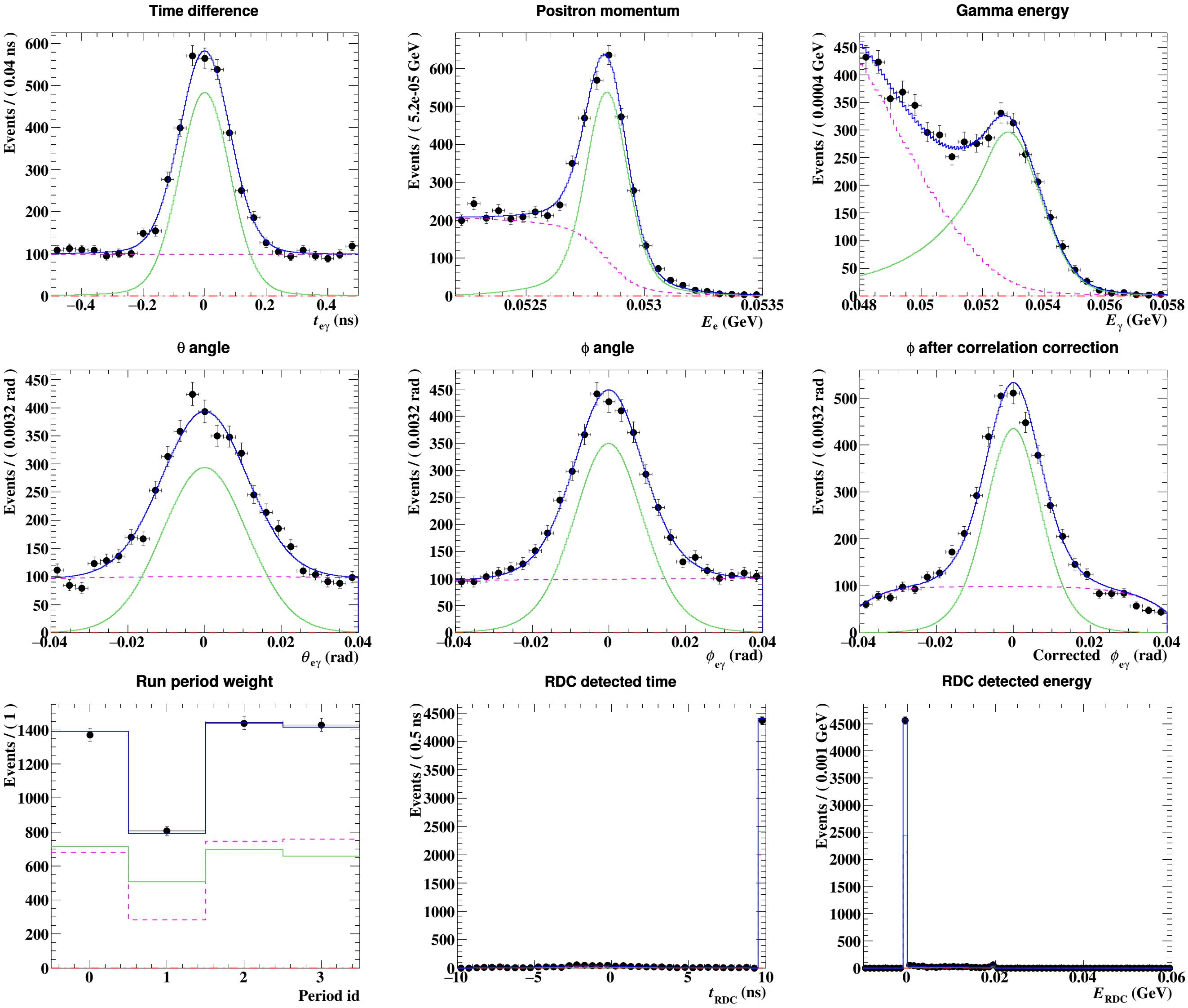

Figure 6.21: One-dimensional projection of toy MC distribution (black markers) and its fit (blue solid line) on each parameter space drawn in a linear scale. The toy MC samples were generated with $N_{\text{sig}} = 2500$ and $N_{\text{Acc}} = 2500$, and the blue fit line is a sum of the accidental PDF (magenta dashed line) and the signal PDF (green solid line) accordingly. The best-fit value and its uncertainty was $N_{\text{sig}} = 2575 \pm 51$, $N_{\text{Acc}} = 2468 \pm 52$, and $N_{\text{RMD}} = 0 \pm 2$, which is consistent within the uncertainties.

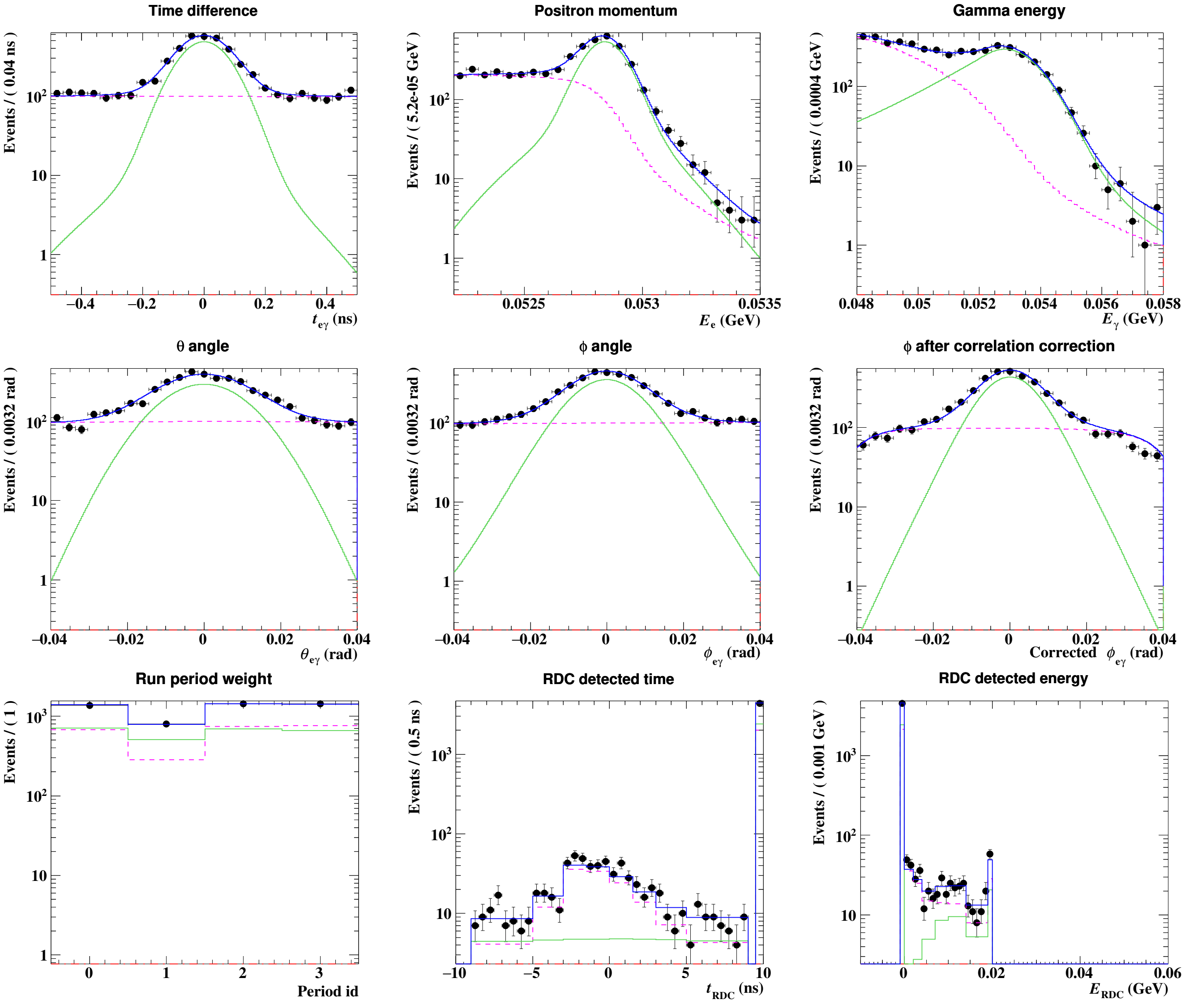

Figure 6.22: The same distribution as Fig.6.21 in a log scale.

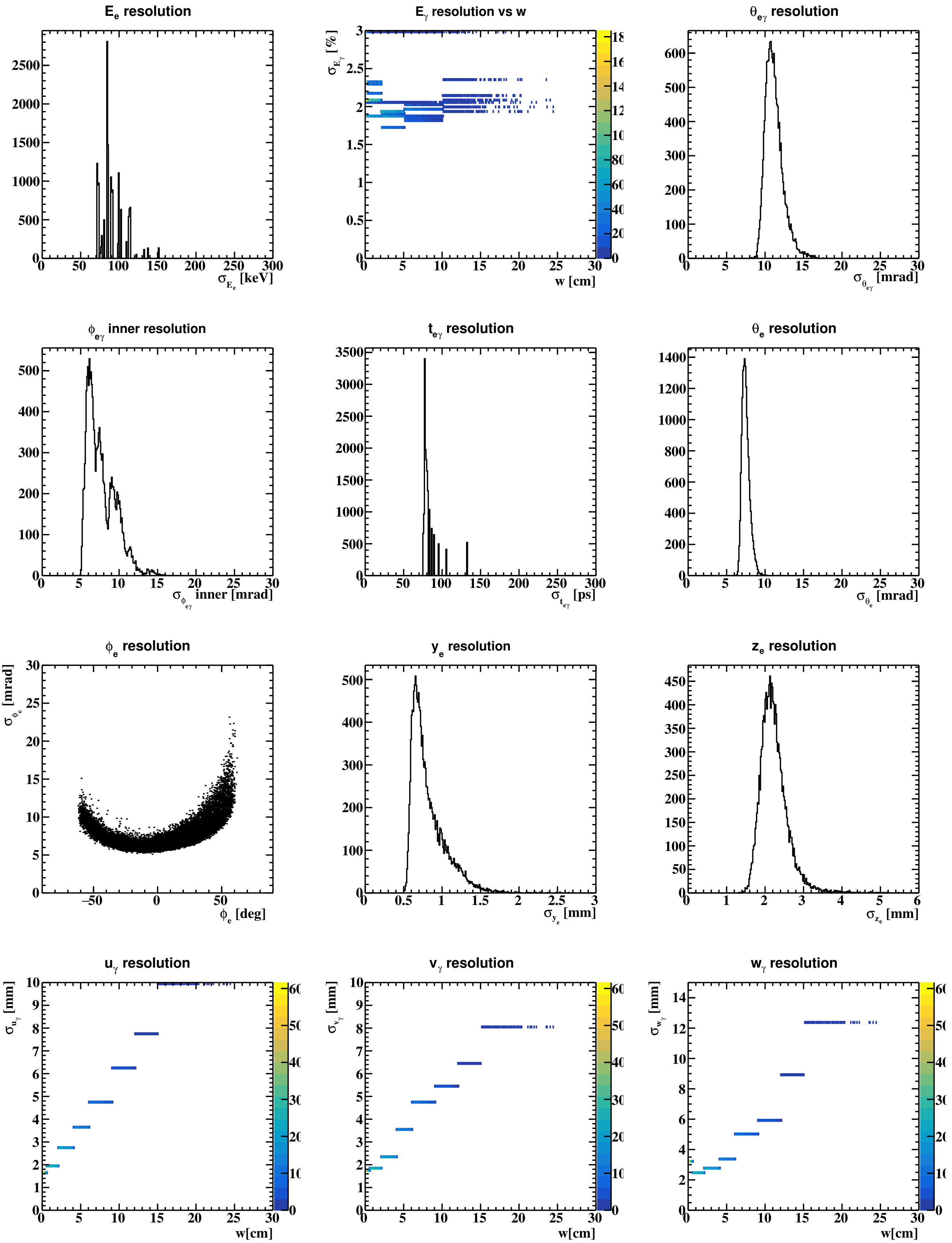

Figure 6.23: Distribution of the main resolution parameters used for signal PDFs. The first five panels shows the full resolution of E_e, E_γ, $\theta_{e\gamma}$, $\phi_{e\gamma}$, and $t_{e\gamma}$. The shown $\theta_{e\gamma}$ and $\phi_{e\gamma}$ resolution values are those after correlation correction. The next four panels (the final three panels) show the positron (gamma) resolution parameters relevant to angle PDFs.

Table 6.4: Summary of uncertain parameters

Parameter	Uncertainty
Target alignment	$100\,\mu\mathrm{m}$
LXe global shift	$1\,\mathrm{mm}$
Normalization	$5\,\%$
E_γ energy scale	$0.3\,\%$
E_e energy scale	$6\,\mathrm{keV}$
$t_{e\gamma}$ center	$4\,\mathrm{ps}$

w_γ. In addition to the strong resolution dependence on w_γ, as can be seen in the plots, the σ_{E_γ} also depends on v_γ, which results in the different resolution values even in the same w_γ ranges. The full angle resolutions — the inner $\sigma_{\phi_{e\gamma}}$ and the $\sigma_{\theta_{e\gamma}}$ — shown in Fig.6.23 are the values with all the correlations taken into account. Here, it can be found that $\sigma_{\theta_{e\gamma}}$ is larger than the simple quadrature sum of σ_{θ_e}, σ_{z_e}, and σ_{u_γ} because δz_e vs $\delta\theta_e$ correlation enhances the combined error of $\delta\theta_{e\gamma}$ (recall Fig.6.18). The inner $\sigma_{\phi_{e\gamma}}$, on the other hand, is smaller than the quadrature sum of each contribution thanks to the correlation corrections.

Visualization of signal vs background separation power

The power of the analysis to separate signal events from accidental events can be evaluated in terms of $R_{\mathrm{sig}}^{(\mathrm{part})}$, which is defined event by event as the ratio of signal likelihood divided by the background likelihood; namely

$$\begin{cases} R_{\mathrm{sig}} = \log_{10}\left(\dfrac{S(\vec{x})}{B(\vec{x})}\right) \\ R_{\mathrm{sig}}^{\mathrm{part}} = \log_{10}\left(\dfrac{S_i(x_i)}{B_i(x_i)}\right), \end{cases} \tag{6.26}$$

where R_{sig} is the full ratio of the full PDF and $R_{\mathrm{sig}}^{\mathrm{part}}$ is its parameter by parameter decomposition with x_i indicating one of $E_\gamma, E_e, \theta_{e\gamma}, \phi_{e\gamma}$ or $t_{e\gamma}$. The background PDF, $B(\vec{x})$, is a sum of the accidental PDF and the RMD PDF, namely

$$B(\vec{x}) = r \cdot A(\vec{x}) + (1-r)\cdot R(\vec{x}), \tag{6.27}$$

where $r \sim 0.02$ is based on the evaluation in Sec.6.4. The $R_{\mathrm{sig}}^{(\mathrm{part})}$ distributions for signal and accidental events are compared in Fig.6.24. The shown $R_{\mathrm{sig}}^{\mathrm{part}}$ distributions correspond to the projections of Fig.6.25, which are scatter plots of $R_{\mathrm{sig}}^{\mathrm{part}}$ vs the kinematical observables. Note here that each plot must be projected with the correct weight according to the distributions of signal and background kinematics.

6.10 Summary of systematic uncertainties

The overall impact of the uncertainties on the signal PDFs is shown in Fig.6.26 with green (yellow) bands indicating 1σ (2σ) of the PDF uncertainties, and major uncertain parameters are tabulated in Tab.6.4. As is visible in the plots, the angle PDFs and the gamma energy PDF have large uncertainties. The dominant cause of the angle PDF (gamma energy PDF) uncertainties is the detector alignment uncertainty (the energy scale calibration uncertainty).

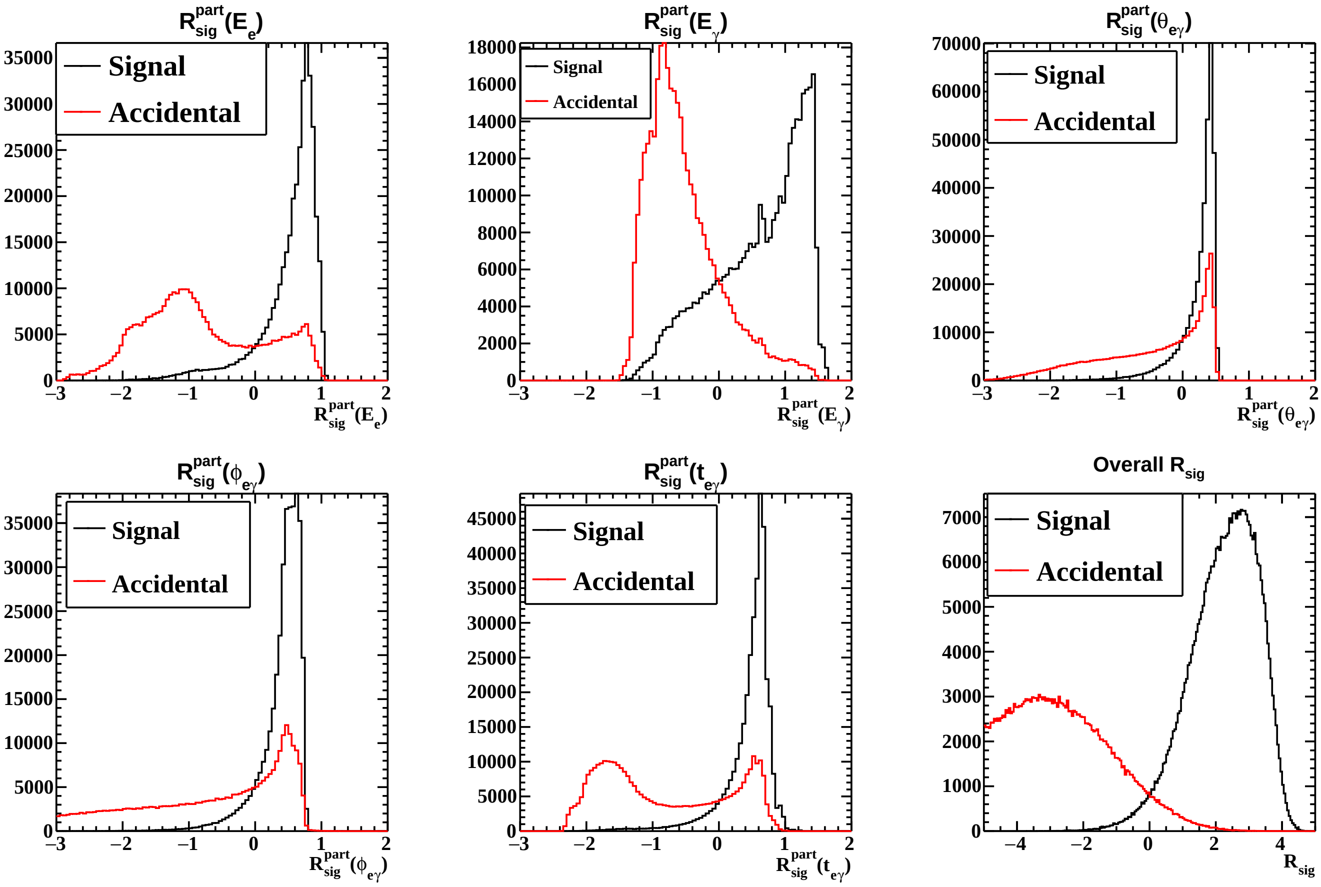

Figure 6.24: Distribution of overall R_{sig} and its parameter-by-parameter decomposition of $R_{\text{sig}}^{\text{part}}$ for signal events (black) and accidental events (red). The probability of finding $R_{\text{sig}}^{(\text{part})}$ at zero is by definition the same between signals and accidentals when contributions from RMD background PDF are approximately ignored.

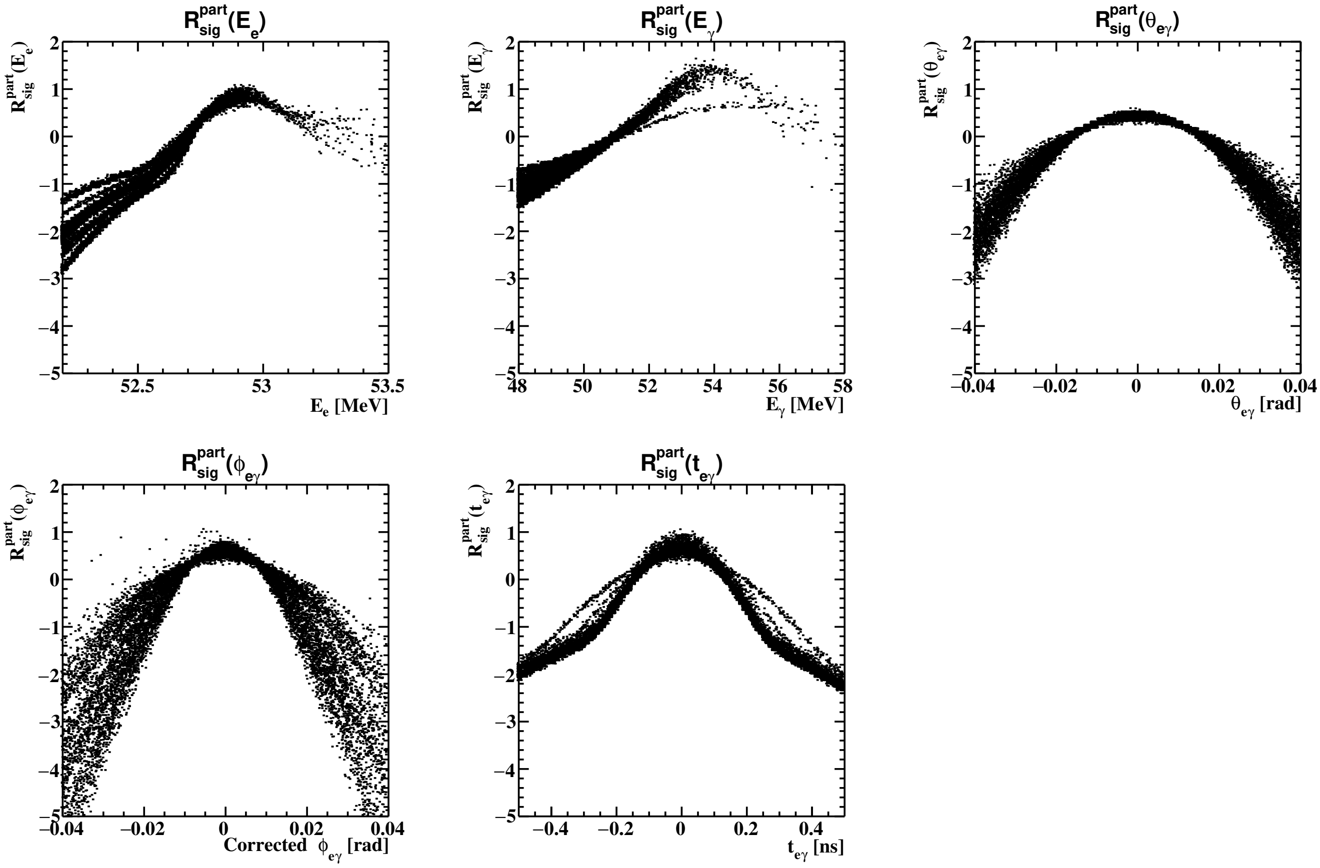

Figure 6.25: $R_{\rm sig}^{\rm part}$ as a function of kinematical observables. The data points are produced from samples mixed both with signal and background samples. Projections of these plots on the y-axis, when weighted correctly with the kinematical distribution, give the distribution shown in Fig.6.24

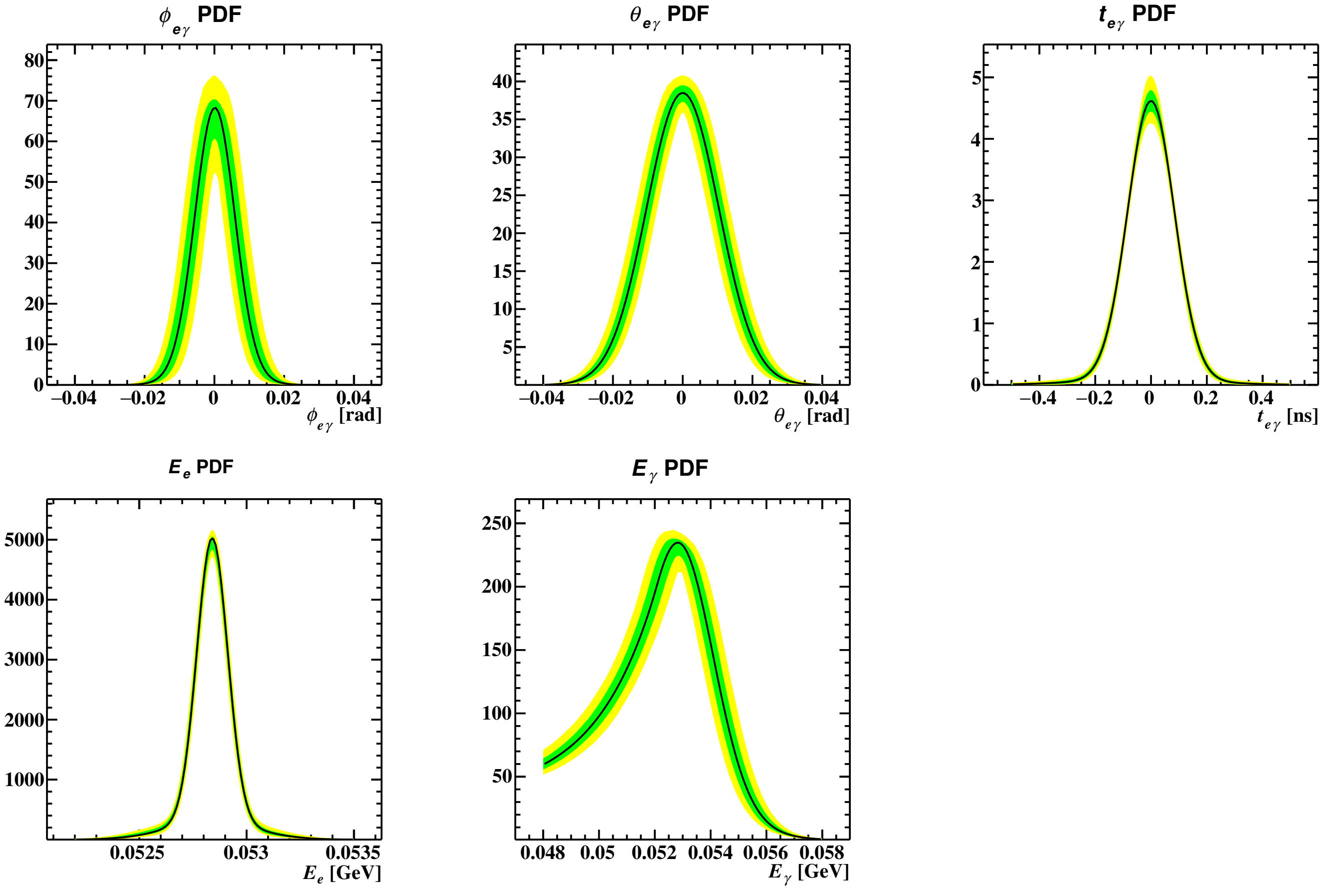

Figure 6.26: Impact of systematic uncertainties on the PDF shape. The solid black lines are the nominal shape of the PDFs, and the green and yellow bands are 1σ (2σ) of the PDF uncertainties.

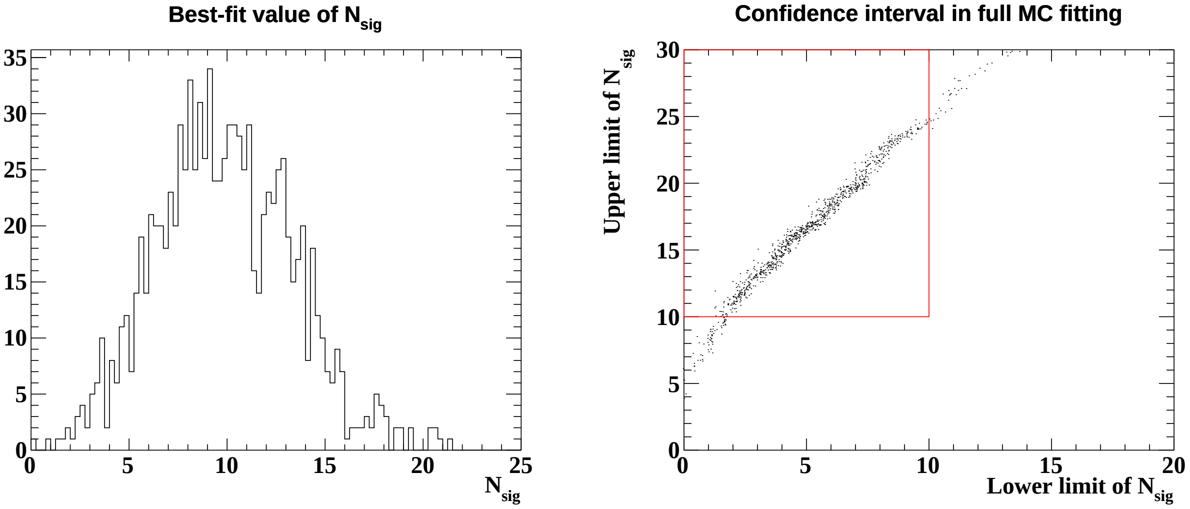

Figure 6.27: N_{sig} best-fit distribution (left) and its confidence interval distribution (right) for $N_{\text{sig}} = 10$ pseudo-experiments that mix full signal detector simulation with background toy MC samples. The red box in the right figure corresponds to the region with $N_{\text{sig}}^{\text{low-limit}} < 10 < N_{\text{sig}}^{\text{up-limit}}$. Each of the plots shows a good agreement with the generated pseudo experiments; the best-fit value of N_{sig} is consistent with 10, and $90\,\%$ experiments satisfy $N_{\text{sig}}^{\text{low-limit}} < 10 < N_{\text{sig}}^{\text{up-limit}}$ as requested by definition.

6.11 Reliability check of analysis with full detector simulation

Let us now discuss the reliability of the likelihood analysis. As presented in Sec.6.6, the accidental background PDF is based on the direct evaluation with data samples, and we do not expect a large mis-modeling. For the RMD background PDF, we have a larger uncertainty in the modeling, which however is not harmful in the fitting because the RMD events are not prominent in the analysis region. With regards to the signal PDF, on the other hand, the fitting is sensitive to signal mis-modeling. Furthermore, the signal PDF may have complicated correlations that are missed in Sec.6.7. Therefore, it is desirable to have a careful reliability check for the signal modeling.

The reliability of the signal modeling was checked by applying the likelihood analyses to signal samples in full detector simulation. The fit samples were generated by mixing signal full MC samples with background toy MC samples. Here, $N_{\text{sig}} = 10$, $N_{\text{Acc}} = 68$, and $N_{\text{RMD}} = 1.2$ expectations were used when toy MCs were generated. There is a large discrepancy in the σ_{E_γ} between the data and simulation; the data gives $2\,\%$ resolution while the simulation gives $1\,\%$ resolution. To compensate for this difference, additional $1.7\,\%$ smearing of E_γ was adopted when the toy MCs were generated. A thousand such samples were generated and fitted in this study.

The distribution of N_{sig} best-fit value is presented in the left plot of Fig.6.27, where its average agrees with the true value of $N_{\text{sig}} = 10$. The confidence interval distribution is also presented in the right figure of Fig.6.27, where $90\,\%$ of all the samples satisfies $N_{\text{sig}}^{\text{low-limit}} < 10 < N_{\text{sig}}^{\text{up-limit}}$, as requested by definition.

Fig.6.28 shows a comparison between the toy MC and full detector simulation in terms of $R_{\text{sig}}^{(\text{part})}$ defined in Eq.(6.26), where we can see good overall agreements. In the parameter by parameter decomposition, small differences can be seen in $R_{\text{sig}}^{\text{part}}(E_\gamma)$ and $R_{\text{sig}}^{\text{part}}(\theta_{e\gamma})$ distributions. These can be understood within the performance differences between the data and the detector simulation.

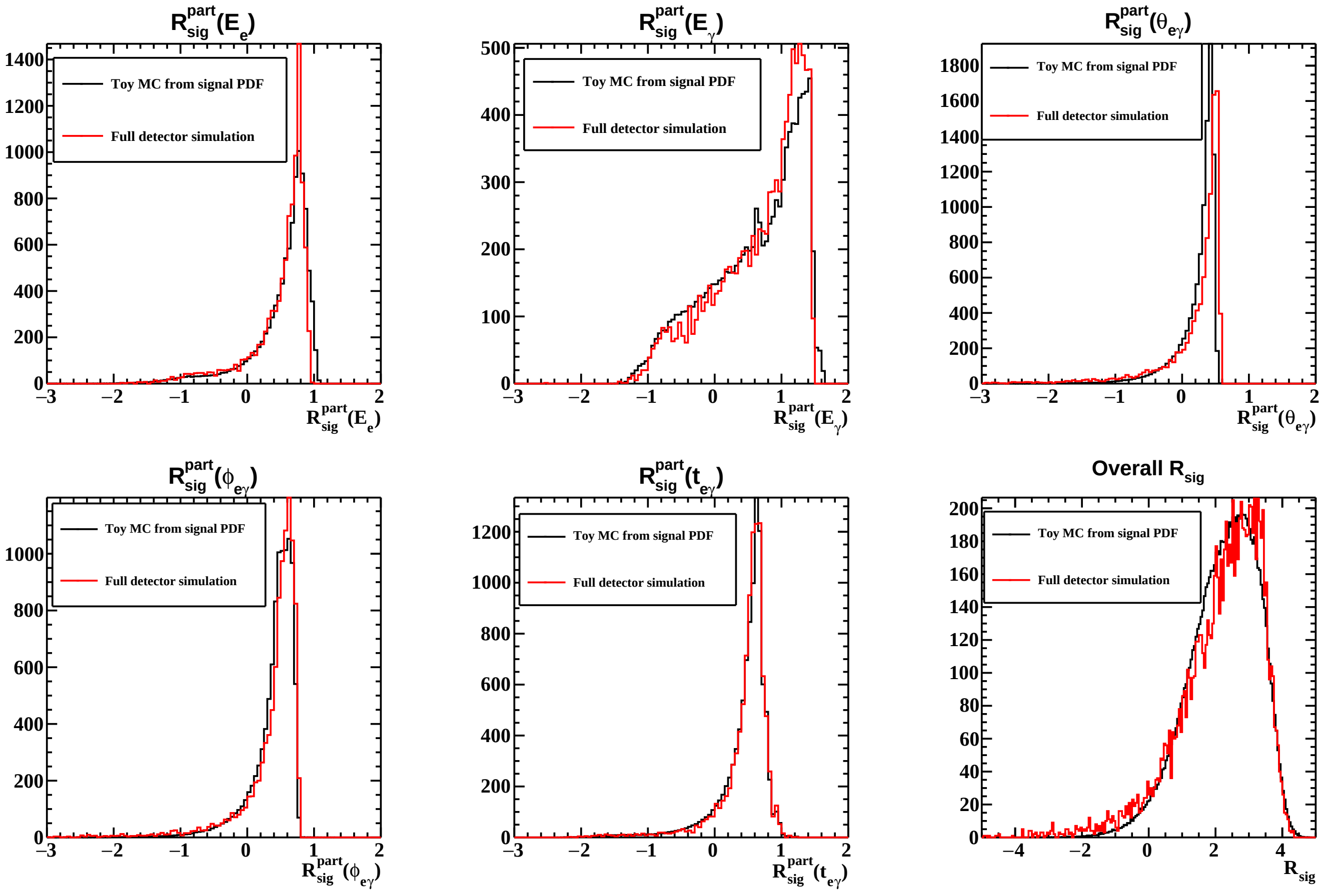

Figure 6.28: Comparison of fitting to signal MC samples from full detector simulation and toy MC.

Chapter 7

Result and Discussion

7.1 Sensitivity

The sensitivity is defined as the median of $90\,\%$ upper limits for toy MCs produced with $N_{\text{sig}} = 0$. The $90\,\%$ upper limit distribution of the toy MC samples is shown in Fig.7.1. The median value of the limit is $\mathcal{B}(\mu \to e\gamma) < 8.4 \times 10^{-13}$ $(N_{\text{sig}} < 2.21)$ without the systematics and $\mathcal{B}(\mu \to e\gamma) < 8.8 \times 10^{-13}$ $(N_{\text{sig}} < 2.31)$ with all the systematics. The 3-sigma discovery power is achieved when $N_{\text{sig}} > 6.5$ or $\mathcal{B}(\mu \to e\gamma) > 2.4 \times 10^{-12}$, which is defined as the value that gives $> 90\,\%$ of experiments p-value < 0.001 for the $N_{\text{sig}} = 0$ hypothesis. The breakdown of systematics uncertainties, which account for $\sim 4\,\%$ sensitivity degradation, is shown in Tab.7.1.

7.1.1 Sensitivity cross-check in timing sideband data fitting

The timing sideband regions were divided into four sub-ranges; ($-3\,\text{ns}$, $-2\,\text{ns}$), ($-2\,\text{ns}$, $-1\,\text{ns}$), ($1\,\text{ns}$, $2\,\text{ns}$), and ($2\,\text{ns}$, $3\,\text{ns}$). The corresponding upper limits on these four sidebands are overlaid in Fig.7.1. In the fourth sideband, which set an interval of $0.41 < N_{\text{sig}} < 6.95$, the best-fit value is $N_{\text{sig}} = 2.65$ and the p-value for the $N_{\text{sig}} = 0$ hypothesis is $4.4\,\%$. It is understood just to be an upward fluctuation of accidental background events. The top 10 highly ranked events, with the order defined by R_{sig} in Eq.(6.26), are shown in Tab.7.2. The best-fit value of $N_{\text{sig}} = 2.65$ in the fourth sideband can be understood to be from the top three events therein.

7.2 Result

There were 66 events in the analysis region, and we did not find any excess of signal events among them with the best-fit value being $N_{\text{sig}} = -0.0003$. Fig.7.2 shows the CL value (defined in Sec.6.1.4) as a

Table 7.1: Breakdown of impact of systematic uncertainties on limits

Parameter	Impact on sensitivity
$\phi_{e\gamma}$ uncertainty	$1.1\,\%$
E_γ uncertainty	$0.9\,\%$
$\theta_{e\gamma}$ uncertainty	$0.7\,\%$
Normalization uncertainty	$0.6\,\%$
$t_{e\gamma}$ uncertainty	$0.1\,\%$
E_e uncertainty	$0.1\,\%$
RDC uncertainty	$< 0.1\,\%$

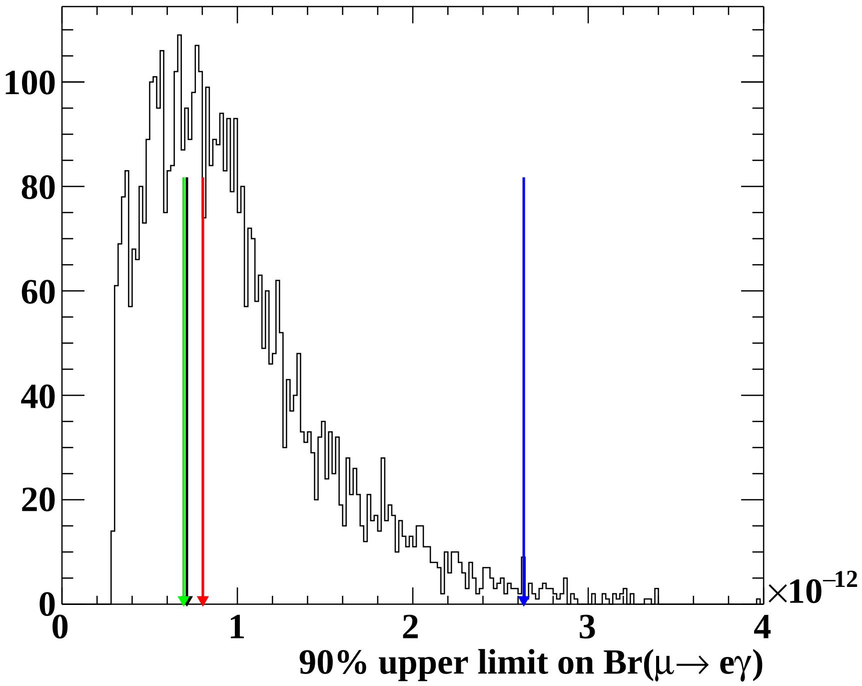

Figure 7.1: Distribution of $90\,\%$ upper limit in toy MCs including systematic uncertainties. The median value is 8.8×10^{-13}. The four arrows indicate the upper limits in the sideband data fitting.

Table 7.2: List of highly ranked events in the timing sideband

Rank	Run	Event	$t_{e\gamma}$ [ns]	E_e [MeV]	E_γ [MeV]	$\phi_{e\gamma}$ [mrad]	$\theta_{e\gamma}$ [mrad]	t_{RDC} [ns]	E_{RDC} [MeV]
1	404797	1970	2.374	52.789	52.407	18.372	-11.755	10	-1
2	402358	1389	2.491	52.779	49.240	3.942	8.631	10	-1
3	398657	329	2.593	52.697	51.048	-5.082	3.582	10	-1
4	406340	1678	-1.629	52.469	52.305	4.106	-5.679	-2.786	19.017
5	402700	2001	-2.656	52.706	52.154	-11.193	-3.821	10	-1
6	404598	1129	-1.327	52.821	51.237	-19.580	16.961	10	-1
7	393087	1188	1.318	52.971	50.940	-18.616	8.304	10	-1
8	403861	912	-2.525	52.776	48.117	19.285	-2.190	10	-1
9	391657	739	-1.643	52.906	49.266	-0.745	-18.509	10	-1
10	405095	848	1.519	52.792	49.998	-22.754	15.431	10	-1

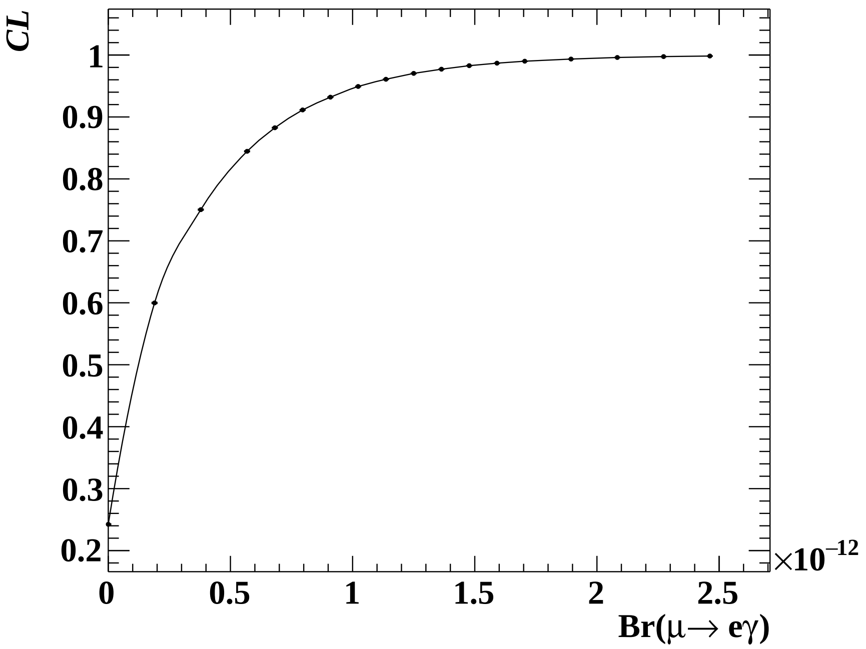

Figure 7.2: CL curve with the MEG II 2021 dataset. The curve crosses $CL = 0.9$ at $\mathcal{B}(\mu \to e\gamma) = 7.5 \times 10^{-13}$, giving a 90 % upper limit accordingly.

Table 7.3: List of highly ranked events

Rank	Run	Event	$t_{e\gamma}$ [ns]	E_e [MeV]	E_γ [MeV]	$\phi_{e\gamma}$ [mrad]	$\theta_{e\gamma}$ [mrad]	t_{RDC} [ns]	E_{RDC} [MeV]
1	401563	1286	-0.108	52.974	51.952	-2.235	-27.659	10	-1
2	402458	22	0.137	52.695	49.514	3.376	1.311	10	-1
3	403059	2406	-0.287	52.738	52.013	-1.397	-13.269	10	-1
4	405442	9	-0.040	52.772	49.721	9.852	-30.290	10	-1
5	401603	2718	-0.099	52.766	49.186	-22.790	23.956	10	-1
6	405131	1189	0.243	53.153	48.518	-1.468	13.603	10	-1
7	402692	2734	-0.107	52.528	51.747	-21.823	32.029	10	-1
8	391935	1276	-0.195	52.521	52.490	20.031	-37.719	10	-1
9	401611	2589	0.211	52.744	48.773	-0.080	-13.500	-1.367	4.435
10	402737	797	-0.423	52.594	48.601	2.509	13.404	10	-1

function of $\mathcal{B}(\mu \to e\gamma)$. We set a limit of $\mathcal{B}(\mu \to e\gamma) < 7.5 \times 10^{-13}$ ($N_{\mathrm{sig}} < 1.98$) at 90 % confidence level. Fig.7.3 and Fig.7.4 show the observed event distribution. A scatter plot of R_{sig} vs observed date is also shown in Fig.7.5. The highest ranked 10 events, shown as the filled red circles in Fig.7.5, are also listed in Tab.7.3. The above results were cross-checked with different analysis methods as detailed in Appendix.C, and they agree well with each other.

7.2.1 Combined result with MEG I final analysis

This analysis was combined with MEG I final result [1], which made use of the likelihood curves shown in Fig.7.6. Here, the combined best fit is $N_{\mathrm{sig}} = 0$ with the physical constraint. As the full-frequentist simulation is not practically possible for the combined analysis, the threshold on the profile likelihood ratio was empirically determined from the full-frequentist simulations for the MEG final analysis and the MEG II 2021 analysis. The threshold on the negative log-likelihood value — the $-\log\lambda$ introduced in Eq.(6.2) — ranges between 1.2 – 1.7, depending on the tested Br($\mu \to e\gamma$) value and the difference

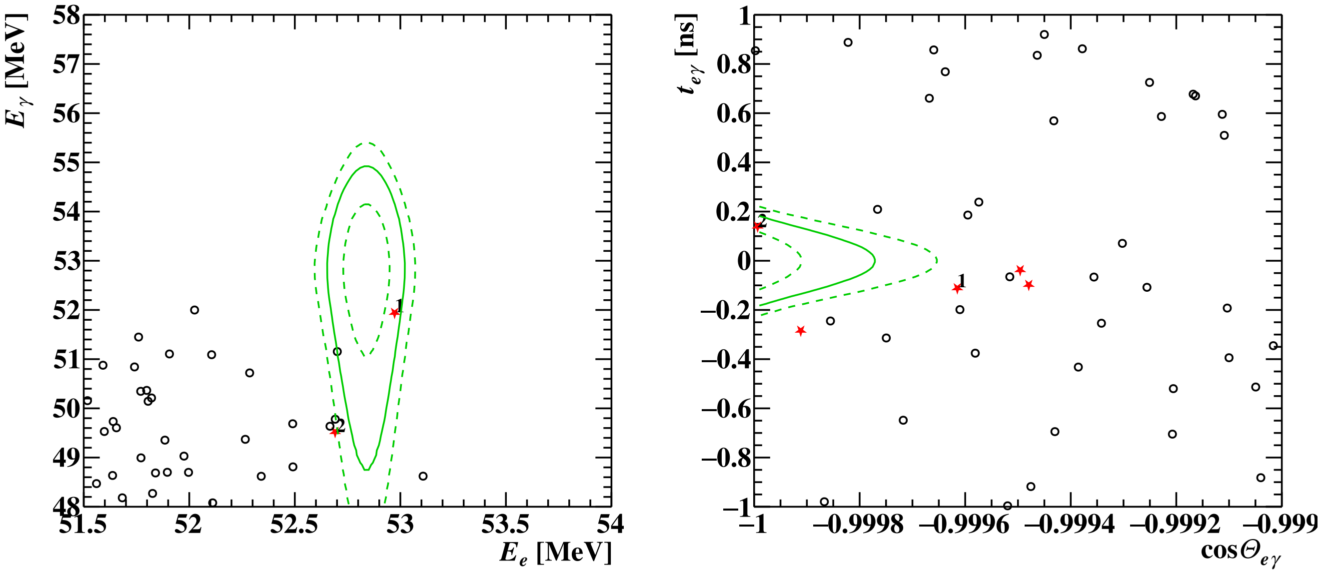

Figure 7.3: Distribution of observed events in the (E_e, E_γ) and $(\cos\Theta_{e\gamma}, t_{e\gamma})$ planes. In the (E_e, E_γ) plot, $\cos\Theta_{e\gamma} < -0.9995$ and $|t_{e\gamma}| < 200\,\mathrm{ps}$ cuts are applied with $97\,\%$ signal efficiency each. In the $(\cos\Theta_{e\gamma}, t_{e\gamma})$ plot, $49 < E_\gamma < 55\,\mathrm{MeV}$ and $52.5 < E_e < 53.2\,\mathrm{MeV}$ cuts are applied with $93\,\%$ and $97\,\%$ efficiency respectively. The green lines indicate 1σ, 1.64σ, and 2σ contours of the signal PDF. The highest ranked five events are drawn as stars with the ranking indices beside them. The third to fifth rank events are not found in the left plot because of the timing or angle cut.

between MEG and MEG II. Here, we found that the threshold of the negative log-likelihood can become large when N_{BG} is small and $N_{\mathrm{sig}} < 5$. This time, we used the full MEG statistics, and we had a large N_{BG}. Therefore, we adopted a threshold of 1.6 for $90\,\%$ confidence interval, which was the largest possible threshold for the MEG final analysis. Here, note that this threshold value is larger than the 1.35 threshold value of the asymptotic method [103]. As a result, the combination of the MEG final data and the MEG II 2021 data gave a limit of $\mathcal{B}(\mu \to e\gamma) < 3.1 \times 10^{-13}$.

The sensitivity for the combined analysis was calculated by combining MEG-only pseudo experiments with MEG II-only pseudo experiments. The upper limit distribution is shown in Fig.7.7, where the median sensitivity is $\mathcal{B}(\mu \to e\gamma) < 4.3 \times 10^{-13}$. The combined data upper limit of 3.1×10^{-13} is equivalent to the bottom $30\,\%$ of the combined toy MC samples. This can be understood from the fact that both the MEG final data and MEG II data are downward fluctuated; 4.2×10^{-13} of the MEG final data is equivalent to the bottom $36\,\%$, and 7.5×10^{-13} is equivalent to the bottom $38\,\%$. As a case study, Fig.7.8 shows the upper limit distribution for combinations of MEG II-only pseudo experiments and the MEG final data. Here, the set of upper limits on data, 7.5×10^{-13} for MEG II and 3.1×10^{-13} for the combined, is found to be consistent.

7.3 Discussion

The sensitivity of this analysis (8.8×10^{-13}) did not exceed the full sensitivity of the previous experiment (5.3×10^{-13}), and the upper limit (7.5×10^{-13}) was not as stringent as the previous one (4.2×10^{-13}). This, however, is just because of the limited time in the data-taking of the first MEG II data. The author stresses that this result, as will be discussed in the next sections, demonstrates the feasibility of sensitivity improvement by an order of magnitude when we consider the planned MEG II data taking in the next few years.

This analysis was purely limited by the statistics of the dataset and it kept almost background-free conditions. On the other hand, the previous search was limited by the number of background events. This makes an important difference in future projections. When the sensitivity is limited by the statistics,

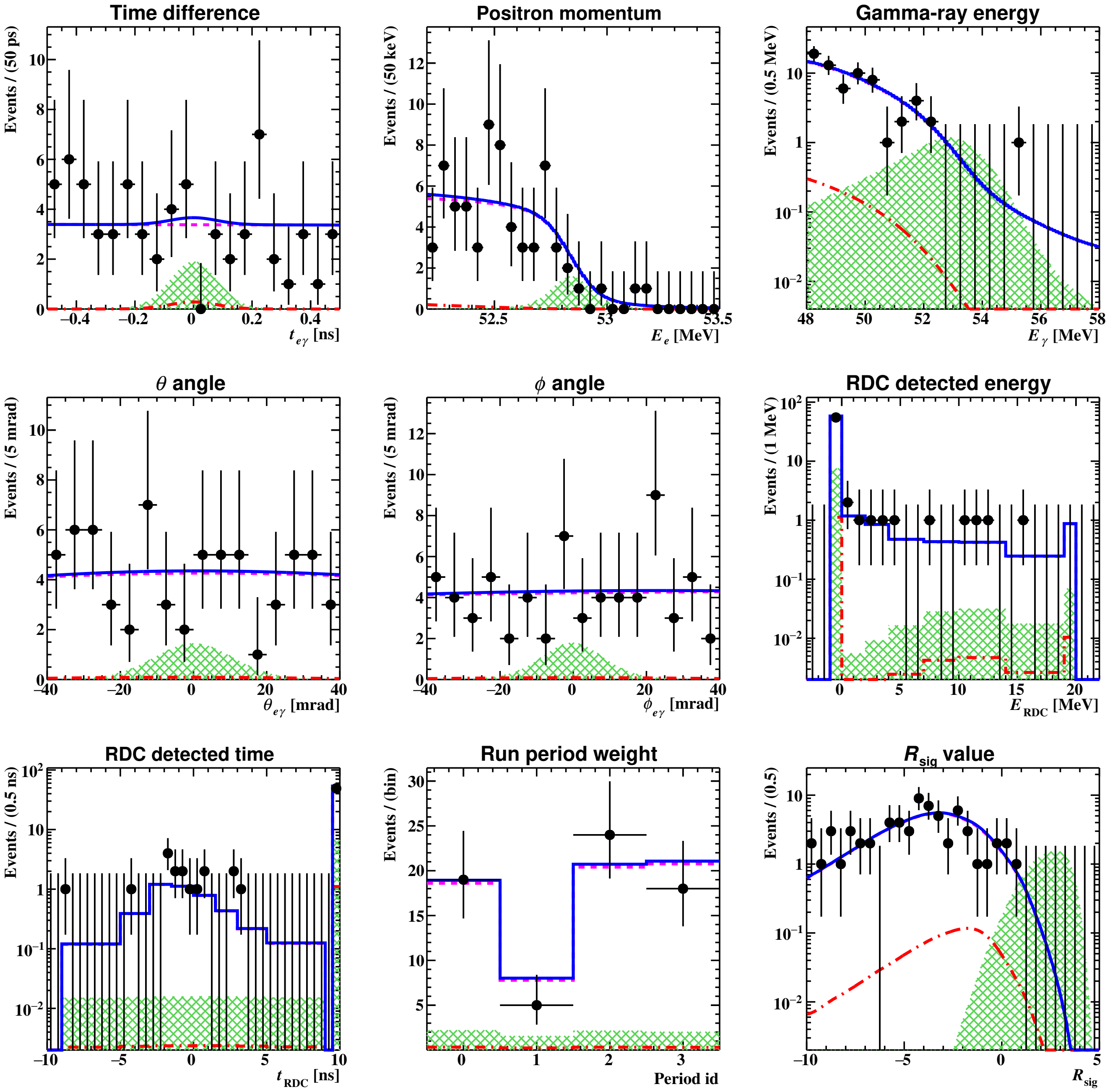

Figure 7.4: Projected distribution of observed events on the parameter space of eight fit observables and R_{sig} parameter (black markers), and the expected shape of the distribution according to the best-fit value (blue solid line). The magenta dashed (red dash-dotted) line represents the component of the accidental background (RMD background) in the fitted PDF. The green hatched region shows the signal PDF with $N_{\mathrm{sig}} = 8$, which is four times larger than the upper limit.

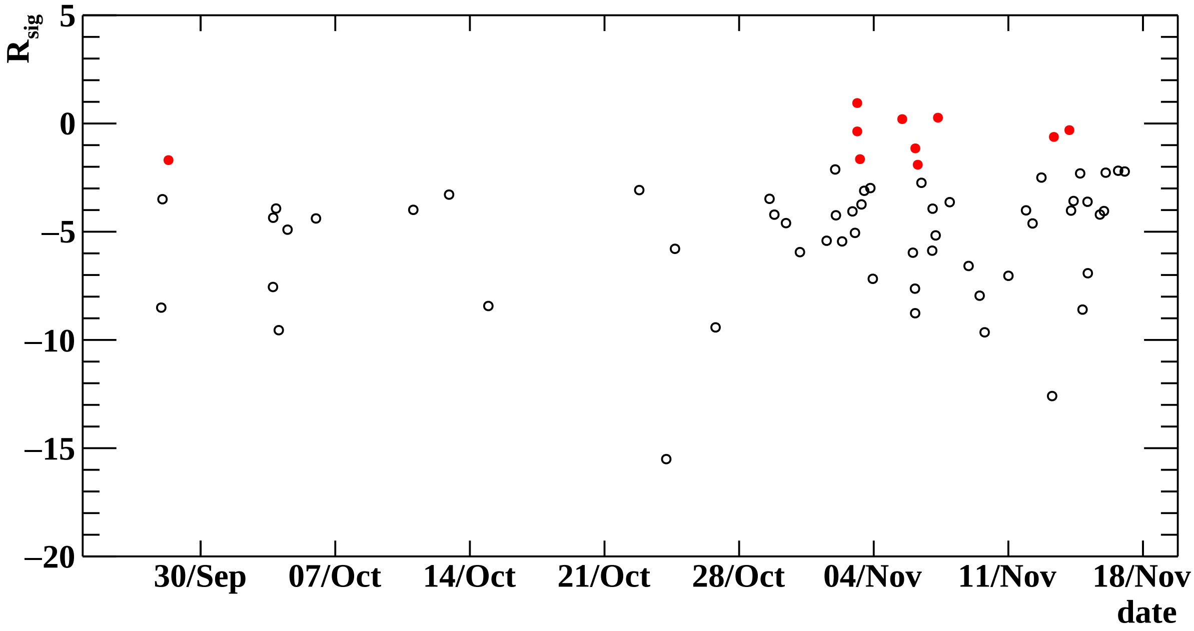

Figure 7.5: The $R_{\rm sig}$ value and the date of the observed 66 events in the analysis region. The filled red circles are the highest-ranked 10 events and the black open circles are the other 56 events. The number of observed events before October 15th (between October 15th – October 28th) is small because of the inefficiency in the DAQ as shown in Fig.3.5 (because of the small beam intensity as presented in Tab.3.1).

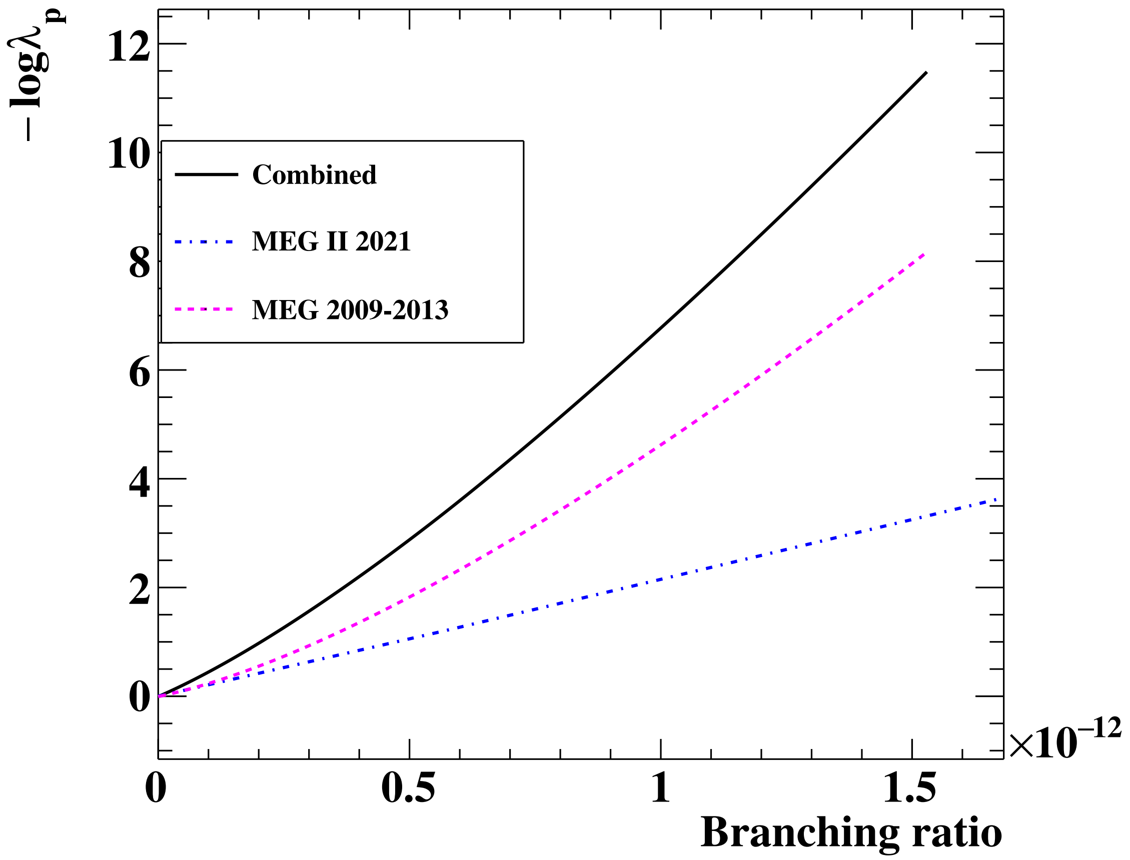

Figure 7.6: The negative log-likelihood ratio for the MEG I final data (magenta dashed line), MEG II 2021 data (blue dash-dotted line), and their combination (black solid line) as a function of $\mathcal{B}(\mu \to e\gamma)$. The offset of the log-likelihood value is defined so that $-\log\lambda = 0$ at the best-fit value with the $N_{\rm sig} = 0$ constraint.

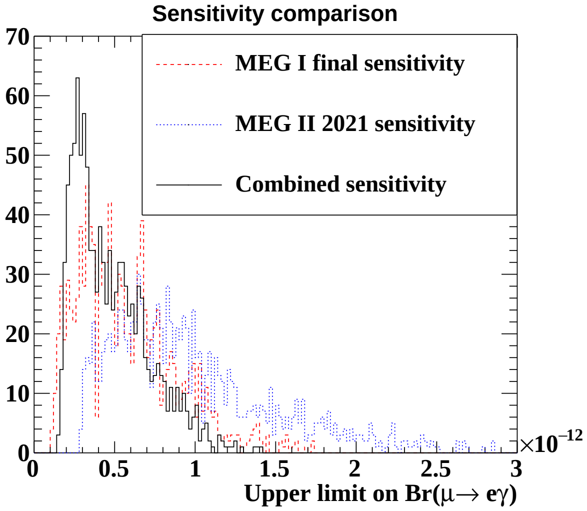

Figure 7.7: Distribution of $90\,\%$ upper limit in toy MCs simulating a combined analysis of the MEG final data and the first MEG II data. The median value is 4.3×10^{-13}.

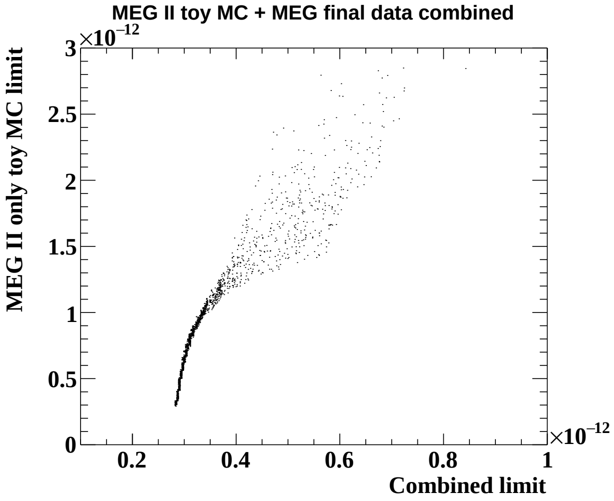

Figure 7.8: Distribution of $90\,\%$ upper limit when the final MEG data is combined with toy MCs simulating the first MEG II data. The x-axis shows the combined upper limit and the y-axis shows the limits of the MEG II toy MCs.

continuous data-taking will improve proportionally to the DAQ time. In the case limited by backgrounds, on the other hand, it becomes useless because the sensitivity improves only by the square root of the DAQ time. Furthermore, the effective DAQ time for the data in this analysis is only four weeks when we scale the DAQ inefficiencies unique to the first commissioning (see Fig.3.1 and Fig.3.5 in particular). This is much smaller than the five years of data-taking in the previous search. Therefore, it is a wonderful result that the sensitivity of this analysis closely approached that of the previous one despite all these limitations.

The improvement of this experiment comes from several reasons. The first improvement is in the efficiency of the positron reconstruction, which is $\times 2$ higher than that of the previous experiment. In addition, the interruption of the data taking was reduced thanks to the stable operation of the detectors. This improvement gives a much higher number of effectively measured muon decays per unit time. A significant reduction in the number of backgrounds was also achieved by resolution improvements. In particular, the positron momentum resolution improvement was significant; $380\,\mathrm{keV} \rightarrow 90\,\mathrm{keV}$. In addition, we succeeded in reducing the impact of systematic uncertainties on the sensitivity, $13\,\% \rightarrow 4\,\%$.

At the moment with limited statistics from the MEG II, it is also useful to combine this analysis with the previous experiment. This gave the sensitivity of 4.3×10^{-13} and the most stringent upper limit of 3.1×10^{-13}. Note that this sensitivity record will be broken shortly (within a year from now) when the MEG II 2022 data analysis is completed, as will be presented in the next section.

7.4 Prospect

This thesis is based on the 2021 data, which was taken for seven weeks in total giving 4.8 weeks of efficiently used *livetime*. At the time of this thesis, we have already taken additional two years of data. In 2022 (2023), we took the physics data for 18 (22) weeks in total from July (May) to November, which gave 12.8 (15.9) weeks of efficiently used *livetime*. Though the fraction of the livetime was small at the beginning of 2022 data taking because of some inefficiencies (in calibration scheme, DAQ computer, etc.), it finally improved to $81\,\%$ in late 2022.

In the future, we plan to continue the experiment till 2026. Here, however, we have uncertainties in the beamtime assignment because of the beamline sharing with other experiments, in particular the Mu3e experiment. Based on the achievements in the DAQ scheme and the beamtime uncertainties, our

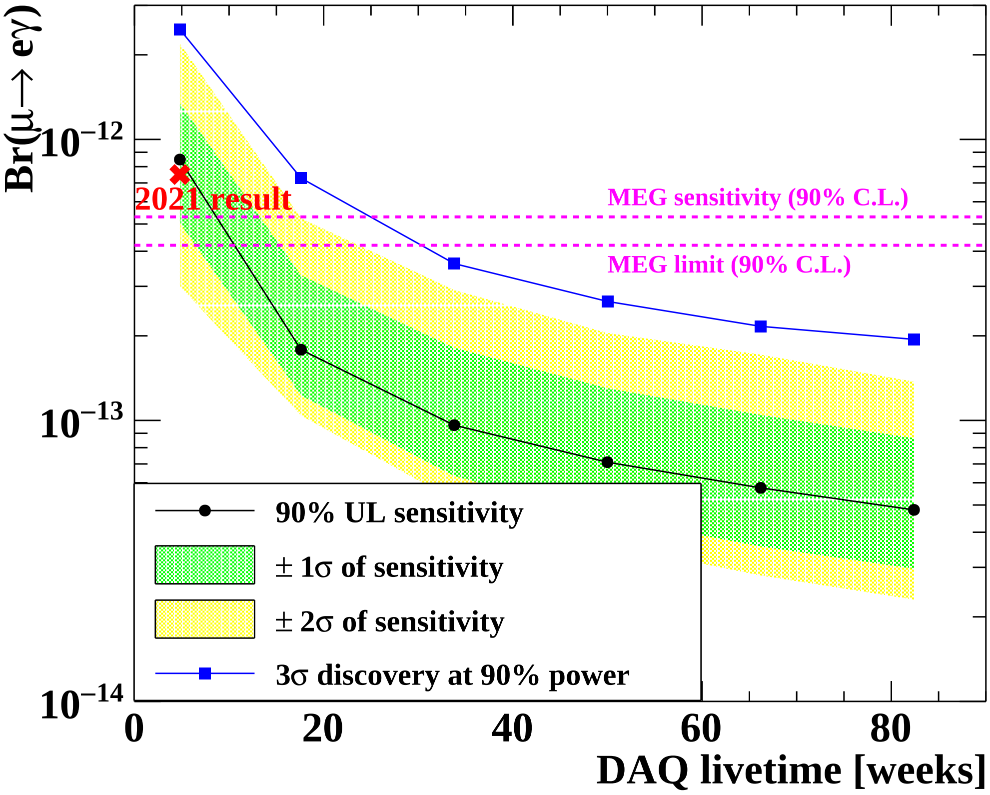

Figure 7.9: Expected sensitivity in the future MEG II data taking as a function of the accumulated DAQ livetime. The black solid line with circular markers indicates the sensitivity (median) and the green (yellow) band indicates a statistical fluctuation at one (two) sigma level. The sensitivity is calculated at the point locations. The blue line with square markers shows a 3 sigma discovery potential at $90\,\%$ power. The red cross marker at the top-left indicates the observed upper limit in this thesis for MEG II only analysis, namely 7.5×10^{-13}.

expectation of the total MEG II livetime is 60 – 80 weeks. Hereafter, we employ this expectation as the baseline scenario of future data taking.

In the future sensitivity calculation, we fully use the knowledge from the 2021 data analysis. The set of PDFs used in the 2021 data analysis is reused in the toy MC simulation and the fitting. The number of effectively measured muon decays is extrapolated according to the result in Sec.6.3.1. If we can assume that the trigger efficiency will be improved to $95\,\%$, the increase of the normalization factor per unit livetime would be

$$\frac{\mathrm{d}k_{\mathrm{Michjel}}}{\mathrm{d}t_{\mathrm{live}}} = 1.85 \times 10^{6} \quad (\text{at } 4 \times 10^{7}\ \mu/\mathrm{s} \text{ beam intensity}). \tag{7.1}$$

The number of background events is also based on the observation in the 2021 dataset as

$$\frac{N_{\mathrm{acc}}}{k} = 2.8 \times 10^{-11} \quad (\text{at } 4 \times 10^{7}\ \mu/\mathrm{s} \text{ beam intensity}). \tag{7.2}$$

Note here that the value on the right-hand side behaves proportionally to the beam rate, $\frac{N_{\mathrm{acc}}}{k} \propto R_{\mu}$.

According to the inputs above, we found that the sensitivity is maximized at $4 \times 10^{7}\ \mu/\mathrm{s}$ beam intensity within 60 – 80 weeks of DAQ livetime. Therefore, we adopted $4 \times 10^{7}\ \mu/\mathrm{s}$ beam rate since the start of the 2023 data taking. The future sensitivity was also estimated with this optimized beam rate, and the result is shown in Fig.7.9. It indicates that a 6×10^{-14} sensitivity can be achieved within 60 weeks of livetime.

Possible performance improvement

As well as the continuous data taking, further improvements in the detector performance are expected. Hardware improvements are expected in the positron spectrometer and the RDC, and reconstruction and calibration improvements are expected both for positron and gamma-ray. In the rest of this section, we will discuss them in detail.

The positron spectrometer hardware is planned to be replaced with new ones in the 2023 – 2024 shutdown period. The CDCH, which is defective now due to the wire breaking problem mentioned in Sec.1.4, will be replaced with a new chamber with one more outermost layer than the present one. With a complete set of wires and the increased detection layer, we can expect a higher tracking efficiency and a better resolution. Given this opportunity to re-install the detector, the pTC will also be updated by replacing some scintillation tiles with new ones. This replacement targets counters of severely radiation-damaged counters, which thus have bad timing resolution. The reported timing resolution in Sec.5.5.4 got worse by $10\,\%$ since the first operation in 2017 [42]. Therefore, this replacement is expected to improve the positron timing resolution accordingly.

In the current data taking, the RDC is only installed in the downstream end (Fig.2.26). This is because of the technological difficulty in achieving a high rate capability and a low material budget, which is because of the operation in the muon beam. An encouraging candidate is a Resistive Plate Chamber based on a novel technology with Diamond-Like Carbon electrodes. In Ref.[55, 56], both the material budget and the rate capability are demonstrated in a measurement at the MEG II beamline. The detector scalability is the remaining challenge, and technological R&D works are in progress to solve it. This will be installed, if everything goes smoothly, in 2025 and will further reduce the background gamma-rays from the radiative decay.

The pileup analysis in the gamma-ray energy reconstruction can be improved by fully exploiting waveform information recorded in the trigger hardware, which is currently not referred to in the reconstruction. This waveform corresponds to the summed waveform of the LXe readout channels and is used to implement the E_γ threshold trigger. This is recorded in a wider time window than that recorded by DRS, and thus, pileup pulses in the baseline region can be found more reliably. The use of this additional information would help to search pileups with a more robust algorithm and thus reduce the background in the E_γ spectrum.

The time calibration for the gamma-ray measurement, presented in Sec.5.4, is found not to perfectly model the sensor-by-sensor measured time. This imperfect modeling causes a correlation between the bias in the measured time and the scintillation light propagation distance. Though this can naively be considered to be a wrong calibration of the scintillation light velocity, we concluded that a simple modeling with a constant velocity cannot explain all the observed effects. This can be mitigated by introducing a more elaborate calibration method, including the machine learning approach, which the author expects to improve the σ_{LXe} down to $50\,\mathrm{ps}$ in the most optimistic case.

The positron track reconstruction efficiency is currently limited by the track finding algorithm as indicated in Sec.5.13. Therefore, its improvement would be helpful to have larger statistics of the dataset. One possible direction of improvement is the introduction of a global pattern recognition, which can find tracks from a set of distant hits, unlike the currently employed local-forwarding pattern recognition. Though a huge amount of studies will be necessary here, it would be an interesting work also in view of tracking detectors in other experiments.

If all these improvements work effectively in addition to the increased data amount, the final sensitivity presented in Fig.7.9 can be improved by up to 20 – $30\,\%$. After all, the experiment will certainly achieve an order of magnitude sensitivity improvement than what we have currently achieved.

Chapter 8

Conclusion

The MEG II experiment started data taking in 2021 to search for the lepton flavor violating muon decay, $\mu \to e\gamma$. In this work, we searched for $\mu \to e\gamma$ by observing 2.64×10^{12} muon decays, which were collected in effectively four weeks. We built a maximum likelihood analysis and the search sensitivity was 8.8×10^{-13}. No signal excess was observed in the analysis and we set an upper limit of

$$\mathcal{B}(\mu \to e\gamma) < 7.5 \times 10^{-13}$$

at $90\,\%$ confidence level.

The sensitivity of this analysis was limited by the statistics of the dataset due to the limited DAQ time in 2021. However, we approached the sensitivity of the previous experiment only in effectively four weeks of data taking. This demonstrates the feasibility of the target sensitivity of the MEG II experiment, which is an order of magnitude higher than the previous experiment. A sensitivity calculation, which is based on the achieved performance presented in this thesis, shows that 6×10^{-14} sensitivity can be reached within 60 weeks of data taking.

In order to achieve the highest sensitivity ever, this analysis was combined with the previous $\mu \to e\gamma$ search [1]. The combined sensitivity was 4.3×10^{-13} , and we set an upper limit of

$$\mathcal{B}(\mu \to e\gamma) < 3.1 \times 10^{-13}$$

at $90\,\%$ confidence level. This gives the most stringent limit for the $\mu \to e\gamma$ branching ratio.

Appendix A

Radiative Muon Decay

A.1 Full energy distribution in radiative decay

The differential branching ratio in muon radiative decay, drawn in Fig.A.1a, can be expressed as [28, 107]

$$\begin{aligned} \mathrm{d}\mathcal{B}(\mu^+ \to e^+\nu\bar{\nu}\gamma) =& \frac{\alpha}{64\pi^3}\beta \mathrm{d}x\frac{\mathrm{d}y}{y}\mathrm{d}\Omega_e\mathrm{d}\Omega_\gamma \\ & \times \left[F(x,y,d) - \beta\vec{P_\mu}\cdot\frac{\vec{p_e}}{|\vec{p_e}|}G(x,y,d) - \vec{P_\mu}\cdot\frac{\vec{p_\gamma}}{|\vec{p_\gamma}|}H(x,y,d)\right], \end{aligned} \tag{A.1}$$

where $\mathrm{d}\Omega_{e,(\gamma)}$ is the solid angle of electron (gamma), $\vec{P_\mu}$ is the polarization vector of the muon, $\vec{p}_{e,(\gamma)}$ is the momentum of electron (gamma), $\beta = |\vec{p_e}|/E_e$, $x = 2E_e/m_\mu$, $y = 2E_\gamma/m_\mu$, and $d = 1 - \beta\frac{\vec{p_e}\cdot\vec{p_\gamma}}{|\vec{p_e}|\cdot|\vec{p_\gamma}|}$. The x and y ranges are given from the four-body kinematics as

$$\begin{aligned} 2\sqrt{r} < x < 1 + r \qquad & (0 < y \leq 1 - \sqrt{r}) \\ (1-y) + \frac{r}{1-y} \leq x \leq 1 + r \qquad & (1 - \sqrt{r} < y \leq 1 - r), \end{aligned} \tag{A.2}$$

where $r = (m_e/m_\mu)^2$. The explicit form of the functions F, G, H are given as

$$\begin{aligned} F =& F^{(0)} + rF^{(1)} + r^2F^{(2)} \\ G =& G^{(0)} + rG^{(1)} + r^2G^{(2)} \\ H =& H^{(0)} + rH^{(1)} + r^2H^{(2)}. \end{aligned} \tag{A.3}$$

Each function component in the above equation is given as

$$\begin{aligned} F^{(0)}(x,y,d) =& \frac{8}{d}\{y^2(3-2y) + 6xy(1-y) + 2x^2(3-4y) - 4x^3\} \\ & + 8\{-xy(3-y-y^2) - x^2(3-y-4y^2) + 2x^3(1+2y)\} \\ & + 2d\{x^2y(6-5y-2y^2) - 2x^3y(4+3y)\} + 2d^2x^3y^2(2+y) \end{aligned} \tag{A.4}$$

$$\begin{aligned} F^{(1)}(x,y,d) =& \frac{32}{d^2}\left\{-\frac{y(3-2y)}{x} - (3-4y) + 2x\right\} + \frac{8}{d}\{y(6-5y) - 2x(4+y) + 6x^2\} \\ & + 8\{x(4-3y+y^2) - 3x^2(1+y)\} + 6dx^2y(2+y) \end{aligned} \tag{A.5}$$

$$F^{(2)}(x,y,d) = \frac{32}{d^2}\left\{\frac{(4-3y)}{x} - 3\right\} + \frac{48y}{d} \tag{A.6}$$

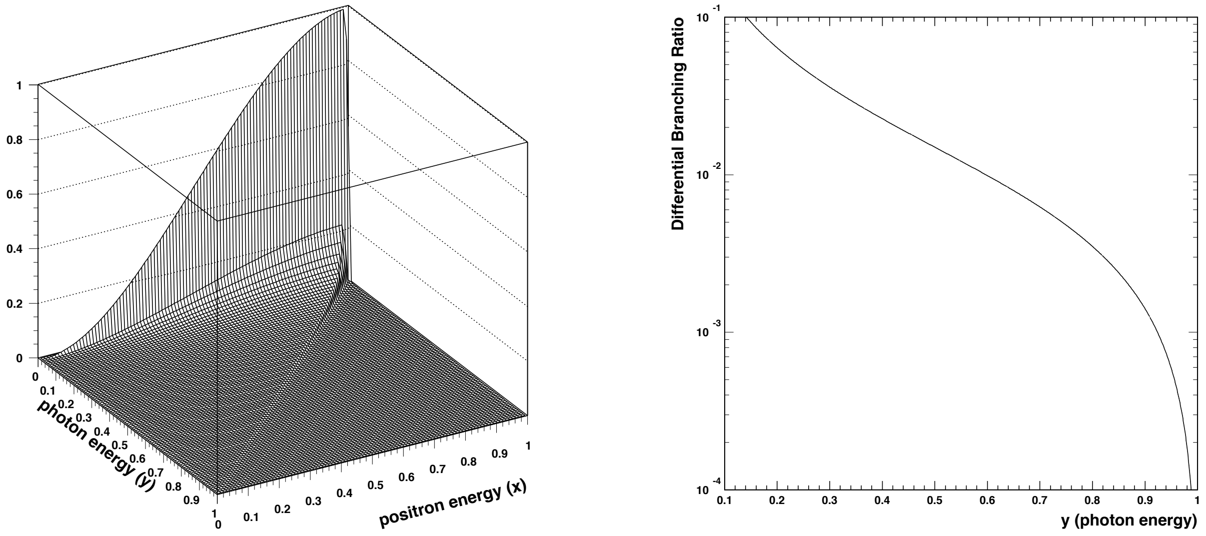

(a) (b)

Figure A.1: Differential branching ratio of radiative muon decay as a function of positron and gamma-ray energy [28]. (a): Two-dimensional energy spectrum of positron energy and gamma-ray energy. (b) The one-dimensional energy spectrum of gamma-ray energy with positron energy integrated out.

$$\begin{aligned} G^{(0)}(x,y,d) =& \frac{8}{d}\{xy(1-2y)+2x^2(1-3y)-4x^3\} \\ &+4\{-x^2(2-3y-4y^2)+2x^3(2+3y)\}-4dx^3y(2+y) \end{aligned} \tag{A.7}$$

$$G^{(1)}(x,y,d) = \frac{32}{d^2}(-1+2y+2x)+\frac{8}{d}(-xy+6x^2)-12x^2(2+y) \tag{A.8}$$

$$G^{(2)}(x,y,d) = -\frac{96}{d^2} \tag{A.9}$$

$$\begin{aligned} H^{(0)}(x,y,d) =& \frac{8}{d}\{y^2(1-2y)+xy(1-4y)-2x^2y\} \\ &+4\{2xy^2(1+y)-x^2y(1-4y)+2x^3y\} \\ &+2d\{x^2y^2(1-2y)-4x^3y^2\}+2d^2x^3y^3 \end{aligned} \tag{A.10}$$

$$\begin{aligned} H^{(1)}(x,y,d) =& \frac{32}{d^2}\left\{-\frac{y(1-2y)}{x}+2y\right\} \\ &+\frac{8}{d}\{y(2-5y)-xy\}+4xy(2y-3x)+6dx^2y^2 \end{aligned} \tag{A.11}$$

$$H^{(2)}(x,y,d) = -\frac{96y}{d^2x}+\frac{48y}{d} \tag{A.12}$$

A.2 Background gamma-ray spectrum for accidental events

Integrating Eq.(A.1) over the electron energy and angle variables, we can calculate the gamma energy spectrum in the accidental background as

$$\frac{\mathrm{d}\mathcal{B}(\mu^+ \to e^+\nu\bar{\nu}\gamma)}{\mathrm{d}y\mathrm{d}(\cos\theta_\gamma)} = \frac{1}{y}\left[J_+(y)(1+P_\mu\cos\theta_\gamma)+J_-(y)(1-P_\mu\cos\theta_\gamma)\right], \tag{A.13}$$

where m_e/m_μ is neglected. Here, $J_\pm$ are

$$\begin{aligned} J_+(y) = \; & \frac{\alpha}{6\pi}(1-y)\left[\left(3\ln\frac{1-y}{r}-\frac{17}{2}\right)+\left(-3\ln\frac{1-y}{r}+7\right)(1-y)\right. \\ & \left.+\left(2\ln\frac{1-y}{r}-\frac{13}{3}\right)(1-y)^2\right] \end{aligned} \tag{A.14}$$

$$\begin{aligned} J_-(y) = \; & \frac{\alpha}{6\pi}(1-y)^2\left[\left(3\ln\frac{1-y}{r}-\frac{31}{4}\right)+\left(-4\ln\frac{1-y}{r}+\frac{29}{3}\right)(1-y)\right. \\ & \left.+\left(2\ln\frac{1-y}{r}-\frac{55}{12}\right)(1-y)^2\right]. \end{aligned} \tag{A.15}$$

Fig.A.1b shows the accidental gamma energy spectrum calculated by Eq.(A.13). The rough scaling of the number of accidental background gamma-rays from radiative decay can be calculated by integrating Eq.(A.13) over y within the resolution,

$$\int_{1-\Delta y}^{1} \mathrm{d}y \int \mathrm{d}(\cos\theta_\gamma)\frac{\mathrm{d}\mathcal{B}(\mu^+\to e^+\nu\bar{\nu}\gamma)}{\mathrm{d}y\mathrm{d}(\cos\theta_\gamma)} \approx \left(\frac{\alpha}{2\pi}\right)(\Delta y)^2[\ln(\Delta y)+7.33].$$

Appendix B

Transformation of positron correlation to $\theta_{e\gamma}$ vs $\phi_{e\gamma}$ correlation

The notation below follows that defined in Sec.6.7.4.

B.1 Correlation and covariance in a simple model

B.1.1 Relation between y vs x covariance, y inner, and $p_x y$

Let us consider a two-parameter model that follows

$$y = p_{xy} \times x + y_{\text{inner}}. \tag{B.1}$$

where x and y_{inner} are independent. In this model, the covariance follows

$$\text{cov}(x, y) = p_{xy} \cdot \sigma_x^2. \tag{B.2}$$

In an ideally distributed Gaussian model, the slope parameter can thus be transformed by dividing the covariance by the σ_x^2. Therefore, we can also derive the following identity,

$$p_{yx} = \frac{\sigma_x^2}{\sigma_y^2} p_{xy}. \tag{B.3}$$

In addition, the y resolution follows

$$\sigma_y^2 = \sigma_{y,\text{inner}}^2 + p_{xy}^2 \sigma_x^2, \tag{B.4}$$

which indicates the relation between the full resolution and the inner resolution.

B.1.2 y vs x correlation when x is a composite of x_1 and x_2

Let us next consider a model of x, y with x that can be decoupled into two independent measurements as $x = x_1 + x_2$, and y is correlated only with x_1 and independent of x_2. Here, the covariance between x, y is identical to that of x_1, y,

$$\text{cov}(x, y) = \text{cov}(x_1, y). \tag{B.5}$$

When they are ideally distributed, the following are satisfied,

$$\begin{aligned} \text{cov}(x, y) &= p_{xy} \cdot \sigma_x^2 \\ &= p_{x_1 y} \cdot \sigma_{x_1}^2 \end{aligned} \tag{B.6}$$

Given $\sigma_x^2 = \sigma_{x_1}^2 + \sigma_{x_2}^2$, one can obtain p_{xy} as

$$p_{xy} = \frac{\sigma_{x_1}^2}{\sigma_{x_1}^2 + \sigma_{x_2}^2} \cdot p_{x_1 y}. \tag{B.7}$$

The y inner in y vs x ($\sigma_{y,\mathrm{inner}-xy}$) then becomes different from that in y vs x_1 ($\sigma_{y,\mathrm{inner}-x_1 y}$),

$$\begin{aligned} \sigma_{y,\mathrm{inner}-xy}^2 &= \sigma_y^2 - p_{xy}^2 \sigma_x^2 \\ &= \sigma_{y,\mathrm{inner}-x_1 y}^2 + \frac{\sigma_{x_2}^2}{\sigma_x^2} p_{x_1 y}^2 \sigma_{x_1}^2. \end{aligned} \tag{B.8}$$

The enlarged inner resolution here can be qualitatively understood that the additional x_2 contribution in the y vs x plot prevents the y vs x_1 correlation from getting perfectly resolved, which thus broadens the y inner distribution.

B.2 Correlation and covariance in $\delta\phi_{e\gamma}$ vs $\delta\theta_{e\gamma}$

We then build the full correlation of $\delta\phi_{e\gamma}$ vs $\delta\theta_{e\gamma}$. Given the positron correlation parameters, they can be decomposed into the following equations,

$$\delta\theta_{e\gamma} = \delta\theta_e + C_z \delta z_e + C_u \delta u_\gamma \tag{B.9}$$

$$\delta\phi_{e\gamma} = \delta\phi_{e,\mathrm{inner}-E_e} + C_v \delta v_\gamma \tag{B.10}$$

$$\delta\phi_{e,\mathrm{inner}-E_e} = \delta\phi_{e,\mathrm{inner}-E_e\theta_e z_e} + p_{\theta_e\phi_e}\delta\theta_e + p_{z_e\phi_e}\delta z_e \tag{B.11}$$

$$\delta z_e = p_{\theta_e z_e}\delta\theta_e + \delta z_{e,\mathrm{inner}} \tag{B.12}$$

$$(\delta\theta_e = p_{z_e\theta_e}\delta z_e + \delta\theta_{e,\mathrm{inner}}), \tag{B.13}$$

where $\delta\phi_{e,\mathrm{inner}-E_e}$ is the inner of ϕ_e after correcting only E_e correlation and $\delta\phi_{e,\mathrm{inner}-E_e\theta_e z_e}$ is the inner of ϕ_e after correcting all E_e, θ_e, z_e correlations. When we describe per-event PDF parameterization, $\sigma_{\phi_{e,\mathrm{inner}-E_e}} = s_{\phi_{e,\mathrm{inner}-E_e}} \times \sigma'_{\phi_e}$ is used hereafter. C_z, C_u, and C_v are parameters that translate Z_e, u_γ, v_γ resolutions into their contributions to $\theta_{e\gamma}$ or $\phi_{e\gamma}$ resolutions. Though y_e contribution, which is in our best knowledge independent of θ_e, ϕ_e, z_e, is dropped in the above equation for simplicity, our analysis implementation includes its contribution too.

The resolution of $\theta_{e\gamma}$, which is the σ of the square of Eq.(B.9) considering z_e vs θ_e correlation, can be written as

$$\begin{aligned} \sigma_{\theta_{e\gamma}}^2 &= \sigma_{\theta_e}^2 + C_z^2 \sigma_{z_e}^2 + 2C_z p_{\theta_e z_e} \sigma_{\theta_e}^2 + C_u^2 \sigma_{u_\gamma}^2 \\ &= s_{\theta_e}^2 \sigma'^2_{\theta_e} + C_z^2 s_{z_e}^2 \sigma'^2_{z_e} + 2C_z p'_{\theta_e z_e} s_{\theta_e}^2 \sigma'_{\theta_e} \sigma'_{z_e} + C_u^2 \sigma_{u_\gamma}^2, \end{aligned} \tag{B.14}$$

where the below substitutions are used

$$p_{\theta_e z_e} = p'_{\theta_e z_e} \frac{\sigma'_{z_e}}{\sigma'_{\theta_e}} \tag{B.15}$$

$$\sigma_{\theta_e} = s_{\theta_e} \sigma'_{\theta_e}. \tag{B.16}$$

Here, note that σ_{z_e} is the full σ including the $p'_{\theta_e z_e}$ correlation, not the inner after correcting it [1].

The covariance between $\theta_{e\gamma}$ and $\phi_{e\gamma}$ follows

$$\begin{aligned}\mathrm{cov}(\delta\theta_{e\gamma}, \delta\phi_{e\gamma}) &= \sigma^2_{\theta_e}(p_{\theta_e\phi_e} + p_{z_e\phi_e} \cdot p_{\theta_e z_e}) + C_z(\sigma^2_{z_e} p_{z_e\phi_e} + \sigma^2_{\theta_e} p_{\theta_e\phi_e} \cdot p_{\theta_e z_e}) \\ &= \sigma^2_{\theta_e}(p_{\theta_e\phi_e} + p_{z_e\phi_e} \cdot p_{\theta_e z_e}) + C_z \sigma^2_{z_e}(p_{z_e\phi_e} + p_{\theta_e\phi_e} \cdot p_{z_e\theta_e}),\end{aligned} \tag{B.17}$$

where a substitution like Eq.(B.3) is used. This will later be used to obtain $p_{\theta_{e\gamma}\phi_{e\gamma}} = \mathrm{cov}(\delta\theta_{e\gamma}, \delta\phi_{e\gamma})/\sigma^2_{\theta_{e\gamma}}$ and the inner $\phi_{e\gamma}$ resolution.

The positron correlation parameters observed in data or MC studies are not necessarily $p_{z_e\phi_e}$ or $p_{\theta_e\phi_e}$ in the above equations because we study "$p_{z_e\phi_e}$" with (θ_e, z_e, ϕ_e) parameter space projected onto (z_e, ϕ_e) or (θ_e, ϕ_e) plane. Let us assume that we evaluate the correlation in the following procedure;

1. ϕ_e vs z_e correlation first, and introduce $q_{z_e\phi_e}$ parameter as the correlation parameter when projected on the (z_e, ϕ_e) plane,
2. After correcting $q_{z_e\phi_e}$ and making a projection on the (z_e, ϕ_e) plane, we then evaluate $q_{\theta_e\phi_e}$ parameter.

By substituting Eq.(B.13) into Eq.(B.11), we obtain

$$\delta\phi_{e,\mathrm{inner}-E_e} = \delta\phi_{e,\mathrm{inner}-E_e\theta_e z_e} + (p_{\theta_e\phi_e} p_{z_e\theta_e} + p_{z_e\phi_e})\delta z_e + p_{\theta_e\phi_e}\delta\theta_{e,\mathrm{inner}}. \tag{B.18}$$

Here, $\delta\phi_{e,\mathrm{inner}-E_e\theta_e z_e}$ and $\delta\theta_{e,\mathrm{inner}}$ are independent of δz_e, therefore,

$$q_{z_e\phi_e} = p_{z_e\phi_e} + p_{\theta_e\phi_e} \cdot p_{z_e\theta_e}. \tag{B.19}$$

The $q_{\theta_e\phi_e}$ parameter can then be evaluated from

$$\delta\phi_{e,\mathrm{inner}-E_e} - q_{z_e\phi_e}\delta z_e = \delta\phi_{e,\mathrm{inner}-E_e\theta_e z_e} + p_{\theta_e\phi_e}(1 - p_{z_e\theta_e} p_{\theta_e z_e})\delta\theta_e - p_{\theta_e\phi_e} \cdot p_{z_e\theta_e}\delta z_{e,\mathrm{inner}}, \tag{B.20}$$

from which we obtain

$$q_{\theta_e\phi_e} = p_{\theta_e\phi_e}(1 - p_{z_e\theta_e} p_{\theta_e z_e}). \tag{B.21}$$

From Eq.(B.17), Eq.(B.21), and Eq.(B.19), we then derive

$$\mathrm{cov}(\delta\theta_{e\gamma}, \delta\phi_{e\gamma}) = \sigma^2_{\theta_e}(q_{\theta_e\phi_e} + q_{z_e\phi_e} \cdot p_{\theta_e z_e}) + C_z \sigma^2_{z_e} q_{z_e\phi_e}. \tag{B.22}$$

The correlation parameter between $\phi_{e\gamma}$ vs $\theta_{e\gamma}$ then follows

$$\begin{aligned}p_{\theta_{e\gamma}\phi_{e\gamma}} &= \frac{\mathrm{cov}(\delta\theta_{e\gamma}, \delta\phi_{e\gamma})}{\sigma^2_{\theta_{e\gamma}}} \\ &= \frac{s^2_{\theta_e}\sigma'^2_{\theta_e}}{\sigma^2_{\theta_{e\gamma}}}(q_{\theta_e\phi_e} + q_{z_e\phi_e} \cdot p_{\theta_e z_e}) + C_z \cdot \frac{s^2_{z_e}\sigma'^2_{z_e}}{\sigma^2_{\theta_{e\gamma}}} q_{z_e\phi_e} \\ &= \frac{s^2_{\theta_e}\sigma'_{\theta_e}\sigma'_{\phi_e}}{\sigma^2_{\theta_{e\gamma}}}(q'_{\theta_e\phi_e} + q'_{z_e\phi_e} \cdot p'_{\theta_e z_e}) + C_z \cdot \frac{s^2_{z_e}\sigma'_{z_e}\sigma'_{\phi_e}}{\sigma^2_{\theta_{e\gamma}}} q'_{z_e\phi_e}.\end{aligned} \tag{B.23}$$

---

[1] If one tries to parametrize it on the inner $\sigma_{z_e,\mathrm{inner}}$ base, the following replacement must be adopted,

$$\begin{aligned}&\sigma^2_{\theta_e} + C_z^2\sigma^2_{z_e} + 2C_z p_{\theta_e z_e}\sigma^2_{\theta_e} \\ =&(1 + C_z p_{\theta_e z_e})^2\sigma^2_{\theta_e} + C_z^2(\sigma^2_{z_e} - p^2_{\theta_e z_e}\sigma^2_{\theta_e}) \\ =&(1 + C_z p_{\theta_e z_e})^2\sigma^2_{\theta_e} + C_z^2\sigma^2_{z_e,\mathrm{inner}},\end{aligned}$$

which corresponds to the σ of $\delta\theta_e + C_z p_{\theta_e z_e}\delta\theta_e + C_z\delta z_{e,\mathrm{inner}}$.

Finally, the inner $\phi_{e\gamma}$ resolution after correcting $\phi_{e\gamma}$ vs $\theta_{e\gamma}$, $\sigma_{\phi_{e\gamma},\mathrm{inner}}$, follows

$$\sigma_{\phi_{e\gamma},\mathrm{inner}} = s^2_{\phi_{e,\mathrm{inner}-E_e}} \times \sigma'^2_{\phi_e} + C_v^2 \sigma_v^2 - p^2_{\theta_{e\gamma}\phi_{e\gamma}} \sigma^2_{\theta_{e\gamma}}. \tag{B.24}$$

When the above correlations are corrected in a different order, Eq.(B.23) would be changed. There are two such possibilities,

1. ϕ_e vs θ_e is corrected first and then correcting ϕ_e vs z_e.
2. Both ϕ_e vs θ_e and ϕ_e vs z_e are corrected without correcting the other correlation.

In the first case, the full correlation follows

$$\begin{aligned} p_{\theta_{e\gamma}\phi_{e\gamma}} &= \frac{s^2_{\theta_e}\sigma'_{\theta_e}\sigma'_{\phi_e}}{\sigma^2_{\theta_{e\gamma}}} q'_{\theta_e\phi_e} + C_z \cdot \frac{s^2_{z_e}\sigma'_{z_e}\sigma'_{\phi_e}}{\sigma^2_{\theta_{e\gamma}}} (q'_{z_e\phi_e} + q'_{\theta_e\phi_e} \cdot p'_{z_e\theta_e}) \\ &= \frac{s^2_{\theta_e}\sigma'_{\theta_e}\sigma'_{\phi_e}}{\sigma^2_{\theta_{e\gamma}}} q'_{\theta_e\phi_e} + C_z \cdot \frac{\sigma'_{z_e}\sigma'_{\phi_e}}{\sigma^2_{\theta_{e\gamma}}} (s^2_{z_e} q'_{z_e\phi_e} + s^2_{\theta_e} q'_{\theta_e\phi_e} \cdot p'_{\theta_e z_e}). \end{aligned} \tag{B.25}$$

In the second case, the full correlation follows

$$p_{\theta_{e\gamma}\phi_{e\gamma}} = \frac{s^2_{\theta_e}\sigma'_{\theta_e}\sigma'_{\phi_e}}{\sigma^2_{\theta_{e\gamma}}} q'_{\theta_e\phi_e} + C_z \cdot \frac{s^2_{z_e}\sigma'_{z_e}\sigma'_{\phi_e}}{\sigma^2_{\theta_{e\gamma}}} q'_{z_e\phi_e}. \tag{B.26}$$

Appendix C

Analysis cross check

C.1 Cross check analysis with different modeling

A cross-check analysis is constructed in the same way as Eq.(6.1), which however uses PDFs parametrized by a different set of observables. The PDFs for this cross-check analysis use four fit observables;

1. E_e,
2. E_γ,
3. $t_{e\gamma}$,
4. $\Theta_{e\gamma}$.

In particular, note that this analysis uses only the opening angle, $\Theta_{e\gamma}$, instead of the set of $(\theta_{e\gamma}, \phi_{e\gamma})$ as described in Sec.6.1.2. This analysis uses constant PDFs, which are commonly parametrized for all the events, except that one conditional observable, w_γ, is employed to take into account the E_γ resolution dependence. This analysis considers the correlation only between E_e and $\Theta_{e\gamma}$, and all the other correlations described in Sec.6.7.4 are integrated out to obtain the constant PDFs.

The consistency between the two analyses is validated with shared toy MC samples. Here, the toy MCs are shared by generating events with the main analysis framework, which are then converted with a $(\theta_{e\gamma}, \phi_{e\gamma}) \to \Theta_{e\gamma}$ transformation. Fig.C.1 shows a scatter plot that compares the upper limits for toy MCs generated with the null signal hypothesis, where we can see a strong correlation between them. Some of the samples with a large disagreement are investigated, and they are concluded to arise from the difference in the angle parametrization. All the investigated toy MC samples with disagreement are found to contain events with $\theta_{e\gamma}$ and $\phi_{e\gamma}$ having the same sign. They are not identified as signal events in the main analysis because it considers the anti-correlation between $\theta_{e\gamma}$ and $\phi_{e\gamma}$ (Fig.6.20). They, however, can be candidate signal events because the opening angle parameter is not sensitive to this anti-correlation. Shared toy MC samples are generated also with finite signal hypothesis, in which the best-fit value of N_{sig} is confirmed to be consistent.

The sensitivity of this analysis is $30\,\%$ worse than that presented in Sec.7.1, which is understood to arise from the broader response function of the constant PDFs. The obtained upper limits for data are consistent between the two analyses, as presented in Fig.C.1 for both the analysis region (black star) and sideband regions (blue circular markers).

C.2 Cross check with counting analysis

As a cross-check of the main likelihood analysis, a counting analysis is also performed with a cut on R_{sig}. The confidence interval is set according to the table presented in Ref.[102]. Fig.C.2 shows the sensitivity as a function of the cut threshold, and we found that the optimal threshold is $R_{\text{sig}} > 1.2$, which gives $N_{\text{BG}} = 0.5$ and 0.84 relative signal efficiency. Here, the relative efficiency is defined by

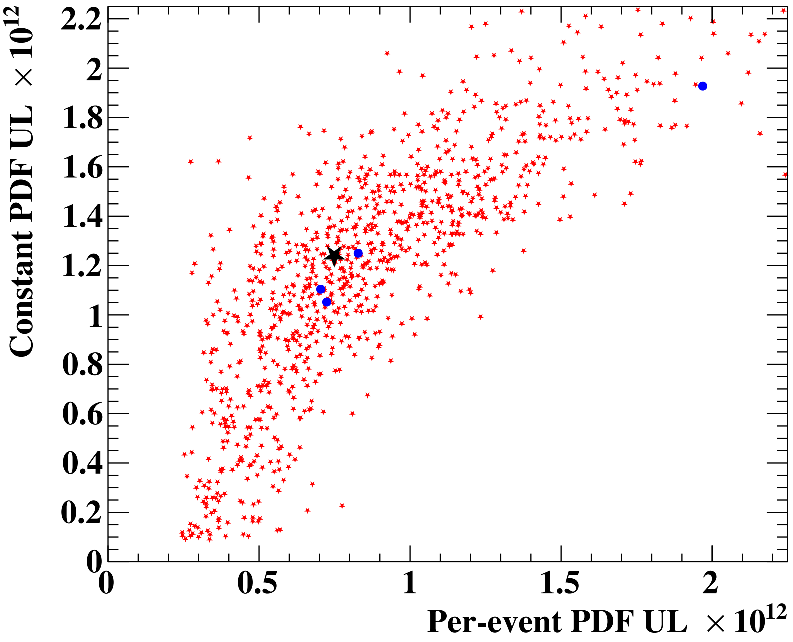

Figure C.1: Comparison of upper limits on $\mathcal{B}(\mu \to e\gamma)$ between the two analyses for shared toy MC samples (red small dots), data samples in the sideband regions (blue circles), data samples in the analysis region (black star) [57].

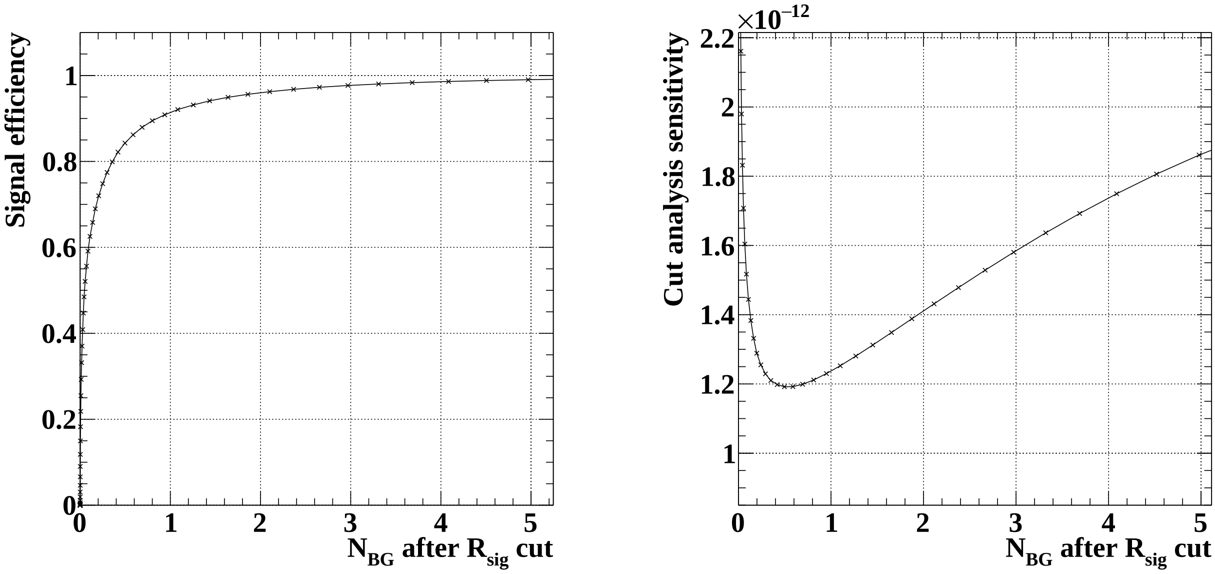

Figure C.2: Plots used for cut optimization. Left: Relation between signal efficiency and the number of background events obtained by threshold scan on R_{sig} obtained from cumulative of Fig.6.24. The signal efficiency is normalized to the efficiency after the selections for the likelihood analysis. Right: Estimated sensitivity as a function of N_{BG}.

Table C.1: Comparison of confidence intervals with different methods.

Data sample	Likelihood analysis interval	Counting analysis interval
Analysis region	$\mathcal{B}(\mu \to e\gamma) < 7.5 \times 10^{-13}$	$\mathcal{B}(\mu \to e\gamma) < 8.8 \times 10^{-13}$
Sideband		
$-3\,\mathrm{ns} < t_{e\gamma} < -2\,\mathrm{ns}$	$< 7.1 \times 10^{-13}$	$< 8.8 \times 10^{-13}$
$-2\,\mathrm{ns} < t_{e\gamma} < -1\,\mathrm{ns}$	$< 8.0 \times 10^{-13}$	$< 8.8 \times 10^{-13}$
$1\,\mathrm{ns} < t_{e\gamma} < 2\,\mathrm{ns}$	$< 6.9 \times 10^{-13}$	$< 8.8 \times 10^{-13}$
$2\,\mathrm{ns} < t_{e\gamma} < 3\,\mathrm{ns}$	1.6×10^{-13} – 2.6×10^{-12}	2.8×10^{-13} – 3.1×10^{-12}

normalizing that in the fit region of the likelihood analysis (Fig.6.2). The sensitivity at the optimized point is $\times 1.4$ larger than that for the likelihood analysis.

In the analysis region, the observed number of events is 0, giving a confidence interval of $\mathcal{B}(\mu \to e\gamma) < 8.8 \times 10^{-13}$. In the sidebands, the observed number of events is 0 for the first three sidebands and 3 for the fourth sideband. In the fourth sideband, the p-value of the $N_{\mathrm{sig}} = 0$ hypothesis is $1.4\,\%$. The intervals in the sideband are summarized in Tab.C.1 and compared with those from the likelihood analysis. As is evident in this table, the results of the counting analysis and those of the likelihood analysis agree with each other.

Appendix D

Full detail of the target hole analysis

D.1 Method and systematics of alignment

The hole analysis firstly estimates the position distribution that we would have without the target holes, interpolating the position distribution in the neighboring region around each hole. This, the expected total number of positrons without the target holes, is then subtracted by the reconstructed position distribution. This gives expected y and z distributions of the positrons associated with the hole (Fig.D.1), and the peak positions are used to give y and z estimates of the holes. The x coordinate is evaluated from the correlation between the estimated hole y position and $\tan\phi_e$ of the positron emission angle (Fig.5.50), which is produced by an additional x misalignment between the nominal and the true hole position.

In studies with MC samples, the y and z estimation from Fig.D.1 is found to be biased by the non-uniform beam profile, and the peak position estimation gets closer to the beam center by $100\,\mathrm{\mu m}$. This effect is also observed in data when the hole-to-hole distance estimation is compared with that from the CT scan. To correct this effect, the original histogram can be scaled according to the observed distribution around the holes (Fig.D.2). This correction, however, overestimates the bias[1] and the estimated peak position gets further from the beam center. This overestimation, also evaluated with MC Michel samples, results in 100 – $200\,\mathrm{\mu m}$ biases. The hole positions are thus estimated by combining the results from two methods with the corrections learned from MC samples. The remaining discrepancies between them are a source of systematic uncertainties.

In addition to the above biases, there is another source of biases unique to data, which comes from the non-Gaussian asymmetric beam profile. As can be seen in Fig.D.2, a non-zero baseline — not existing in MC samples — can be found in the position distribution associated with the holes. Biases on the peak position due to this baseline structure are evaluated by fitting different models to the distribution; simple Gaussian function, Gaussian function with a constant offset, and Gaussian function with a linear offset function. The differences between the fit models were found to be as large as $400\,\mathrm{\mu m}$ in z coordinate and $200\,\mathrm{\mu m}$ in y coordinate.

The final y and z estimation combines the results from different methods with different systematics as discussed above, and 100 – $200\,\mathrm{\mu m}$, half of the differences between them, are included as a systematic uncertainty. The x estimate of the holes does not show strong method dependence because the biases in the y coordinate only produce y-shift in the Fig.5.50 plot with little impact on the slope. Therefore, the systematics in x coordinate are $\sim 50\,\mathrm{\mu m}$, smaller than the statistical uncertainties.

D.2 Results of target hole analysis

The additional misalignment estimated from the hole analysis is tabulated in Tab.D.1. Fitted to

---

[1] Probably because this correction does not correctly weight the correction according to the circular shape of the holes

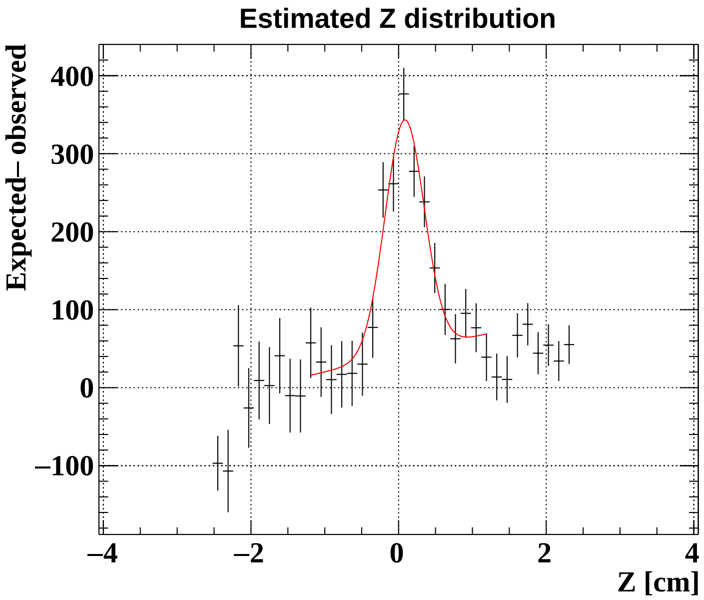

Figure D.1: Estimated z_e distribution of the number of lost positrons at a target hole.

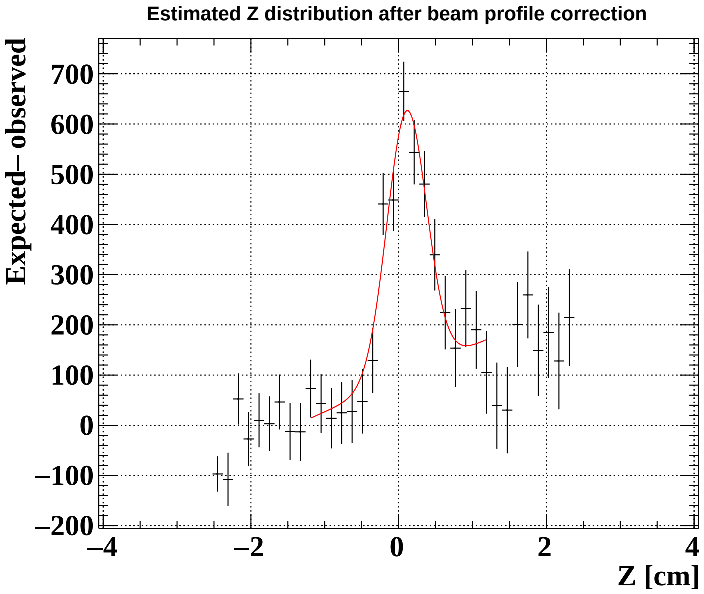

Figure D.2: Estimated z_e distribution of the number of lost positrons at a target hole after correcting for the beam rate non-uniformity.

Table D.1: Hole analysis results

Hole position in survey in MEG coordinate [cm]	Estimated difference from photograph + CT-scan $(\delta x, \delta y, \delta z)$ each with $\pm$stat $\pm$ syst [µm]
$(2.3601, -0.313624, -8.53115)$	$(200 \pm 180 \pm 50, 550 \pm 110 \pm 70, 250 \pm 160 \pm 120)$
$(1.30243, -0.319128, -4.69109)$	$(280 \pm 80 \pm 50, 620 \pm 50 \pm 70, 100 \pm 100 \pm 150)$
$(-0.0312347, 0.97017, 0.138845)$	$(200 \pm 80 \pm 50, 900 \pm 50 \pm 100, 680 \pm 90 \pm 130)$
$(-0.0414534, -1.62367, 0.14167)$	$(-50 \pm 150 \pm 50, 740 \pm 100 \pm 100, 560 \pm 180 \pm 130)$
$(-1.32782, -0.314651, 4.97927)$	$(-240 \pm 180 \pm 50, 760 \pm 100 \pm 70, 800 \pm 180 \pm 200)$

the above results, the target position and rotation — parametrized as additional corrections to the photographic estimations — are estimated with $100\,\mu\mathrm{m}$ uncertainties in the translations and $6\,\mathrm{mrad}$ $(1.4\,\mathrm{mrad})$ uncertainty in the rotation around the target long (short) axis. The overall offsets in the best fit, $100\,\mu\mathrm{m}$ in x, $700\,\mu\mathrm{m}$ in y and $400\,\mu\mathrm{m}$ in z, are understood to be global offset shifts of the CDCH, which were also found in CDCH vs COBRA alignment studies. The hole-to-hole discrepancies from the best fit — especially large for z estimation — are not fully understood. Nevertheless, the most suspicious causes are underestimations of the uncertainties or mis-evaluation of the bias corrections according to the observations in Fig.D.1 and Fig.D.2. On the other hand, the additional rotation was small and can be explained by the precision of the target survey.

Acknowledgements

First and foremost, I would like to express my deepest gratitude to my academic supervisor Prof. Wataru Ootani for giving me an educational opportunity as a Ph.D. student. Under his mentorship, I was able to have a smooth student life and enjoy the research activities. I am also grateful to the spokespersons of the MEG II experiment, Prof. Toshinori Mori and Prof. Alessandro Baldini for the opportunity to join the MEG II experiment. It was both challenging and exciting to get involved at the start of the DAQ and complete the first analysis of the MEG II experiment. I also acknowledge Dr. Toshiyuki Iwamoto, Dr. Angela Papa, and Dr. Malte Hildebrandt for their coordination of the MEG II data taking. I would also like to thank Dr. Toshiyuki Iwamoto for his special support during my stay in Switzerland.

I heartily appreciate cooperation in the analysis works. Dr. Yusuke Uchiyama gave me many suggestions and discussions to improve the analysis as well as his contributions. He also gave me essential support in computing and software management. Dr. Fabrizio Cei, who is in charge of the cross-check analysis, shared many important results and stimulated many meaningful discussions. Dr. Francesco Renga was always helpful in developing the analysis with his extensive knowledge and experience. The analysis also strongly relied on enormous contributions by Dr. Satoru Kobayashi, Dr. Dylan Palo, and Mr. Kensuke Yamamoto. Dr. Luca Galli and Dr. Marco Francesconi were always cooperative in the DAQ-related analyses with their expertise in the hardware. Needless to say, I am grateful to all the other members in the positron and photon analysis groups for their contributions and discussions to complete this work, especially Dr. William Molzon, Dr. Fedor Ignatov, and Mr. Antoine Venturini in the positron group and Dr. Rina Onda and Ms. Ayaka Matsushita in the photon group.

I express my special gratitude to the hardware group of the experiment, especially Dr. Toshiyuki Iwamoto, Dr. Sei Ban, and Dr. Lukas Gerritzen for the LXe detector, Dr. Yusuke Uchiyama, Dr. Paolo W Catttaneo, Dr. Matteo De Gerone, and Mr. Taku Yonemoto for the pTC, Dr. Marco Chiappini for the CDCH, Dr. Angela Papa, Dr. Patrick Schwendimann, Mr. Giovanni Dal Maso, Mr. Bastiano Vitali, and Mr. Hicham Benmansour for the beam group, and Dr. Stefan Ritt, Dr. Luca Galli, and Dr. Marco Francesconi for the DAQ hardware. Additionally, I also sincerely appreciate the exciting R&D works of RPC with Prof. Atsuhiko Ochi, Dr. Kei Ieki, Mr. Kensuke Yamamoto, and Mr. Masato Takahashi.

I am grateful to ICEPP secretaries and all the other laboratory members. Especially, I would like to mention that I shared a joyful time with Dr. Shinji Ogawa, Dr. Mitsutaka Nakao, Dr. Masashi Usami, Mr. Linghui Liu, Dr. Naoki Tsuji, Mr. Kazuki Toyoda, Mr. Kosuke Yanai, Mr. Kohei Shimada, Mr. Ryunosuke Masuda, Mr. Fumihito Ikeda, Mr. Tatsuki Murata, Mr. Keisuke Yoshida, Mr. Yuki Ueda, Mr. Rintaro Yokota, and Mr. Weiyuan Li.

Last but not least, I also extend my thanks to my family. Their constant love and support were the driving forces behind my pursuit of this thesis.

References

[1] Baldini, A. M. *et al.* Search for the lepton flavour violating decay $\mu^+ \to e^+\gamma$ with the full dataset of the MEG experiment - MEG Collaboration. *Eur. Phys. J. C*, 76(8):434, 2016.

[2] R. L. Workman et al. Review of Particle Physics. *Progress of Theoretical and Experimental Physics*, 2022(8), 08 2022. 083C01.

[3] N. Aghanim *et al.* Planck 2018 results. *Astronomy and Astrophysics*, 641, 2020.

[4] Y. Fukuda *et al.* Evidence for Oscillation of Atmospheric Neutrinos. *Phys. Rev. Lett.*, 81:1562–1567, Aug 1998.

[5] Q. R. Ahmad *et al.* Measurement of the Rate of $\nu_e + d \to p + p + e^-$ Interactions Produced by ^8B Solar Neutrinos at the Sudbury Neutrino Observatory. *Phys. Rev. Lett.*, 87:071301, Jul 2001.

[6] S. Weinberg. Implications of dynamical symmetry breaking: An addendum. *Phys. Rev. D*, 19:1277–1280, Feb 1979.

[7] E. Gildener. Gauge-symmetry hierarchies. *Phys. Rev. D*, 14:1667–1672, Sep 1976.

[8] L. Susskind. Dynamics of spontaneous symmetry breaking in the Weinberg-Salam theory. *Phys. Rev. D*, 20:2619–2625, Nov 1979.

[9] S. P. Martin. A Supersymmetry Primer. 1997.

[10] T. Yanagida. Horizontal Symmetry and Masses of Neutrinos. *Progress of Theoretical Physics*, 64(3):1103–1105, 09 1980.

[11] M. Gell-Mann, P. Ramond, R. Slansky. Complex Spinors and Unified Theories, 2013,Originally published in 1979.

[12] R. N. Mohapatra, G. Senjanović. Neutrino Mass and Spontaneous Parity Nonconservation. *Phys. Rev. Lett.*, 44:912–915, Apr 1980.

[13] S. Vagnozzi *et al.* Unveiling ν secrets with cosmological data: Neutrino masses and mass hierarchy. *Phys. Rev. D*, 96:123503, Dec 2017.

[14] B. W. Lee, R. E. Shrock. Natural suppression of symmetry violation in gauge theories: Muon- and electron-lepton-number nonconservation. *Phys. Rev. D*, 16:1444–1473, Sep 1977.

[15] S. Bilenky, S. Petcov, B. Pontecorvo. Lepton mixing, $\mu \to e\gamma$ decay and neutrino oscillations. *Physics Letters B*, 67(3):309 – 312, 1977.

[16] Y. Kuno. Rare lepton decays. *Progress in Particle and Nuclear Physics*, 82:1 – 20, 2015.

[17] J. Hisano *et al.* Enhancement of $\overrightarrow{\mu}\ e\gamma$ in the supersymmetric SU(5) GUT at large $\tan\beta$. *Phys. Rev. D*, 58:116010, Nov 1998.

[18] R. Barbieri, L. Hall. Signals for supersymmetric unification. *Physics Letters B*, 338(2):212 – 218, 1994.

[19] J. Hisano *et al.* Exact event rates of lepton flavor violating processes in supersymmetric SU(5) model. *Physics Letters B*, 391(3):341 – 350, 1997.

[20] J. Hisano *et al.* Lepton-flavor violation via right-handed neutrino Yukawa couplings in the supersymmetric standard model. *Phys. Rev. D*, 53:2442–2459, Mar 1996.

[21] S. Antusch *et al.* Impact of θ_{13} on lepton flavour violating processes within SUSY seesaw. *Journal of High Energy Physics*, 2006(11):090–090, nov 2006.

[22] T. Moroi, M. Nagai, T. T. Yanagida. Lepton-flavor violations in high-scale SUSY with right-handed neutrinos. *Physics Letters B*, 728:342–346, 2014.

[23] H. Nilles. Supersymmetry, supergravity and particle physics. *Physics Reports*, 110(1):1–162, 1984.

[24] J. Ellis, D. Nanopoulos, K. Tamvakis. Grand unification in simple supergravity. *Physics Letters B*, 121(2):123–129, 1983.

[25] M. Dine, A. E. Nelson. Dynamical supersymmetry breaking at low energies. *Phys. Rev. D*, 48:1277–1287, Aug 1993.

[26] M. Dine, A. E. Nelson, Y. Shirman. Low energy dynamical supersymmetry breaking simplified. *Phys. Rev. D*, 51:1362–1370, Feb 1995.

[27] M. Dine *et al.* New tools for low energy dynamical supersymmetry breaking. *Phys. Rev. D*, 53:2658–2669, Mar 1996.

[28] Y. Kuno, Y. Okada. Muon decay and physics beyond the standard model. *Rev. Mod. Phys.*, 73:151–202, Jan 2001.

[29] J. Hisano, D. Nomura. Solar and atmospheric neutrino oscillations and lepton flavor violation in supersymmetric models with right-handed neutrinos. *Phys. Rev. D*, 59:116005, Apr 1999.

[30] L. Calibbi *et al.* Lepton flavor violation from supersymmetric grand unified theories: Where do we stand for MEG, PRISM/PRIME, and a super flavor factory. *Phys. Rev. D*, 74:116002, Dec 2006.

[31] L. Calibbi *et al.* Status of supersymmetric type-I seesaw in SO(10) inspired models. *Journal of High Energy Physics*, 2012(11):40, Nov 2012.

[32] K. Hirao, T. Moroi. Leptonic CP and flavor violations in SUSY GUT with right-handed neutrinos. *Phys. Rev. D*, 104:035038, Aug 2021.

[33] T. Kinoshita, A. Sirlin. Radiative Corrections to Fermi Interactions. *Phys. Rev.*, 113:1652–1660, Mar 1959.

[34] Baldini, A. M. *et al.* The design of the MEG II experiment - MEG II Collaboration. *Eur. Phys. J. C*, 78(5):380, 2018.

[35] D. Kaneko. *The final result of $\mu^+ \to e^+\gamma$ search with the MEG experiment.* PhD Thesis, The University of Tokyo, 2016.

[36] Adam, J. *et al.* The MEG detector for $\mu^+ \to e^+\gamma$ decay search. *Eur. Phys. J. C*, 73(4):2365, 2013.

[37] A. M. Baldini *et al.* MEG Upgrade Proposal. 2013.

[38] M. Chiappini. *The construction and commissioning of the ultra low mass MEG II drift chamber for the search of the $\mu^+ \to e^+\gamma$ decay at branching ratios below* 10^{-13}. PhD Thesis, University of Siena and INFN Pisa, 2019.

[39] A. M. Baldini *et al.* The Search for $\mu+ \to$ e+ γ with 10–14 Sensitivity: The Upgrade of the MEG Experiment. *Symmetry*, 13(9), 2021.

[40] M. Usami. *Innovative positron spectrometer for $\mu^+ \to e^+\gamma$ search beyond* 10^{-13} *sensitivity with most intense μ^+ beam.* PhD Thesis, The University of Tokyo, 2021.

[41] G. Boca *et al.* The laser-based time calibration system for the MEG II pixelated Timing Counter. *Nuclear Instruments and Methods in Physics Research Section A: Accelerators, Spectrometers, Detectors and Associated Equipment*, 947:162672, 2019.

[42] M. Nishimura. *Positron Timing Measurement to Search for Lepton Flavor Violating Decay in MEG II.* PhD Thesis, The University of Tokyo, 2018.

[43] G. Boca *et al.* Timing resolution of a plastic scintillator counter read out by radiation damaged SiPMs connected in series. *Nuclear Instruments and Methods in Physics Research Section A: Accelerators, Spectrometers, Detectors and Associated Equipment*, 999:165173, 2021.

[44] K. Ieki *et al.* Large-area MPPC with enhanced VUV sensitivity for liquid xenon scintillation detector. *Nuclear Instruments and Methods in Physics Research Section A: Accelerators, Spectrometers, Detectors and Associated Equipment*, 925:148–155, 2019.

[45] S. Ogawa. *Liquid xenon detector with highly granular scintillation readout to search for $\mu^+ \to e^+\gamma$ with sensitivity of* 5×10^{-14} *in MEG II experiment.* PhD Thesis, The University of Tokyo, 2020.

[46] S. Kobayashi *et al.* Precise measurement of 3D-position of SiPMs in the liquid xenon gamma-ray detector for the MEGII experiment. *Nuclear Instruments and Methods in Physics Research Section A: Accelerators,*

Spectrometers, Detectors and Associated Equipment, 936:189–191, 2019. Frontier Detectors for Frontier Physics: 14th Pisa Meeting on Advanced Detectors.

[47] T. Libeiro *et al.* Novel X-ray scanning technique for in-situ alignment of photo-detectors in the MEGII calorimeter. *Nuclear Instruments and Methods in Physics Research Section A: Accelerators, Spectrometers, Detectors and Associated Equipment*, 1048:167901, 2023.

[48] S. Kobayashi. *Full Commissioning of Liquid Xenon Scintillation Detector to Search for* $\mu^+ \to e^+\gamma$ *with the Highest Sensitivity in MEG II Experiment.* PhD Thesis, The University of Tokyo, 2022.

[49] R. Onda. *Suppression of* γ *-ray backgrounds for the highest sensitivity of* $\mu^+ \to e^+\gamma$ *search in MEG II experiment.* PhD Thesis, The University of Tokyo, 2021.

[50] A. Matsushita. Calibration and Timing Resolution Evaluation of Liquid Xenon Gamma Ray Detector in MEG II experiment. Masters Thesis (in Japanese), The University of Tokyo, 2023.

[51] A. Matsushita *et al.* Commissioning of liquid xenon gamma-ray detector for MEG II experiment. *Nuclear Instruments and Methods in Physics Research Section A: Accelerators, Spectrometers, Detectors and Associated Equipment*, 1047:167877, 2023.

[52] S. Nakaura. Development of Radiative Decay Counter for ultimate sensitivity of MEG II experiment. Masters Thesis, The University of Tokyo, 2016.

[53] R. Iwai. Development and commissioning of MEG II Radiative Decay Counter. Masters Thesis, The University of Tokyo, 2017.

[54] K. Ieki *et al.* Prototype study of $0.1\%\ X_0$ and $\mathrm{MHz/cm^2}$ tolerant Resistive Plate Chamber with Diamond-Like Carbon electrodes, 2024.

[55] A. Oya *et al.* Development of high-rate capable and ultra-low mass Resistive Plate Chamber with Diamond-Like Carbon. *Journal of Physics: Conference Series*, 2374(1):012143, nov 2022.

[56] K. Yamamoto *et al.* Development of ultra-low mass and high-rate capable RPC based on Diamond-Like Carbon electrodes for MEG II experiment. *Nuclear Instruments and Methods in Physics Research Section A: Accelerators, Spectrometers, Detectors and Associated Equipment*, 1054:168450, 2023.

[57] K. Afanaciev *et al.* A search for $\mu^+ \to e^+\gamma$ with the first dataset of the MEG II experiment, 2023.

[58] K. Afanaciev *et al.* Operation and performance of MEG II detector, 2023.

[59] A. M. Baldini *et al.* Performances of a new generation tracking detector: the MEG II cylindrical drfit chamber, 2023.

[60] M. Seidel et al. Production of a 1.3 MW Proton Beam at PSI. *Conf. Proc. C*, 100523:TUYRA03, 2010.

[61] G. Cavoto *et al.* A photogrammetric method for target monitoring inside the MEG II detector. *Review of Scientific Instruments*, 92(4):043707, 2021.

[62] D. Palo *et al.* Precise photographic monitoring of MEG II thin-film muon stopping target position and shape. *Nuclear Instruments and Methods in Physics Research Section A: Accelerators, Spectrometers, Detectors and Associated Equipment*, 944:162511, 2019.

[63] H. NISHIGUCHI. *An Innovative Positron Spectrometer to Search for the Lepton Flavour Violating Muon Decay with a Sensitivity of* 10^{-13}. PhD Thesis, The University of Tokyo, 2008.

[64] A. Ferrari. The KLOE drift chamber. *Nuclear Instruments and Methods in Physics Research Section A: Accelerators, Spectrometers, Detectors and Associated Equipment*, 494(1):163–172, 2002. Proceedings of the 8th International Conference on Instrumentatio n for Colliding Beam Physics.

[65] S. Kubota, M. Hishida, J. Raun. Evidence for a triplet state of the self-trapped exciton states in liquid argon, krypton and xenon. *Journal of Physics C: Solid State Physics*, 11(12):2645, jun 1978.

[66] S. Kubota *et al.* Dynamical behavior of free electrons in the recombination process in liquid argon, krypton, and xenon. *Phys. Rev. B*, 20:3486–3496, Oct 1979.

[67] S. Kubota *et al.* Recombination luminescence in liquid argon and in liquid xenon. *Phys. Rev. B*, 17:2762–2765, Mar 1978.

[68] A. Hitachi *et al.* Effect of ionization density on the time dependence of luminescence from liquid argon and xenon. *Phys. Rev. B*, 27:5279–5285, May 1983.

[69] E. Aprile, T. Doke. Liquid xenon detectors for particle physics and astrophysics. *Rev. Mod. Phys.*, 82:2053–2097, Jul 2010.

[70] T. Haruyama *et al.* Development of a High-Power Coaxial Pulse Tube Refrigerator for a Liquid Xenon Calorimeter. *AIP Conference Proceedings*, 710(1):1459–1466, 2004.

[71] A. Baldini *et al.* Absorption of scintillation light in a 100l liquid xenon γ-ray detector and expected detector performance. *Nuclear Instruments and Methods in Physics Research Section A: Accelerators, Spectrometers, Detectors and Associated Equipment*, 545(3):753–764, 2005.

[72] S. Mihara *et al.* Development of a method for liquid xenon purification using a cryogenic centrifugal pump. *Cryogenics*, 46(9):688–693, 2006.

[73] R. Sawada. *A Liquid Xenon Scintillation Detector to Search for the Lepton Flavor Violating Muon Decay with a Sensitivity of* 10^{-13}. PhD Thesis, The University of Tokyo, 2008.

[74] H. Photonics. MPPC.

[75] T. Gosei. E1L49–3B1A–02.

[76] Kingbright. KA-3021QBS-D.

[77] A. Baldini *et al.* A radioactive point-source lattice for calibrating and monitoring the liquid xenon calorimeter of the MEG experiment. *Nuclear Instruments and Methods in Physics Research Section A: Accelerators, Spectrometers, Detectors and Associated Equipment*, 565(2):589–598, 2006.

[78] J. Spuller *et al.* A remeasurement of the Panofsky ratio. *Physics Letters B*, 67(4):479–482, 1977.

[79] S. Ritt. The DRS chip: cheap waveform digitizing in the GHz range. *Nuclear Instruments and Methods in Physics Research Section A: Accelerators, Spectrometers, Detectors and Associated Equipment*, 518(1):470 – 471, 2004. Frontier Detectors for Frontier Physics: Proceedin.

[80] S. Ritt. Design and performance of the 6 GHz waveform digitizing chip DRS4. In *2008 IEEE Nuclear Science Symposium Conference Record*, pages 1512–1515, Oct 2008.

[81] Maximum Integrated Data Acquisition System.

[82] R. Brun, F. Rademakers. ROOT — An object oriented data analysis framework. *Nuclear Instruments and Methods in Physics Research Section A: Accelerators, Spectrometers, Detectors and Associated Equipment*, 389(1):81–86, 1997. New Computing Techniques in Physics Research V.

[83] J. R. Klein, A. Roodman. BLIND ANALYSIS IN NUCLEAR AND PARTICLE PHYSICS. *Annual Review of Nuclear and Particle Science*, 55(1):141–163, 2005.

[84] A. M. Baldini *et al.* Muon polarization in the MEG experiment: predictions and measurements. *The European Physical Journal C*, 76(4):223, Apr 2016.

[85] S. Agostinelli *et al.* Geant4—a simulation toolkit. *Nuclear Instruments and Methods in Physics Research Section A: Accelerators, Spectrometers, Detectors and Associated Equipment*, 506(3):250–303, 2003.

[86] Garfield++.

[87] The Spice Page.

[88] R. E. Kalman. A New Approach to Linear Filtering and Prediction Problems. *Journal of Basic Engineering*, 82(1):35–45, 03 1960.

[89] R. Frühwirth. Application of Kalman filtering to track and vertex fitting. *Nuclear Instruments and Methods in Physics Research Section A: Accelerators, Spectrometers, Detectors and Associated Equipment*, 262(2):444–450, 1987.

[90] P. Abreu *et al.* Performance of the DELPHI detector. *Nuclear Instruments and Methods in Physics Research Section A: Accelerators, Spectrometers, Detectors and Associated Equipment*, 378(1):57–100, 1996.

[91] A. Strandlie, R. Frühwirth. Track and vertex reconstruction: From classical to adaptive methods. *Rev. Mod. Phys.*, 82:1419–1458, May 2010.

[92] R. Frühwirth, A. Strandlie. Track fitting with ambiguities and noise: A study of elastic tracking and nonlinear filters. *Computer Physics Communications*, 120(2):197–214, 1999.

[93] A. Strandlie, R. Frühwirth. Reconstruction of charged tracks in the presence of large amounts of background and noise. *Nuclear Instruments and Methods in Physics Research Section A: Accelerators, Spectrometers,*

Detectors and Associated Equipment, 566(1):157–165, 2006. TIME 2005.

[94] J. Rauch, T. Schlüter. GENFIT — a Generic Track-Fitting Toolkit. *Journal of Physics: Conference Series*, 608(1):012042, apr 2015.

[95] C. Piemonte, A. Gola. Overview on the main parameters and technology of modern Silicon Photomultipliers. *Nuclear Instruments and Methods in Physics Research Section A: Accelerators, Spectrometers, Detectors and Associated Equipment*, 926:2–15, 2019. Silicon Photomultipliers: Technology, Characterisation and Applications.

[96] R. Klanner. Characterisation of SiPMs. *Nuclear Instruments and Methods in Physics Research Section A: Accelerators, Spectrometers, Detectors and Associated Equipment*, 926:36–56, 2019. Silicon Photomultipliers: Technology, Characterisation and Applications.

[97] FARO.

[98] V. Blobel. Millepede-II, 2007.

[99] R. Barlow. Extended maximum likelihood. *Nuclear Instruments and Methods in Physics Research Section A: Accelerators, Spectrometers, Detectors and Associated Equipment*, 297(3):496–506, 1990.

[100] W. Verkerke, D. Kirkby. The RooFit toolkit for data modeling, 2003.

[101] RooFit manual.

[102] G. J. Feldman, R. D. Cousins. Unified approach to the classical statistical analysis of small signals. *Phys. Rev. D*, 57:3873–3889, Apr 1998.

[103] Cowan, Glen et al. Asymptotic formulae for likelihood-based tests of new physics. *Eur. Phys. J. C*, 71(2):1554, 2011.

[104] R. D. Cousins, V. L. Highland. Incorporating systematic uncertainties into an upper limit. *Nuclear Instruments and Methods in Physics Research Section A: Accelerators, Spectrometers, Detectors and Associated Equipment*, 320(1):331–335, 1992.

[105] J. Conrad *et al.* Including systematic uncertainties in confidence interval construction for Poisson statistics. *Phys. Rev. D*, 67:012002, Jan 2003.

[106] S. S. Wilks. The Large-Sample Distribution of the Likelihood Ratio for Testing Composite Hypotheses. *The Annals of Mathematical Statistics*, 9(1):60–62, 1938.

[107] C. Fronsdal, H. Überall. μ-Meson Decay with Inner Bremsstrahlung. *Phys. Rev.*, 113:654–657, Jan 1959.